

Polymer - Carbon Nanostructures Composites: from Chemistry to Physics, to Material Science

THÈSE N° 7368 (2016)

PRÉSENTÉE LE 15 DÉCEMBRE 2016

À LA FACULTÉ DES SCIENCES DE BASE

LABORATOIRE DE PHYSIQUE DE LA MATIÈRE COMPLEXE

PROGRAMME DOCTORAL EN SCIENCE ET GÉNIE DES MATÉRIAUX

ÉCOLE POLYTECHNIQUE FÉDÉRALE DE LAUSANNE

POUR L'OBTENTION DU GRADE DE DOCTEUR ÈS SCIENCES

PAR

Maryam MAJIDIAN

acceptée sur proposition du jury:

Prof. P. Murali, président du jury
Prof. L. Forró, Dr A. Magrez, directeurs de thèse
Prof. J. Coleman, rapporteur
Prof. J. W. Seo, rapporteuse
Prof. J. Brugger, rapporteur



ÉCOLE POLYTECHNIQUE
FÉDÉRALE DE LAUSANNE

Suisse
2016

One, remember to look up at the stars and not down at your feet. Two, never give up work. Work gives you meaning and purpose and life is empty without it. Three, if you are lucky enough to find love, remember it is there and don't throw it away.

- Stephen Hawking

To Ramin...

Abstract

Synthesis and characterization of polymer-based composites containing carbon nanostructures is the focus of this dissertation. The main polymer which has been used for this research is SU8, a popular epoxy in microelectromechanical systems. The motivation of the work is to overcome the drawbacks of SU8 e.g. (high electrical and thermal resistance, brittleness) by addition of the carbon-based nanofillers. Understanding the chemical and physical characteristics and properties of the obtained composites is the crucial step towards the optimized composite design.

In this thesis, three classes of carbon nanostructures have been used as composite fillers: 2-dimensional graphene, 1-dimensional carbon nanotubes and 0-dimensional onion-like carbons. The idea behind this material selection is to study the influence of dimensionality of the fillers on the electrical transport properties of the composites. In addition, we have performed comprehensive characterizations of graphene composites and addressed some questions about carbon nanotubes and nano-onions composites.

SU8-graphene composites were prepared using solution mixing method. The microstructure analysis of the composite with scanning and transmission electron microscopy showed a homogeneous dispersion of the graphene flakes. The study of electrical properties of the composite as the function of the filler loading exhibited superior electrical conductivity compared to other graphene-base polymer composites. It also revealed vanishingly low percolation threshold and the transport exponent, $t \approx 7$, which is far larger than what is expected ($t \approx 2$) for percolation model. Therefore, we suggested the tunneling model as the dominant transport mechanism. Likewise, the study of the viscoelastic behavior of the composites showed that the rheological percolation is very close to zero, which we attribute to the polymer chain restriction due to the high aspect ratio graphene fillers (the calculated value for graphene aspect ratio based on rheological percolation model is ~ 482). The mechanical properties were evaluated with nanoindentation technique. 67% enhancement for Young's modulus and 75% enhancement for hardness were acquired. The possibility of the linkage between the filler and the matrix was investigated by spectroscopy techniques including Photoluminescence, Raman and Fourier Transform Infrared spectroscopy. Our findings suggest that the presence

of graphene has a dual effect on the ongoing chemical reactions during the polymerization of the composite. On one hand, graphene flakes may hinder the cross-linking reactions of the SU8; on the other hand covalent bonds are formed between SU8 and the functional groups on the surface of the graphene flakes.

SU8-CNT composites were synthesized using both randomly dispersed and well-aligned tubes. For composites with randomly dispersed CNTs, the effect of nanotube length and polydispersity was investigated with experimental approach, for the first time. We have shown that the conductivity in such composites is proportional to mean length of CNTs, L_n , rather than weighted average length, L_w (which is predicted by theory). For the case of aligned CNTs, we have measured the thermal conductivity, κ , parallel and perpendicular to the orientation of the tubes, which exhibited an anisotropy ($\kappa_{\parallel}/\kappa_{\perp}$) close to 20. The study was motivated by thermal management applications. From the same composite, lamellas with thickness ranged 20 – 100nm were prepared using ultramicrotomy technique, for proton channeling applications. The successful sample preparation and pioneering channeling experiments give an encouraging outlook for future investigations in this field.

Composites containing Poly(methyl methacrylate) (PMMA) as matrix and onion-like carbon as fillers were prepared for transport studies. The temperature- and pressure-dependence of the conductivity were measured. Due to the complexities associated to non-homogeneous structure of these composites, we do not have a unified model to describe the dependence of conductivity upon concentration, temperature and pressure, and this question has remained open.

Key words:

Nanocomposites, SU8 epoxy, Graphene, Carbon Nanotube (CNT), Onion-Like Carbon (OLC), Electrical Transport, Mechanical Properties, Thermal Conductivity, Optical Spectroscopy, Rheology, Photolithography, Polydispersity.

Résumé

Ce travail de thèse a pour sujet la synthèse et la caractérisation de composites à base de polymères et de nanostructures de carbone. Le polymère principalement utilisé est le SU8. C'est une résine epoxy utilisée dans les systèmes de microélectroniques. Néanmoins, ce polymère est non conducteur électronique et thermique. Il possède des propriétés mécaniques limitées. L'objectif fut d'améliorer ces propriétés tout en conservant celles qui font du SU8 un polymère très utile. La compréhension et la caractérisation des propriétés physico-chimiques des composites est une étape essentielle à l'optimisation des caractéristiques de ces nouveaux matériaux. Dans cette thèse, trois classes de nanostructures de carbone ont été utilisées : le graphène - 2D, les nanotubes - 1D et les oignons de carbone - 0D. Ceux-ci ont été sélectionnés afin d'étudier l'influence de leur dimensionnalité sur les propriétés de transport thermiques et électriques. En plus de cette étude, quelques expériences supplémentaires ont été entreprises pour chacune des trois nanostructures de Carbone.

Pour le graphène, la synthèse ainsi que l'étude de la microstructure des composites a montré que ces matériaux étaient homogènes. Les particules de graphène sont distribuées statistiquement dans la matrice de SU8. Ces matériaux possèdent des niveaux de conductivités supérieurs à d'autres composites Graphène - Polymère en particulier pour les fractions de graphène les plus faibles. L'étude détaillée des mécanismes de conduction révèle que le mécanisme de transport se fait par effet tunnel dans ces composites. D'autre part les propriétés viscoélastiques ainsi que l'étude par spectroscopie optique montre une restriction des chaînes polymériques car les flocons de graphène interfèrent dans la réticulation assistée par ultraviolet du SU8. Néanmoins, ces matériaux restent performants pour la photolithographie avec une bonne résolution spatiale malgré la présence de graphène. Au final, les mesures des propriétés mécaniques montrent des performances bien supérieures pour les composites SU8-Graphène.

Dans les cas des composites SU8-Nanotubes, deux études ont été menées. La première a permis l'étude de l'influence de la longueur des nanotubes sur les propriétés de transport électrique. Les résultats montrent pour la première fois l'effet de la distribution de la longueur des tubes sur le transport électrique des composites. Elle révèle que les niveaux de conductivité

sont proportionnels à la longueur moyenne des nanotubes. La deuxième étude utilisant des forêts de nanotubes (structures de nanotubes parallèles) a permis de mettre en évidence une forte anisotropie (d'un facteur proche de 20) dans la conductivité thermique. Celle -ci est facilité le long des nanotubes tandis qu'elle est plus faible perpendiculairement aux nanotubes. Des études préliminaires de canalisation ionique à travers de coupes transversales de ces composites fabriqués a partir des forêts de nanotubes sont très encourageant pour de futures études plus approfondies.

La dernière partie de ce manuscrit est consacrée à l'étude de composites de PMMA fabriqués par mélange avec des oignons de carbone. Les niveaux de conductivité mesurés sont plus élevés que pour les composites à base de nanotubes ou de graphène pour des fractions volumiques nominales équivalentes. Ceci est dû à une inhomogénéité marquée dans le cas des oignons de C. Nous n'avons pas réussi à développer un modèle unique qui permette d'expliquer la dépendance de la conductivité des composites PMMA - Oignons en fonction de la température et de la pression. Cette question reste donc ouverte à l'heure de la rédaction de ce manuscrit.

Mots clefs :

Nanocomposites, Résine Epoxy SU8, Graphène, Nanotubes de Carbone, Oignons de Carbone, Transport Electrique, Propriétés Mécaniques, Conductivité Thermique, Spectroscopie Optique, Rhéologie, Photolithographie, Poly-dispersion

Contents

Abstract (English/Français/Deutsch)	i
List of figures	v
List of tables	vii
Introduction	1
1 Background information	7
1.1 Nanocomposites	7
1.2 Carbon nanomaterial fillers	8
1.2.1 2 Dimentional fillers: Graphene	9
1.2.2 1 Dimentional fillers: Carbon nanotubes	10
1.2.3 0 Dimentional fillers: Carbon nano-onion	12
1.3 Polymer matrix	13
1.3.1 SU8	13
1.4 Transport properties in conductive polymer composites	18
1.5 Mechanical properties of composites	25
1.6 Thermal properties of the polymer composites	29
1.7 Optical spectroscopy	31
1.7.1 Raman Spectroscopy	31
1.7.2 FTIR Spectroscopy	32
1.8 Rheology	34
1.9 Applications	38
2 Composites with 2D fillers: SU8-graphene composites	41
2.1 Composite preparation	41
2.1.1 Structural characterization	45
2.2 Composite patterning	47

Contents

2.3	Properties of the composites	51
2.3.1	Electrical characterization	51
2.3.2	Mechanical characterization	57
2.3.3	Optical characterization	63
2.3.4	Rheological properties	75
2.4	Conclusion	80
3	Composites with 1D fillers: SU8-carbon nanotube composites	81
3.1	Composites with controlled length of nanotubes	82
3.1.1	Motivation	82
3.1.2	Theoretical studies	82
3.1.3	Preparation Methods	84
3.1.4	Composite preparation and structural characterization	86
3.1.5	Electrical characterization	88
3.1.6	Summary	91
3.2	SU8 composites with aligned carbon nanotubes	92
3.2.1	Channeling of charged particles	92
3.2.2	Anisotropic thermal conductivity	100
3.3	Conclusion	109
4	Composites with 0D fillers: PMMA-carbon nano-onion composites	111
4.1	Motivation	111
4.2	Materials and measurement techniques	112
4.3	Structural characterization	113
4.4	Room temperature electrical conductivity	114
4.5	Temperature dependence of the electrical conductivity	118
4.6	Conclusion	123
5	Conclusions and outlook	125
A	Statistical analysis of the nanotube lengths	129
A.1	Distribution of the length for as-milled CNTs	129
A.2	CNTs with bimodal distribution of lengths	129
	Bibliography	153
	List of acronyms	155
	Acknowledgements	169

Curriculum Vitae

171

Prologue

This is a doctoral dissertation in materials sciences. This branch of technical sciences is nowadays an interdisciplinary field that expands to chemistry, physical chemistry, physics, advanced characterization techniques, engineering skills, very often mathematical modellings and good feeling for applications. It has become one of the most complex branches in natural sciences. The advent of nanotechnology has given a new dimension to this field, as materials exhibit novel and superior physical, chemical, and biological properties, functions and phenomena owing to their nano-scale size.

During the past four years of my doctoral training, I worked on the topic of carbon nanostructure based composites. I dealt with challenges in chemistry of nano-materials, and was more exposed than ever to physical approaches, since this work is done in the laboratory of condensed matter physics.

Composites, as the name tells, are composed of two or more components. The goal is to obtain a material which has a superior property than the individual components themselves. For example, it is easy to prepare in a desired form, but it is weak against mechanical load, it deforms, it breaks easily. This could be radically changed if one mixes in carbon fibers or carbon nanotubes. These fillers lend to the matrix a mechanical strength but are still keeping it light. The procedure of making composites is very much application driven. We are looking for materials which are useful in products. Few examples of application of composites are given below.

The first example is the “Solarimpulse”, the revolutionary airplane that uses only solar energy for propulsion. The power of its electromotors is not comparable with the turbines or jet engines of the conventional airplanes, so Solarimpulse has to be light but mechanically solid. This very elegant airplane is made of carbon and glass fibers in a polymer matrix. It has demonstrated in July 2016 that a world around flight exclusively based on solar energy is feasible. The second aviation based example is the Orion space capsule, which is designed for

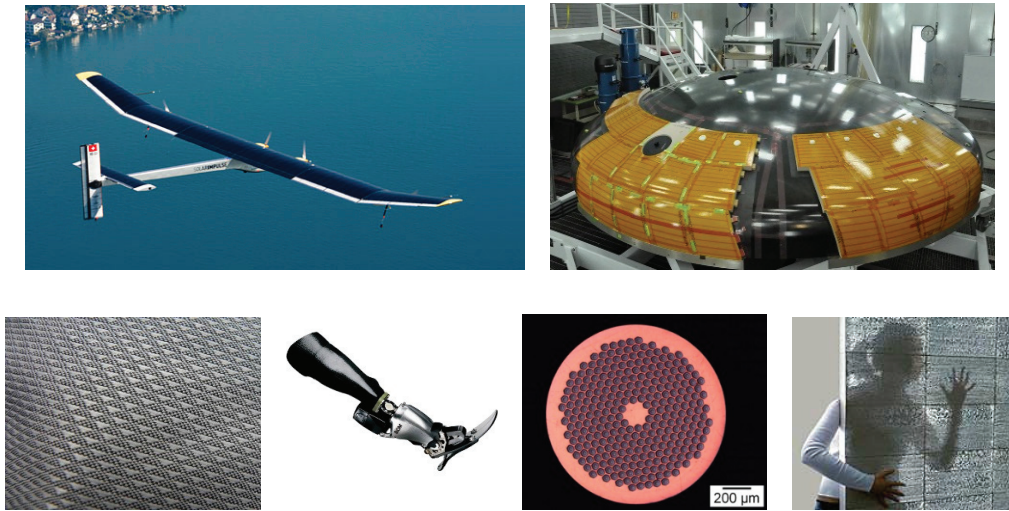


Figure 1: A limited number of illustrations showing the omnipresence of composite materials in everyday life (from upper left to lower right). Solarimpulse, revolutionizing aviation, is made of carbon and glass composites; Orion space capsule's heat shield made of a titanium and carbon fibers withstanding temperatures beyond 2000°C; antibacterial tissue using silver nanowires; bioprosthetics made of carbon composites; metallic composite of superconducting wires made up of Nb_3Sn filaments, surrounded by a low resistivity copper matrix; transparent concrete composite with thousands of parallel optical fibers. (Source: Google's image gallery).

bringing back a crew from missions near the moon. Its heat shield is composed of a titanium skeleton and carbon fibers skin. It withstands outside temperature (coming from the friction with the atmosphere) over 2000 °C, while the inner one stays in the mid 20°C.

Textiles interwoven from silver nanowires have antibacterial effects and serve health issues. Bio-prosthetics based on carbon fibers are very much developed which largely help the mobility of handicapped persons. Very useful are metallic composites, for example in producing high magnetic fields needed in MRI, and needed in medical diagnostics. The image in Figure 1 shows a micron thick Nb_3Sn superconducting wires embedded in copper, which serves for thermal management and failure protection. The last illustration is showing a transparent concrete which is realized by embedding into the matrix parallel running glass fibers. It is very much appreciated in high-end constructions where money is not an issue.

My PhD program has targeted a very popular epoxy, which was developed and patented by IBM in 1989, it is called SU8 (Figure 2). The great advantage of SU8 is that one can selectively polymerize it by UV illumination (in other words doing lithography), one can make long pillars, hollow cylinders with internal structure, gears or other complex geometries at will, or even one can make AFM cantilevers for multiple purposes, e.g. bio-sensing. They are used

extensively in microfluidics, in micro and nano-mechanics, for making research tools etc. This is absolutely a great material for ease of formability, but it has some less advantageous properties: it is electrically insulating (it can charge up easily), mechanically it is brittle, and it is a lousy thermal conductor. These properties could be real drawbacks; it could even result in a device failure (just to imagine the accumulation of static charges on SU8 component which can cause electric breakdown).

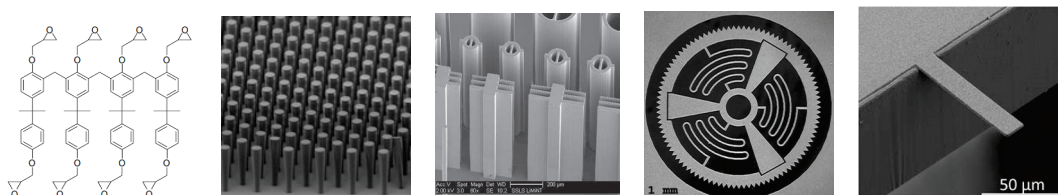


Figure 2: The main matrix of the composites in this dissertation is the SU8 epoxy. The sketch of the chemical formula is shown, and few representative structures made of this epoxy by UV lithography: pillars, channels, gears, cantilever. (Source: google image gallery).

If one uses SU8 as a matrix for a composite and introduces fillers which have a strength, electrical and thermal conduction, one can get a great material. The fillers that we have chosen are carbon nanostructures, which have been the subject of basic research in the last 25 years, but they are getting more and more into applications. These nanostructures are: graphene, carbon nanotubes and onion-like carbons. One fact can emphasize how important, how unique are these structures which is the following: two of them, graphene and the spherical carbon molecule have received the Nobel prize in 1996 and 2010. They revolutionized condensed matter physics and organic chemistry. In Figure 3, high resolution electron microscopy images (HRTEM) are shown with corresponding graphical sketches.

My task was to introduce these carbon nanostructures into the SU8 matrix and prepare

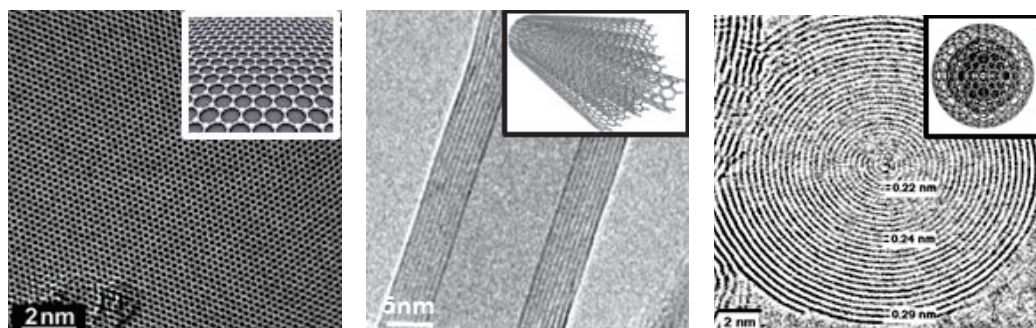


Figure 3: HRTEM images of graphene, multi-walled carbon nanotubes and carbon onions and their graphical sketches for easier visualization. (Source: google image gallery).

Contents

composites where the fillers have different concentrations with the goal of optimizing the composites' properties. For graphene and carbon nanotubes it is known that they can improve the conductivity and mechanical response of the composites, while for onion-like carbons it was unknown. In a good composite, one needs to disperse homogeneously the fillers, which means that the matrix, the SU8 should wet well the carbon nanostructures. But it does not. So one has to use a good surfactant, which helps the wetting and the dispersion. To reduce the brittleness one needs to bind the carbon nanostructures to the matrix, otherwise there is no efficient improvement of the mechanical properties. But the chemistry of these, so called sp^2 carbon structures is difficult. One has to open the sp^2 bond, transform it into sp^3 , but in a controlled manner. Since with the sp^3 bonds, one loses the conductivity, which is counterproductive. So one has to optimize: open some of the sp^2 bonds in order to bind the nanostructures to the SU8, but keep a good number of them to preserve the conductivity. Once we have a series of concentrations, one has to measure them, characterize their physical properties. For instance, one has to know how the conductivity evolves with the volume fraction of carbon nanostructures. Once it is measured, one has to model it in order to better understand the charge transport in such a composite, with the goal to optimize it in the future. The same should be done for the thermal conductivity and mechanical performance of the composites. The composites viscosity is also important for applications, so it should be measured and controlled. Once we are convinced that we have a good composite, with very advantageous properties, there remains still the question whether we can process it by UV illumination and lithography into well-defined microstructures. The flow chart of research process is shown in Figure 4 for the case of graphene.

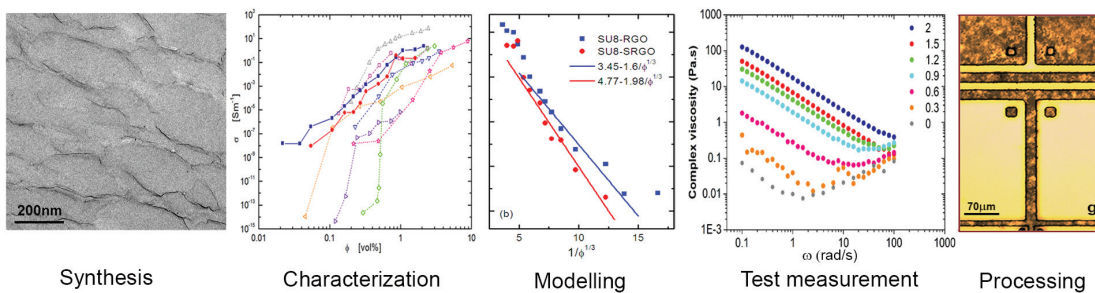


Figure 4: Illustration of the steps in research, from synthesis to lithographic processing, for graphene-SU8 composites.

This work is presented in details for graphene, and some questions were addressed for carbon nanotubes and carbon onions, as well. The outline is the following. In the 1st chapter I present the materials (SU8, carbon nanostructures) and the background notions about the properties of carbon-based polymer composites. In the 2nd chapter, I studied synthesis, characterization

and processing of composites with 2-dimensional fillers, graphene. A comprehensive picture of properties of the composite is presented. In the 3rd chapter, in the first part I will address one of the important but less investigated issues regarding the carbon nanotube, and in general, 1-dimensional fillers in composites. In the second part, having an eye for applications, the thermal properties of SU8 composites with aligned carbon nanotubes is presented, and the potential of such composite for channeling of charged particles is considered. In the 4th chapter, the electrical transport properties of polymer composites with 0-dimensional spherical carbon onions is addressed for the sake of fundamental scientific studies. In the last chapter the conclusions and outlook are given.

At the end, I should say that I enjoyed a lot these 4 years of training and I am very glad to contribute to this research. I have learnt how to put together different pieces of the puzzle: material synthesis, physical measurements, modelling and processing in order to develop a useful material for applications.

1 Background information

1.1 Nanocomposites

During the last few decades, numerous efforts have been devoted to the design and development of nano-structured materials with novel properties and engineered functionalities. One of the most widely investigated types of nanomaterials are polymer nanocomposites, which consist of nano-metric “fillers” embedded in a polymer “matrix”. Significant enhancements have been reported for polymer nanocomposites compared to their counterparts with conventional micron-sized filler. The most important morphological characteristic of the reinforcement nanofillers is the surface area to volume ratio of the nanofillers. With a large interfacial area (thanks to 3 orders of magnitude miniaturization in particle diameter, layer thickness, or fibrous material diameter from micrometer to nanometer) the properties of the composite become dominated by the properties of the fillers. Therefore, polymer nanocomposites deliver significant property enhancements at much lower loadings compared to polymer composites. Among these properties, one can remark low electrical resistivity and percolation threshold, improved thermal conductivity and thermal stability as well as reduced gas permeability and coefficient of thermal expansion. In addition, improved mechanical properties such as high tensile modulus, tensile strength, stiffness and toughness have been achieved, due to the considerably enhanced load transfer efficiency in these composites [1]. These multifunctional property enhancements in lower component weight along with possibly simplified processing, may create new applications of polymers [2, 3]. Future multifunctional materials may possess integrated sensing, actuation, energy storage, and healing capabilities, much like biological systems [4]. When designing a nanocomposite, the material properties are tailored for the desired performances based on selection and processing of matrix and filler materials. Engineering and optimization of the filler/matrix interface through a bottom-up

Chapter 1. Background information

approach, requires a comprehensive understanding of the material's characteristics from nano-scale phenomena to macroscopic evidences.

In this thesis we have investigated nanocomposites based on two polymers commonly used for microelectronics and MEMS fabrication: the epoxy resin SU8 and Poly (methyl methacrylate) (PMMA) , containing carbon nano-structures with different morphologies and aspect ratios. In this chapter, first each of these materials and their properties will be briefly introduced. Then, we present the background notions about the common properties of composite materials in general, based on which this work is developed.

1.2 Carbon nanomaterial fillers

Carbon nanomaterials have attracted significant scientific interest in development of novel functional materials due to their outstanding properties. Nowadays, one can find carbon based composites almost everywhere, from aerospace, automotive to medical technology. An interesting opportunity provided by carbon nanostructures as fillers, is the variety in their morphology (1.1) [5].

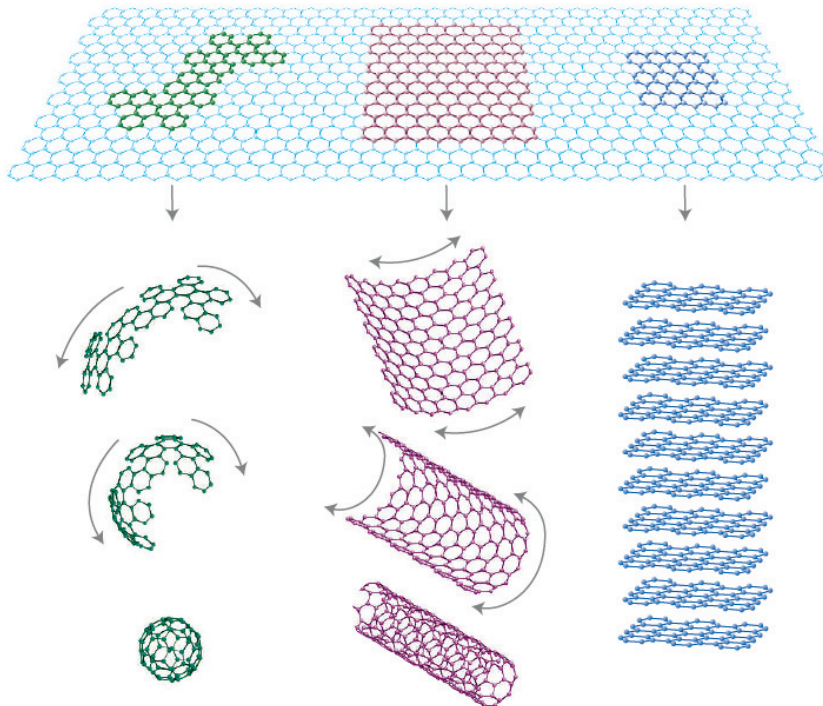


Figure 1.1: Various morphologies and dimensionalities of carbon nanostructures [5]. Copyright 2007, Nature Publishing Group.

The importance of filler morphology is due to its influence on the overall properties of the polymer composites. As reported in the literature [6], the filler morphology can affect the content of fillers in the composite, and therefore, alter flexural strength, flexural modulus, hardness, and fracture toughness of the composites. Further more, it is very well-known that the morphology of fillers (spherical, platelet or fibrous), as well as their aspect ratio have a substantial impact on electrical properties and the percolation threshold (see section 1.4) of nanocomposites. The viscoelastic properties of polymer composites and consequently their ease of processing is also highly dependent on the filler morphology (subsection 2.3.4).

Three main categories of carbon nano-structures have been studied in this dissertation: 0D-onion-like carbon (OLC) particles, 1D- carbon nanotubes (CNT) and 2D- graphene flakes. The surface area to volume ratio is an important morphological characteristic of these fillers. In the following we briefly introduce each type of these materials.

1.2.1 2 Dimentional fillers: Graphene

Graphene can be described as a one-atom thick layer of the mineral graphite. Many layers of graphene stacked together effectively form crystalline flake graphite. The work of Novoselov et al. in 2004 [7], ignited the exponential increase of interest in graphene research. A single layer of graphene consists of hexagonal packed structures of carbons. This layer of sp^2 bonded carbons has shown many extraordinary properties such as, high carrier mobility at room temperature ($10000 \text{ cm}^2 \text{ V}^{-1} \text{ s}^{-1}$) [7, 5], remarkable theoretical specific surface area ($2630 \text{ m}^2 \text{ g}^{-1}$), good optical transparency (97.7 %), high Young's modulus (1 TPa) and outstanding thermal conductivity ($3000\text{--}5000 \text{ W m}^{-1} \text{ K}^{-1}$) [8, 9]. Advantages like, possibility of preparation by range of techniques, along with unusual properties like the ones named earlier has made graphene to be considered as a promising material for nanoelectronic and optoelectronic applications. One of the most immediate applications for graphene is its integration in polymer matrices to form advanced multifunctional composites. The production of such composites requires the graphene sheets to be produced in sufficient scale [8]. High quality defect-free graphene have been produced by several techniques, such as micro-mechanical exfoliation of graphite, growth by chemical vapor deposition (both of discrete monolayers onto a substrate and agglomerated powders), and growth on crystalline silicon carbide [2]. However, these methods do not concede large enough quantities for the manufacturing of composites.

One scalable, cost-effective and versatile approach for the production of graphene, is chemical exfoliation of graphite and its derivatives (such as graphite oxide) from colloidal suspensions.

Chapter 1. Background information

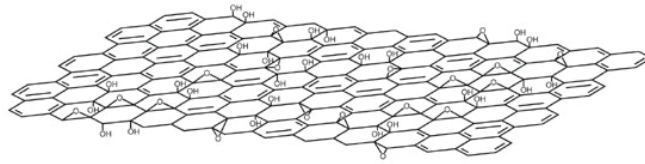


Figure 1.2: Chemical structure of graphene oxide (GO) [11]. Copyright 2009, Nature Publishing Group.

Briefly, the layers of graphite are being isolated by proper chemical treatment followed by sonication [10]. The outcome of these steps is Graphene Oxide (GO) as shown in Figure 1.2.

The sp^2 network of graphene is strongly disrupted due to the bonding between carbon atoms and functional groups mainly hydroxyl and epoxide groups (Figure 1.2) and consequently the electrical properties of graphite are significantly diminished. To restore the graphitic structure and electrical conductivity of the GO flakes, various methods have been suggested [12, 11]. The final product of these chemical treatments would be Reduced Graphene Oxide (RGO). The schematic summary of this process is depicted in Figure 1.3. Although the electrical conduction of RGO is still much lower than that of graphene sheets, the presence of functional groups such as epoxide, carbonyl and carboxyl on the surface of RGO flakes facilitate the dispersion of the flakes within the matrix and allows for stronger bonding with polymer matrix.

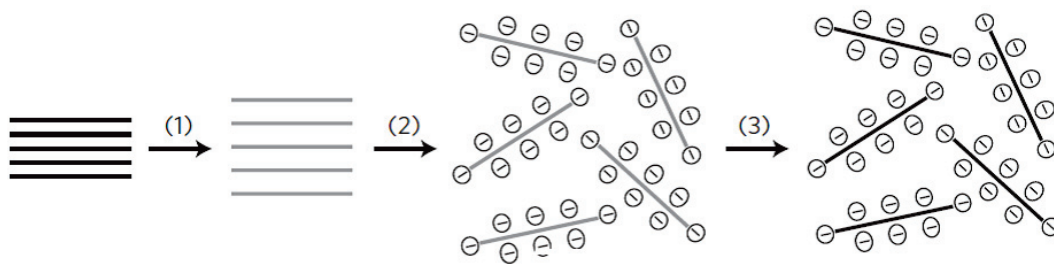


Figure 1.3: Chemical process of reduced graphene oxide synthesis.(1) Oxidation of graphite to graphite oxide. (2) Exfoliation of graphene oxide in water by sonication of graphite oxide. (3) Controlled reduction of graphene oxide sheets [11]. Copyright 2009, Nature Publishing Group

1.2.2 1 Dimensional fillers: Carbon nanotubes

Carbon nanotubes consist of one (single wall nanotube) or several (multiwall nanotube) sheets of graphene rolled around a certain axis. The morphology of a carbon nanotube is defined by

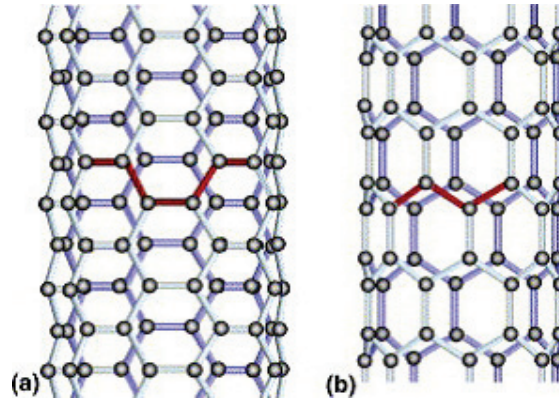


Figure 1.4: Atomic structures of (a) armchair and (b) zig-zag carbon nanotubes [13]. Copyright 2001 Elsevier Science Ltd.

the orientation and magnitude of its chiral vector, which defines how the graphene sheet is "wrapped up" to form the nanotube [13]. The possible configurations are called armchair and zigzag, shown in Figure 1.4.

A review on different production methods of CNT, along with a detailed study of CNT growth by CVD method is presented in Ref.[15].

Single wall carbon nanotubes (SWCNTs) have remarkable physical properties. They have a relatively low density of about 1.33 to 1.40 gcm^{-3} and an elastic modulus comparable to that of the diamond (1.2 TPa). The tensile strength is higher than that of any steel (2 GPa). They also have a great resilience, bending elastically to large angles. Their current carrying capacity is estimated to reach values of 109 Acm^{-2} , three orders of magnitude higher than

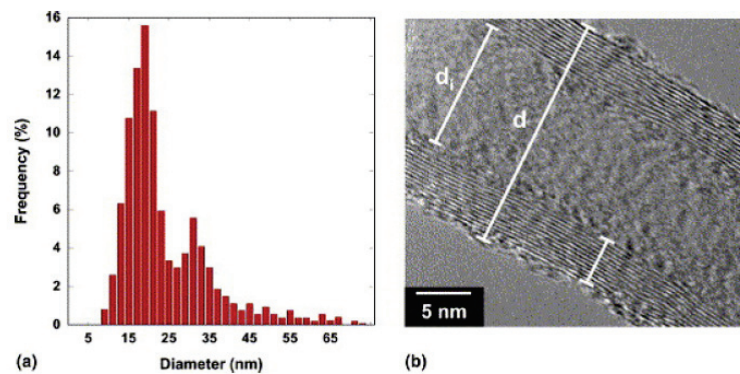


Figure 1.5: (a) Diameter distribution of CVD-grown multi-walled carbon nanotubes (b) TEM micrographs of a multiwall carbon nanotube taken from Ref.[14]. Copyright 2003 IOP Publishing.

Chapter 1. Background information

that of copper. In addition, their thermal conductivity has a value close to $6000 \text{ Wm}^{-1}\text{K}^{-1}$, twice that of the diamond. These excellent properties, along with large aspect ratios, have provided a huge research interest in nanotube composites for both structural and functional applications. One should point out that the producing of MWCNTs in large scales is easier. MWCNTs have similar properties to those of SWCNTs, except that their aspect ratio is lower since their diameters are larger. In particular, MWCNT lengths and diameters obtained from common growth techniques such as Chemical Vapor Deposition (CVD) are difficult to monitor. Instead of a fixed value a certain distribution gives a more precise idea of the diameter. Using CVD-grown carbon nanotubes and TEM micrographs, Thostenson et al. analyzed the MWCNT outer diameter distribution [14].

1.2.3 0 Dimensional fillers: Carbon nano-onion

Onion-like carbon (OLC) nanostructures, also called carbon onions, are quasi-spherical particles consisting of multi-shell graphitic layers. They have moderately high specific surface area of $\sim 500 \text{ m}^2/\text{g}$, and electrical conductivity of $\sim 4 \text{ S/cm}$. The transformation of ultra-dispersed nano-diamonds through annealing above 1200 K results in the production of carbon onions [16].

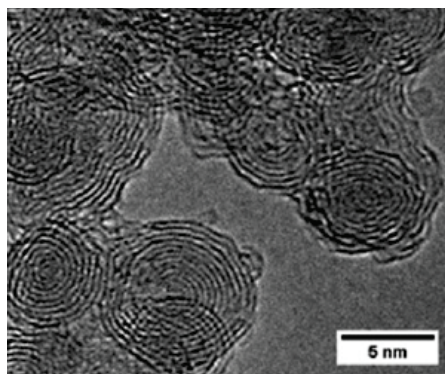


Figure 1.6: TEM images of OLC aggregates with average primary particle size of 4-7 nm [17].

Figure 1.6 illustrates TEM micrograph of OLC clusters. OLC particles have average primary size of about 4–7 nm. However, OLCs have a tendency to form agglomerates, covering the onions by graphitic interlayer, leading to a so-called pod-of-peas geometry [18]. Typical size of OLC agglomerates varies between 100-200nm depending on the primary size and shape of the nano-diamonds, but also the method and temperature of the OLC preparation [16, 18]. Transformation of nano-diamonds to OLC and the obtained structures at different temperatures are shown schematically in Figure 1.7.

Many efforts have been devoted to understand the phase transformation from nanodiamond (ND) to carbon onions and the final structure OLCs with both experimental studies and computer modeling [19]. onion-like carbons (OLCs), thanks to their light weight and inert nature are very favorable for electromagnetic(EM) shielding applications. Moreover, OLC EM shielding capacity can be controlled by optimizing the OLC cluster size and nanodiamond annealing temperature [18]. Having high charge-discharge rate abilities make OLC an interesting candidate for high power applications. They are also attractive for energy storage applications, acting as electrical double-layer micro-capacitors [19].

These potential applications, along with their specific spherical morphology made the OLCs interesting material for the theoretical study of their behavior in polymer composites.

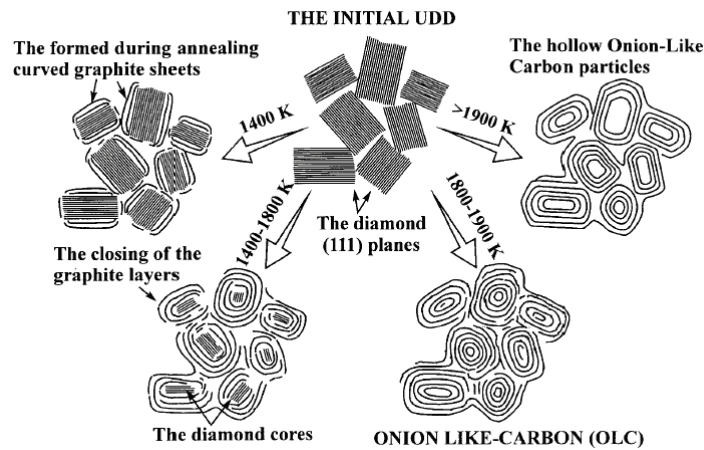


Figure 1.7: The scheme of OLC formation model [20]. Copyright 2001 Elsevier B.V.

1.3 Polymer matrix

1.3.1 SU8

SU8 is a negative tone epoxy resin which has been developed by IBM in 1989. Great intrinsic properties of SU8 such as: high sensitivity, high resolution, low optical absorption, high thermal stability and in particular the chemical and mechanical robustness led the MEMS (Micro Electro Mechanical Systems) community to use it for fabricating structural and active components of their device [22, 23]. For the preparation, an organic solvent (Normally gamma-butyrolactone, GBL) is used for dissolution of the EPON® resin that is the main component of SU8 photoresist, the amount of solvents defines the viscosity and consequently the achievable

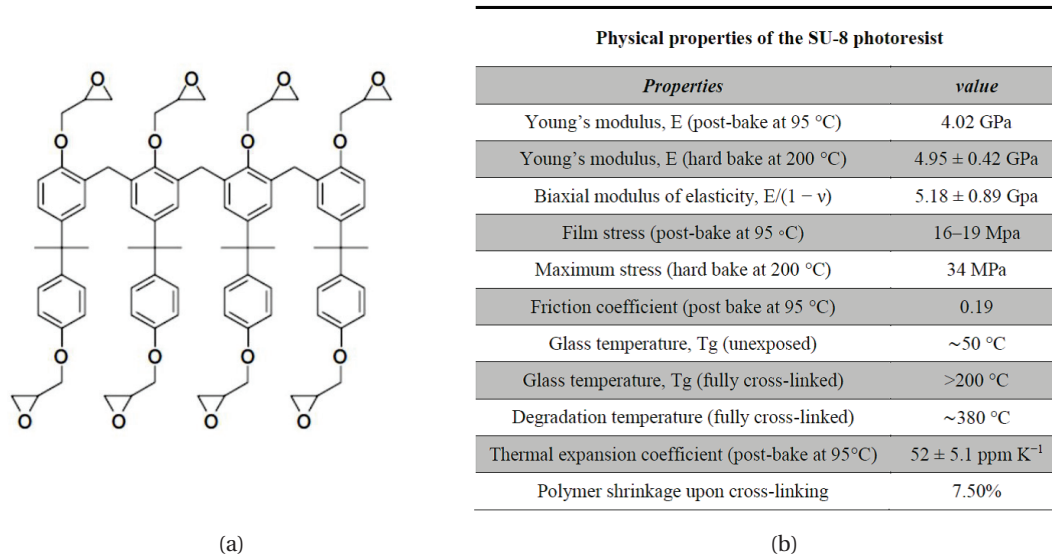


Figure 1.8: (a) Chemical structure of the Bisphenol A Novolak epoxy oligomer contained in SU-8 formulations. Eight reactive epoxy functionalities allow a high degree of cross-linking after photo-activation [21]. (b) Table of properties for the SU8.

film thickness. Finally a Photoinitiator (PI) is added, e.g. 10 wt% of the resin mass [23] to activate the cationic polymerization of the SU8 upon UV-irradiation. SU8 is particularly well suited for thick-film applications, e.g. high aspect ratio structures, since it can be dissolved at high concentrations and demonstrates a low absorbance in the near-UV range [24]. Figure 1.8 illustrates the molecular structures of the SU8 oligomer that consists of eight epoxy groups along with physical properties of SU8 photoresist.

The most common process of fabrication of high aspect ratio patterns is UV assisted photolithography. This fabrication consists of a combination of thermal and UV curing. The

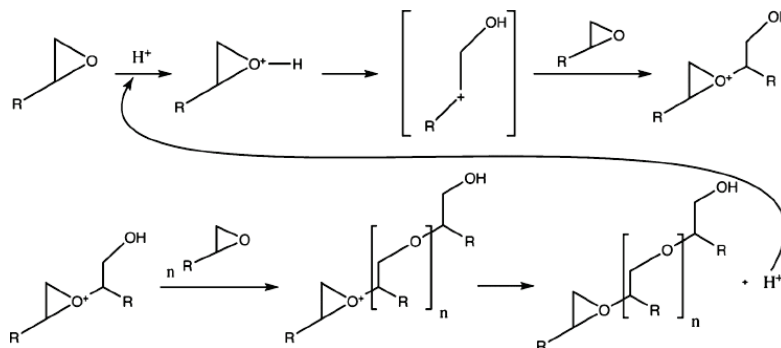


Figure 1.9: The mechanism of cationic polymerization of the SU8 [25]. Rights managed by AIP Publishing LLC.

process steps include: substrate pretreatment, coating, soft baking in order to remove the solvent, UV exposure, post-exposure baking to continue curing and development, rinsing, drying and hard baking. Upon irradiation, the photo initiator decomposes to form hexafluoroantimonic acid that protonates the epoxides on the oligomer. These protonated oxonium ions are available to react with neutral epoxides in a series of cross-linking reactions after application of heat. The cationic mechanism for SU8 cross-linking is presented in Figure 1.9. Each monomer molecule, Figure 1.8, contains eight reactive epoxy sites, and therefore high degree of cross-linking can be obtained after photothermal activation. This results in high mechanical and thermal stability of the lithographic structures after processing [21].

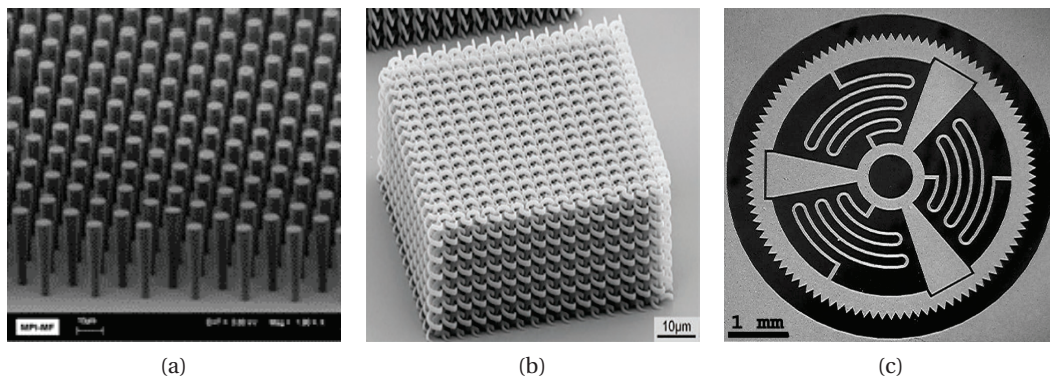


Figure 1.10: (a) High aspect ratio pillars made out of SU8 [26] (b) 3D bi-chiral structures made from SU-8 negative photoresist by two-photon polymerization [27] (Copyright 2009 WILEY-VCH Verlag GmbH & Co. KGaA, Weinheim), (c) Optical image of a 5 mm diameter wheel made out of SU8 nanocomposite [28] (Copyright 2006 Elsevier B.V.).

Great properties of SU8 have led to significant interest in SU8 for different applications in MEMS area. For example in microfluidic (Figure 1.10a) [26], 3D patterning (Figure 1.10b) [29], packaging and sensors [30], microparts and micromolds (Figure 1.10c) [28], lab on a chip [26], Bio-MEMS [31], cantilevers for sensing applications [32] and many more applications.

Besides attractive features, SU8 has few drawbacks: some applications require easy removal of SU8 from the substrate that is a challenging issue even when using sacrificial layers. SU8 is an electrically insulating material, with very low thermal conductivity, high internal stress which leads to the bending of the substrate, and it is also quite brittle [21, 26, 33]. In order to overcome some of these disadvantages and add more functionalities, especially conductivity, our strategy has been to prepare SU8 composite containing carbon-based nanofillers.

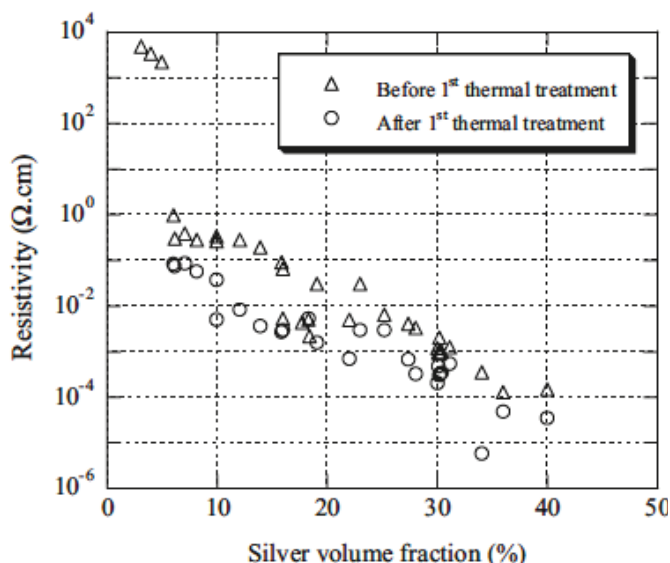


Figure 1.11: Evolution of the electrical resistivity of the SU8 silver composites versus silver volume fraction, before and after thermal treatment. The percolation threshold is at 6 vol% [34]. Copyright © 2005 WILEY-VCH Verlag GmbH & Co. KGaA, Weinheim.

Review of SU8-based composites

Modification of SU8 properties incorporating of nanostructures has been the concern of many researchers in the past decade. In the frame of our work, we review some of the studies that have been done on SU8 composites for different purposes. In a pioneering work, Jiguet et al. [34] investigated SU8 Silver particles (200 nm to 1 μm) composites. They reported a sudden increase in electrical conductivity of the composite structures at percolation threshold, around 6 vol.%, Figure 1.11. Increasing the silver particles content resulted in enhancement of electrical conductivity ranges from 10 to 10⁴S.cm⁻¹. By application of a soft thermal treatment in order to evaporate the residuals of developer and rinsing agent the electrical conductivity further increased by one order of magnitude. However, they ran into difficulties with lithographically patterning the SU8 silver particle composites. The polymerization thickness was reduced by increasing the silver particle content. They suggested two methods in order to increase the polymerization thickness. First, by increasing the irradiation dose, e.g. in composites with 10 vol% of silver particles and 10 wt% of photoinitiator the polymerization thickness increased from 20 μm to 25 μm by increasing the irradiation dose from 400 mJ.cm⁻² to 1800 mJ.cm⁻². Second, by increasing the PI content, they report that the polymerization thickness increased with the increase of photoinitiator wt% for constant irradiation dose and certain amount of silver particles, however, the enhancement is lower for higher silver particle contents.

Chiamori et al. [35] studied SU8-gold particles (~ 10 nm diameter) and also observed a reduction of the internal stress up to 14 vol% above which they encountered difficulties with spin casting and lithography. Damean et al. [36] physically incorporated nickel nanospheres in SU8 and fabricated magnetically responsive samples by spin-casting and lithography for fractions higher than 6 vol%, they suggested that diffraction and reflection around particles of 5 nm diameter provide a high degree of transmission from the 365 nm wavelength exposure source. In summary, metal fillers are effective for improvement of the electrical conductivity and obtained composites can also be patterned using conventional UV-light photolithography. However, the resolution is degraded due to the light scattering in presence of metal particles.

Besides metallic fillers carbon nanostructures can also be a candidate for synthesizing conductive polymer composites. MWCNTs are produced today in mass and at low cost by the catalytic chemical vapour deposition (CCVD) process [37, 38, 39]. Zhang et al. [40] were able to successfully suspend functionalized multi-walled carbon nanotubes in SU8. A more extensive and elaborated study was done in the Laboratory of Nanostructures and Novel Electronic Materials at EPFL, Lausanne. Mionic et al. [37] showed that GBL (Gamma Butyrolactone), which is conventionally used to process SU8, is also suitable for making CNTs suspensions. In addition to pristine CNTs, composites were prepared with functionalised nanotubes. The surface was functionalized using a strongly oxidizing acid treatment (mixture of H_2SO_4 and HNO_3) of the nanotubes. Their surface is consequently decorated mainly with COOH groups. They reported a dramatic enhancement of dispersion of functionalized nanotubes in composites compared to pristine nanotubes regardless of the type of the solvent used; however, the best dispersion was obtained when using GBL as solvent [37].

Grimaldi et al. [41] studied electrical percolation threshold of these composites by means of four probe transport measurements on bulk samples. According to their results, in Figure 1.12a, the percolating network of CNTs is formed above 0.2 wt% CNTs at the end of the soft-baking when GBL is evaporated. During cross-linking and polymerisation, composites shrink and the percolation threshold is reduced below 0.2wt% (The concept of percolation is explained in section 1.4). It has to be noted that the resistivity is reduced by about 10 orders of magnitude as compared to pure SU8 with only 1wt% of CNTs. The mechanical properties of the composites were also measured by nano-indentation (Figure 1.12b). The study of CNT-SU8 composites is continued to find and insight in the effect of the aspect ratio of the CNTs on SU8 electrical properties. The results of this study are reported in chapter 3. The thermal properties of SU8 composites made of aligned CNTs are also investigated in this chapter.

Graphene is expected to be a promising replacement for CNTs to be added to SU8. As previ-

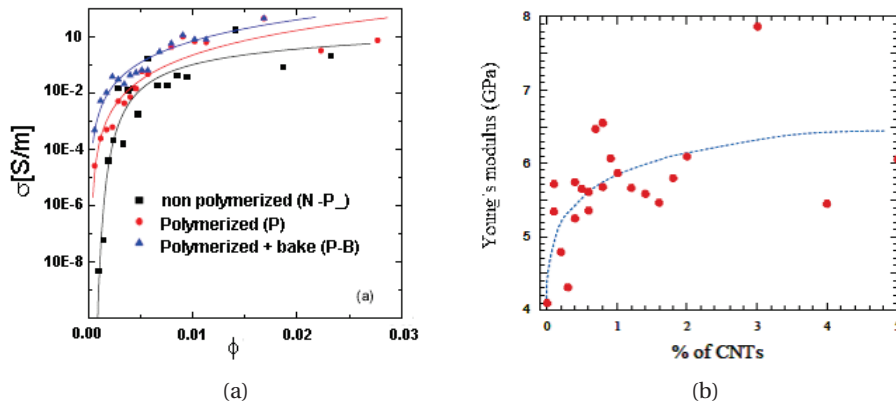


Figure 1.12: (a) Variation of electrical resistivity of the SU8-CNTs composites as function of CNT volume fraction [41] (Rights managed by AIP Publishing LLC.), (b) evolution of young modulus as function of CNT contents [15].

ously mentioned in subsection 1.2.1 large scale production of graphene is realized by reduction of oxidized graphene (RGO) obtained by a chemical exfoliation of graphite [12]; electrical conductivity and other properties have shown significant improvement in polymers filled with graphene [2, 8, 9]. We have reported the preparation SU8-graphene composite for the first time [42]. A comprehensive study on characteristics of these composites is presented in chapter 2.

But before moving on to the results chapter and discussing about the characteristics of the prepared composites, a general background on the properties of composite materials is given in the following sections.

1.4 Transport properties in conductive polymer composites

As mentioned in previous sections, for a functional polymer composite, having higher conductivity at lower filler fraction is greatly favorable. In order to achieve such a material, it is important to recognize the morphology of the composites (shape of the fillers and their respective location inside the matrix), to understand how the charge carriers move through the nanocomposite structure. The important question here is what is the mechanism for the electrical conduction inside a conductive polymer composite? The insulator-to-conductor transition of polymer composites is associated to the formation of a path of electrically conductive fillers through the insulator polymer matrix.

Below the transition, as the filler fraction is reduced, the connected network will shrink into

1.4. Transport properties in conductive polymer composites

finite clusters and eventually disappears (the overall conductivity of the composite drops abruptly to that of the polymer matrix). Likewise, the increase of the volume fractions above the transition and the growth of a global (infinite) percolating network, leads to a significant increase in overall conductivity. This phenomenon, which is referred to as percolation mechanism, has been vastly studied in the literature [43, 44, 45, 46].

Percolation theory [44, 45, 46] gives a phenomenological equation (Equation 1.1) for the conductivity of a system near to this conductor-insulator transition, which happens at a critical volume fraction, ϕ_c . Apart from for regular lattices, this theory is widely used to define the conductivity of continuum systems like of the composite medium:

$$\sigma = \sigma_0(\phi - \phi_c)^t \quad (1.1)$$

here, t is the transport exponent and has a universally accepted value of $t \approx 2$ for three dimensional systems. Unlike t , the critical volume fraction, ϕ_c , (also known as the percolation threshold) is system dependent and varies with the type of the fillers, their aspect ratio, and their thickness.

For the case of carbon composites, as Balberg [47] has stated, “*all the particles are electrically connected to each other by tunneling and thus the basic criterion of whether two particles are connected, which is fundamental to percolation theory is missing*”. To take this in to account, he has considered two cases for defining the local conductivity in a continuum.

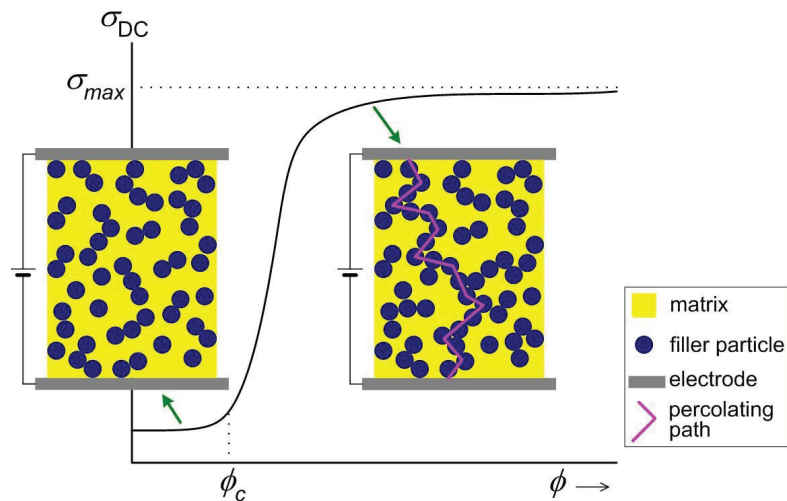
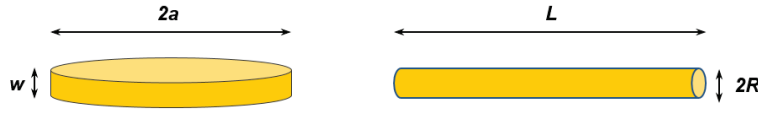


Figure 1.13: Conductivity as a function of the filler fraction. A steep increase in conductivity is observed at a critical filler fraction ϕ_c [43].

Chapter 1. Background information

Table 1.1: Approximation of the percolation threshold for composites containing permeable fillers with different morphologies.

System (3D)	B_c [49]	ϕ_c [47]
Continuum, deformable spheres or parallel objects	2.8	0.16
Continuum, randomly oriented, infinitely thin rods	1.4	$B_c R/L$
Continuum randomly oriented, infinitely thin disks	1.8	$B_c w/a$



First, permeable objects or so-called soft core (SC) particles, which are considered connected if there is any partial overlap between them; Second, partially permeable objects or hard core soft shell (HCSS) particles, which are considered connected if there is a partial overlap between their soft shells. To realize the relation between the aspect ratio of the fillers and the percolation threshold in these composites, the excluded volume argument [48] has been suggested as follow:

$$B_c = N_c \cdot V_{ex} \quad (1.2)$$

where B_c is the morphological invariant, N_c is the critical value of the uniform particle density, and V_{ex} is the excluded volume. V_{ex} is described as the volume around the center of an object in which the center of another similarly shaped object is not allowed to overlap. Based on these definitions, the highest critical filler fraction is obtained for spheres, while ϕ_c reduces for flat disks or rods. The estimations of the percolation threshold values for systems containing permeable objects with different morphologies are given in Table 1.1. Detailed discussions on this matter could be found in Refs. [43, 48, 49, 47].

A point that should be emphasized here is that the percolation for conduction does not necessarily mean that the percolating fillers are in contact with each other. In fact, thanks to tunneling and hopping the conduction is still possible between two conducting particles that are closer than a specific distance to each other but do not touch [43]. The following section will describes the main charge transport mechanisms in disordered systems such as polymer

composites: Tunneling and hopping.

Tunneling

Tunneling is a general quantum mechanical concept, which refers to particles traveling through a potential barrier. The wave function of the particles will decay exponentially over distance, at positions that are energetically unfavorable for existence of the particle. Figure 1.14 demonstrates two locations with their wave functions.

Due to the overlap of the wave functions, there is a possibility for the particle to shift from one site to another. Tunneling is in fact, this transfer between the sites, which share the same energy level. This phenomenon allows the charge carriers to pass through the barrier of the insulating matrix between two conducting regions.

Hopping

The term hopping speaks of an “inelastic tunneling” of an electron between two localized electronic states. In many disordered systems (e.g. organic polymers, glass oxides and biological materials) the wave functions are localized and the energies of the sites differ from one to another. This is shown in Figure 1.15. (this figure illustrates a similar exponential fall out of the wave function as the previous figure). In other words, the difference here with tunneling is that the switching between the sites is accompanied by either a decrease or an increase in the energy of the electrons.

The rapid growth of interest in hopping transport thus followed the rapid development of physics of disordered systems during the last three decades.

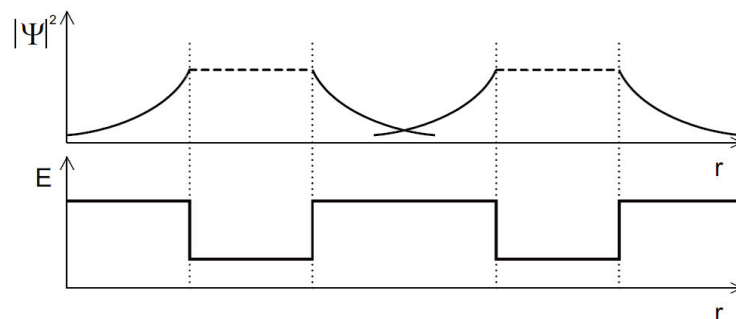


Figure 1.14: exponential decay of the wave functions. The overlap of the wave functions allows the tunneling from one site to the other [43].

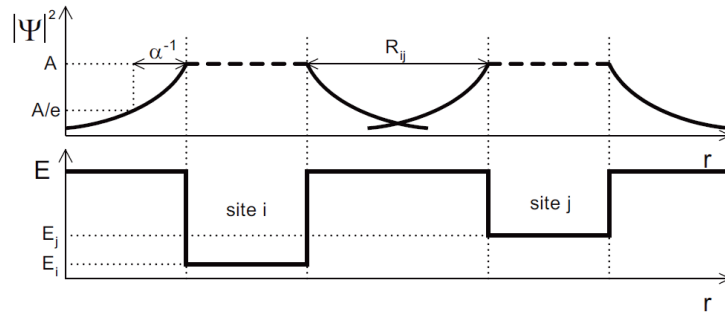


Figure 1.15: Illustration of a disordered material with localized wave functions and energies which vary from site to site. [43]

Variable and Fixed range hopping

In the case of thermally activated charge transport if one plots the $\log[\sigma(T)]$ versus $(1/T)$ one gets a straight line, whose slope is giving the activation energy. In the case of disordered materials in most of the cases, this curve bends downwards as one goes to low temperature, so one cannot extract a well-defined activation energy. The microscopic description of this phenomenon elaborated by Mott [50] gave one of the most known theories for disordered materials with a constant density of states around the Fermi level, called the Variable Range Hopping (VRH). Originally, it was used for the interpretation of the temperature dependence of conductivity at low temperatures. The VRH model is based on the calculation of Miller and Abrahams [51] for the hopping rate between two individual localized states i and j , and it is the best illustrated by Figure 1.16. The sketch shows the sites i and j , in real space r , and their energies. The extension of the electronic wave function (decay length) on the site is given by ξ . The Figure 1.16a represents the low temperature case (LT) and Figure 1.16b the high temperature one (HT) where more thermal energy is available to promote hopping. The

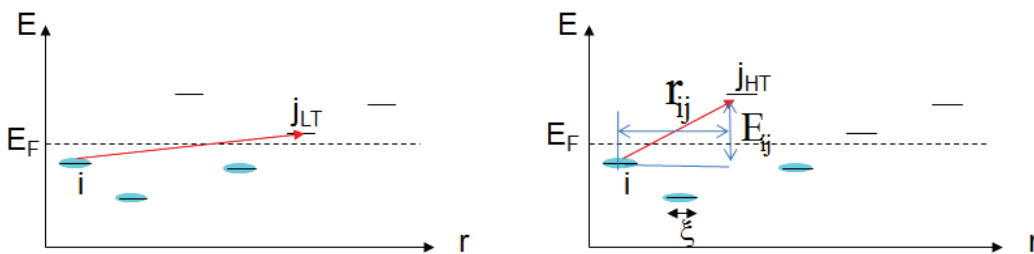


Figure 1.16: Hopping of charge carriers from site i to j , separated by the distance r_{ij} and by the energy E_{ij} at (a) low temperatures and (b) high temperatures. At low temperatures the hopping is of variable range hopping type, while at high temperatures it is a fixed range hopping.

1.4. Transport properties in conductive polymer composites

conductivity (or the resistivity) is proportional to the hopping rate:

$$1/\rho = \sigma \propto \Gamma_{ij} \quad (1.3)$$

which was expressed by Miller and Abrahams [51] for the low temperature case as:

$$\Gamma_{ij} \propto \exp[-r_{ij}/\xi - E_{ij}/k_B T] \quad (1.4)$$

where E_{ij} is the energy difference between the two sites at distance r_{ij} . The essential point is that the charge carriers can choose to hop close in space (small r_{ij}) or farther away but closer in energy (small E_{ij}). This gives the variable range notion to the hopping. The distribution of r_{ij} depends on the dimensionality of the system. Taking into account this fact, the conductivity could be expressed by:

$$\sigma \propto \Gamma_{ijMott} \cong \exp[-(T_0/T)^{1/(D+1)}] \quad (1.5)$$

where $T_0 = 1/N(E_F)\xi^3$, $N(E_F)$ being the density of localized states. The D parameter in the exponent $1/(D+1)$ expresses the dimensionality of the system, $D = 3, 2, 1$. Plotting $\log[\sigma(T)]$ versus $(1/T)^{1/(D+1)}$, one can find the dimensionality of the hopping by the straightest line in such representation. The slope can serve to calculate the hopping range (close to ξ if one knows the $N(E_F)$ from other measurement, e.g. from spin susceptibility.

The situation changes at high temperatures, where there is lot of thermal energy, the electron does not have to optimize, it can hop to the next site even if it is higher in energy, and the Fixed Range Hopping is defined with the formula:

$$\Gamma_{ij} = \gamma t_{ij} \exp[-(E_{ij}/k_B T)] \quad (1.6)$$

The t_{ij} is the transfer integral between the two sites and γ is the phonon population number. In this case the hopping should have a simple activated behavior.

Multiphonon Assisted Hopping

However, the above situation can change if one considers that γ carries a temperature dependence itself, if the number of phonons strongly increases by temperature. This was realized by Emin, who expressed it in:

$$\gamma(T) = \gamma_0 t_{ij} \exp[-(T_\omega/T)^{1/4}] \quad (1.7)$$

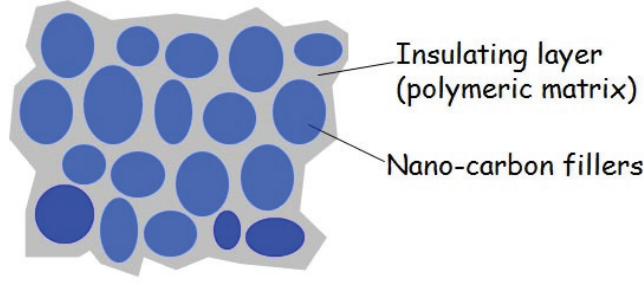


Figure 1.17: Sketch of a granular metallic system imbedded in an insulating matrix. In such a case the charging energy of the fillers determines the hopping transport.

where T_ω is proportional to a phonon energy. This multi-phonon assistance to hopping adds a $T^{1/4}$ dependence to the fixed range hopping:

$$\sigma \propto \exp[-(T_\omega/T)^{1/4}] \exp[-(E_{ij}/k_B T)] \quad (1.8)$$

giving the resemblance to VRH. This fact is usually overlooked by many authors by attributing the multi-phonon assisted hopping to a VRH.

Hopping through grain boundaries

An additional twist could be if disorder is present at different length scales: at microscopic (as above) and at macroscopic scales, e.g. grain boundaries in a polycrystalline sample. The barriers (Δ_B) over the grain boundaries bring an additional activated behavior modifying the expression of conductivity to:

$$\sigma \propto \exp[-(T_\omega/T)^{1/4}] \exp[-(\Delta_B + (E_{ij}/k_B T))] \quad (1.9)$$

Charging Energy Dominated Hopping

There is an additional subtlety to charge transport in a disordered system when it consists of inhomogeneities in an insulating matrix as depicted in Figure 1.17, the conducting nanostructures are dispersed. In this case the hurdle for charge transport may come from the charging effect of the nanostructures, that is if there is already a charge on a “sphere” it is more difficult to put a second charge on it because of Coulomb repulsion. It is expressed by the charging energy $E_C = e^2/C$, where e is the electronic charge and C is the capacitance of the nano-object.

In this case, the conductivity takes the form:

$$\sigma = \sigma_0 \exp[-(E_c/k_B T)^{1/2}] \quad (1.10)$$

This is also a very popular expression in the description of hopping transport in a medium where Coulomb repulsion is present. Usually C is a fitting parameter, since the size and the shape, in consequence the capacitance could vary a lot within the same sample. We will use the advantage of carbon nano-onions which have a very narrow (almost mono-disperse) size distribution, to see if we can learn something about charge hopping in such a system.

This short overview of the transport mechanisms in disorder systems shows that it is very important to know the structure, the microstructure and the texture of the system under investigation. Without detailed x-ray, TEM and SEM investigations one can only guess the electronic transport in composites, disordered systems.

1.5 Mechanical properties of composites

Carbon nano materials, in particular graphene and carbon nanotubes are very promising candidates to be used in composite materials for enhancing the mechanical properties. Many reviews [52, 4, 9, 53] have been published to summarize tremendous works on mechanical reinforcement of various polymers with CNT. Here, we remark general conclusions of these studies.

Defect free single-layer graphene show the highest strength among all materials ever measured, having Young's modulus of 1 TPa and ultimate strength of 130 GPa [54] . Although the sp^2 structure of RGO is disrupted by chemical treatment, the elastic modulus of 0.25 TPa is reported for it [55]. In case of carbon nanotube, the reported experimental and theoretical values of elastic modulus and strength diverge very much due to the different growth condition, structural defects, variation in morphology of CNTs (diameter, number of concentric walls). However, generally speaking, the elastic modulus is close to 1000 GPa and strengths in excess of 10 *GPa* [4]. One major advantage of graphene and carbon nano tubes for composite reinforcement is their large aspect ratio. It is well known that in general, high aspect ratio fibers convey load better than short ones (this subject will be further discussed in the theories of reinforcement). Therefore, more improvement in modulus and stiffness is anticipated for composites loaded with higher aspect ratio fillers.

Apart from the aspect ratio, from geometrical point of view, good dispersion of the fillers

Chapter 1. Background information

and their alignment (particularly for fibrous fillers) are crucial requirements for mechanical reinforcement of the composites. The more uniform the dispersion of the fillers inside the matrix is, the more efficient the load transfer would be. This homogeneous distribution also minimize the stress concentration centers in the composite. Aggregation of the fillers is reported [56] to diminish the strength and Young modulus. This is especially the case for over loaded composites.

The effective stress transfer in composites depends on filler/matrix interface. From a mechanical point of view, the filler/matrix interface is the surface through which stress is transferred to the reinforcements. A good filler/matrix adhesion allows efficient stress transfer. For this reason, the formation of the chemical bonding at the interface is very desirable and many efforts has been devoted to this issue. The structural coherency of the composites is enhanced by chemical cross-linking reactions between the components of the composite. For both CNT and graphene, bearing covalently attached polymer chains result in mechanical enhancement of the material [53]. As another example, significant improvement is achieved for the stiffness of the epoxy, due to the strong hydrogen bonding between oxygen functionalized graphene and matrix. In addition, the mechanical entangling at the crumpled surface of graphene may lead to mobility restriction of polymer chains [3, 57].

To have a better understanding of the role of the composite morphology (filler content and aspect ratio, dispersion,...) and the effect of load transfer on final mechanical behavior of the composites, it is worth to have a brief review on theories of reinforcement in composites.

Among the numerous theoretical works for modeling the mechanical properties of composites, here are briefly mentioned the two most common ones: the rule of mixtures and the Halpin–Tsai equations. The rule of mixture is described for composites containing fibrous fillers, for which the matrix and filler are equally strained under the stress in direction of the fiber alignment [52]. In the most ideal case, when the fibers are well bonded to the matrix, are aligned and have the same length as the specimen, the tensile strength of the composite (σ_c) can be expressed by equation (1.11):

$$\sigma_c = V\sigma_{ultf} + (1 - V_f)\sigma_m \quad (1.11)$$

Where σ_{ultf} , σ_m and λ are tensile strength of fiber, tensile stress of matrix and volume fraction of fiber, respectively. For non-ideal cases, e.g. the fibers have not the same length as the testing specimen, one can find many theoretical models in the literature. Cox et al. [58], considered the case of composites in which fibers do not have the full length of the specimen. In this case,

the stress from the matrix must be transferred to the fiber by shear forces, τ , at the matrix-fiber interface. The tensile stress at a distance x from one end of the fiber can be expressed as

$$\sigma_f = 2\tau(x/r) \quad (1.12)$$

Shear forces can scale up with the fiber's length, at critical length of l_c , the fiber breaks.

$$l_c = \frac{\sigma_{ultf}}{\tau} \left(\frac{r^2 - r_i^2}{r} \right) \quad (1.13)$$

where r and r_i are external and internal radius of a hollow fiber, e.g. carbon nanotube, respectively [58]. This means that the shorter fibers can carry loads less efficiently compared to longer fibers. Therefore, one can re-write the Equation 1.11 as follow [59].

$$\sigma_{ultc} = V_f \sigma'_f + (1 - V_f) \quad (1.14)$$

Then we have

$$\sigma_{ultc} = V_f \sigma'_f + (1 - l_c/2l) + V_m \sigma'_m \quad \text{for } l \geq l_c \quad (1.15)$$

and

$$\sigma_{ultc} = V_f \frac{\tau l}{2r} + V_m \sigma_{ultm} \quad \text{for } l < l_c \quad (1.16)$$

where σ'_f and σ'_m are the average stress in a fiber at composite failure and the stress on the matrix when the fibers reach their ultimate tensile stress in the composite, respectively. $\frac{1}{2}l_c$ is called load transfer l_c , the critical length and $\frac{l}{2r}$ the critical aspect ratio.

Two mechanisms for failure can be recognized, first, when $l > l_c$, the fibers break under large applied stress. Second, when $l < l_c$, enough stress cannot be transferred to the fibers to break them and the matrix fails with the fiber pulling out of the matrix [52]. In certain cases, the polymer–nanotube interaction may result in the formation of an interfacial polymer region with mechanical properties different to those of the bulk polymer [10]. At such circumstances, the composite strength is then given by

$$\sigma_{ultc} = \left(1 + \frac{2b}{2r}\right) \left[\sigma_{shear} \frac{l}{2r} - \left(1 + \frac{2b}{2r}\right) \sigma_m\right] V_f + \sigma_m \quad (1.17)$$

where b is the thickness of the interfacial region and σ_{shear} and σ_m are the shear strength of the interface and matrix strength, respectively [60]. Comparable equations can be drawn for

Chapter 1. Background information

stiffness modulus of composites [52, 59].

$$Y_c = (\eta_0 \eta_1 Y_f - Y_m) V_f + Y_m \quad (1.18)$$

Where η_1 is length efficiency coefficient

$$\eta_1 = 1 - \frac{\tanh\left(\sqrt{\frac{-3Y_m}{2Y_f \ln V_f}} \frac{l}{2r}\right)}{\sqrt{\frac{-3Y_m}{2Y_f \ln V_f}} \frac{l}{2r}} \quad (1.19)$$

And η_0 is the alignment efficiency factor that has values of 1 for aligned, 3/8 for in-plane alignment and 1/5 for randomly oriented Fibers.

Another commonly used model is developed by Halpin and Tsai [61]. This model originally was developed by Hill [62]. For aligned composites the model is expressed as

$$Y_C = Y_m \frac{1 + \varepsilon \eta V_f}{1 - \eta V_f} \quad (1.20)$$

where $\varepsilon = \frac{2l}{d}$ and $\eta = \frac{Y_f/Y_m - 1}{Y_f/Y_m + 1}$

Randomly oriented composites are expressed by

$$\frac{Y_c}{Y_m} = \frac{3}{8} \frac{1 + \varepsilon \eta_L V_f}{1 + \varepsilon \eta_L V_f} + \frac{5}{8} \frac{1 + \varepsilon \eta_T V_f}{1 + \varepsilon \eta_T V_f} \quad (1.21)$$

Where

$$\eta_L = \frac{Y_f/Y_m - 1}{Y_f/Y_m + \varepsilon} \quad \text{and} \quad \eta_T = \frac{Y_f/Y_m - 1}{Y_f/Y_m + 2}$$

Y is tensile modulus. At low volume fractions, this model is shown to fit data very well but to underestimate at high volume fractions. In summary both models show that the composite stiffness scales with volume fraction and the aspect ratio. Coleman et al. [52] suggest that good measure of the reinforcement is given by dY_c/dV_f at low V_f . This takes into account both the magnitude of the stiffness increase and the amount of fiber required to achieve it and has the advantage that it can easily be extracted from experimental data. For 2D fillers, e.g. graphene, the modulus can be expressed by modified rule of mixture [63], for relatively aligned fillers

$$Y = (\eta_{LY} Y_G - Y_p) V_f + Y_p \quad (1.22)$$

where

$$\eta_{LY} = 1 - \frac{\tanh(nL/t)}{(nL/t)} \quad \text{and} \quad n = \sqrt{\frac{G_p V_f}{Y_g(1 - V_f)}}$$

L and t being length and thickness of the filler, respectively and G_p shear modulus of polymer.

As a final remark, It must be pointed out that the degree of reinforcement of the polymer and the nature of the interface depends very much on the polymer itself. In case of graphene reinforce polymers for instance, elastomers show more efficient stiffness improvement compare to glassy polymers (ductile matrices compared to brittle ones in general) due to the higher stiffness contrast between matrix and filler [9, 53]. In this regard, SU8 as a widely used photo-polymer is a very interesting material for such fundamental studies as a composite matrix.

1.6 Thermal properties of the polymer composites

Thermal conductivity could be a very interesting feature to be tailored to polymers, since it can offer the possibility for various applications e.g. circuit boards in power electronics, heat exchangers, electronic motors and generators, etc. However, the thermal conductivity of the polymer materials are often very limited. The reason is that in amorphous polymers, the mean free path of the phonon (the primary mechanism for the heat conduction [64]) is extremely small, due to phonon scattering from abundant defects [65].

In this regards, carbon based fillers and carbon nanotubes in particular, are considered as the promising candidates to be added as fillers to the polymer matrix, coupling high thermal conductivity and lightweight. For single and multiwall carbon nanotubes, the thermal conductivities of about $2000 \text{ Wm}^{-1}\text{K}^{-1}$ [66] and $3000 \text{ Wm}^{-1}\text{K}^{-1}$ [67] has been reported, respectively. However, considering the intrinsic thermal conductivity of CNTs, the values attained for CNT-based polymer composites are lower than expectation [68].

Several models have been suggested for prediction of the polymer composites' thermal conductivity [69, 70, 71, 72]. Among these models, the *rule of mixture* and the *series model* are two basic equations representing the upper bound and the lower bound for thermal conductivity of composites, respectively. The rule of mixture assumes that each phase contributes independently and proportional to its volume fraction:

$$\kappa_c = \kappa_f \phi_f + \kappa_m \phi_m \tag{1.23}$$

Chapter 1. Background information

where $\kappa_c, \kappa_f, \kappa_m$ are the thermal conductivities of the composite, filler, matrix, and ϕ_f, ϕ_m are the volume fractions of the filler and the matrix, respectively. This model assumes the perfect contact between particles in a fully percolating network and therefore, overestimates the contribution of the conductive part. Although it is relevant to some extent for the composites containing aligned fibers in the orientation of the alignment, in general the predicted result is maximized.

The basic series model, on the other hand assumes no connection between the particles and so the fillers contribution is confined. This model is presented by the equation:

$$\kappa_c = \frac{1}{\kappa_f / \phi_f + \kappa_m / \phi_m} \quad (1.24)$$

Usually the experimental data range between these two models, but the lower bound seems to be more realistic, and a number of second-ordered models derived from the basic series model, which fit quite well with the experimental results [68].

These macroscopic approaches could be attractive from the engineering aspects; however, they neglect the physical behavior inside the composite systems.

In fact, the transfer of the phonon, which dominates the heat conduction within the composites, could be prohibited by high interracial thermal resistance between the fillers and the matrix. Thus, the large thermal conductivity of the fillers cannot be harvested efficiently. Furthermore, for the nanotubes themselves, the phonon conduction depends on the atomic structure, the tube size, the morphology and the defects. Several processes such as the number of phonon active modes, the boundary surface scattering, the length of the free path for the phonons and inelastic Umklapp-scattering (an anharmonic phonon–phonon or electron–phonon scattering process), which originate from the structural factors of the CNTs and composites, can hinder the thermal transport.

Therefore, in order to build an effective conductive network for heat transfer inside the polymer-CNT composites, these critical issues are needed to be addressed. A good understanding of the physical phenomena for thermal conduction is required to benefit from the exceptional characteristics and intrinsic thermal conductivity of CNTs.

1.7 Optical spectroscopy

As already mentioned in previous chapters, interfacial bonding (including covalent bonding, van der Waals and quadrupolar interactions) between the graphene flakes and the host polymer dictates the global properties of the reinforced polymer nanocomposites. In the context of the polymer nanocomposites mechanically reinforced with carbon nanostructures, Raman spectroscopy is assumed as a straightforward method to assess the interfacial filler/matrix shear strength [52]. We are convinced that this method along with Fourier transform infrared (FTIR) spectroscopy can also provide information about the nature of chemical interactions between the filler and the matrix. Concerning optical spectroscopy studies reported on the SU8 photoresist, at present for Raman spectroscopy there are only two articles focusing on a bonding technique for microfluidic devices [73] and the changes from hydrophilic to superhydrophobic state of the SU8 surfaces [74]. Fourier transform infrared (FTIR) spectroscopy has been used to assess the curing process and the degree of conversion of SU8 photoresist [75, 76] and SU8-based composites [77], as well as during the fabrication of microfluidic devices [78]. A special attention was given to FTIR monitoring of the chemical changes induced to the SU8 (photochemical generation of hexafluoroantimonic acid ($HSbF_6$) followed by monomer cross-linking) by the exposure to UV-light [77, 78, 79]. To our knowledge the polymerization of the SU8 has never been studied with photoluminescence technique.

Here, in the third chapter of this thesis, we are aiming to give a new insight into the role of RGO on the mechanism of photo-polymerization for the composites as well as the nature of interactions between RGO and SU8. For this purpose, we have used a combination of Raman scattering, FTIR and photoluminescence (PL) techniques. To our knowledge, this is the first report on PL studies of photo-polymerization mechanism of the SU8 and SU8-based composites. The principles of these methods are being discussed in the following.

1.7.1 Raman Spectroscopy

Raman spectroscopy is an easy, fast and nondestructive method which uses inelastically scattered photons for the study of vibrating states (phonons) of molecules. Raman scattering by intrinsic phonon modes, which are sensitive to internal and external perturbations, provides information on the structural phase transition, composition (having reference data), and crystal orientation. The following diagram depicts the basic process that takes place in Raman spectroscopy.

The scattered photons have lower (or higher) energy than incident photon, thus higher (or

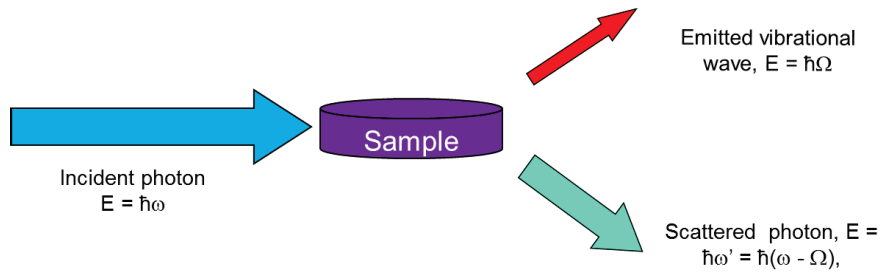


Figure 1.18: Basic process happening in Raman spectroscopy

lower) wavelength, the spectrum at this shifted wavelength is related to the frequency of vibration that itself is a function of the material's structure. A typical Raman spectrum is plotted vs $\omega - \omega_0 = \Omega$ that routinely is shown as $\Omega/2\pi c$ named as wave number or Raman shift. The electronic structure of Carbon nanomaterials can be captured by Raman spectroscopy [80]. Raman spectrum of a single layer graphene, shown in figure Figure 1.19 has two main peaks, an in-plane vibrational mode, (G at 1580 cm^{-1}), and a second-order overtone of a different inplane vibration, D (1350 cm^{-1}). In a multilayer graphene, due to intraction of other layers, the 2D peak splits.

1.7.2 FTIR Spectroscopy

Fourier Transform InfraRed (FTIR) is nondestructive optical spectroscopy, that provides a molecular finger print of a sample, like Raman spectroscopy. An infrared radiation passes through a sample and the resulting spectra consist of absorption and transition peaks that are unique to the sample. The energy at which any peak in an absorption spectrum appears

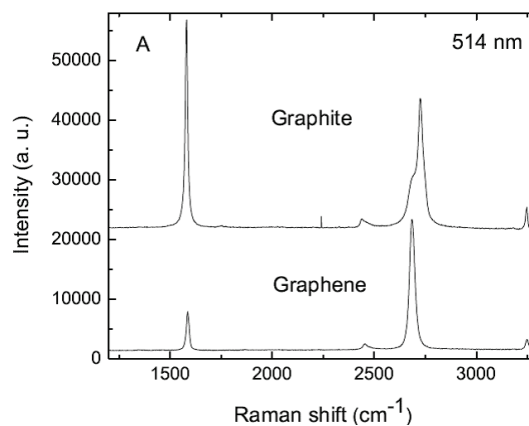


Figure 1.19: Raman spectra graphene sheet [80]. Copyright 2007 Elsevier Ltd.

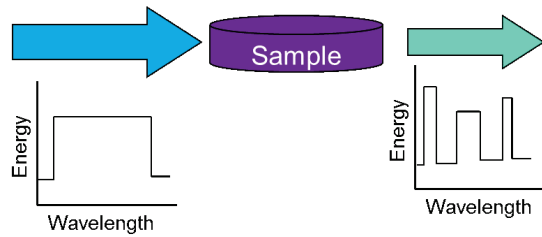


Figure 1.20: Basic principle of FTIR

corresponds to the frequency of a vibration of a part of a sample. Figure 1.20 shows the basic principle of FTIR.

The essential part of an FTIR spectrometer is an interferometer. The simplified schematic of Michelson interferometer is shown in figure Figure 1.21. In this figure, a monochromatic beam shining from the source goes through a beam splitter. Half of the beam is reflected to the fixed mirror and comes back to the beam splitter, traveling a distance of $2L$ (L is the distance between the fixed mirror and beam splitter). The other half of the beam travels a distance of $2(L+x)$, where x is the displacement of the moving mirror. Both halves of the beam again will recombine at the beam splitter and go through the sample and finally will be focused into the detector. However, due to the different optical pass (x) they will make constructive and destructive interference. The intensity of the output beam (beam going to the detector) as function of x can be expressed as a cosine wave

$$I(x) = S(\nu) \cos(2\pi x/\lambda) = S(\nu) \cos(2\pi\nu x) \quad (1.25)$$

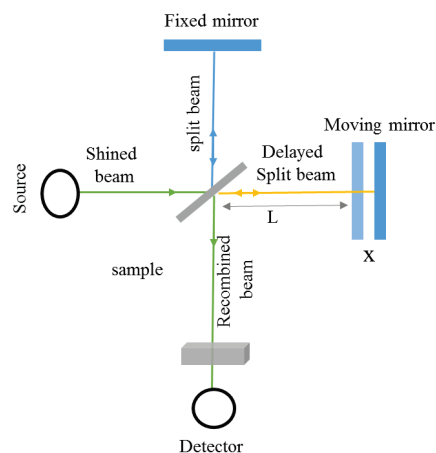


Figure 1.21: Schematic diagram of a Michelson interferometer

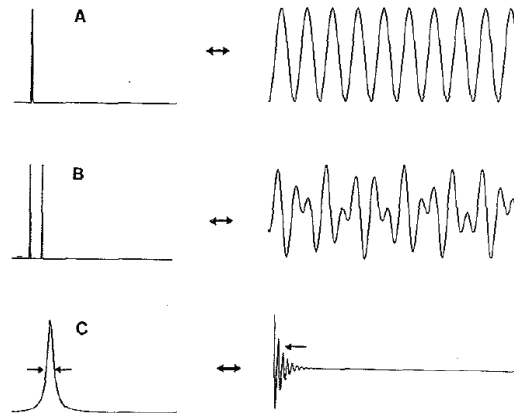


Figure 1.22: examples of spectrums (on the left) and their corresponding interferograms, A) one monochromatic beam, B) Two monochromatic beams, C) lorentzian beam [81]

where $S(\nu)$ is the intensity of shined wave and ν is the wavenumber. The intensity vs x plots is called interferogram (see Figure 1.22). The interferograms must be converted to spectrum by means of mathematical transformation called Fourier Transform that can be expressed as following:

$$F(\omega) = \int_{-\infty}^{+\infty} f(x)e^{i\omega x} dx \quad (1.26)$$

where ω is angular frequency and x is the optical path difference in our case. $F(\omega)$ is the spectrum and $f(x)$ is the interferogram. The reverse FT is expressed as

$$f(x) = \frac{1}{2\pi} \int_{-\infty}^{+\infty} F(\omega)e^{-i\omega x} d\omega \quad (1.27)$$

Figure 1.22 shows examples of the spectra and their corresponding interferograms. To obtain the final transmittance spectrum, two spectra are required, first a reference spectrum that is spectrum of beam, going out of the interferometer, without going through sample $S(\nu)$, second, the spectrum of the outgoing beam after going through the sample $T(\nu)$. The final transmittance spectrum is the ratio $T(\nu)/S(\nu)$, Figure 1.23.

1.8 Rheology

The greatest advantage of using nano-sized fillers compared to micron-sized ones is their significantly higher impact on enhancement of matrix properties, due to their extremely large specific surface area. This characteristics of nanofillers, however, has another effect. Very small loadings of well-dispersed nanofillers in composite can change severely the viscoelastic

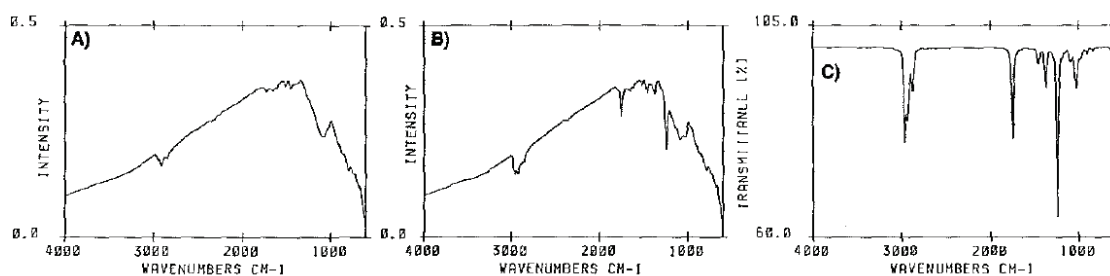


Figure 1.23: a) Reference spectrum, b) Spectrum of the absorbing sample, c) Transmittance spectrum equal to spectrum b divided by spectrum a. [81]

properties of the polymer [82, 83]. Drastic augmentation in viscosity (or even liquid to solid transformation) that may occur because of addition of nanofillers is a limiting factor for processing of advanced nanocomposites. Thus, to fulfill the requirements for processing of the composites, one must recognize and control the rheological properties of the material [84]. In fact, rheology offers an effective tool to assess the state of dispersion but also can predict the processability of the composite [9]. As an example, in a recent work White et al. [85] have used rheology as a technique to confirm disentanglement and stability of CNTs and evaluate the interaction between two types of nanoparticles in a hybrid composite containing CNTs and ZrP nanoplatelets as fillers. The rheological behavior of the composite also gave information about strengthening mechanism of the highly cross-linked, brittle material and give a perspective for a better material design. A literature review over the investigations performed on the viscosity of nanofluids reveals that volume fractions, particle size and shape, along with temperature have the highest impact on viscosity of nanofluids. However, it seem that there are some inconsistencies among the published results and debates going on about the effect of these parameters on the viscosity of nanofluids [86]. For this reason, in order to establish a valid basis for our upcoming results and discussions, in the following we go through some theoretical aspects which predict the viscous behavior of dispersed particle. Concerning the volume fraction, the liquid (highly viscous fluid) to solid transition occurs at the critical volume fraction (ϕ^*) above which shear viscosity goes toward infinity ($\eta \rightarrow \infty$). This value is equal to $\phi^* \sim 0.64$ for random close-packed spherical particles at low shear rate, and ~ 0.7 at high shear rate [83]. However, for well-dispersed systems with high interfacial surface area, the ϕ^* is attained at much lower volume fractions (as low as 10%) because of powerful interparticle attractions. Among the theoretical formulas developed for the estimation of the suspension viscosity, the pioneer work is the equation suggested by Einstein [87] for linear

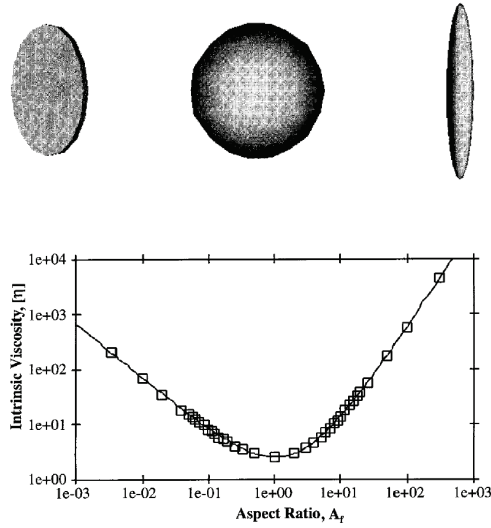


Figure 1.24: Isotropically averaged $[\eta]$ of dilute dispersions of ellipsoids as a function of their aspect ratio [82]. Copyright 1999 Taylor & Francis.

viscous fluid holding dilute spherical particles at low particle volume fractions of $\phi < 0.02$:

$$\eta_d = \eta_f(1 + 2.5\phi) \quad (1.28)$$

Here, η_d is the viscosity of dispersed suspension; η_f is the viscosity of base fluid and ϕ is the volume fraction of particle in base fluid. A more general derivation of Equation 1.28 is developed in a power series in the particle volume fraction ϕ [82].

$$\eta_{relative} \equiv \frac{\eta_d}{\eta_f} \approx 1 + [\eta]\phi + k_H\phi^2 + \dots \quad (1.29)$$

Where $[\eta]$ is the intrinsic viscosity and k_H is the Huggins coefficient. These quantities are dimensionless. The influence of the particle shape on shear viscosity, η , is proportional to intrinsic viscosity, $[\eta]$. It has been shown by Douglas and Garboczi [88] that unsurprisingly, the aspect ratio of the fillers has a drastic impact on the intrinsic viscosity for anisotropically shaped rigid particles. They determined the “aspect ratio” $A_f = (c/a)$ for a biaxially symmetric ellipsoid, where c is the length of major axis of the ellipsoid, and $a = b$ is the length of the two minor axes. Therefore, $A_f > 1$ approximates fibers, $A_f = 1$ is for spheres, and $A_f < 1$ represent platelets. The results for intrinsic viscosity $[\eta]$ as a function of filler aspect ratio are illustrated graphically in Figure 1.24.

The results demonstrated in Figure 1.24 for $[\eta]$ are valid for an infinitely dilute dispersion at low shear rate. Nevertheless, anisotropic particles have a tendency for alignment under

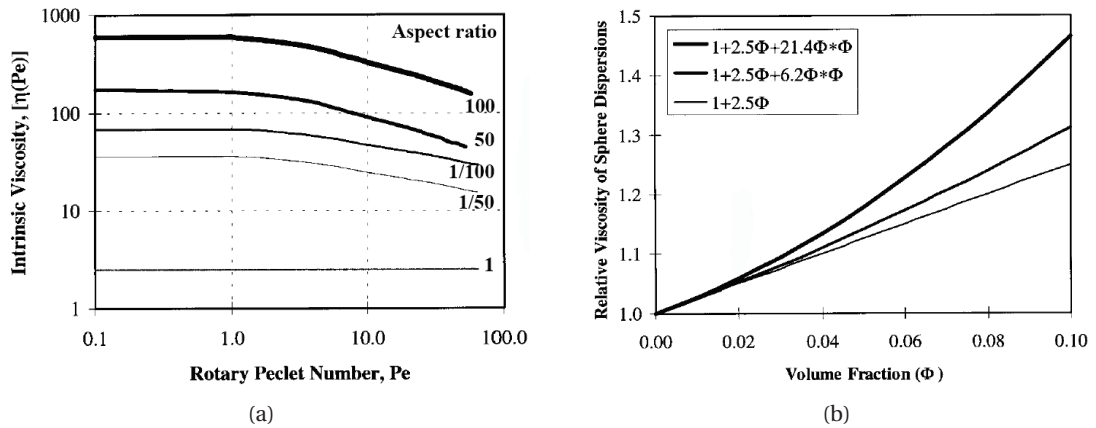


Figure 1.25: (a) Effect of shear on intrinsic viscosity $[\eta]$ of ellipsoids with different aspect ratio as a function of the rotary Peclet number (Pe). (b) Effect of the coefficient k_H in Equation 1.29 for the viscosity of the spherical particles [82]. Copyright 1999 Taylor & Francis.

shear. In fact, as the shear rate increases, the particles are being oriented in the flow direction due to strong hydrodynamic forces reducing. In this case, for higher aspect ratio fillers, shear thinning effect is observed. Shear thinning is the most common form of non-Newtonian behavior in suspensions and polymer solutions. It is referred to a decrease in viscosity as the shear rate is increasing. Figure 1.25a depicts the dependence of intrinsic viscosity on shear rate. (The rotary Peclet number, Pe , which appears in x axis of Figure 1.25a is a dimensionless parameter which represents the shear rate, but also considers particle shape, temperature and Brownian motion. (For more details about Pe see ref [82].)

Besides particle morphology, interparticle interaction is the other factor that affects the viscosity. The coefficient k_H in Equation 1.29 is an informative parameter regarding the particle shape as well as the strength and nature of interparticle interactions. Many calculations have been done in order to estimate the value of k_H . For hard spheres, the value of k_H varies from 6.2 for repulsive spherical particles to 21.4 for slightly attractive particles. This broad range of k_H displays its strong dependence on interparticle interactions. Figure 1.25b demonstrates how the involvement of the term $k_H\phi^2$ impacts the Equation 1.29 for hard spheres. In case of nonspherical anisotropic particles and particles with attractive interactions, extension of these results is a theoretical challenge. Based on these notions Becerano et al, have suggested a simple predictive model for the shear viscosities of dispersions. This model is a combination of mathematical arguments and phenomenological observations and considers influence of particle volume fraction, morphology and flexibility; shear rate and temperature on the dispersion viscosity.

Concerning the influence of graphene fillers on the viscoelastic behavior of composites there are some studies in the literature [9, 89, 90]. However, a relative lack of experimental data about the viscosity of graphene based composites is felt to exist throughout the broad research in this field [86]. Hence, it has been motivating for us to study the rheological behavior of our newly introduced composite.

1.9 Applications

Since the start of nanotechnology concept in the second half of the 20th century, many nanomaterials with excellent or even exceptional properties have been synthesized or discovered. Carbon nanostructures (including nanotubes, graphene, onion-like carbon) represent one of the most exciting discoveries in materials research over the last 30 years. In recent years, the balance between publications on basic research and applications has clearly shifted towards application. Adding CNTs into polymeric matrix has been widely investigated over the last two decades. Many CNT polymer composites exhibiting significantly improved properties over pure polymers have been reported [41, 91, 53]. The exceptional properties enhancement in CNT polymer composites has been a driving force for studying their application in many fields. In terms of electrical properties, CNT polymer composites have been studied for applications like fabrication of transparent and flexible conductive materials [92]. Great electron transport properties of carbon nanotubes (CNTs) has extended the application CNT/polymer composites to photovoltaics [93, 94]. The disadvantages associated with the conventional metal oxide-based sensors have encouraged many groups to look for new alternative like CNT based polymers. CNTs are assumed promising material for thermal management since they can be used for heat dissipation, which is an essential requirement towards microelectronics future development [95, 96].

Graphene/polymer nanocomposites are important newcomers in the field of nanoscience which exhibit significant properties, as for CNTs. Enhanced thermal and electrical properties compared to the polymer matrix itself might be useful for heat or electrically activated shape memory, static charge dissipation and electro- magnetic wave reflective materials. Literature shows that graphene is a better nanofiller than CNT in some properties such as thermal and electrical conductivity. Electrical conductivity of composites may significantly be altered by external conditions (e.g. temperature change, presence of gas, external strain) particularly close to percolation threshold. This on-off sensation can be a great potential for sensor fabrication [9].

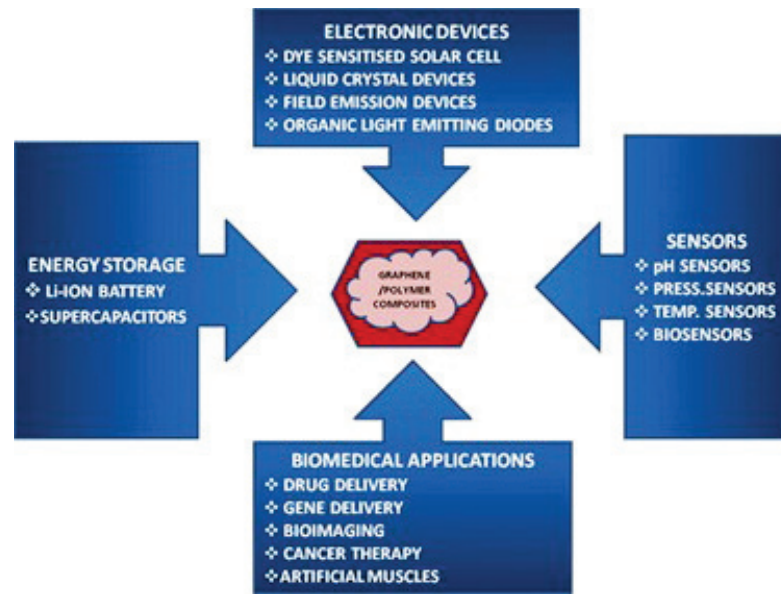


Figure 1.26: Range of applications of Graphene/polymer in different fields [97].

On the other hand, SU8 as a very popular photoresist for MEMS, has a wide range of application from packaging to microfluidics, sensors and actuators. However, electrical , optical , or mechanical properties, of the resist can be tuned by mixing with materials that can bring new functionalities and new potential applications.

This multidisciplinary thesis aims at the preparation of novel carbon nanostructures based composite materials, which could be applied in a large spectrum of applications for fundamental as well as applied research including MEMS, bio-applications or energy related applications.

2 Composites with 2D fillers: SU8-graphene composites

This chapter focuses on the preparation of SU8-graphene composites with superior electrical and mechanical properties, and consistent with current MEMS technology. Various characterization techniques have been employed to study the chemical and physical properties of these composites. The results of this research gives a comprehensive picture of the composites from microscopic and macroscopic point of view, shedding light on design and engineering of new composites.

2.1 Composite preparation

The most important challenge regarding the composite preparation, is to overcome the high tendency of nanofillers for creating agglomerations (due to their high surface energy) and achieve a homogeneous dispersion. It is crucial because the performances of the composites such as mechanical, electrical, thermal properties, as well as the impermeability are directly influenced by the efficiency in dispersing the nanofillers in the epoxy matrix. Among several methods that have been used in the literature (reviewed in Ref. [2]) for dispersing nanofillers, “solution mixing” is probably the most straight-forward one. This is the method that we have employed for composite preparation in this thesis. Although there are reports of insufficiency of this method for dispersion of the fillers, in this section we will argue that by a proper combination of long stirring and sonication, a very efficient dispersion is achievable.

The reduced graphene oxide flakes (hereafter referred to as RGO), purchased from ACS materials, were used as nanofillers. The general characteristics of the RGO flakes are summarized in Table 2.1.

The Raman spectrum of reduced graphene oxide flakes shown in Figure 2.1 displays a well-

Chapter 2. Composites with 2D fillers: SU8-graphene composites

Table 2.1: Characteristics of the RGO flakes (<http://www.acsmaterial.com>).

BET surface area (m^2/g)	650 - 750
Conductivity (S/m)	500 - 700
Layers	1-5 atomic layer graphene
Lateral size μm	0.5 - 5
Oxygen (atm%)	7 - 7.5

defined G band at $\sim 1580\text{ cm}^{-1}$, the defect induced D band at $\sim 1350\text{ cm}^{-1}$, and the 2D band at $\sim 2680\text{ cm}^{-1}$ originating from a two phonon second order scattering process. The comparison of the position and the symmetric shape of the 2D band with previous works [98, 99] is a confirmation that the number of layers of the RGO flakes is between 1 and 5. Furthermore, the RGO flakes do not show the presence of large graphitic particles or unexfoliated material, as evidenced in Figure 2.2b and Figure 2.2c where we show a representative SEM image along with low- and high-magnification TEM images of RGO flakes.

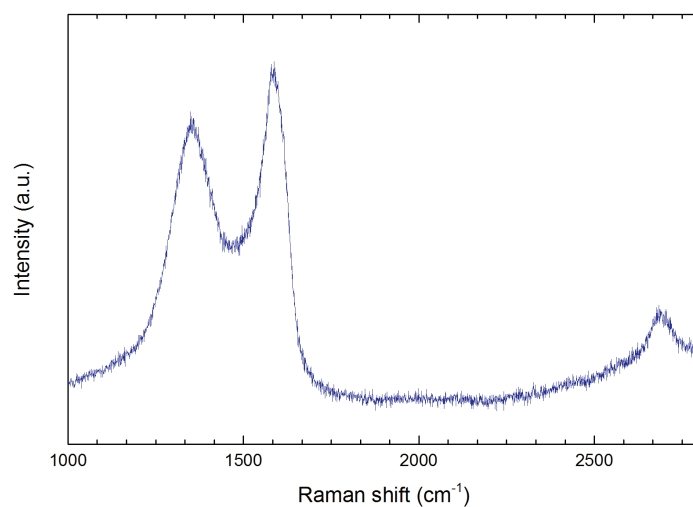


Figure 2.1: Raman spectrum of RGO fillers.

A wide range of concentrations, from $x=0.04\text{ wt } \%$ to $x=3\text{ wt } \%$ with respect to the weight of SU8, was selected for composites preparation. The SU8 polymer matrix used in this work was purchased from Gersteltec (grade GM 1060 and GM1075). It contains SU8 resin dissolved in gamma-butyrolactone (GBL) as solvent (from Merck). It also contains a mixture of propylene carbonate and triarylsulfonium hexafluoroantimonate salt (TSHAS) as photoinitiator for activation of the cationic cross-linking of the polymer as exposed to UV irradiation.

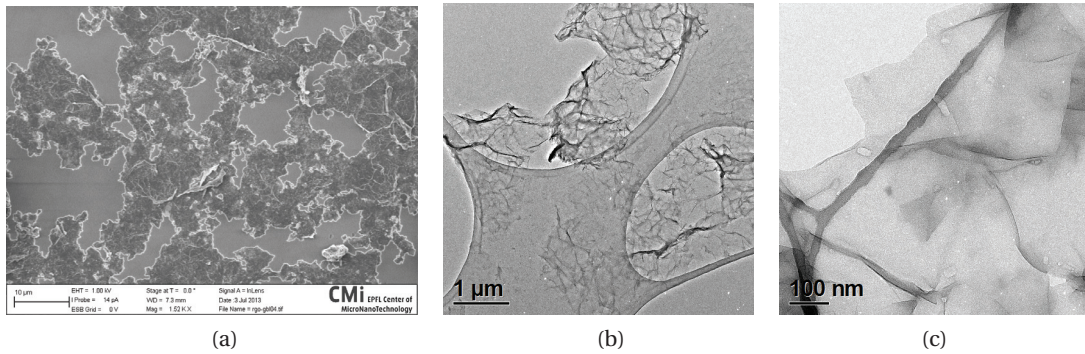


Figure 2.2: (a) Scanning electron micrograph of RGO fillers (b) and (c) Transmission electron micrograph of RGO fillers.

In solution mixing, the extent of exfoliation of the RGO flakes before mixing with polymer, will affect severely the quality of the dispersion in the final composite. Therefore, as first step, RGO flakes were dispersed in GBL, which is a compatible solvent for both SU8 and carbon nanomaterials [37]. To ensure the homogeneity of the mixture, a long lasting vigorous stirring was applied to the suspension (minimum 24 hours), followed by 90 minutes of sonication in the bath. SU8 (in form of monomer solution) was added to the suspension immediately afterwards. Further sonication was performed for 2 to 3 hours (depending on the RGO content and volume of the composite) using ultra-sonication probe with 80 to 120 W power. After this step, the RGO flakes remained individually dispersed in the matrix, as shown in the subsection 2.1.1. We explain the reason behind the efficiency of this simple method based on reported attempts in the literature.

It has been reported for nanoplatelet-reinforced composites containing clay that the penetration of the polymer into the clusters forms intercalated structure which leads to the exfoliation of the layers [100]. Coleman et al. [101] also showed that only by soaking single wall carbon nanotube (SWCNT) sheets (Buckypaper) in polymer solutions, polymers can be intercalated into Buckypaper. This process is shown schematically in Figure 2.3. We can use the same argument for the exfoliation of the possible agglomerates existing in the suspension when they are being stirred or sonicated with SU8.

In addition, the local increase in temperature while the mixture is being sonicated may result in short range polymerization of the SU8 but also formation of the chemical bonding between the functional groups on the surface of RGO with the matrix. More evidences are given in subsection 2.3.3. This effect is to some extent similar to in situ polymerization method which is one of the most successful techniques to attain a well dispersed polymer nanocomposites

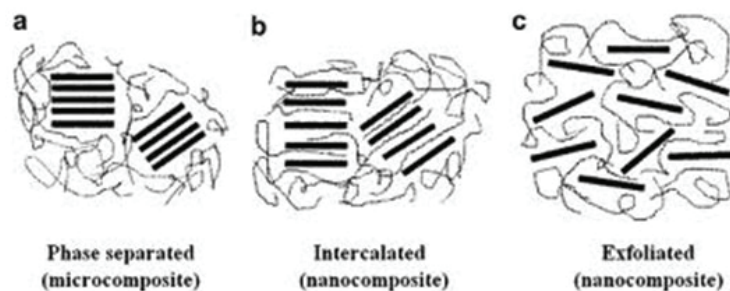


Figure 2.3: Intercalation and exfoliation of layered fillers in polymer matrix (image taken from Ref.[102]. Copyright © 2000 Elsevier Science S.A.)

[2, 8]. In situ polymerization for the composites designates cross-linking of monomers or a solution of monomers in presence of the dispersed fillers, which leads to a very good dispersion of the fillers without the need for a pre-dispersion in a solvent. Both cases of formation of non-covalent [103, 104] and covalent bonding [105] between matrix and filler following the in situ polymerization are reported. Potts et al. [2] have noted that for some polymers, reaction with functional groups allows the covalent linkage between filler and matrix during the polymerization, without prior functionalization. Based on the above mentioned discussion, we are convinced that our method has been an efficient technique to prepare very well-dispersed composites which remain stable for long time. Results of electrical and mechanical measurements are another confirmation for this statement.

To obtain even better dispersions, in another set of composites (denoted hereafter as SU8-SRGO) the surfactant Disperbyk-145, which is a phosphoric acid ester salt of a high molecular copolymer with pigment affine groups, was employed for composite fabrication [91, 15]. In this case, the surfactant was added to GBL and the mixture was completely homogenized, before making the GBL-RGO suspension.

In all composites the amount of photoinitiator was kept constant with respect to the amount of SU8, while the concentration of RGO flakes varied from $x=0.04$ wt % to $x=3$ wt % with respect to the weight of SU8. The RGO/GBL ratio was equal to 7 mg/ml for all samples presented in this work. This is the optimized value in order to control the viscosity of the ink and to preserve the uniformity of composite during solvent evaporation. For composites containing surfactant, the surfactant/RGO ratio was also kept constant and equal to 40 wt %.

In order to prepare samples for electron microscopy as well as electrical and mechanical characterization, the ink was spread on a clean glass slide by a doctor blade, and was soft-baked at 95°C on a flat leveled hot plate. This was followed by a cross-linking step at 150°C.

2.1. Composite preparation

Sample preparation steps are demonstrated in Figure 2.4a. After this process, samples weight loss reached a plateau and no more solvent evaporation took place.

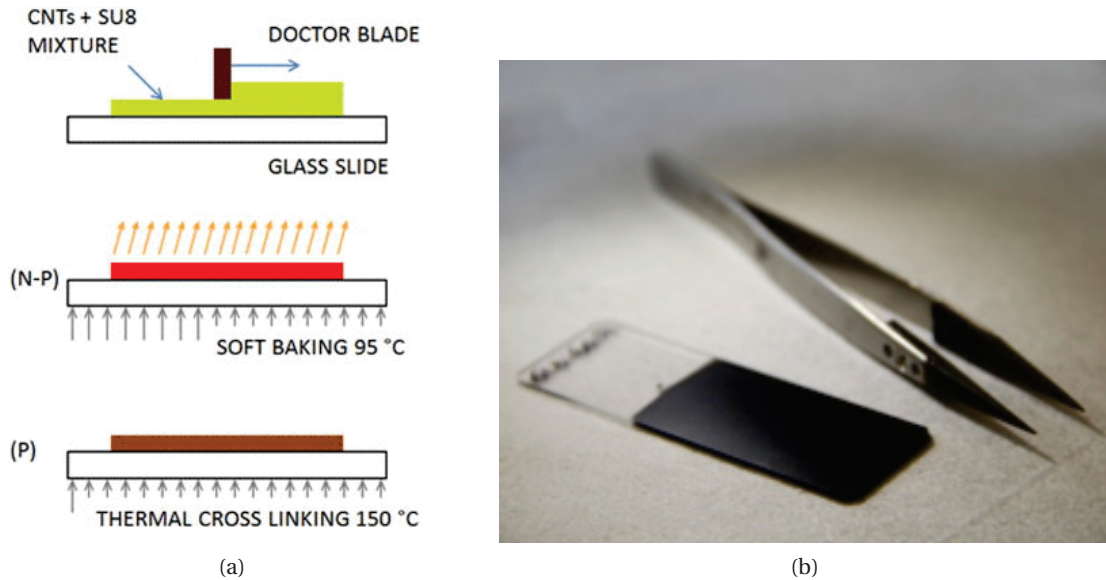


Figure 2.4: (a) The preparation steps of SU8-RGO samples for characterization [41] (Rights managed by AIP Publishing LLC.). (b) SU8-RGO film deposited on a glass slide.

2.1.1 Structural characterization

Investigating the microstructure of the composites is essential in order to be able to realize the physical and chemical phenomena ongoing in the material and their influence on the macroscopic properties. In order to assess the micro-structure of the composite (state of dispersion, morphology of the fillers, etc.) scanning and transmission electron microscopy were utilized. The results of these analysis are shown in micrographs of Figure 2.5 and Figure 2.6.

Figure 2.5 presents high resolution scanning electron microscope (HRSEM) images obtained from fracture surfaces of SU8 composite samples containing (a) 0.2 wt% and (b) 0.9 wt% of RGO, and (c) 0.2 wt% and (d) 0.9 wt% of SRGO. For comparison, the inset of Figure 2.5a shows the SEM micrograph of pure SU8.

Figure 2.5 demonstrates that for both concentrations, the RGO flakes are uniformly dispersed within the polymer matrix. Since from HRSEM images we cannot clearly deduce the morphology of the RGO flakes within the polymer matrix, we employed transmission electron microscope (TEM) for further analysis. Figure 2.6 presents TEM images of microtome slices of SU8 composite with (a) 0.2 wt% and (b) 0.9 wt% of RGO, and (c) 0.2 wt% and (d) 0.9 wt% of

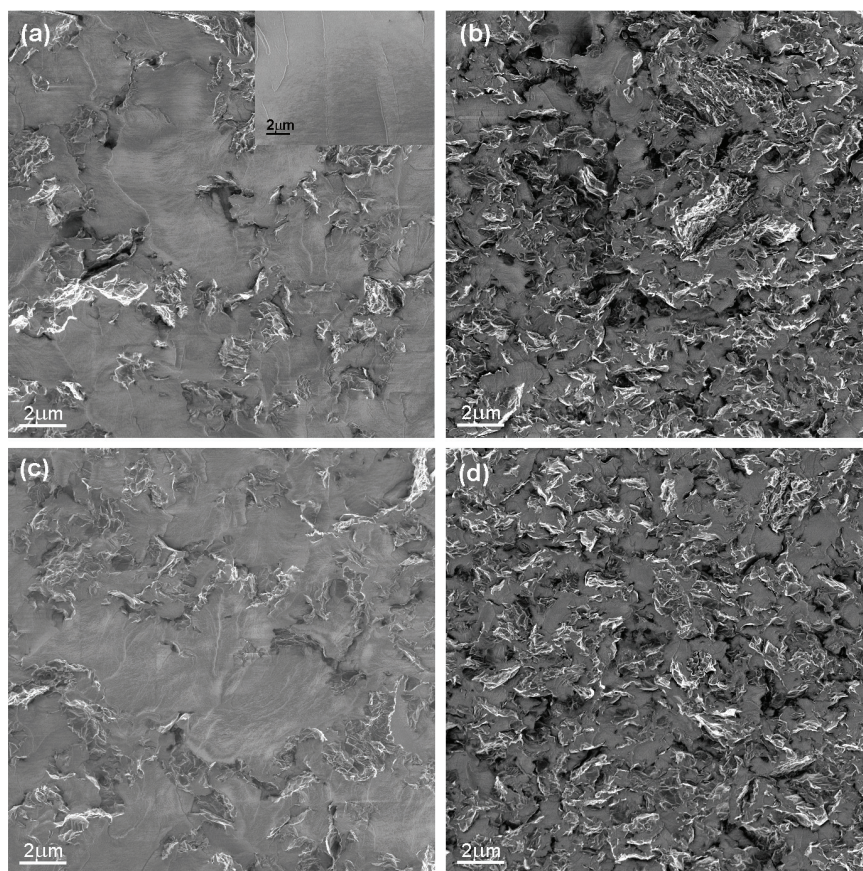


Figure 2.5: Scanning electron microscopy image of SU8 nanocomposites with (a) 0.2 wt% and (b) 0.9 wt% RGO, and (c) 0.2 wt% and (d) 0.9 wt% SRGO. The inset of (a) shows SEM image of pure SU8. Good dispersion of RGO flakes within the SU8 matrix is observed [42]. Copyright 2014 Elsevier Ltd.

SRGO. In these images, RGO flakes can be recognized by the dark curvy lines in accordance to previous observations [106], indicating that the flakes in the composites are folded and crumpled, contrary to the typically flat shape that flakes are assumed within the solvent.

Figure 2.6 also illustrates the network formed by RGO flakes inside the SU8 matrix; this network is constituted by highly conductive and well-dispersed RGO fillers which are separated by regions of cross-linked SU8. It is through these regions that electrons can tunnel between neighboring fillers, establishing thus electrical connectedness which allows current to flow throughout the composite. From the mechanical point of view, these are interfaces through which the load transfer occurs.

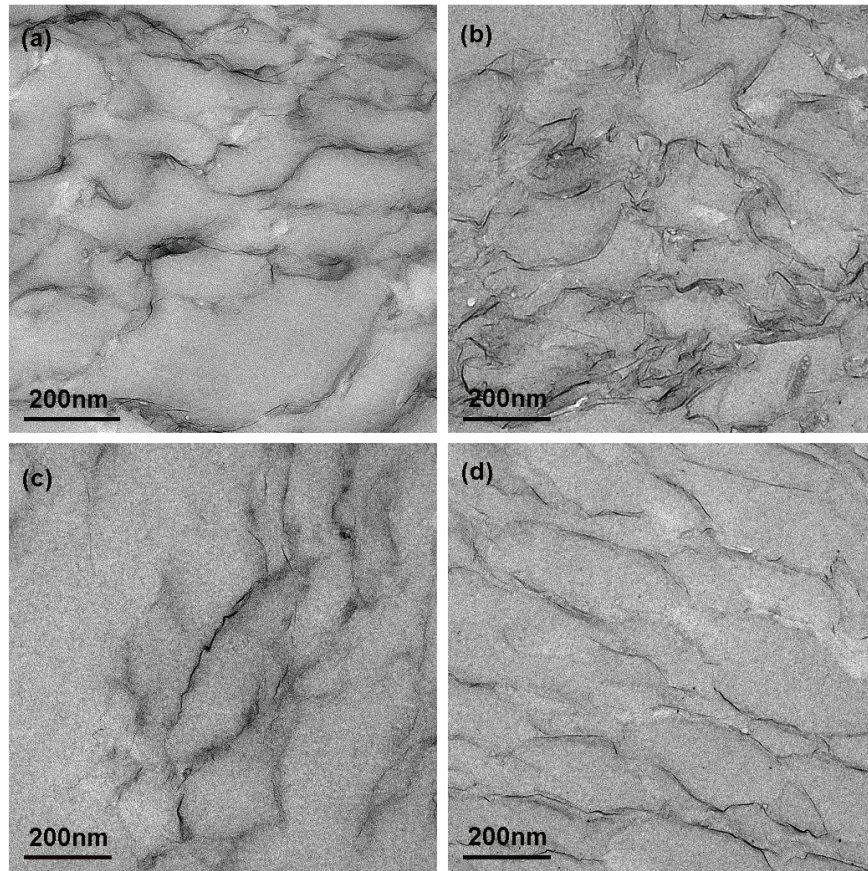


Figure 2.6: Transmission electron microscopy image of microtome slice of SU8 nanocomposites with (a) 0.2 wt% and (b) 0.9 wt% RGO, and (c) 0.2 wt% and (d) 0.9 wt% SRGO [42]. Copyright 2014 Elsevier Ltd.

2.2 Composite patterning

The main application of the SU8 as a photo-resist is in microelectronics, thus, it is very important for SU8-based composites to preserve their favorable properties (e.g. photo-patternability, transparency) for MEMS application. Therefore, once the well-structured composites are developed their compatibility with common technologies must be checked and adapted. In a photolithography process, a pattern is transferred from mask to a photo-sensitive polymer (called photo-resist, negative tone is referred to a resist for which the final pattern matches the area exposed to radiation, while for a positive resist the patterned area is the unexposed one). Figure 2.7 shows the standard process flow for photolithography of SU8. However, due to the presence of the fillers, the patterning process must be modified. All the experiments of this section were performed in the Center of MicroNanoTechnology (CMi), EPFL.

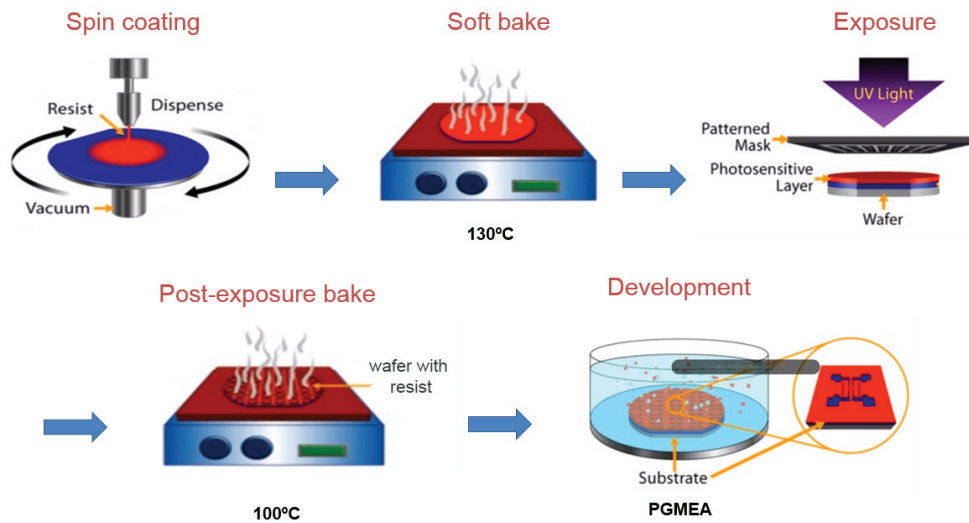


Figure 2.7: different steps of photolithography process for SU8.

In the first step, SU8–RGO nanocomposites with 0.3, 0.6, 0.9, and 1.2 wt% of RGO with respect to SU8 were spin-coated onto Pyrex substrates with rotational speed of 200 rpm. This spinning speed is much lower compared to standard value for pure SU8 (at least 2000 rpm), in order to avoid the segregation between the matrix and the fillers, and to preserve the uniformity of the composite. Such a low rotational speed may cause some non-uniformity in the thickness of the coated layer, in particular in the center and at the edge of the wafer, which must be taken into account in the mask design.

In the second step, a soft bake at 130 °C for 10 min, with temperature ramps of 5 °C/min was performed. Soft baking at 130 °C was twice as long compared to the standard procedure for pure SU8 with similar viscosity, since solvent evaporation is slower in the presence of RGO flakes. Higher temperatures of soft baking ($T > 137$ °C) may result in the initiation of thermal cross-linking during the soft bake or hindering of cross-linking during the UV-irradiation [21].

Next, UV irradiation was performed using Suss MJB4 single side mask aligner, with UV wave length of 365 nm and exposure dose of 15 mWcm^{-2} , to activate the photoinitiator. The polymerization process was accomplished during post-exposure baking at 100 °C for 30 min.

During the exposure to UV light, cross-linking occurs in two stages: (1) formation of a strong protoacid and (2) acid-initiated cationic polymerization. In the first stage hexafluoroantimonic acid is created by the decomposition of the photo-acid generator. The produced acid protonates the epoxides on the oligomer, acting as a catalyst. Subsequent heating will cause the protonated oxonium ions to react with neutral epoxides in a series of cross-linking reactions.

In fact, heating of the polymer activates cross-linking and regenerates the acid catalyst.

SU8 absorbs light in the UV range. The chemical changes induced during the photo-activation process, cause an increase in absorption throughout the exposure, which causes intensity loss across the film thickness when a UV beam penetrates the resist layer from top to the bottom. The gradient of irradiation (the top part of the film is exposed more than the bottom part) generates a T-profile instead of vertical profiles in photolithographic SU8 structures. The absorption change during the exposure is a function of wavelength. At shorter wavelengths the UV absorption of the unexposed SU8 resist is much higher and in addition the absorbance change is more pronounced. This means that at the longer wavelength of the irradiation source, the penetration depth is higher and exposes the bottom part. For this reason, wavelengths below 365 nm should be filtered out during the exposure.

Introducing nanoparticles into the photo-polymer will have a strong effect on its ability for photo-polymerization. A severe fall down in the degree of conversion is stated for epoxy with adding carbon nanotube (CNT) fillers [107, 15] as well as silver nanoparticles [34]. This observation can be explained by the absorbance and reflectance of the silver filler, which governs the overall absorption and reflection of the light in the composite resist. A larger irradiation dose, however, could be applied to achieve higher cured depth. Jiguet et al. [34]

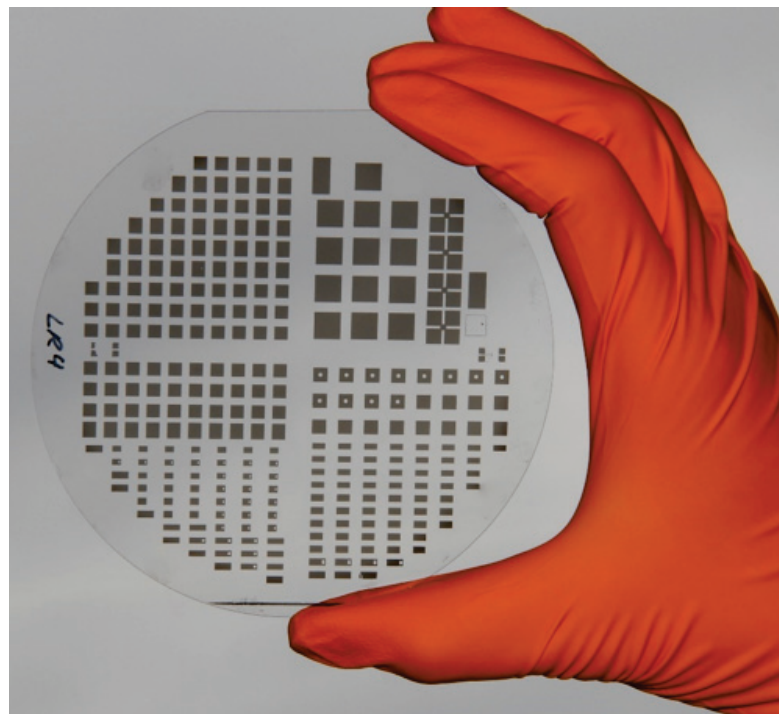


Figure 2.8: Photo-patterned SU8-RGO composite on a four inch Pyrex wafer.

Chapter 2. Composites with 2D fillers: SU8-graphene composites

reported that for a composite containing 5 vol.% of filler, the polymerized thickness raised from 15 to 35 μm by increasing the incident energy of exposure from 400 to 900 mJcm^{-2} .

Based on the discussion above we increased the UV exposure time compared to standard procedure to enhance the curing. The optimum exposure times for RGO loading of 0.3, 0.6, 0.9, and 1.2 wt% were 25, 35, 50, and 70 s, respectively, giving incident energies of 375, 525, 750 and 1050 mJcm^{-2} . These modifications enabled us to pattern the composites with various compositions in wafer scale (Figure 2.8) with delicate structures and improved lateral resolution. Finally, the exposed structures were developed in propylene glycol monomethyl ether acetate (PGMEA) with mild sonication in a bath and rinsed by isopropanol.

Figure 2.9 illustrates well-defined structures patterned by UV-lithography process. Continuous films of 15 μm SU8-RGO composites, with various concentrations and approximately uniform thicknesses, have been patterned on 4 inch Pyrex wafers. A minimum resolution of 10 μm was obtained for SU8-0.3 wt% RGO, as illustrated in Figure 2.9f, which is as good as the value reported for SU8-CNT composites prepared by spray coating [108]. Nevertheless, as observed in Figure 2.9a and e, the quality (adhesion and lateral resolution) of patterned film with 1.2 wt% RGO is not as good as the quality of films with lower concentration e.g. 0.6 and 0.3 wt% RGO (Figure 2.9c and Figure 2.9d, respectively). The lower quality of patterning at high RGO loadings is due to the fact that above a maximal concentration of RGO flakes, the photoresist

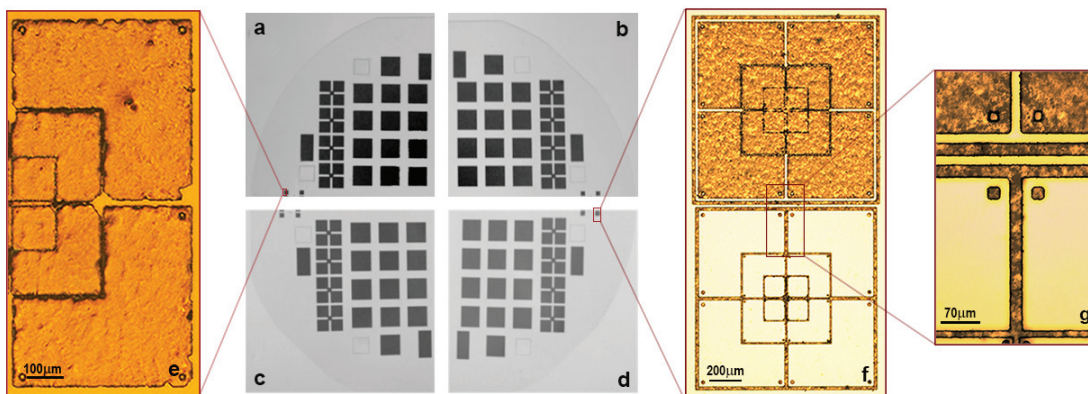


Figure 2.9: Well defined SU8-RGO nanocomposite, patterned by UV-lithography process containing: (a) 1.2 wt%, (b) 0.9 wt%, (c) 0.6 wt% and (d) 0.3 wt% reduced graphene oxide as filler. The transparency of the composite can be tuned with RGO content. Higher magnification of patterned structure is illustrated for (e) SU8-1.2wt% RGO and (f and g) SU8-0.3wt% RGO. The last two images demonstrate very good lateral resolution of the patterned structures. Minimal feature resolution of 10 μm was obtained for SU8-0.3 wt% RGO composite. Copyright 2014 Elsevier Ltd.

cannot fully polymerize. This challenge has also been observed for SU8 composite containing over 1 wt% CNT [15]. As a consequence of optical and chemical phenomena induced by the flakes or surfactant, deep penetration of UV inside the photo-polymer will be diminished and the activation of photo-initiator will be limited. Therefore, thermal polymerization plays a more significant role at high filler concentrations. While we achieved very good quality of processing of composites at concentrations below 1 wt%, patterning of composites has still rooms for improvement. Altering the exposure dose and baking time along with the quantity of the photoinitiator are the strategies that can be considered in this respect. Furthermore, the transparency of the composites can be tuned by varying the content of RGO nanofillers, (as illustrated in Figure 2.9a–d), which is favorable for many applications. Optical transmission of the composites with 5 μm thickness, measured by UV-Visible spectroscopy for a 700 nm wavelength light, as a function of the graphene loading is demonstrated in Figure 2.10.

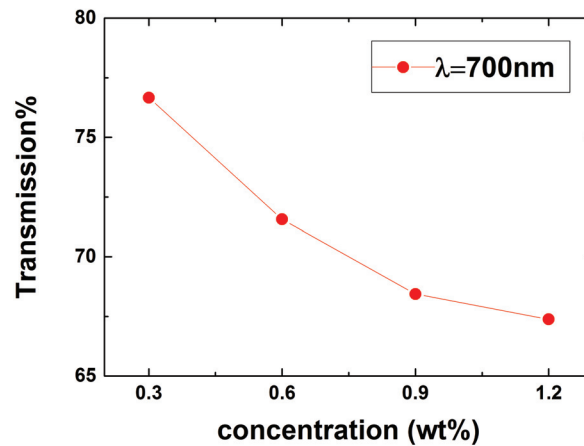


Figure 2.10: Optical transmission versus RGO loading at $\lambda = 700\text{nm}$.

2.3 Properties of the composites

2.3.1 Electrical characterization

Electrical characterization of the composites with the aim of understanding charge carriers transport is an important step for the description of the material and to achieve a better material design.

Electrical conductivity of the composites was measured by the four probe method using a Keithley 2400 current source and a Keithly 2182 nano voltmeter. For samples with very high resistivity (typically samples below 0.1 wt% RGO), Keithley 6517 source meter was used for

two probe measurement.

The results of these measurements are shown in Figure 2.11 for both SU8-RGO and SU8-SRGO series as a function of volume fraction $\phi = x\rho_{SU8}/(\rho_G + x\rho_{SU8})$ of the conducting fillers, where $\rho_{SU8} = 1.218\text{gcm}^{-3}$ and $\rho_G = 2.25\text{gcm}^{-3}$ are the mass densities of cross-linked SU8 and of RGO, respectively, and "x" denotes the fractional weight of RGO or SRGO with respect to SU8. Sample preparations for conductivity measurements are described in the experimental section 2.1. Compared to the RGO samples, the SRGO series display somewhat lower values of the conductivity σ , possibly due to a larger mean inter-filler separation as a result of the addition of surfactant. This hypothesis is partially supported by the TEM images of Figure 2.6b and Figure 2.6d, where the composite with added surfactant (Figure 2.6d) appears to have more homogeneously distanced RGO flakes compared to the composite without surfactant (Figure 2.6b). This effect is less visible for the lower concentrations composites, Figure 2.6a and Figure 2.6c.

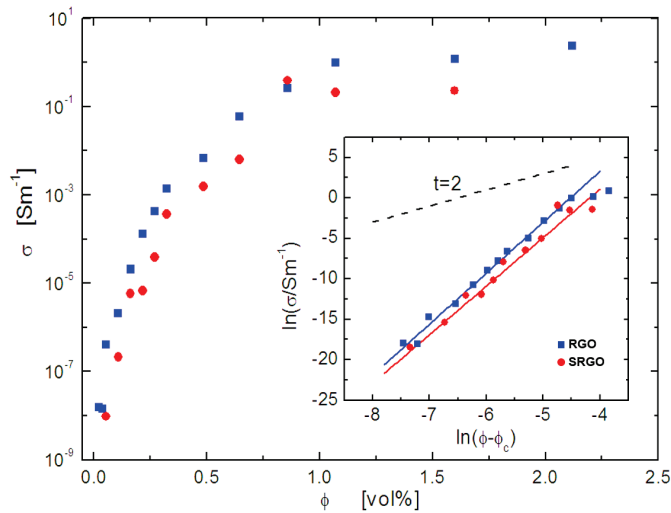


Figure 2.11: Measured conductivity σ as a function of RGO volume fraction ϕ for both RGO (filled squares) and SRGO (filled circles) SU8 composites. Inset: ln-ln plot of σ as a function of $\phi - \phi_c$. Solid lines are the best fits of Equation 2.1 to the data. As a comparison, we plot Equation 2.1 with $t = 2$ (dashed line) [42]. Copyright 2014 Elsevier Ltd.

Besides this difference, both SU8-RGO and SU8-SRGO show exceptional electrical properties when compared to other graphene-based systems [109], as evidenced in Figure 2.12 where we show the conductivity data of SU8-RGO and SU8-SRGO (filled symbols) together with those of other polymer-graphene composites (open symbols) taken from recent literature [8, 110, 111, 112, 113, 114, 115]. As it is immediately apparent from the figure, the drop of σ as ϕ goes to zero is remarkably smooth: even at loadings as small as 0.038 % for RGO and 0.054 %

for SRGO, the measured value $\sigma \approx 10^{-8} Sm^{-1}$ for the composite conductivity is still far larger than that of pure SU8 (about $10^{-14} Sm^{-1}$). SU8 composites of reduced graphene oxide show thus electrical transport properties that are even comparable to those reported for several polymer-CNT materials [116].

The behavior highlighted in Figure 2.11 and Figure 2.12 has rather striking consequences when the ϕ -dependence of σ is interpreted in terms of a percolation transition [44, 45], according to which the composite conductivity is predicted to follow a power-law behavior of the form

$$\sigma = \sigma_0(\phi - \phi_c)^t \quad (2.1)$$

where ϕ_c is the percolation threshold (explained in section 1.4) and t is the transport exponent. According to the theory of percolation transitions [44, 45], ϕ_c depends on the particular microstructure of the composite, while the value $t \approx 2$ of the transport exponent is universal for all systems in three dimensions. We have fitted the conductivity data to Equation 2.1 for $\phi \leq 0.645$ % using a standard non-linear fitting algorithm. Apparently, the measured conductivity of both SU8-RGO and SU8-SRGO are very well reproduced by Equation 2.1 in the whole range of concentrations below 1 %, as shown in the inset of Figure 2.11. Interestingly, however, the values of ϕ_c and of the transport exponent t that best fit the experimental data are incompatible with the percolation mechanism of transport, and so with the premises of Equation 2.1.

Indeed, for SU8-RGO and SU8-SRGO we find respectively $\phi_c = 0.04\% \pm 0.02\%$ and $\phi_c = 0.01\% \pm 0.03\%$, pointing to vanishingly small (for SU8-SRGO) or even negative (for SU8-RGO) critical volume fractions. More importantly, the transport exponent values $t = 6.4 \pm 0.8$ and $t = 6 \pm 1$ obtained from the fits of SU8-RGO and SU8-SRGO data are much larger than the universal value $t \approx 2$ (dashed line in the inset of Figure 2.11) predicted by the percolation theory [44, 45]. Even though the values of the percolation threshold show some dispersion around $\phi_c = 0\%$, the fitted transport exponents are systematically much larger than $t \approx 2$. In particular, excluding from the fit the data for the smallest volume fractions we find positive, albeit practically zero, percolation thresholds ($\phi_c = 0.02\% \pm 0.02\%$ for SU8-RGO and $\phi_c = 0.02\% \pm 0.05\%$ for SU8-SRGO), while we still obtain transport exponents significantly larger than $t \approx 2$ ($t \approx 5$ for both series of composites), confirming thus our conclusion that the conductivity data of SU8-RGO and SU8-SRGO are inconsistent with a percolation mechanism of transport.

Although strong deviations from $t \approx 2$ have been vastly reported in literature for several classes of composites [116, 117], their significance concerning the intrinsic mechanism of

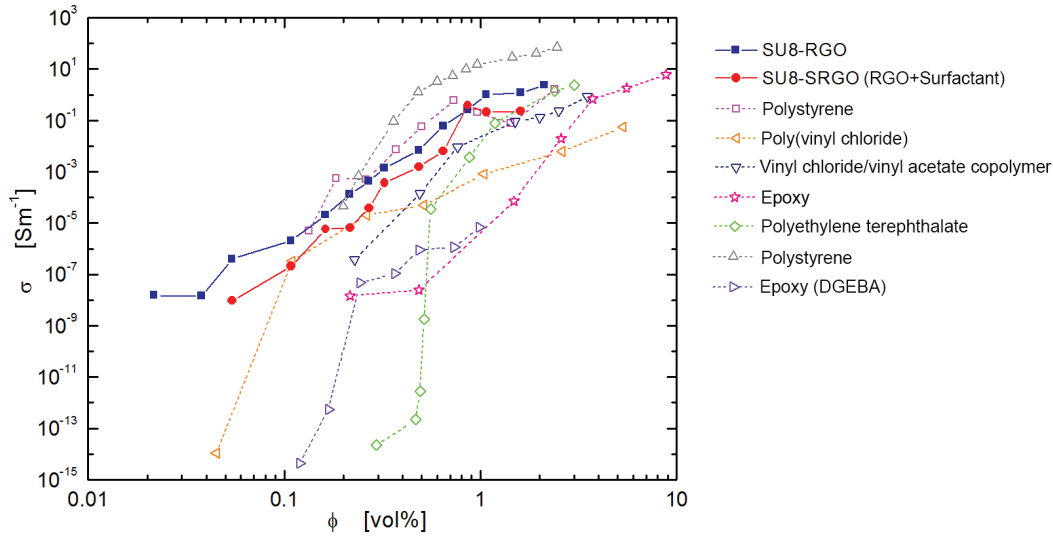


Figure 2.12: Conductivity of SU8–RGO and SU8–SRGO composites (filled symbols) as a function of the volume fraction (ϕ) of reduced graphene oxide. Open symbols are the measured conductivity values of different polymer–graphene composites derived from Refs. [8, 110, 111, 112, 113, 114, 115] (Plot taken from Ref. [42]). Copyright 2014 Elsevier Ltd.)

transport in conductive composites is still often overlooked [118]. The reason of the observed inconsistency of the measured data with a percolation transport mechanism can be traced back to the interplay between the tunneling mechanism of conduction between the fillers and the type of filler dispersion in the composite. Indeed, since charge carriers have to tunnel across the insulating barrier separating the conducting fillers, the distribution of the inter-particle separations plays a predominant role in governing the overall transport dependence on ϕ , because the probability of tunneling decays exponentially with the particle separation (see Figure 1.14). In particular, a percolating-like behavior as given in Equation 2.1 with $t \approx 2$ is expected as long as the distribution of inter-particle separations is such that it is possible to label the inter-particle tunneling conductance as being either “on” or “off” [44, 45]. This case is well illustrated by the discrete distribution of inter-particle separations in lattice-like systems [119], in which the conducting particles occupy randomly the sites of a lattice: the “on” conductance is given by tunneling between nearest-neighbor particles, while the “off” conductance is given by the much smaller tunneling between farther neighboring particles [119]. In this situation, there is a well defined percolation threshold ϕ_c given by the smallest ϕ such that a cluster of nearest-neighboring particles spans the entire system. On the contrary, when hard-core conducting fillers are homogeneously dispersed in a continuous insulating matrix, there is no clear distinction between “on” and “off” tunneling conductances, because the distribution of inter-particle separations is continuous [119]. In this case, a reduction of

ϕ induces a gradual enhancement of the mean inter-particle separation and, consequently, a gradual reduction of the inter-particle tunneling. It can be shown that the composite conductivity resulting from tunneling processes between particles in the continuum follows [120]:

$$\sigma \simeq \sigma_0 e^{-\frac{2\delta(\phi)}{\xi}} \quad (2.2)$$

where ξ is the tunneling decay length, which ranges from a fraction to a few nanometers, and $\delta(\phi)$ is a typical distance between two particle surfaces. For homogeneous dispersions, $\delta(\phi)$ increases continuously as ϕ decreases, leading to vanishingly small σ only for $\phi \rightarrow 0$. The particular functional form of $\delta(\phi)$ depends on the shape of the particles and on the details of the continuum dispersion of the conductive fillers within the insulating matrix [121].

From the above considerations, we see thus that the different ϕ dependences of the conductivities shown in Figure 2.12 could be interpreted in terms of different kinds of distributions of the graphene-like particles in the composites. In particular, the strong deviation of the transport exponent from $t \simeq 2$ observed in both SU8-RGO and SU8-SRGO composites suggests that Equation 2.2 could be more appropriate than Equation 2.1 to describe the conductivity data of these composites. To test this hypothesis, we first note that the functional dependencies of $\delta(\phi)$ can be obtained from the study of geometrical connectedness properties of distributions of impenetrable fillers. In particular, $\delta(\phi)$ (often referred to as “critical distance”) is identified as the shortest among all inter-particle distances such that the subset of particle separations shorter than $\delta(\phi)$ still spans the entire sample [120, 122, 123, 124, 121]. The resulting functional forms of $\delta(\phi)$ have been shown to adequately describe through Equation 2.2 the measured conductivity data for several polymer nanocomposites with fillers of different shapes [121, 125].

For the specific case of fluids of rigid and flat disk-like fillers, theories [126] and simulations [127] predict that $\delta(\phi)$ does not depend on the diameter D of the disks and that $\delta(\phi)$ scales as h/ϕ in the $\delta(\phi) \ll D$ regime, where $h \ll D$ is the disk thickness. The resulting $\ln(\sigma) \propto -1/\phi$ behavior is however not observed in our composites, as shown in Figure 2.13a, where the $\ln(\sigma)$ data do not follow a straight line when plotted as a function of $1/\phi$. We have checked that modeling plate-like fillers by impenetrable oblate spheroids, which yields $\delta(\phi) \propto h/\phi^{4/3}$ with a weak dependence on the aspect ratio [121], does not reproduce the ϕ -dependence of the measured σ as well.

Instead, we find a better linear dependence, especially for the SU8-SRGO samples and apart from the lowest concentration of the SU8-RGO system, when $\ln(\sigma)$ is presented as function of $1/\phi^{1/3}$, as shown Figure 2.13b. Interestingly, a dependence of the form $\delta(\phi) \propto 1/\phi^{1/3}$,

implied by Equation 2.2 and Figure 2.13b, has already been observed in various polymer nanocomposites [116, 128, 129].

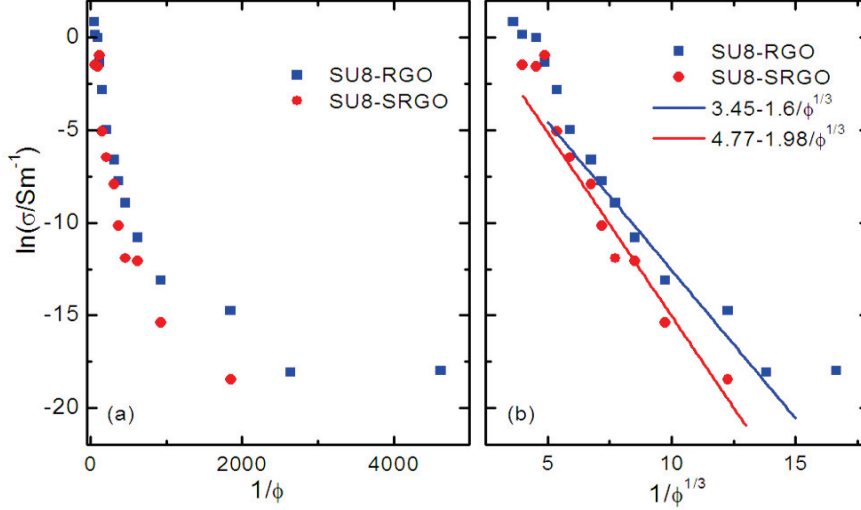


Figure 2.13: Natural logarithm of the measured conductivity of SU8-RGO and SU8-SRGO composites as a function of (a) $1/\phi$ and (b) $1/\phi^{1/3}$. Copyright 2014 Elsevier Ltd.

The relation $\delta(\phi) \propto 1/\phi^{1/3}$ is expected to hold true for point particles that occupy random positions in three dimensions [120, 130] or, more generally, when the shortest distances between particles are completely random and independent of filler hard-cores and shapes. Here, we argue that such a reduction of hard-core effects on $\delta(\phi)$ could be due to the more or less crumpled shape that flexible graphene flakes assume in the composite (as evidenced in Figure 2.6), analogously to what has been recently proposed in the context of continuum percolation theory [47]. In dispersions of extended flexible fillers, indeed, we do not expect that the critical distance between filler surfaces is correlated with the position of the filler centroids, and so $\delta(\phi) \propto 1/\phi^{1/3}$ appears to be a plausible assumption. Assuming that the diameter D is irrelevant also when the disks are not flat, we thus propose that $\delta(\phi) \sim h/\phi^{1/3}$. Using this expression in Equation 2.2, from the fits shown in Figure 2.13b we obtain $2h/\xi \sim 1.6$ and $2h/\xi \sim 2$ for the SU8-RGO and SU8-SRGO composites, respectively. Since the thickness h is in the nanometer range, we obtain the tunneling decay length ξ in the same range, which is the expected order of magnitude. We note furthermore that the fitted value of $2h/\xi$ for the SU8-SRGO composites is slightly enhanced compared to that for SU8-RGO, which is consistent with an enhanced effective thickness h due to the presence of surfactants.

In summary, electrical conduction measurements have evidenced large conductivities at low loadings, which are superior to those reported for other polymer-graphene composites and even comparable to SU8-CNT systems [41] and several other CNT-based composites [116].

This remarkable behavior of transport results from the combination of effective homogeneous dispersions of the graphene flakes in the SU8 matrix and the tunneling mechanism of electron transfer between the flakes. The conductivity data are reasonably well understood in terms of random tunneling connections between the RGO fillers. The observed randomness of tunneling and the lack of hard-core effects of the fillers are due to the flexibility and the crumpled shape of the graphene flakes in the matrix.

2.3.2 Mechanical characterization

The mechanical reinforcement in composites occurs by load transfer through filler/matrix interface. Thus, the good dispersion of the fillers in the matrix and their strong affinity is crucial (explained in more details in section 1.5). In this respect, nanoindentation is a valuable technique to assess the improvement of mechanical characteristics such as Young's modulus, hardness and creep for composite materials upon incorporation of the fillers [131], due to the fact that this method has shown sensitivity to important composite features like filler loading, dispersion, and interfacial adhesion [132, 133]. Moreover, the homogeneity of the nanocomposites can be evaluated across the thickness and the surface of the composite [134, 135].

The need for designing new functional materials for different applications has been the driving force for numerous studies on mechanical properties of nanocomposites of polymer-carbon nanostructures [52, 131]. In general, the enhancement of Young's modulus and hardness in the presence of carbon nanofillers (graphene platelet, CNT) is more effective for thermoplastic matrices compared to their thermoset counterparts like epoxy. Usually the increase in the value of the Young's modulus for CNT reinforced thermosets does not exceed 100% for concentration range of 0.1–5.5 wt% [136, 137, 138]. In some cases the reduction in stiffness have been reported [134, 139, 140] which is attributed to poor dispersion of the fillers. In the case of epoxy-graphene nanocomposites, there are reports of limited enhancement of the Young's modulus [131]. Aggregation of graphene into stacks, as well as inefficient matrix-filler interaction might be the possible reasons. It should be pointed out that in these cases the fillers had been incorporated without functionalization.

In this section, the nanoindentation method is first explained and then the results of these measurements on SU8-RGO composites are discussed.

Nanoindentation principles

Nanoindentation is a widely used technique for the surface mechanical characterization of bulk materials and thin films down to nanoscale level. Briefly, a diamond indenter (usually a three-sided pyramid known as Berkovich indenter) is pressed into a specimen (Figure 2.14a) of the material up to a maximum load (P_{max}) or a maximum penetration depth (h_{max}). In the case of samples on substrate, the penetration depth is preserved below 10% of the sample's thickness, to avoid the effect of the substrate. During the loading and unloading of the indenter a load-displacement graph (like the one presented in Figure 2.14b) can be acquired, by measuring the applied force versus the penetration depth. This graph is used to determine two important characteristics of the tested material: the hardness (H) and the elastic modulus (E), as explained by Oliver and Pharr [141].

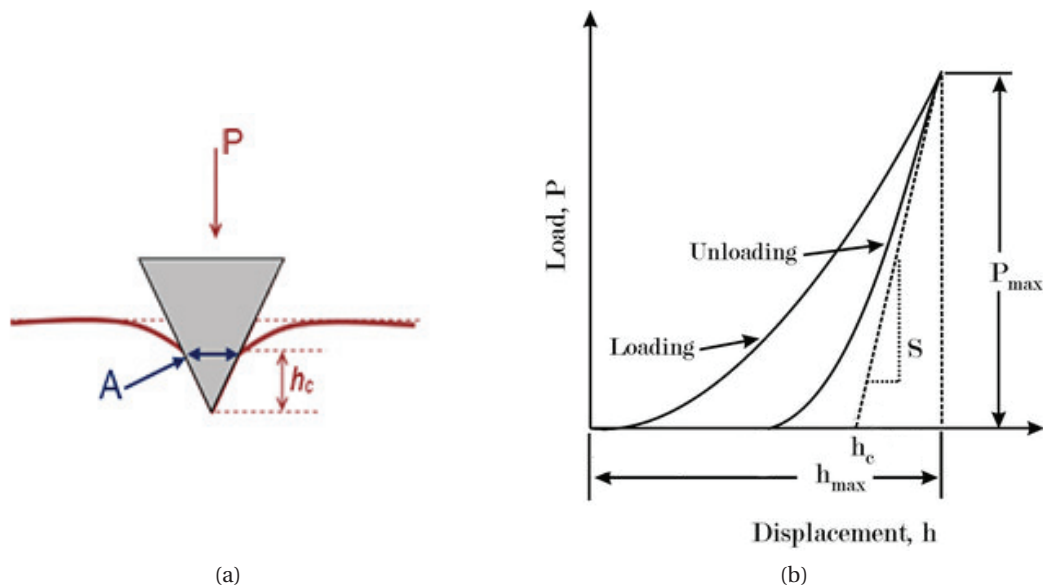


Figure 2.14: (a) Schematic representation of a Nanoindentation test. (b) A typical load-displacement curve.

Hardness is defined as the resistance of a solid matter to permanent deformation when a compressive force is applied, so it is a fundamental parameter concerning the application. It is calculated by dividing the maximum load by the contact area (A_c) of the indenter.

$$H = \frac{P_{max}}{A_c} \tag{2.3}$$

The Stiffness of the material is given by the slope of the unloading curve at maximum load

($S = \frac{dP}{dh}$). This parameter is used for the calculation of the reduced elastic modulus, E_r :

$$E_r = \frac{\sqrt{\pi}}{2} \cdot \frac{S}{\sqrt{A_c}} \quad (2.4)$$

Where A_c is equal to $24.5h_c^2$ for a Berkovich indenter.

The reduced modulus is given as a sum of the compliance of the material and the diamond indenter:

$$\frac{1}{E_r} = \frac{1-\nu^2}{E} + \frac{1-\nu_i^2}{E_i} \quad (2.5)$$

where E and ν are the elastic modulus and poisson's ratio, respectively, for the material under test, and E_i and ν_i are the same parameters for the indenter tip. Hence, using Equation 2.5, one can calculate the Young's modulus of the tested specimen.

Concerning the operation of the system a constant indentation strain rate should be applied at all penetration depths in order to have valid results. Compared to tensile test method, where generally uniaxial tensile forces are exerted, in a nanoindentation test the load direction is being altered radially from the first contact point. Hence, the material is under a combination of compressive, tensile and shear stresses. In addition, the volume of deformation is varying constantly underneath the indenter, due to this distribution of stresses, which is not the case for tensile testing [131]. Based on the above mentioned discussion, one cannot expect a perfect match of results between nanoindentation and macroscopic techniques, and in many cases, higher Young's modulus values have been measured by nanoindentation. However, a number of reports suggest a fair consistency between the values obtained with the two techniques [142, 143, 144] and the general conclusion is that the nanoindentation measurements are in reasonable agreement with macroscopic ones.

Nanoindentation results for SU8-RGO composites

SU8-RGO composites with a wide range of compositions (0.3-7 wt% RGO) were prepared following the procedure described in section 2.1 and polished for nanoindentation test. The measurements of the SU8-RGO samples were performed using an XP indenter (NanoInstrument Inc.) with a Berkovich tip which operates in a continuous stiffness measurement (CSM) mode. For each sample at least 9 indentation tests were performed with a maximum displacement set to $2\mu m$.

Chapter 2. Composites with 2D fillers: SU8-graphene composites

One advantage of the nanoindentation is the possibility of investigating the mechanical homogeneity of a sample by doing several tests at different locations of a sample [15]. Figure 2.15 demonstrates the load-displacement curves of the 9 overlapping indents for SU8-0.6wt% RGO composite, implying the mechanical homogeneity of the composites.

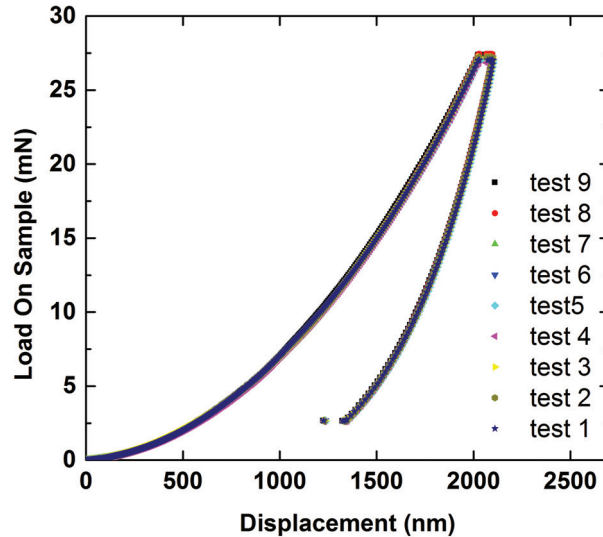


Figure 2.15: Load-displacement curves for composite SU8-0.6 wt% RGO. The obtained curves for all 9 indents overlap implying the homogeneity of the sample.

For every other composite (ranged 0.1 to 7 wt%) the overlap of load-displacement curve was observed.

One should mention that, although the composite containing 7 wt% showed acceptable results in nanoindentation, macroscopic cracks appeared during its thermal curing which questions the relevance of such composite for application and technological aspects. We think that at such high concentration, the surface area of the graphene sheets is too large to be covered by SU8 monomers. In addition, the high internal stress is predictable because of the large fillers content. Normally the maximum nanofiller content that in practice can be added to thermoset matrix is limited to 5 wt%, while thermoplastic matrices may hold up to 10 wt% fillers. This is known to be a limiting factor in the processing of epoxy based composites [131]. The evolution of Young's modulus (E) and hardness (H) as function of RGO wt% is illustrated in Figure 2.16 for indenter displacement of 750 nm.

As demonstrated in Figure 2.16, for pristine SU8 the acquired value for the Young's modulus is equal to the values measured by the traction test, which is a confirmation for the validity of

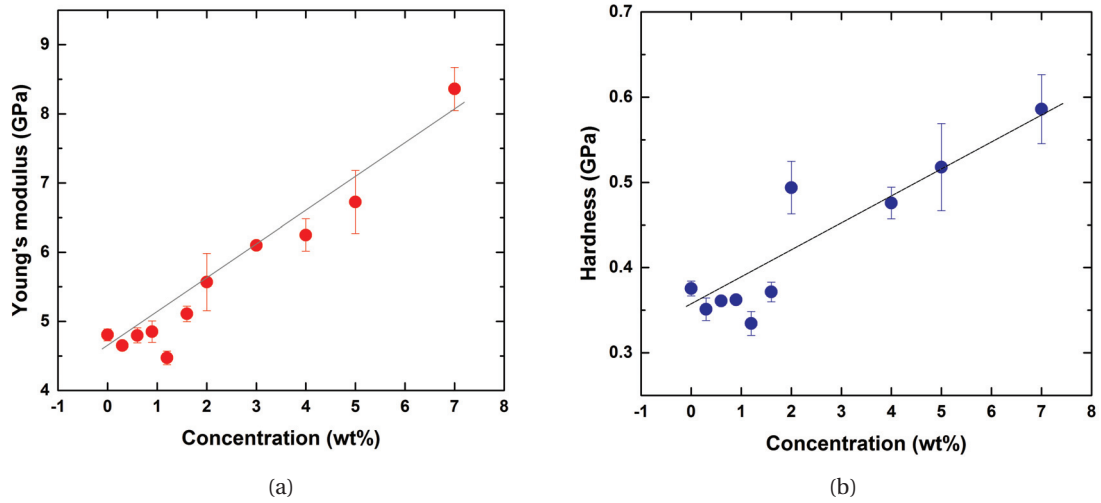


Figure 2.16: The average (a) Young's modulus and (b) hardness of SU8-graphene composites versus RGO loading at the displacement of 750 nm. The line is guide for the eye.

the nanoindentation method for this measurement. In the case of hardness, the value that we measured is slightly higher than what is known as the hardness of the cross-linked SU8 (0.3 GPa). In consistency with the literature [145, 2] we observed a linear increase for both H and E (it is known that hardness and modulus often behave analogously). Our results show a maximum improvement of $\Delta H \approx 66\%$ and $\Delta E \approx 75\%$ for displacement of 750 nm. Where $\Delta E = E_{composite} - E_{SU8} / E_{SU8}$ and $\Delta H = H_{composite} - H_{SU8} / H_{SU8}$. These values are not too far from the maximum improvement observed for CNT/Epoxy composites ($\Delta E \sim 100\%$) [131]. We chose a displacement of 750 nm to avoid the indentation size effect which was observed for some measurements close to the surface (this effect is further discussed in the next section). In addition, for few samples e.g. SU8-7 wt% RGO, we observed an unexpected increase in E as the penetration depth augments (Figure 2.17). The origin of this phenomenon is still under investigation.

Indentation size effect

In many studies on polymer based composites reinforced with carbon nanostructures, a dependence of hardness or Young's modulus on the indenter displacement is observed. Usually with increase in penetration depth, E or H reduces but the opposite result is also observed. This effect, which is especially critical at displacements below a few hundred nanometers, is known as "indentation size effect". The surface roughness, time-dependent plastic deformation or other nanostructural features due to the processing, are among the reasons which have been

used to explain the indentation size effect. The condition of the indentation tip (too sharp or blunt) can also cause such an influence. Indeed, with further increment in penetration depth and approaching to micrometer scales, the effect of above-mentioned error sources is less and the intrinsic properties of the material are dominant [131].

Mionic et al. [15] have reported that for SU8-CNT composites, the depth dependence of the Young's modulus (for displacements greater than 300 nm) is associated to the type of solvent used for pre-dispersing of the fillers. In fact, for most cases in their study (PGMEA, Aceton, MEK), the solvent get trapped inside the composite during the cross-linking and E drops while the indenter penetrates.

For the case of GBL, however, this reduction in Young's modulus is not observed for a penetration depth in the range of 2 μm . The reason is the contribution of GBL in SU8 polymerization by bridging two neighboring epoxy groups leading to longer aliphatic segments in the network [15].

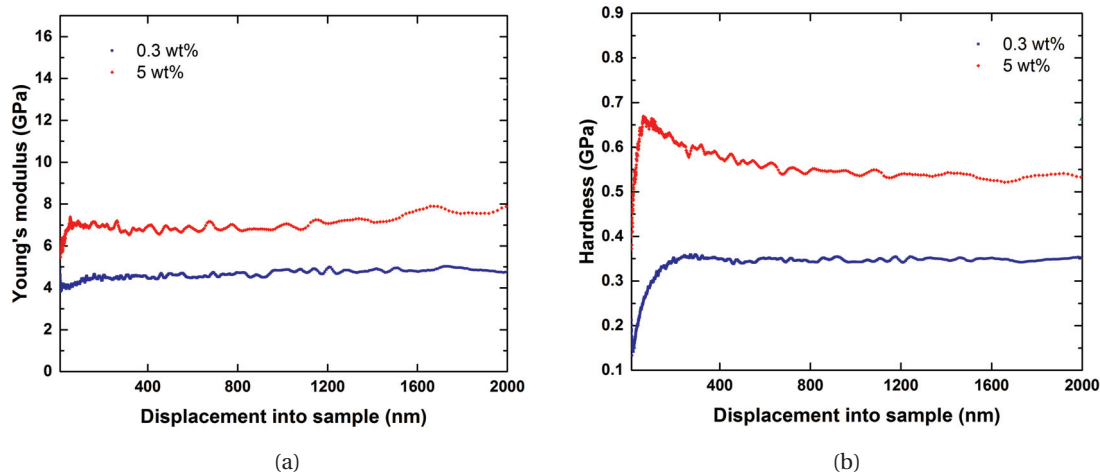


Figure 2.17: General trend for the dependence of (a) E and (b) H to penetration depth of the indenter. Representative Load-displacement curves for composite SU8-0.3 wt% RGO (blue) and SU8-5 wt% RGO (red) are demonstrated.

We had a similar observation for SU8-RGO composites, using GBL as dispersing solvent. Figure 2.17a illustrates the Young's modulus as a function of penetration depth for the lowest and one of the highest concentrations. As one can see in this plot, the indentation size effect on E is trivial close to the surface for SU8-RGO composites. A more dramatic effect is observed for H , notably for higher RGO contents (Figure 2.17b). We assume that this is due to the less efficient polymerization of SU8 in presence of high RGO content.

In this section we showed that the addition of RGO fillers to SU8 improved the Young's modulus by $\sim 75\%$ and the hardness by $\sim 67\%$. The enhancement of mechanical properties is more efficient when chemical bonding occurs between the filler and the matrix. In order to investigate the possibility for the presence of such bindings in our composites, optical spectroscopy was employed to give insights of filler/matrix interactions. The results of these investigations are presented in the next section.

2.3.3 Optical characterization

The optical spectroscopy techniques are valuable tools for non-destructive characterization of the composites. In this part of the work, we have employed Raman and Infrared spectroscopy as well as photoluminescence to study the chemical structure of the SU8 photoresist as well as the SU8-RGO composites. The goal of this study was to gain insights into: 1) the possible covalent bonding of the polymer matrix with the functional groups attached to the RGO fillers; 2) the influence of the RGO on the photo-polymerization mechanism of SU8. This work was performed in collaboration with the Prof. Mihaela Baibarac and Prof. Ioan Baltog from the Laboratory of Optical Processes in nanostructured Materials at the National Institute of Materials Physics in Bucharest, Romania.

Sample preparation for optical spectroscopy

The preparation of the SU8-RGO composite inks was carried out according to the protocol described in section 2.1. The ink were spin-coated with a rotational speed of 300 rpm onto glass supports coated with a 100 nm thin film of Au. The five films were soft baked at 130 °C, using a Sawatec HP200 hotplate, for 5 min with a temperature ramp of 5 °C/min for solvent removal. The obtained films of RGO-SU8 monomers are labeled A_1, A_2, A_3, A_4 and A_5 for RGO concentration of the 0, 0.001, 0.005, 0.0075 and 0.01 wt%, respectively. A second set of samples was prepared with same conditions but illuminated with 365 nm-UV for 2 min to activate the TSHAS photo-initiator (Suss MJB4 single side mask aligner, exposure dose of 20 $mW\text{cm}^{-2}$) before the baking at 85 °C. The samples cross-linked by UV light are labeled S_1, S_2, S_3, S_4 and S_5 with same respective RGO loading as the composites set A.

The IR spectra of the composites were recorded with a FTIR spectrophotometer, Vertex 80 model, from Bruker using the KBr pellets method. In order to prepare KBr pellets, powders from the $A_1 - A_4$ and $S_1 - S_4$ samples were obtained by detaching of the films deposited onto the substrate and grinding them vigorously. The Raman spectra were acquired with a FT

Chapter 2. Composites with 2D fillers: SU8-graphene composites

Raman spectrophotometer, RFS100 model, from Bruker in the backscattering geometry. The PL spectra were recorded in the right-angle geometry, at room temperature (RT), using a Horiba Jobin Yvon Fluorolog-3 spectrometer, model FL 3-22.

Vibrational and photoluminescence properties of SU8

In this section, the results of optical spectroscopy will be discussed for blank (filler free) SU8, as a reference. The comparison of the photochemical behavior of SU8-RGO composites with blank SU8 will allow to understand the influence of RGO on the photo-polymerization mechanism of SU8.

The photoluminescence emission spectrum of pure SU8 monomer film (sample A_1) as a function of illumination time under 350 nm light is shown in Figure 2.18. The PL spectrum of

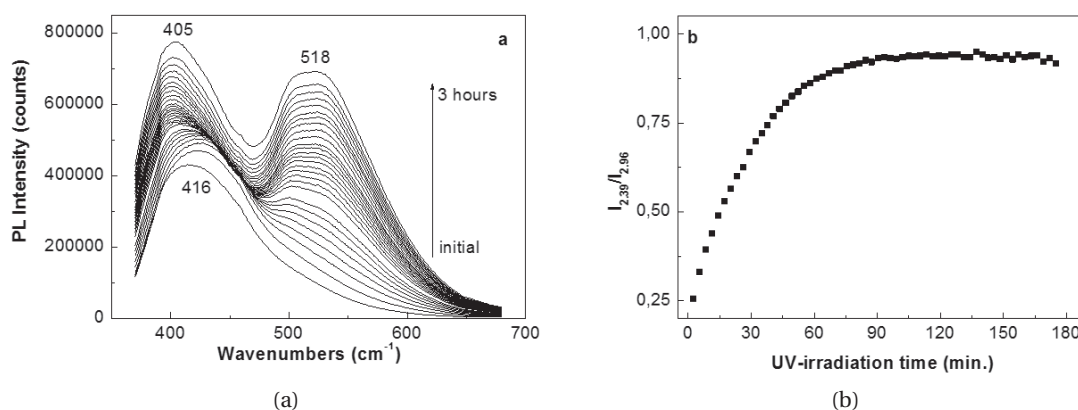


Figure 2.18: (a) The evolution of the PL spectra of A_1 sample UV-irradiated for 3 hours. (b) The dependence of the intensities of PL bands peaked at 2.39 eV (518 nm) and 2.96 eV (418 nm) ($I_{2.39}/I_{2.96}$) as a function of UV-irradiation time.

sample A_1 in the initial state is characterized by an emission band peaked at 2.98 eV (416 nm), which shows an asymmetrical profile at low energies. According to Figure 2.18, significant changes are induced in the PL spectrum of the sample A_1 with increasing the exposure time at the excitation wavelength of 350 nm. During 3 hours, a gradual increase in the intensity of the emission band situated in the spectral range 350-450 nm is observed simultaneously with an up-shift from 2.98 eV (416 nm) to 3.06 eV (405 nm). Along with these features, an additional PL band peaked at 2.39 eV (518 nm) appears and its intensity increase with UV-illumination time. The ratio between the intensities of the two PL bands peaked at 3.06 and 2.39 eV reaches ~ 1.12 after 3h of UV irradiation. All these changes could be correlated with the cross-linking

reactions of the SU8 photoresist by activation of the photoinitiator TSHAS, a process which involves the generation of $HSbF_6$ [79, 146].

In order to prove this statement, Figure 2.19 shows FTIR spectra of the SU8 photoresists before and after exposition to UV light for 3 hours. The black curves in Figure 2.19a and Figure 2.19b show FTIR spectra of the A_1 (SU8 in form of monomer) and S_1 (photo cross-linked SU8) samples. The main IR absorption bands of the SU8 are summarized in Table 2.2.

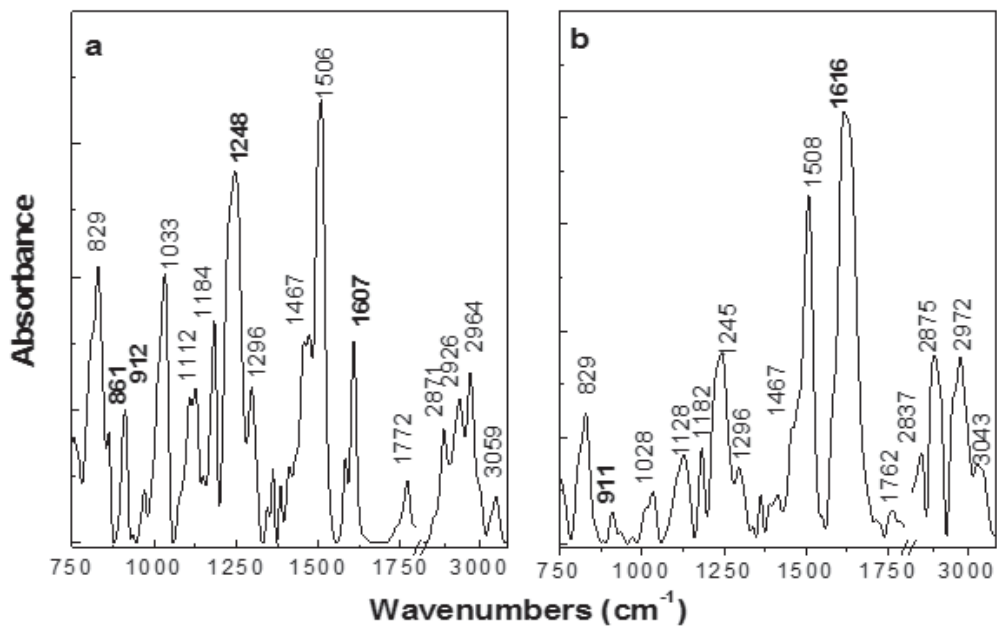


Figure 2.19: FTIR spectra of the (a) A_1 and (b) S_1 samples.

The cross-linking of sample S_1 (2 min UV illumination and baking at 85 °C for 30 min) induces significant changes in the vibrational properties of the SU8 photoresist. In the FTIR spectrum of S_1 , the IR absorption band at 861 cm^{-1} disappeared while the absorbance of the IR band peaked at 912 cm^{-1} decreases, which is in good accordance with Ref. [146]. The intensity ratio of the 1246 and 1504 cm^{-1} bands decrease from 0.84 (for A_1) to 0.54 (for S_1). These modifications of the vibrational modes confirm the opening of epoxy rings under UV light (in accordance with the cross-linking mechanism of SU8 published by Lima et al.[79]). Several other changes are observed in Figure 2.19a and Figure 2.19b: i) The position of the IR band situated in the spectral range 1600-1650 cm^{-1} , is up-shifted from 1607 cm^{-1} to 1616 cm^{-1} simultaneously with its increase in absorbance and the full width at half maximum. This fact indicates that new covalent bonds of C-C and C=C are formed during the cross-linking reactions

Chapter 2. Composites with 2D fillers: SU8-graphene composites

Table 2.2: Vibration modes observed by IR spectroscopy in the SU8 sample.

Observed frequencies (cm^{-1})	Assignment	Ref.
829	epoxy ring	[146]
861	C–O stretching of cis substituted epoxy rings	[75]
912	C–O stretching of trans substituted epoxy ring	[75]
1033, 1112	C–O–C stretching in ethers	[75]
1184	aryl-C-aryl	[76]
1246	asymmetric stretching of C-O-C group in mono-substituted epoxy ring	[146]
1296	symmetric stretching of epoxy ring	[76]
1467, 1508	C–C + C=C stretching in benzene ring	[76, 75]
1581, 1607	C-C stretching of the benzene ring	[74, 147]
1772	C=O vibrational mode of GBL	[148]
2871	C-H symmetric stretching in CH_3 and CH_2 groups	[149]
2926	C-H anti-symmetric stretching in CH_3 and CH_2 groups	[149]
2964	– CH_2 stretching	[76]
3059	=C-H stretching in benzene ring	[73]

of SU8, as a result of the photochemical activation of TSHAS; ii) The IR band assigned to the C=O vibrational mode of GBL is down shifted from 1772 cm^{-1} to 1762 cm^{-1} simultaneously with a significant decrease in the absorbance. As shown in Ref. [148], the coexisting of GBL in SU8 in the sample UV-irradiated can lead to the appearance of IR band with maximum at 1735 cm^{-1} assigned to the C=O stretching vibrational mode in linear ester [150] as a consequence of the co-polymerization of GBL and SU8. In our case, the decrease in absorbance of the IR band at 1772 cm^{-1} assigned to the C=O vibrational mode of GBL and the absence of an IR band at $\sim 1735\text{ cm}^{-1}$ indicates that the co-polymerization of GBL and SU8 does not occur, above variations being assigned to the cross-linking process of SU8.

Vibrational and photoluminescence properties of the SU8/RGO composites

Figure 2.20 shows PL spectra of the $A_2 - A_5$ composites and their changes during 3 hours of UV-irradiation. Figure 2.21 illustrates the variations in PL spectra of SU8-RGO composites in presence of RGO.

As shown in Figure 2.21, increasing the RGO content in the $A_1 - A_5$ samples leads to a gradual decrease in the intensity of the PL band situated in the spectral range of 350-450 nm, both at initial stage and after 3h illumination with UV. For the highest RGO loading, the PL intensity is reduced by a factor of about 2 as compared to pure SU8 Figure 2.21a. This behavior

2.3. Properties of the composites

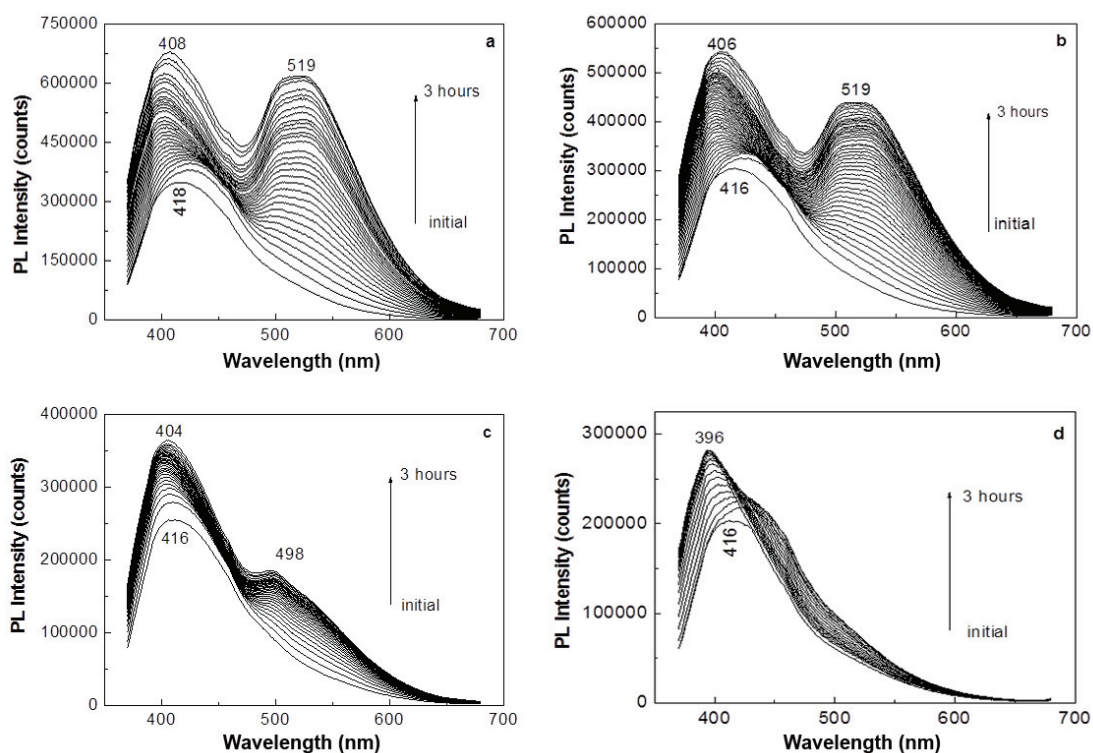


Figure 2.20: The evolution of the PL spectra of the A_2 (a), A_3 (b), A_4 (c) and A_5 (d) samples exposed to the UV-irradiation for 3 hours.

evidences the SU8 PL quenching effect induced by RGO. As one can see in Figure 2.20 and Figure 2.21, the intensity of the PL band at 3.06 eV, which appears upon UV illumination for pure SU8 (Figure 2.18), is dependent on the RGO content. Indeed the ratio between the intensities of the two PL bands peaked at 3.06 and 2.39 eV ($I_{3.06}/I_{2.39}$) changes from 1.1 to 3.71 (Figure 2.21b). This fact indicates that the chemical structure of the polymerized SU8 and perhaps the polymerization mechanism is being changed in the presence of RGO.

Additional information concerning the interaction of RGO with SU8 at the time $t = 0$ h of UV-irradiation are shown hereafter using FTIR spectroscopy and Raman scattering spectroscopy.

As demonstrated in the Figure 2.22, there are no drastic differences between the IR spectra recorded on A_2 , A_3 and A_5 (composite monomers before UV-illumination). Comparing the FTIR spectrum of sample S_1 (polymerized SU8, Figure 2.19b) with samples A_2 , A_3 and A_5 (UV-polymerized composites, Figure 2.22b), the main variation is observed for the IR band positioned at 912 cm^{-1} . The significant intensity drop of this peak is a well-understood sign of the epoxy ring opening. In addition, Figure 2.22b evidences the appearance of a shoulder at 1637 cm^{-1} .

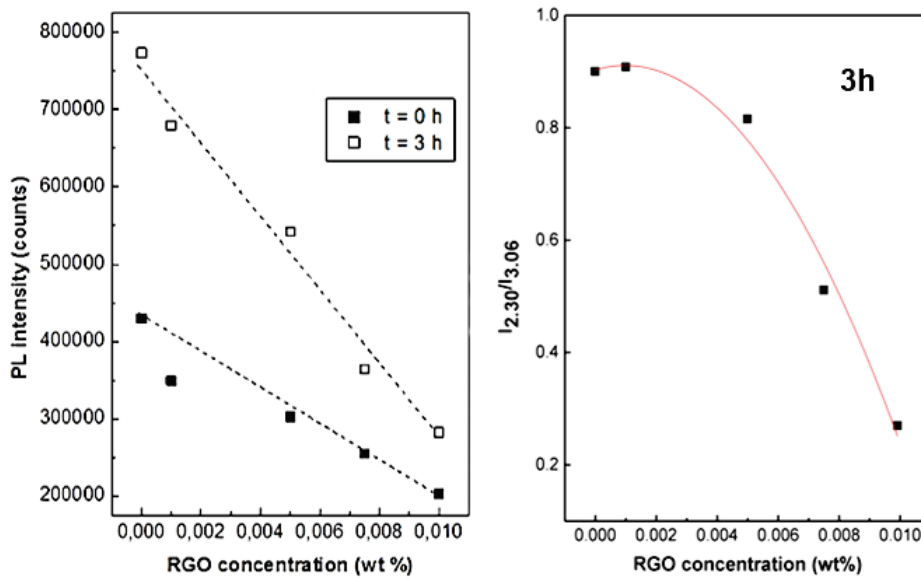


Figure 2.21: (a) Evolution of PL intensity, as a function of RGO content for samples $A_1 - A_5$ at the time $t = 0$ (filled square), and after 3 hours of UV illumination (open square). (b) The ratio between the intensity of PL bands at 3.06 and 2.39 eV as a function of RGO content after 3h UV-illumination of the samples $A_1 - A_5$.

Figure 2.23 confirms that the IR absorption band at 1637 cm^{-1} is associated with RGO, however it exhibits a shift from the original position. The FTIR spectrum of pure RGO shows three IR absorption bands located at 1631 , 2926 and 3437 cm^{-1} , these are assigned to the vibrational modes of C-C stretching in benzene rings [151], CH_3 stretching [152] and OH stretching [152], respectively. Several other changes are observed in Figure 2.23:

- i) The increase in the absorbance of the IR band peaked at 2966 cm^{-1} simultaneously with a slight decrease of the absorbance of the IR band at 3485 cm^{-1} in the case of the A_1 and A_5 samples; the IR band peaked at 3485 cm^{-1} belongs to the propylene carbonate impurities which show $<0.002\text{ wt}\%$ water.
- ii) Increase in the ratio between the absorbance of IR bands peaked at 3452 and 1608 cm^{-1} (A_{3452}/A_{1608}) from 0.04 to 4, as a consequence of the cross-linking of SU8, when new OH bonds are formed.
- iii) Decrease in the absorbance of the IR bands peaked at 1637 and 3452 cm^{-1} , which leads to a change of the A_{3452}/A_{1608} ratio from 4 to 1.1 in the case of the S_1 and S_5 samples, respectively.

Additional information on the vibrational properties of SU8 based composites can be obtained by Raman spectroscopy (Figure 2.24). The main Raman bands of sample A_1 are summarized

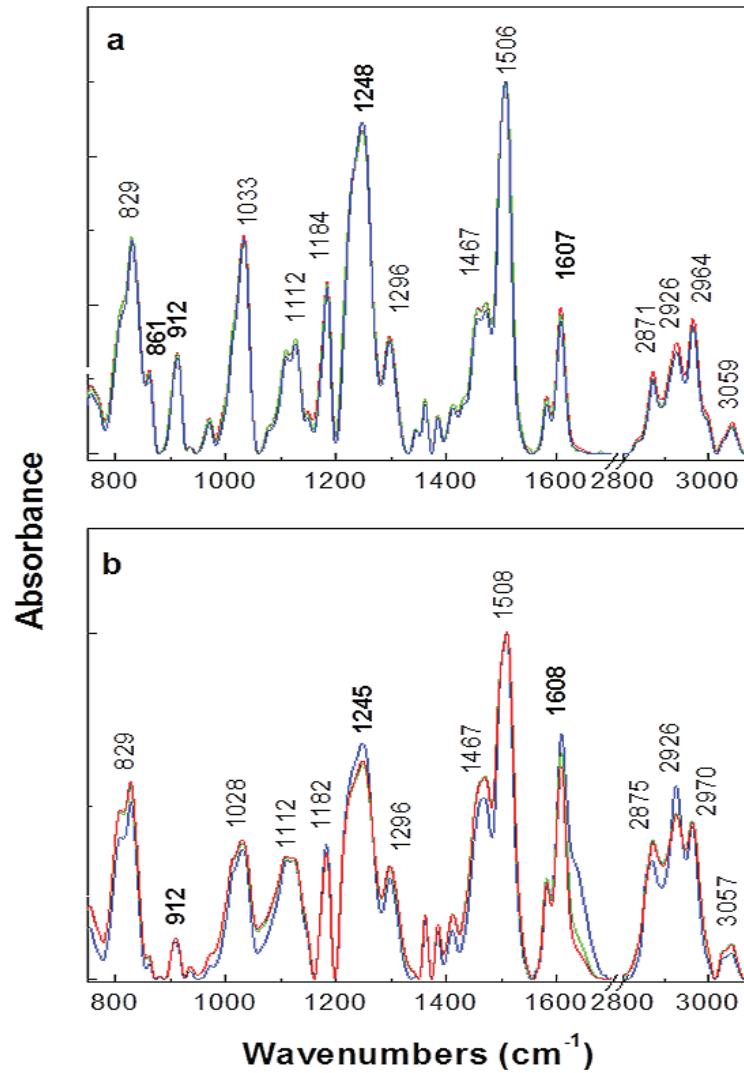


Figure 2.22: FTIR spectra of the samples (a) A_2 , A_3 , A_5 and (b) S_2 , S_3 , S_5 , with a concentration of RGO of 0.001 %wt. (green curves), 0.005 %wt. (red curves) and 0.01%wt. (blue curves), respectively.

in Table 2.3. Comparing Raman spectra of the samples A_1 and S_1 (black curves in Figure 2.24a and Figure 2.24b), the main differences are observed for the relative intensities (normalized to the 1606 cm^{-1} peak, since this band is associated to the phenyl rings of the SU8 and will remain intact upon the cross-linking) of the Raman lines peaked at 1253 , 2929 and 3066 cm^{-1} as follows: i) in the case of the sample A_1 , the ratios are equal to $I_{1606}/I_{1253} = 1.5$, $I_{1606}/I_{2929} = 1.2$ and $I_{1606}/I_{3066} = 1.6$. ii) in the case of the S_1 sample, the ratios are equal to $I_{1606}/I_{1253} = 2.3$, $I_{1606}/I_{2929} = 1$ and $I_{1606}/I_{3066} = 1.3$.

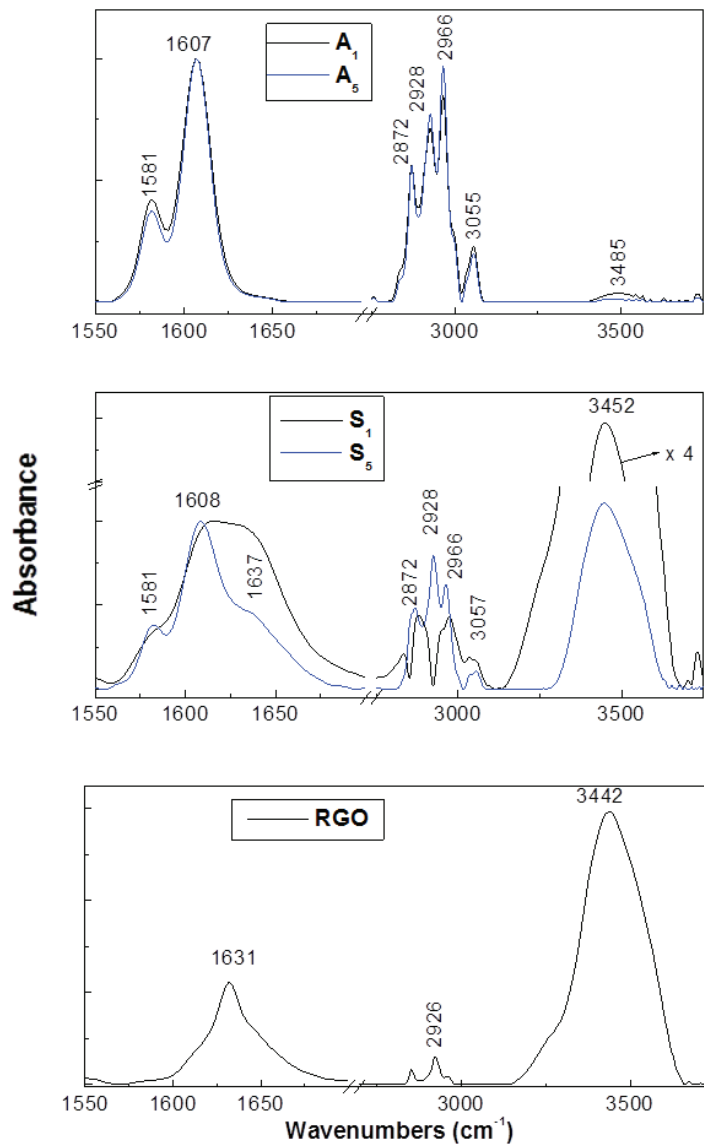


Figure 2.23: The FTIR spectra of the samples A_1 , A_5 , S_1 , S_5 and RGO.

In addition, Figure 2.24a (red, green and blue curves) evidences: i) a progressive decrease in the relative intensities of the Raman lines situated in the spectral ranges $500\text{-}1200\text{ cm}^{-1}$ and $1350\text{-}1500\text{ cm}^{-1}$ and ii) a gradual increase in the relative intensities of the Raman lines peaked at 1301 and 1584 cm^{-1} .

Comparing Figure 2.24a with Figure 2.24b, the main difference is for the Raman line from 1301 to 1296 cm^{-1} . According to the inset of Figure 2.24b, in the spectral range of $1200\text{-}1700\text{ cm}^{-1}$ RGO shows two Raman bands located at 1309 and 1589 cm^{-1} , labeled as D and G bands,

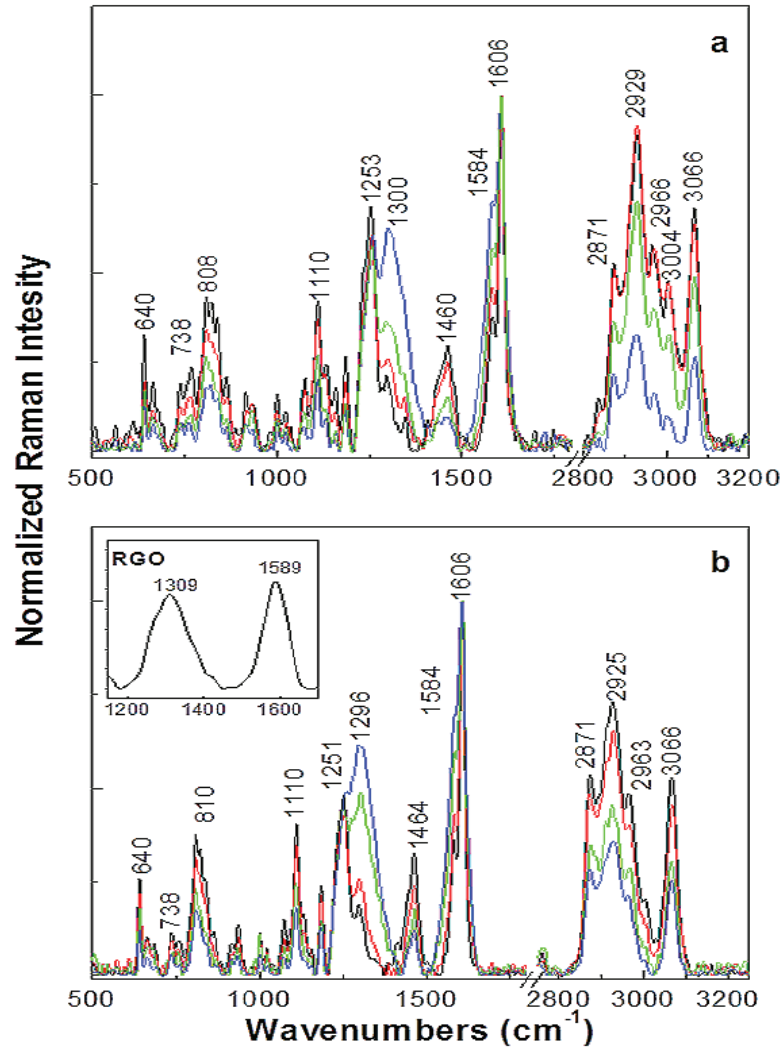


Figure 2.24: Raman spectra of the samples (a) A_1 , A_2 , A_3 and A_5 and (b) S_1 , S_2 , S_3 and S_5 , with a RGO concentration of 0 wt% (black curves), 0.001 wt% (red curves), 0.005 wt% (green curves) and 0.01 wt% (blue curves), respectively. The inset of (b) shows Raman spectrum of RGO.

which are assigned to disorder state and vibrational mode of graphitic materials [146]. The shift of the D band of RGO for 9 and 15 cm^{-1} in the case of the A_2 – A_5 and S_2 – S_5 samples, respectively, indicates a covalent functionalization of RGO with the SU8 photoresist.

The chemical mechanism for the cross-linking interactions of the SU8 in the presence of RGO is shown in Figure 2.25. Three stages describe this photochemical process: i) photochemical activation of TSHAS in the presence of RGO; ii) the epoxy ring opening with protons generated in the previous stage, the propagation of cross-linking reactions and the macromolecular

Chapter 2. Composites with 2D fillers: SU8-graphene composites

Table 2.3: Vibration modes observed by Raman spectroscopy of the SU8 sample [74, 149].

observed Raman frequencies (cm^{-1})	Assignment
640	vibrational modes of C-S stretching in TSHAS + in-plan benzene ring deformation
738	C-S stretching
808, 866	C-O-C in epoxy groups
1110	asymmetric stretching of C-O-C group in mono-substituted epoxy ring
1253	symmetric stretching of C-O-C group in mono-substituted epoxy ring
1460	anti-symmetric stretching in CH_3 and CH_2 groups
1584, 1606	C=C-C-C stretching in benzene ring
2871, 2925, 2968	anti-symmetric stretching in CH_3 and CH_2 groups
3004, 3066	$-CH_2$ stretching and $=C-H$ stretching in benzene ring

chain growth; and iii) the termination of the polymerization process of the SU8 photoresist in the presence of RGO.

Information concerning the photochemical activation reaction of TSHAS in the presence of RGO are shown in Figure 2.25. The main Raman lines of TSHAS extracted from Figure 2.26 are summarized in Table 2.4.

The main changes induced by the photochemical activation reaction of TSHAS in the presence of RGO are: i) the disappearance of the Raman lines assigned to the vibrational modes of the benzene ring and C-H bending of the TSHAS. Simultaneously, an increase in the relative intensity of the Raman line assigned to the C-S stretching vibrational mode; ii) the appearance of a new Raman bands assigned to RGO, at 1290 cm^{-1} and 1604 cm^{-1} . The shoulder at 1604 cm^{-1} causes the broadening of the Raman line at 1573 cm^{-1} towards the higher energies (Figure 2.26b). Above-mentioned changes confirm that the photochemical activation reaction of TSHAS in the presence of RGO leads to the formation of new covalent bonds between the two constituents. The down-shift of $\sim 19\text{ cm}^{-1}$ for the D band, from 1309 cm^{-1} (the inset of Fig. 8b) to 1290 cm^{-1} (Figure 2.26b), can be attributed to the creation of new defects in the SP^2 network of the RGO sheets.

Summary

In this section we reported for the first time photoluminescence study of the cationic photopolymerization of the SU8 photoresist in the absence and in the presence of reduced graphene

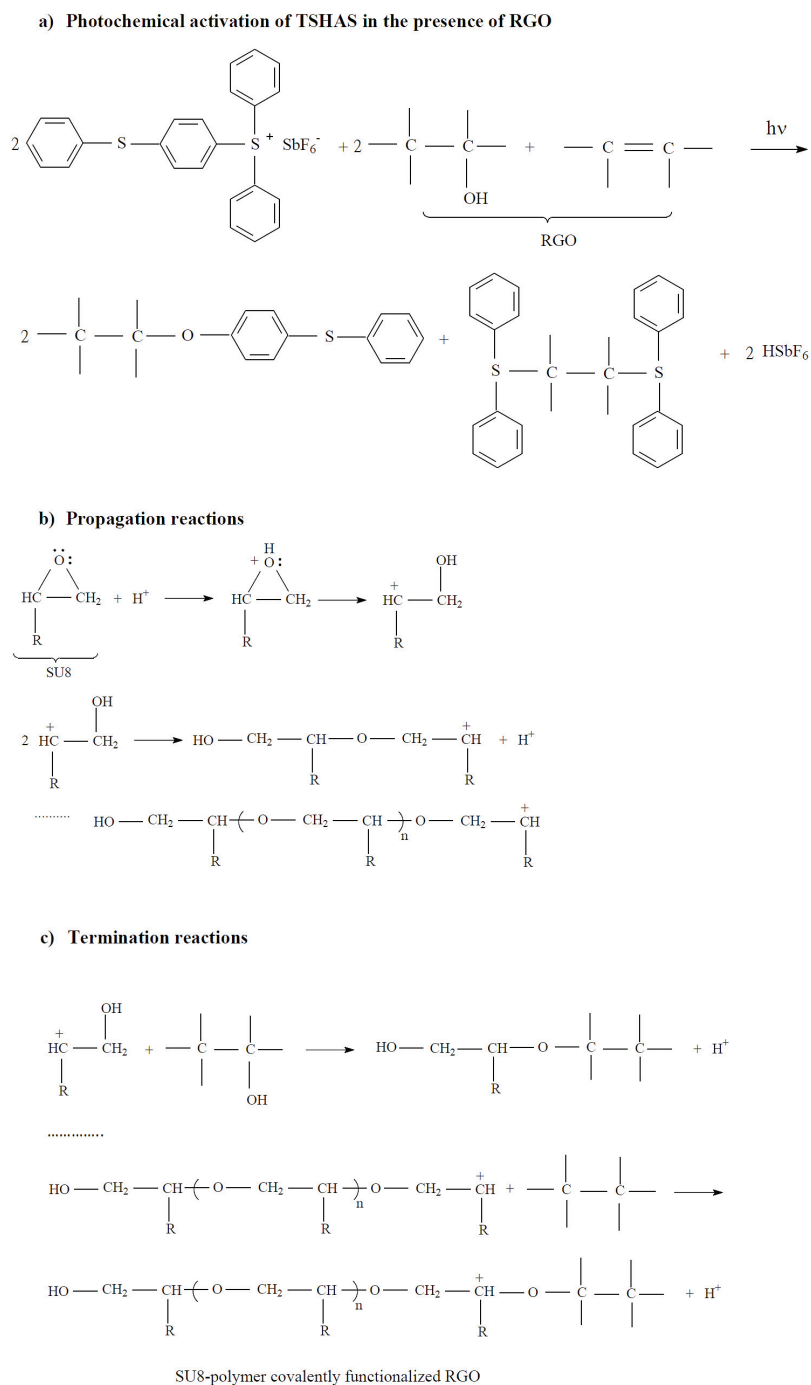


Figure 2.25: (a) Activation role of TSHAS photoinitiator in the cure process of the SU8 photoresist; (b) the propagation reactions and (c) the termination reactions of polymerization process of the SU8 photoresist in the presence of RGO (in all SU8 formulas, $R = C_{87}H_{95}O_{15}$).

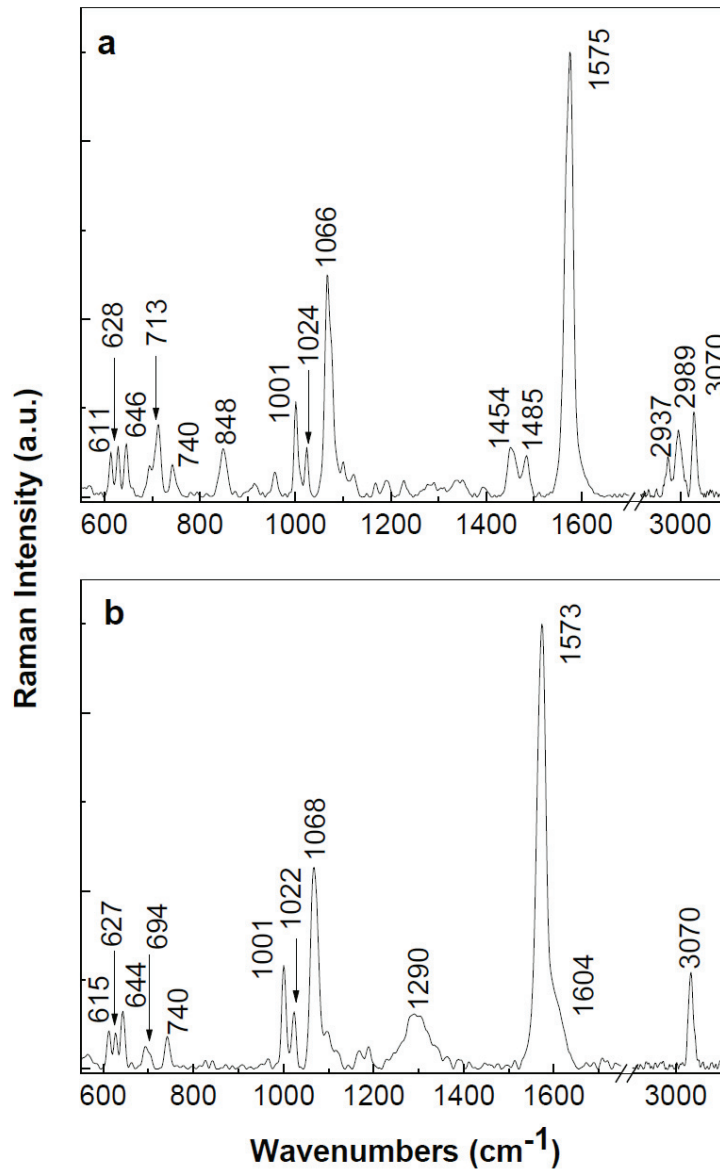


Figure 2.26: Raman spectra of the samples of TSHAS in initial state and after the photochemical activation reaction in the presence of RGO.

oxide (RGO). We have demonstrated that:

i) PL is a valuable tool in highlighting the cross-linking reactions of the SU8 photoresist. A complete cross-linking of the SU8 photoresist is reported when the ratio between the intensities of the PL bands peaked at 3.06 and 2.39 eV becomes equal to ~ 1.12 . The UV-irradiation of the SU8 leads to the disappearance or significant decrease of the IR absorption bands associated with the epoxy ring, as a result of the cross-linking of the SU8 photoresist.

Table 2.4: Vibration modes observed by Raman spectroscopy of the TSHAS photoinitiator.

Raman frequencies (cm^{-1})	Assignment	Ref.
611-646	C-S stretching	[153]
694-713	C-H out-of-plane in benzene ring	[154]
740	C-S stretching	[74, 149]
848	out-of-plane C-H deformation	[153]
1001-1024	in-plane ring deformation	[153]
1066	C-S in aryl sulfide	[155]
1454-1485	C-C stretching + C-H bending in benzene ring	[154]
1575	C=C + C-C stretching in benzene ring	[155]
2937-2989	C-H bending	[153]
3070	=C-H stretching in benzene ring	[74, 154]

ii) By increase of the RGO weight fraction from 0.001 to 0.01 wt% in the SU8-RGO composites, the variation in intensities of the PL bands observed. This is a consequence of the interaction between the functional groups of RGO and SU8 photoresist surfaces and formation of new covalent bonds between the two constituents. Changes reported in the FTIR and Raman spectra of the cross-linked SU8-RGO samples confirm the covalently functionalization of the RGO with the SU8 epoxy during the chemical cationic photo-polymerization process.

2.3.4 Rheological properties

The processability of the composite is directly related to its rheological behaviour which varies dramatically depending on the filler parameters such as loading and aspect ratio. Thus, from the application point of view, in particular for composite design, it is of interest and importance to study the rheology of the composite. In this section the rheological behavior of SU8 epoxy, as well as SU8-RGO composite are investigated in terms of viscoelastic properties as a function of RGO flakes concentration. This work is performed in collaboration with Dr. Yves Leterrier at the Laboratory of Composite and Polymer Technology of EPFL. Before presenting the results, in order to have a better understanding of viscoelastic behavior and the method of the measurements, the principles are presented in the next section.

Rheology principles

In order to measure the viscoelastic behavior of SU8-RGO composites we have used the oscillatory rheological analysis. In this technique, the sample (composite ink) is placed between two plates (Figure 2.27a). Once the upper plate rotates, a time dependent sinusoidal

Chapter 2. Composites with 2D fillers: SU8-graphene composites

strain ($\gamma = \gamma_0 \sin \omega t$) is imposed to the sample and concurrently the sinusoidal stress, σ , response is recorded by measuring the torque that the sample applies on the bottom plate. Considering this time dependent stress, the materials can be classified into three different categories from rheological point of view:

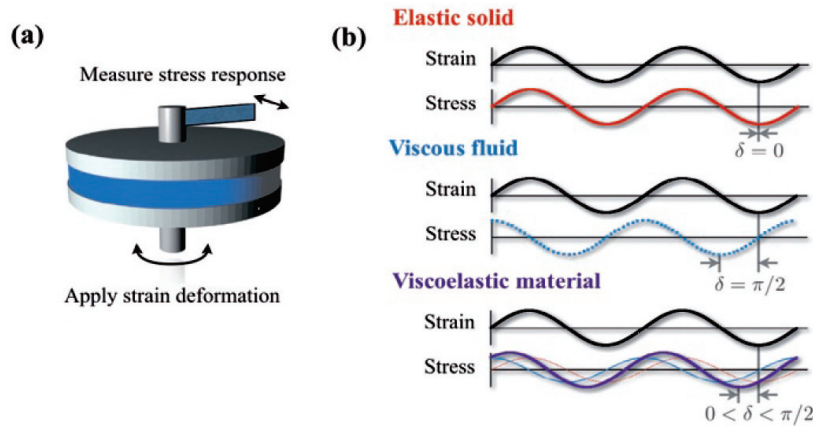


Figure 2.27: (a) Schematic representation of a typical rheometry setup. (b) Schematic stress response to oscillatory strain deformation for an elastic solid, a viscous fluid and a viscoelastic material [156].

1. Elastic solid, for which the sample stress, is in phase with the strain, (phase shifts, δ , equal to zero), and the shear modulus of the material, G , is defined as the proportion between deformation stress and strain: $\sigma = G\gamma$.
2. Viscous fluid, for which the imposed strain and response stress are out of phase with phase shift of $\delta = \pi/2$ and proportionality constant of viscosity of the fluid, η . For these fluids: $\sigma = \eta\dot{\gamma}$.
3. Viscoelastic materials which exhibit a combination of both viscous (out of phase) and elastic (in phase) behavior. Therefore, the phase shift (purple line in Figure 2.27b) is somewhere between that of solids and liquids, $0 < \delta < \pi/2$, depending on the extents of solid-like (red line) and liquid-like (blue dotted line) behavior.

The time dependent stress is given by $\sigma = \gamma_0(G' \sin \omega t + G'' \cos \omega t)$ where G' , storage shear modulus, is the characteristic of solid-like behavior, and G'' , loss modulus is the characteristic of fluid-like behavior.

G' and G'' are both function of the angular frequency, ω : $G'(\omega) = \frac{\sigma_0}{\gamma_0} \cos \delta$ and $G''(\omega) = \frac{\sigma_0}{\gamma_0} \sin \delta$

The three above-mentioned types of behaviors are summarized in Figure 2.27b.

Viscoelastic behavior of SU8-RGO composites

The viscosity measurements of SU8-RGO composites were carried out on a strain-controlled rotational rheometer (ARES, Rheometric Scientific, 2kFRT transducer), using a plate-plate geometry with a diameter of 25 mm, and a gap of $\sim 1000 \mu\text{m}$.

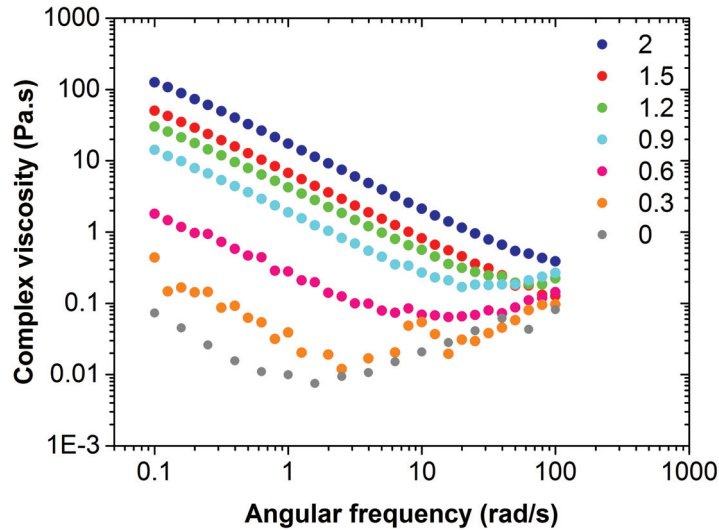


Figure 2.28: Viscosity of SU8-RGO composites as a function of frequency and filler weight fraction for 0 to 2 wt%.

Figure 2.28 represents the viscosity, as a function of angular frequency (ω) and weight fraction of RGO fillers. It can be clearly seen that the presence of RGO fillers has a dramatic effect on the viscoelastic behavior of the polymer, especially at low frequencies. At $\omega = 0.1 \text{ rad/s}$, a 3 orders of magnitude increase in the viscosity value is observed for adding only 2 wt% of RGO to the polymer. However, at high frequencies, the influence of the RGO filler on the rheological behavior is less pronounced. For larger concentrations of RGO the shear thinning is the dominant behavior. This is quite common in polymer solutions [157] specially when suspended solids are added to a fluid [83]. The unexpected behavior though, is the shear thickening of the SU8 solution and the low concentrated composite SU8-0.3 wt% RGO, in the frequency range of $\omega = 2 - 100 \text{ rad/s}$. The reason for this phenomenon is not completely clear to us, but we suppose that it originates from the linkage of the monomers, during the sonication step while the sample is being prepared. (In general shear thickening is the consequences of a temporary clustering of particles which came in contact under shear forces.)

Figure 2.29 shows the storage shear modulus, G' , and loss shear modulus, G'' , as a function of frequency and RGO weight fraction for the composites. As the loading augments, both G' and

G'' increase, especially for lower RGO weight fractions. Here, the low frequency moduli can be informative about the dispersion of the fillers [9, 158, 145]. For instance, at 0.6% the storage modulus, G' (Figure 2.29a), becomes almost frequency independent at lower range (below $\omega = 10 \text{ rad/s}$) which is an indication for rheological percolation owing to a ‘solid-like’ network formation. The elasticity of the fluid as a function of the volume fraction can be defined with a power-law:

$$G' \propto (\phi - \phi^*)^\nu \quad (2.6)$$

where ϕ^* is the percolation threshold and ν is a power-law exponent. For the RGO fillers, these parameters are determined by fitting the Equation 2.6 to the low-frequency storage modulus dependent on RGO volume fraction data (Figure 2.30). We find the value of $\phi^* = 0.09$ for the rheological percolation and $\nu = 2.23$ for the exponent. Here, the critical value for percolation is very close to zero similar to what we have found for electrical percolation threshold.

In fact, regarding the rheological percolative behavior, the storage shear modulus for polymer composites often shows a sharp decrease at ϕ^* [159]. In our composites, however, one observes a smooth drop in G' as the RGO loading decreases (Figure 2.30). This observation is consistent with the electrical conductivity results (see subsection 2.3.1), where the continuous decrease in conductivity was explained in terms of a tunneling model, rather than the percolation mechanism with discrete percolation threshold for the composites.

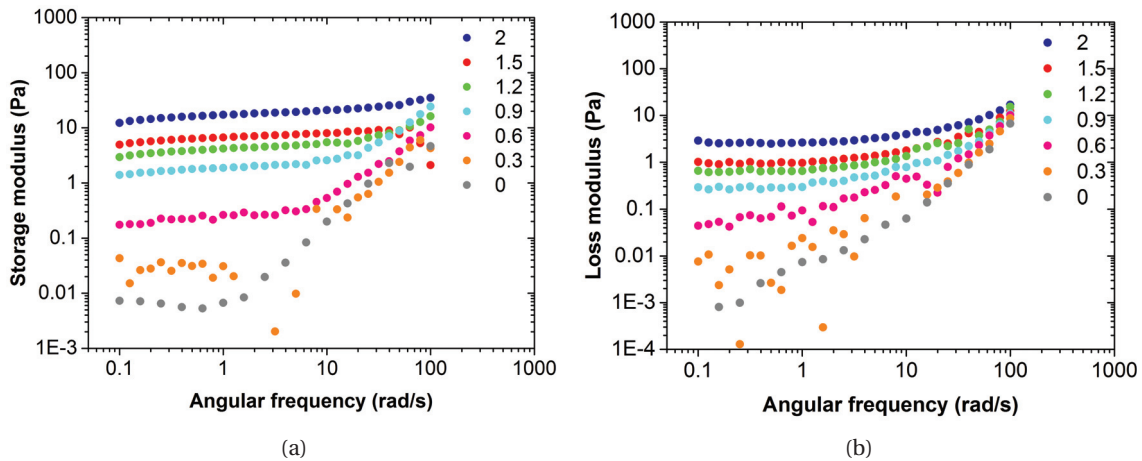


Figure 2.29: (a) Storage shear modulus, G' , and (b) loss shear modulus, G'' , of SU8-RGO composites as a function of angular frequency and RGO weight fraction.

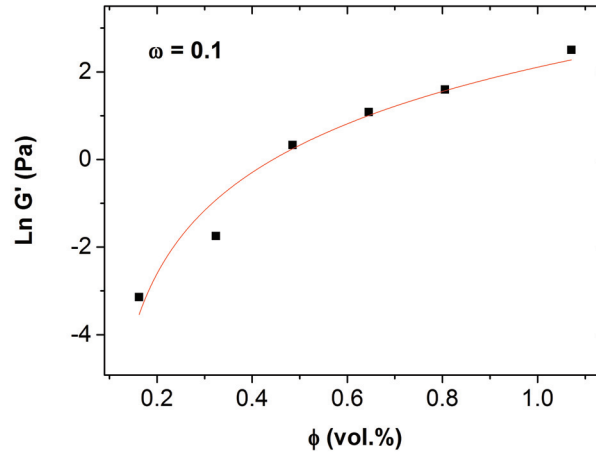


Figure 2.30: Storage modulus, G' , of the SU8-RGO nanocomposites as a function of the RGO volume fraction at a fixed frequency of 0.1 rad/s.

Using the rheological critical volume fraction, an estimation of the aspect ratio of the fillers is given by equation Equation 2.7 [9], (assuming randomly oriented, monodispersed, and disk-shaped particles):

$$A_f = \frac{3\phi_{sphere}}{2\phi^*} \quad (2.7)$$

where $\phi_{sphere} = 0.29$, the onset of percolation for impenetrable, randomly packed spheres [9]. Using the data extracted from Figure 2.30, the aspect ratio $A_f = 483$ is determined for the RGO fillers.

Such a high aspect ratio can be the reason of vanishingly low rheological percolation, as the fillers can easily form a network inside the matrix and restrict the polymer chains.

2.4 Conclusion

In this chapter we presented SU8-graphene-based nanocomposites containing reduced graphene oxide (RGO) flakes, as a new patternable conductive polymer with electrical properties superior to other graphene-based polymer composites for MEMS applications. Our composites preserve the photo-patternability and after optimization of UV lithography parameters, well-defined structures can be drawn at wafer scale with a minimum lateral resolution of 10 μm . SEM and TEM analysis of the composites microstructure showed a well-dispersed network of RGO fillers within the epoxy matrix.

The physical properties of these composites can be controlled by tuning the content of graphene flakes within the SU8 matrix. The electrical conductivity, σ , of the composites as a function of volume fraction, ϕ , is not consistent with the classical percolation model of transport. Instead, we suggest that the dominant mechanism of the transport is the tunneling of the electrons between the graphene flakes. The high electrical conductivity compared to that of pure SU8 and other graphene-based composites, even at very low filler loadings, is a result of homogeneous dispersion of the flexible graphene flakes in the SU8 matrix. In accordance with the electrical conductivity, the storage modulus of the SU8-RGO composites exhibits vanishingly low rheological percolation when plotted versus the volume fraction of the fillers. This can be due to the very large aspect ratio of the RGO fillers which constrain the mobility of the polymer chains.

Addition of RGO fillers to the SU8 results in the enhancement of the Young's modulus ($\Delta E \simeq 75\%$) and hardness ($\Delta H \simeq 67\%$) of the composites, due to the formation of covalent bonds between the functional groups on the RGO surface and SU8. The optical spectroscopy of the samples have confirmed the presence of such covalent bondings. In fact the spectroscopy evidenced that the presence of the fillers will alter the ongoing chemical reactions during the polymerization and changes the chemical structure of the composites.

3 Composites with 1D fillers: SU8-carbon nanotube composites

Since their discovery [160], carbon nanotubes have been the subject of extended research for many applications, thanks to their unique mechanical, electrical and thermal properties combined with high aspect ratio, low density and excellent chemical stability. One of the most immediate applications for CNTs was to be used as fillers in composite materials and many attempts have been devoted to this field of research in particular to create Polymer-CNT composites.

The preparation and characterization of CNT-SU8 composites have been the topic of a previous thesis [15] in our laboratory. In this chapter we follow up on this work by focusing on two major critical characteristics of CNTs that affect the final properties of the CNT reinforced polymers: i) aspect ratio and polydispersity; and ii) alignment of the nanotubes.

In the first section, we studied the effect of tuning the length of the nanotubes, as well as the polydispersity of their length, on transport mechanism of SU8-CNT composites. The experimental results will be discussed in accordance with the theoretical predictions for composites containing fibrous fillers.

In the second section, SU8-based composites containing well-aligned carbon nanotubes have been prepared for applications such as thermal management and channeling of the charge particles through a membrane.

3.1 Composites with controlled length of nanotubes

3.1.1 Motivation

On the modeling and theory side, it is well established that the electrical transport properties of nanocomposites are enhanced by conducting fillers with high aspect ratios. Polymer-CNT composites are typical examples which display relatively large conductivities even at very low nanotube loadings. However, depending on the production processes of the composites, nanotubes exhibit a notable size polydispersity, which can be a possible reason for huge quantitative discrepancies between theory and experiments.

This size polydispersity, which almost inevitably exists in real-world CNTs is a major disadvantage for a full optimization of electrical and mechanical properties of CNT-polymer nanocomposites. Understanding the effects of the polydispersity in length and diameter of the nanotubes is therefore an important step towards the control of CNT-based nanocomposite systems.

Recent theoretical studies of models of CNTs [161, 162, 163, 164, 165, 126] suggest that the electrical conductivity, σ , of CNT-polymer nanocomposites depends on the polydispersity of the nanotubes through the weighted average length, L_w , (see subsection 3.1.2). The aim of section 3.1 is to evaluate this theoretical prediction by measuring σ of CNT-SU8 composites with purposely tailored distribution of length, L . Before explaining the experimental procedure designed to test this prediction, we go briefly through the background notions of these theoretical studies.

3.1.2 Theoretical studies

In CNT-polymer composites, as generally in other polymer nanocomposites, the electrical connections between the conducting particles are established by tunneling of electrons across the thin polymer layer separating the conductive fillers. The enhanced electrical connectedness of polymers filled with carbon nanotubes (CNTs) is understood as being driven by the increased excluded-volume associated with the high aspect-ratios of CNTs [48, 166], which has the net effect of reducing the minimal (or critical) inter-particle distance (δ_c) that the electrons have to tunnel in order to establish a system-spanning tunneling connectivity [121, 167, 168, 169, 170, 171]. For this reason, polymers filled with longer CNTs are expected to be conductive at lower CNT concentrations, as it is generally observed in experiments [172, 173]. The optimization of the electrical-mechanical performances of CNT-polymer ma-

3.1. Composites with controlled length of nanotubes

materials is however hindered by the almost inevitable polydispersity in length (L) and diameter (D) of the nanotubes, which is one factor responsible for major discrepancies observed in the conductivities of apparently similar CNT-polymer composites [116, 174].

Recent theoretical studies on the geometrical percolation of slender, straight rod-like particles have clarified the role of the particle length polydispersity by showing that the minimum filler loading required to establish a system-spanning cluster of connected rods, also referred to as the percolation threshold, is inversely proportional to the weighted average lengths $L_w = \langle L^2 \rangle / \langle L \rangle$ of the rods [161, 162, 163, 164, 165, 126], where the brackets denote averages over the distribution of L . The physical reason for the presence of the second moment of L in the relevant rod length scale is that in a mixture of rods of different lengths, longer rods are more effective in forming a connected network than the shorter rods. Numerical simulations have confirmed and extended the results of Refs. [161, 162, 163, 164, 165, 126] by showing that the percolation threshold is a quasi-universal function of L_w even for dispersions of straight rods of intermediate aspect ratios [175, 169, 176].

When applied to the dispersions of rods with inter-particle tunneling, these results amount to predict that the critical tunneling distance δ_c depends upon the rod length distribution only through $1/L_w$ for a given volume fraction of the nanotubes [169, 177, 171]. The resulting bulk conductivity σ , which closely follows the critical distance approximation $\sigma \propto \exp(-2\delta_c/\xi)$ where ξ is the tunneling decay length, [121, 178, 179, 170, 170] is thus expected to display a similar quasi-universal behavior as a function of $1/L_w$. In particular, in terms of the variable $1/L_w$, it is predicted that $\ln(\sigma)$ has the same functional dependence of δ_c .

Although theories and simulations agree in identifying L_w as the relevant rod length scale governing the conductivity of polydispersed rod-like particles, to the best of our knowledge there are no experiments specifically designed to verify this prediction in real composites.

Here, we address this issue by study the conductivity of CNT-epoxy composites with different length dispersions of CNTs. We measured the conductivities of composites with dissimilar distributions of the CNT lengths, but with equal concentration of CNTs and compared the trends of conductivity depending on the weighted average L_w , and the number average $L_n = \langle L \rangle$ of the CNT lengths.

3.1.3 Preparation Methods

Synthesis of carbon nanotubes

Multiwalled CNTs were synthesized by catalytic chemical vapor deposition of acetylene using Fe-Co catalytic particles supported by calcite. The synthesis of CNTs was carried out in a horizontally mounted quartz furnace at 720 °C under flow of acetylene and Nitrogen for 2 hours [180]. In order to remove the catalytic particles and the supporting material, as-grown CNTs were purified by stirring in hydrochloric acid of 1 Molar, filtered and washed with distilled water and ethanol. The average length and diameter of the as-produced CNTs were approximately 10 μm and 16 nm, respectively. To determine the degree of polydispersity of the diameter D of the nanotubes, we have manually measured D from TEM images of microtome slices of CNT-SU8 composites. A representative TEM image is shown in Figure 3.4b. The resulting diameter distribution obtained from 140 values of D is shown in Figure 3.1. The first and second moment of D extracted from the measured diameters are, respectively, $\langle D \rangle \approx 16$ nm and $\langle D^2 \rangle \approx 346$ nm². The shape of the distribution is approximately of lognormal form.

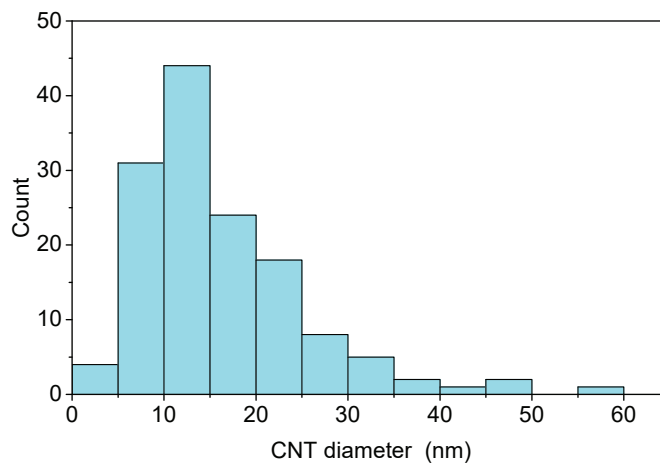


Figure 3.1: Histogram of the CNT diameters obtained from 140 values measured from TEM images of CNT-SU8 composites.

Tuning the length dispersion of carbon nanotubes

We produced different batches of CNTs with specific nanotube length distributions by cutting the as-grown CNTs by planetary ball milling in a liquid (GBL) environment. The use of the ball milling apparatus enabled the tailoring of the CNT lengths through specific combinations of milling times and rotational speeds [181]. We have processed standard batches consisting

3.1. Composites with controlled length of nanotubes

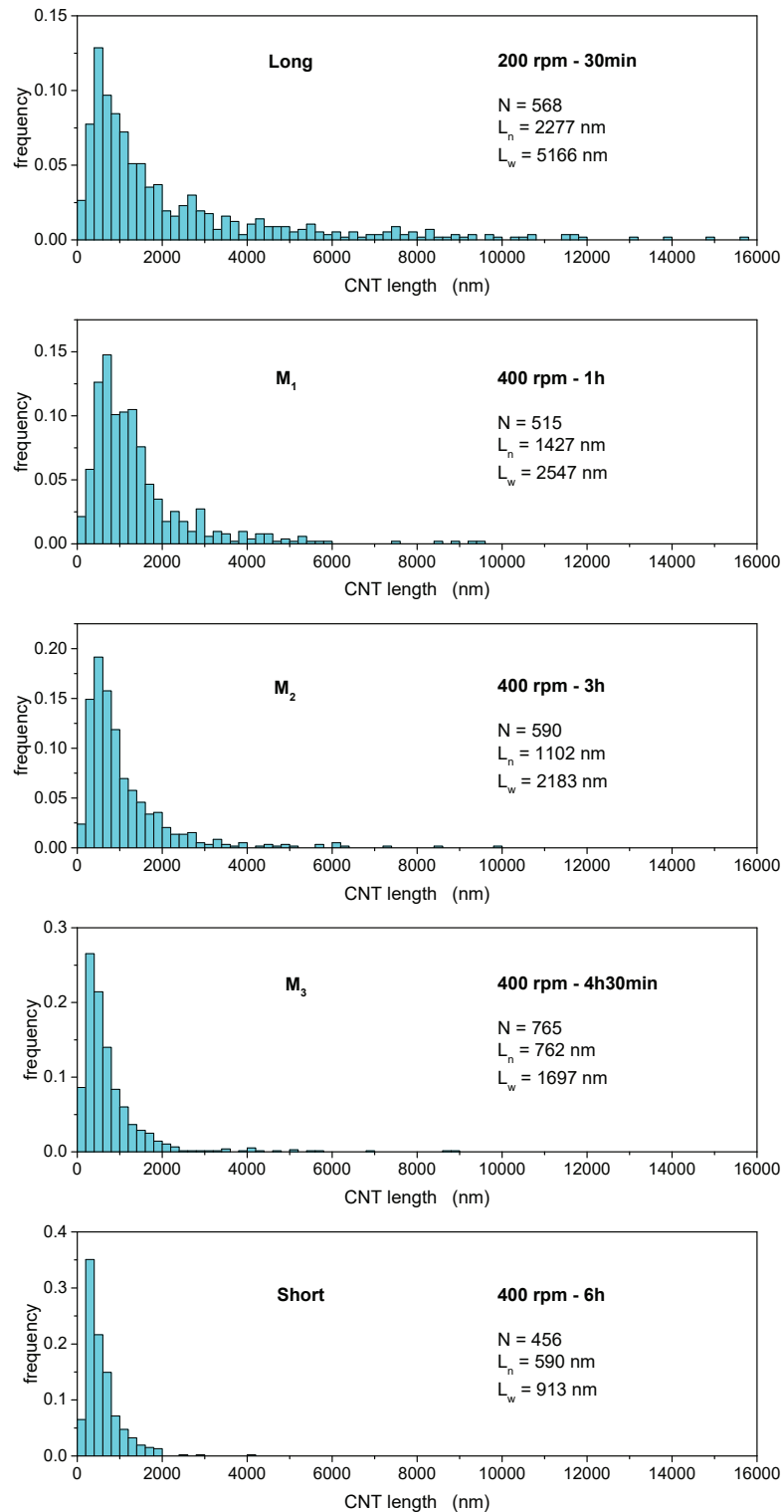


Figure 3.2: Normalized distribution of the as-milled CNT lengths as measured from SEM images. From the top panel to the bottom panel, the distributions become increasingly narrow.

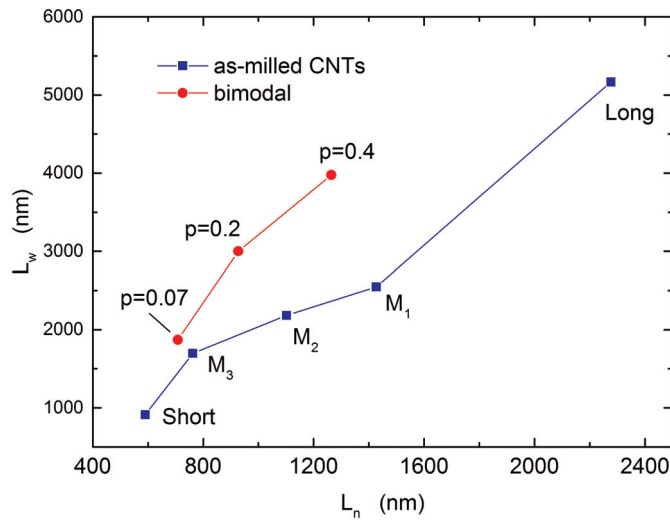


Figure 3.3: The weighted average L_w and the number average L_n of the CNT lengths for the as-milled nanotubes (filled squares) and for the bimodal length distributions (filled circles).

of ZrO_2 balls of 3 mm of radius, GBL, and CNTs in mass proportion of 40 : 20 : 1 in 250ml zirconium oxide-lined jars.

The resulting CNT length distributions obtained from about 500 manually measured nanotube lengths from SEM micrographs, are shown in the histograms of Figure 3.2 for five different combinations of the milling time and rotational speed. We have labeled the different batches as indicated in Figure 3.2. To a good approximation, all distributions follow a lognormal distribution function, as shown in Appendix A and observed in a previous report [181].

The L_w - L_n plot of Figure 3.3 shows that the weighted and number averages of the CNT lengths obtained from Figure 3.2 decrease gradually from $L_w = 5166$ nm and $L_n = 2277$ nm (“Long” CNTs) to $L_w = 913$ nm and $L_n = 590$ nm (“Short” CNTs), respectively, as the milling time and the rotational speed change from 30 min at 200 rpm to 6 h at 400 rpm.

3.1.4 Composite preparation and structural characterization

Composites with as-milled CNTs

The five batches of CNTs with different length distributions were dispersed by sonication in the presence of surfactant in a SU8 epoxy matrix (Gersteltec, grade GM1060), which is constituted by SU8 resin and 40% of solvent. The CNT concentration was kept at $x = 0.6$ %wt with respect to the weight of the resin. Subsequently, the ink was spread on a clean glass slide

3.1. Composites with controlled length of nanotubes

by doctor blading and was soft-baked following a temperature ramp lasting 15 min up to 95 °C to evaporate the solvent. The baking temperature was low enough to prevent cross-linking of the epoxy. The resulting composites, apart from the modified CNT length distribution, are similar to the non-polymerized CNT-SU8 samples studied in Ref. [41]. These have been shown to exhibit a conductivity behavior as a function of the CNT volume fraction that was consistent with a tunneling-dominated transport mechanism [41]. Examples of the morphology of the so-obtained CNT-SU8 composites are shown in the SEM and TEM images of Figure 3.4.

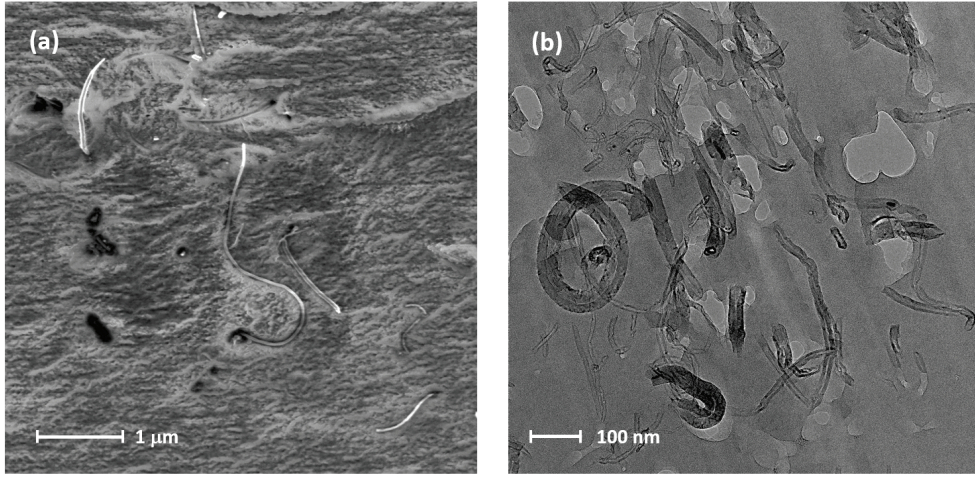


Figure 3.4: SEM (a) and TEM (b) images of the CNTs dispersed in the SU8 epoxy matrix.

Bi-modal composites

A second set of CNT-SU8 composites with specially engineered nanotube lengths were prepared, in order to check the agreement between theory and experiment. For this set, we have mixed nanotubes taken from the Long and Short batches of the as-milled CNTs with chosen values of the number fraction, p , of the Long nanotubes. In this way, the distribution of the nanotube lengths becomes bimodal: $\rho_p(L) = p\rho_{\text{Long}}(L) + (1 - p)\rho_{\text{Short}}(L)$ where ρ_{Long} and ρ_{Short} are the length distribution functions of the Long and Short CNT batches, respectively. Characterization by SEM analysis shows that the CNT length distribution follows the predicted bimodal distribution function, as shown in the Appendix A. In preparing the new CNT-SU8 samples, we have taken the same CNT concentration of the as-milled composites ($x = 0.6$ %wt) with $p = 0.07, 0.2, \text{ and } 0.4$.

The resulting number and weighted length averages, obtained respectively from $L_n(p) = p\langle L \rangle_{\text{Long}} + (1 - p)\langle L \rangle_{\text{Short}}$ and $L_w(p) = [p\langle L^2 \rangle_{\text{Long}} + (1 - p)\langle L^2 \rangle_{\text{Short}}] / L_n(p)$ where the subscript

“Long” (“Short”) denotes an average over $\rho_{\text{Long}}(L)$ [$\rho_{\text{Short}}(L)$], are shown in Figure 3.3 (filled circles). Increasing the fraction of Long CNTs results in a growth of L_w as L_n increases that is steeper than that of the as-milled sets, as seen in Figure 3.3.

3.1.5 Electrical characterization

The conductivity data obtained from 4-point-probe measurements of the five sets of CNT-SU8 composites are shown in Figure 3.5a (filled squares) as a function of the inverse of the weighted average of the CNT lengths, $1/L_w$. For comparison, we replot in Figure 3.5b the measured σ as a function of $1/L_n$, where L_n is the CNT mean length. The conductivity gradually increases as L_w (or L_n) is enhanced, which is consistent with the general trend expected in dispersions of conducting rod-like particles. As mentioned above, theories and simulations on systems of polydispersed rods predict that the tunneling conductivity depends on the length distribution of the rods only through L_w .

Specifically, in the limit of slender rods ($L_w/D \gg 1$) the conductivity resulting from tunneling processes between the rods follows approximately

$$\sigma \approx \sigma_0 \exp\left(-\frac{D^2}{\xi L_w \phi}\right) \quad (3.1)$$

where σ_0 is a conductivity prefactor and ξ is the tunneling decay length. The above expression stems from imposing the critical distance approximation $\sigma \propto \exp(-2\delta_c/\xi)$ to a system of tunneling connected rods homogeneously dispersed in an insulating matrix and from using $\delta_c \simeq D^2/2L_w\phi$ for the critical tunneling distance [169, 177, 171]. Interestingly, if we exclude the case for the shortest L_w , the $\ln(\sigma)$ vs. $1/L_w$ data of Figure 3.5a follow a straight line, as predicted by Equation 3.1, with a slope equal to about $m = -9200$ nm. Using Equation 3.1 with $D \simeq 16$ nm and $\phi = 0.28\%$, this value of m leads to $\xi \simeq 9$ nm, which is within the expected value range of the tunneling decay length [119]. A somewhat larger value ($\xi \simeq 12$ nm) is obtained if we replace $D^2 \simeq 256$ nm² in eq. 3.1 with $\langle D^2 \rangle \simeq 346$ nm², as obtained from the distribution of the CNT diameters, Figure 3.1.

We now test the apparent agreement between theory and experiment using the bi-modal CNT-SU8 composites. The rationale behind this approach is that the predicted scaling of σ with $1/L_w$ should not depend on the specific distribution function of L (which is approximately lognormal for the as-milled samples of Figure 3.2) and that the same scaling should therefore be observed in other types of the CNT length distribution.

3.1. Composites with controlled length of nanotubes

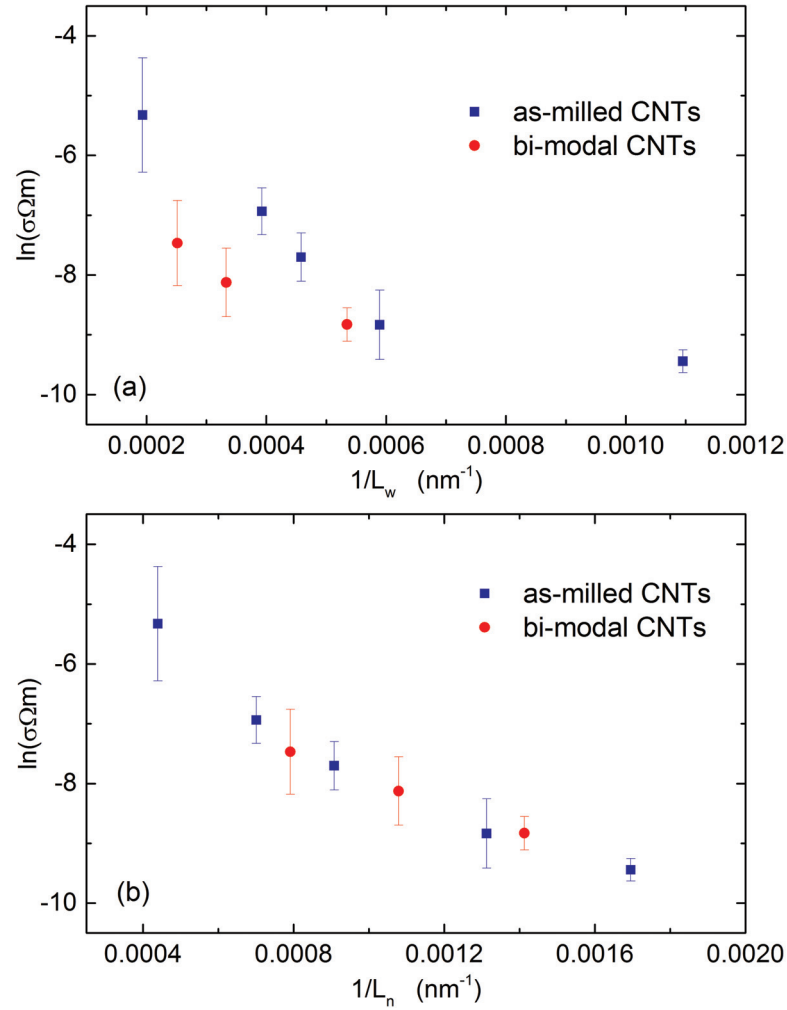


Figure 3.5: Natural logarithm of the conductivity measured in CNT-SU8 nanocomposites as a function of $1/L_w$ (a) and $1/L_n$ (b). Each symbol represents an average over five independent conductivity measurements. Data for the composites with as-milled CNTs are shown by filled squares, while those with bi-modal CNT length distributions are shown by filled circles.

When plotted as a function of $1/L_w$, the conductivity of CNT-SU8 composites with bimodal CNT distributions differs from that of the CNT-SU8 samples with as-milled CNTs. This is clearly seen in Figure 3.5a where σ for the bimodal samples (red circles) is well below that of the as-milled systems (blue squares) for comparable values of $1/L_w$. The finding that the conductivities of the two sets of composites fail to follow a common curve when plotted as a function of $1/L_w$ means that the weighted average of L is not the relevant CNT length scale in our CNT-SU8 systems. This is in conflict with the prediction for model systems of polydispersed rods, and it implies that the agreement between theory and experiment discussed above is, actually, only apparent.

Chapter 3. Composites with 1D fillers: SU8-carbon nanotube composites

The lack of universality found in the $\ln(\sigma)$ vs. $1/L_w$ plot of Figure 3.5a can have different explanations related to the differences between models of rod-like particles and real CNT composites. For example, the $1/L_w$ scaling is found in models of straight and randomly oriented rods that are homogeneously dispersed in the matrix. The CNTs in the SU8 epoxy are certainly not morphologically equivalent to straight rods, as seen in the SEM and TEM image of Figure 3.4 where the nanotubes show a rather marked waviness. Furthermore, the dispersion of the nanotubes within the SU8 matrix may be non-ideal, as seen in Figure 3.4b where a local cluster of nanotubes is shown. Another possibility for the breakdown of the $1/L_w$ scaling is that the nanotubes may have lengths that are correlated with their diameters, as discussed in Ref. [126]. The approximately lognormal distribution of L observed in the as-milled sets seems to exclude this possibility, as it suggests that the cutting events in the milling process act independently of the CNT size [181].

Although our CNT-SU8 composites do not follow the $1/L_w$ scaling, they do however show a clear universal behavior with respect to the inverse of the mean CNT length. This is demonstrated in Figure 3.5b where, surprisingly, the conductivity data of composites with bimodal and as-milled CNT length distributions collapse into a single curve as a function of $1/L_n$. This finding implies that the rod length scale that is relevant for transport in CNT-SU8 composites is L_n rather than L_w .

A similar scaling has been recently predicted in Refs. [164] and [177], where the requirement that the network of electrically connected rods be tree-like (that is, without closed loops) was relaxed to account for particle clustering. In the limit of maximal clustering between the rods, the tunneling conductivity has been shown to follow approximately [177]:

$$\sigma \approx \sigma_0 \exp\left(-\frac{K^2 D^2}{\xi L_n \phi^2}\right) \quad (3.2)$$

where K is a dimensionless positive parameter that quantifies the amount of correlations among the rods ($K = 1$ for uncorrelated particles). Equation 3.2 implies that $\ln(\sigma)$ decreases linearly with $1/L_n$, which is in partial agreement with the experimental data of Figure 3.5b. However, a linear fit of the data plotted as $\ln(\sigma)$ vs. $1/L_n$ gives a slope of about -3500 nm, which implies that K must be as small as ≈ 0.04 in order to have ξ of a few nanometers. According to the model of Refs. [164, 177], such a small value of K mimics a strongly attractive interaction between the rods, which is hardly justifiable for the present CNT-SU8 composites. Furthermore, the $1/\phi^2$ dependence of $\ln(\sigma)$ predicted by Equation 3.2 is not observed in CNT-SU8 composites with non-polymerized SU8, which rather follow a relation of the form $\ln(\sigma) \propto 1/\phi$ [41]. We note, however, that Equation 3.2 has been derived by assuming that the

3.1. Composites with controlled length of nanotubes

rods are straight and rigid, while the nanotubes are flexible and form spaghetti-like networks when dispersed in the epoxy (Figure 3.4).

Although Equation 3.2 does not explain all aspects of the data shown in Figure 3.5b, the theory of Refs. [164, 177] has nevertheless the merit of identifying the contribution of the closed loops (or, equivalently, of clustering) as a possible mechanism responsible for the $1/L_n$ scaling of $\ln(\sigma)$ which we have experimentally observed. We note that, in addition to enhanced local clustering possibly induced by a non-ideal dispersion of the CNTs in the epoxy, the waviness of the nanotubes may be a possible factor facilitating the occurrence of closed loops in the nanotube network. This consideration is partially supported by the lowering of the calculated conductivity obtained from simulations of dispersions of flexible rods with increasing waviness [182, 183, 184, 185]. Since the waviness has little, if not negligible, effect on σ if closed loops are neglected, as predicted by the liquid-state theory of percolation of slender wavy rods within the second virial approximation [186, 161], the lowering of the conductivity observed in simulations should forcefully stem from closed loops effects promoted by the rod waviness.

We conclude by pointing out that the waviness and local clustering of the nanotubes are typical in real CNT-polymer nanocomposites. If these factors are ultimately responsible for the observed universality of σ with respect to L_n in CNT-SU8 systems, quasi-universal features similar to that shown in Figure 3.5b should be therefore common in other CNT-polymer nanocomposites.

3.1.6 Summary

We have designed a set of experiments to evaluate the theoretical models which suggest that the electrical conductivity of CNT polymer nanocomposites depends on the polydispersity of the nanotubes length and is proportional to weighted average length $L_w = \langle L^2 \rangle / \langle L \rangle$. Here we tested this prediction by measuring σ of CNT-epoxy composites with purposely-tailored distributions of L . We found that the predicted dependence upon L_w is unable to explain our conductivity data, which follow instead a remarkable quasi-universal dependence upon the CNT mean length $L_n = \langle L \rangle$. We suggest that the relevance of L_n , rather than L_w , arises from enhanced clustering effects and possibly from the waviness of the nanotubes in our CNT-epoxy materials, and that it should be a common feature in CNT-polymer nanocomposites.

3.2 SU8 composites with aligned carbon nanotubes

3.2.1 Channeling of charged particles

Motivations and goals

In general, controlling of the transport of charged or neutral species, e.g. electrons, protons and especial atoms and molecules through nanopores is becoming increasingly important and it is a developing research direction in nanotechnologies. It could serve to deliver specific molecules into living cells with high precision, be used in sequencing applications, focusing energetic particles for precise implantations or tailoring at nanoscales. Carbon nanotubes can serve especially for the last topic through channeling charged particles.

Channeling of highly energetic charged particles is a well-known phenomenon, where the crystalline planes (their potential) are guiding the particles. Since the intensity of focused beam strongly depends on the alignment of the charged particle velocity vector and the crystallographic planes this technique is used to test the quality of the crystals, their defects etc. However, it has strong limitations for focusing high intensity beams. It could be more advantageous to use carbon nanotubes for channeling. The idea to use carbon nanotubes and carbon nanotubes arrays was suggested by Klimov and Letokhov [188] soon after their discovery. Nowadays, channeling of positively charged particles in nanotubes is becoming a real possibility with the advance of the synthesis of well-ordered carbon nanotubes. The theoretical modelling of focusing a proton beam is shown in Figure 3.6.

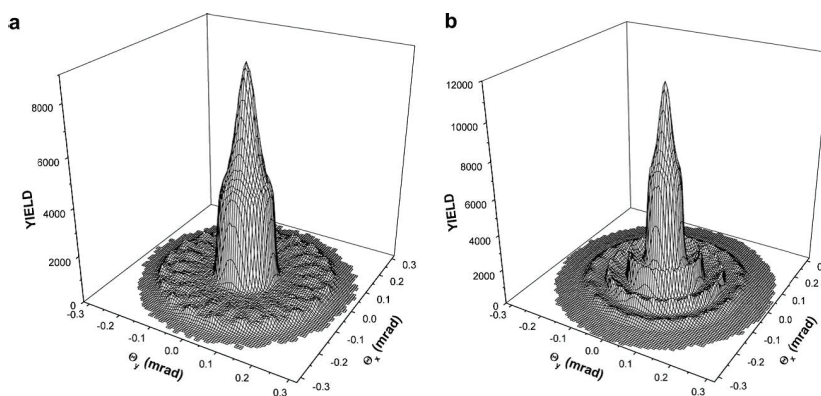


Figure 3.6: Illustration of the focusing capability of carbon nanotube of a beam of charged particles. Angular distributions of 1 GeV protons channeled in (10, 10) SWCNTs of length: (a) 10 μm (b) 30 μm . The intensity of the particle flux is plotted as the angle (θ) between the velocity vector and the tube axis [187]. Copyright 2009 Elsevier B.V.

3.2. SU8 composites with aligned carbon nanotubes

The advantages of CNTs over crystals considering the guiding of charged particles are that initial ion beam angular width and ion de-channeling length can be made larger. This can be important for the extraction and bending of positively charged particles with energies below 1 GeV, for producing of ultra-stable low emittance beams for medical and biological applications. Besides, ion beam guiding with CNTs enables two-dimensional beam manipulation whereas a bent crystal yields merely a one-dimensional one. It has to be mentioned that focusing the charged particles by channeling is very efficient, for a comparable effect one would need a magnetic field close to 1000 T. The importance of channeling by CNTs is in creating and transporting highly focused nano-sized particle beams which are useful in implantation in electronics, biology and medicine with high spatial resolution. It could be easier to do this way beam extraction, collimation and steering at accelerators than with high magnetic fields. In the long run, this technique might also have a strong economic impact.

Despite the great need for such studies, there is only one set of experimental data reported on channeling in CNT grown in porous anodic aluminum oxide (AAO) membrane [189]. Such a synthesis does not yield high quality nanotubes, so the de-channeling might be quite severe. It could be more promising to use high quality carbon nanotubes (Figure 3.7), oriented and embedded into SU8 matrix and cut to lamellas of various thickness, since the length of the nanotubes is also a parameter in channeling. This is what we have addressed.

Beyond the importance of ion channeling in focusing and bending charged particles, e.g. protons, it can also carry information of basic science character. Namely, since the scattering

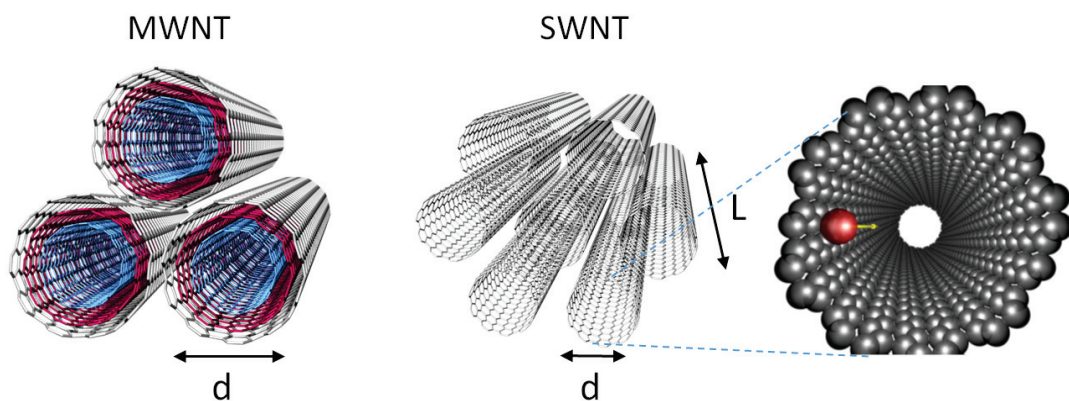


Figure 3.7: Bundles of multi walled (MWNTs) and single walled (SWNTs) carbon nanotubes which should be imbedded into a matrix (preferentially SU8 epoxy) and cut to a length $L \sim 0.1-1 \mu m$. They could serve as excellent structures for channeling (illustrated on right). The typical diameter d are 20 nm and 1.4 nm for MWNTs and SWNTs, respectively.

Chapter 3. Composites with 1D fillers: SU8-carbon nanotube composites

of charged particles happens on the array of atomic rows and on their electronic cloud, it gives an axial pattern in the scattered charge distribution. In the jargon of this field it is called a rainbow effect (see Figure 3.6 and Figure 3.8). Looking at the rainbow pattern one could read with a good precision the chirality of the nanotube. In the case of an ordered rope of carbon nanotubes the space in-between them is also channeling the charged particles. From this additional modulation of the rainbow pattern one could determine the architecture of the atomic order in-between the nanotubes [190, 191].

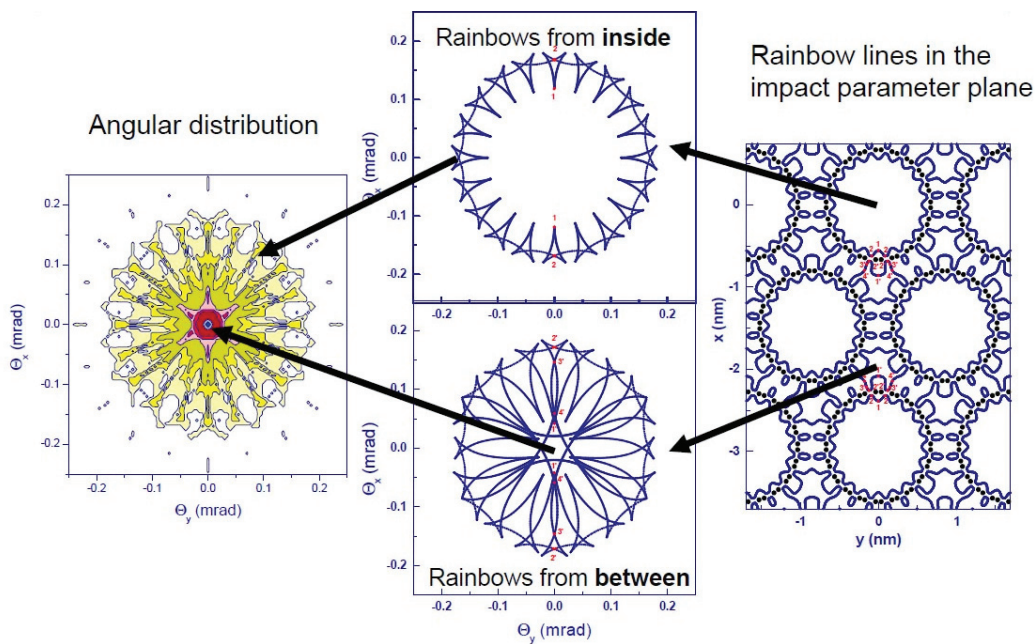


Figure 3.8: Simulation of rainbow channeling pattern of a $1 \mu\text{m}$ long rope of (10,10) single walled (SWNTs) carbon nanotubes[190, 191]. Copyright 2005, EDP Sciences/Societ  Italiana di Fisica/Springer-Verlag.

Most of the works are theoretical, mainly done the group of Dr. Nebojsa Neskovic at Vinca Institute of Nuclear Sciences in Belgrade, whose group is one of the leaders in this field [190, 191, 192, 193]. The test measurements will be performed in the group of Prof Mark B H Breese at the NUS Nanoscience and Nanotechnology Institute in Singapore. For the need of this study, we have set up a scientific collaboration with both these groups. The goal is to prepare a series of SU8 impregnated MWNTs and SWNTs with various diameters, ranging from 1.4 to 20 nm. The length will be adjusted by microtome or FIB tailoring. By cutting the composite we will produce a membrane where the whole diameter will be determined by the diameter of CNTs. The L of the CNTs (or the thickness of the membrane) could be an important parameter in the de-channeling of the beam.

3.2. SU8 composites with aligned carbon nanotubes

Since our laboratory controls well the growth of oriented carbon nanotubes (mainly MWNTs) and the preparation of composites we have attempted to prepare thin lamellas of SU8 and short MWNTs imbedded for test measurements. Cutting the lamellas and keeping the nanotubes within the matrix is far from being a trivial task. Since the MWNTs are not bound to the matrix, the diamond knife tends to pull them out during the cutting. The first promising results of this project are shown below. Due to the high interest in this project it will be certainly continued beyond the present PhD project.

Composite preparation

Vertically aligned Multiwalled Carbon Nanotube (MWCNT) forests were synthesized by water-assisted CCVD (Catalytic Chemical Vapor Deposition) at 750 °C in a horizontally mounted quartz furnace over a 5 nm thick catalyst film of *Fe-Co* (molar ratio of 2:1) nanoparticles, supported by a 10 nm *Al₂O₃* layer on silicon substrate. 10 nm thick film of alumina was deposited by e-beam evaporation. *Fe₂Co* thin film was grown by the RF magnetron sputtering technique from a *Fe₂CoO₄* target. The deposition was carried out in a vacuum chamber at a pressure of 6×10^{-3} Torr. For annealing and CNT growth experiments the substrates were cut into small pieces of 0.5cm × 0.5cm. First, the catalyst wafers were pre-treated in *Ar* (100 sccm) and *H₂* (80 sccm) for 10 min, then ethylene gas (100 sccm) was introduced to the reaction chamber for 30 min, diluted with the mixture of *Ar* and *H₂* gas. In addition, *H₂O* was introduced by bubbling *Ar* (20 sccm) in liquid water in each case. The obtained carbon nanotubes form a well-aligned array, shown Figure 3.9, in which the tubes are parallel and have a height about few hundred microns.

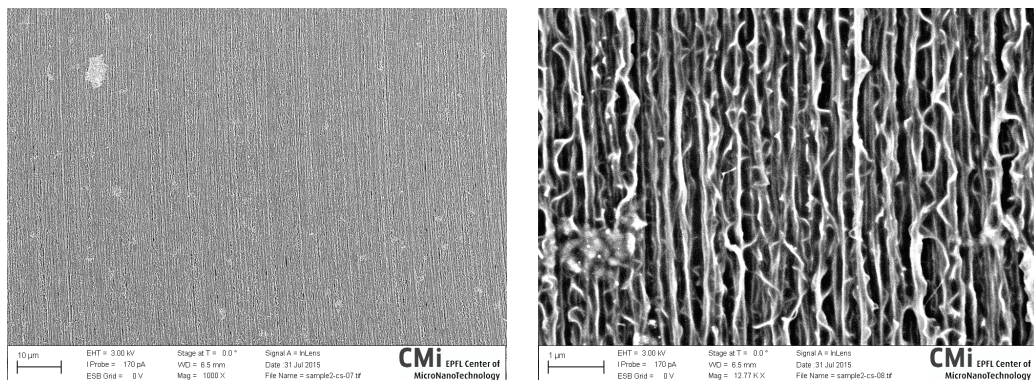


Figure 3.9: SEM micrograph of aligned CNT carpets.

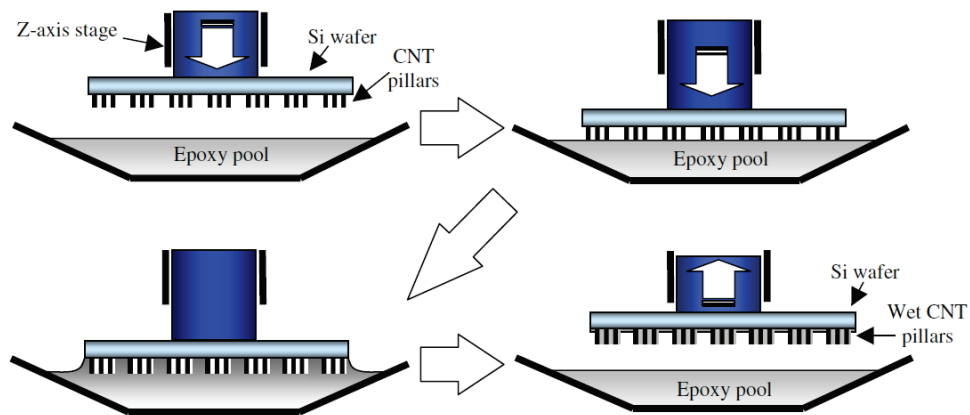


Figure 3.10: Schematic of the submersion method used to prepare SU8-oriented CNT composites [195]. Copyright 2007 IOP Publishing.

In the literature, the most employed method for embedding CNT forests into a polymer matrix is to place a drop of the polymer solution on top of the CNT carpet [194]. However, in our case this method was not suitable for producing well-structured composites. The reason being the distortion of the tubes and the formation of macroscopic cracks in the carpet structure while the polymer diffuses through the CNT forest. To overcome this problem, Garcia et al. [195] have suggested an effective technique, so-called “submersion process”. Following their procedure, CNT carpet grown on Si wafer was fixed on a stage that allows displacement along the z-axis. A small pool of SU8 with appropriate viscosity was placed below the stage. The stage was moved down slowly until the top surface of the carpet came into contact with the SU8. Thanks to capillary forces the polymer is sucked into the forest. This procedure is depicted in Figure 3.10. Once the carpet has been fully impregnated and removed from the stage, an extra drop of SU8 was placed on the top of the SU8 to compensate for the shrinkage of the SU8 occurring during the polymerization. This process was followed by a thermal cross-linking of SU8 by curing at 150 °C for 10 minutes with a temperature ramp of 4.5 °C/min.

Several preliminary tests were performed in order to find the optimal viscosity of the SU8 solution for effective penetration into the forest with minimized induced structural damages. The selected solution contained 75% of Gamma butyrolactone as solvent. It is worth mentioning that we observed that the thermal treatment of the CNTs for functionalization of their surface, would intensify the formation of macro-cracks during the impregnation with SU8. This effect is less problematic for as-grown non-heat treated forests. We assume that it is due to the hydrophobic nature of SU8 that rejects the hydrophilic surface of functionalized CNTs.

Preparation of the SU8-oriented CNTs lamellas

The SU8-CNT lamellas were prepared with ultramicrotomy technique. Two types of diamond knives (standard and oscillatory) were used to cut lamellas with thickness ranging from 20 to 100 nm (as demanded by Prof. Mark Breese). Various cutting speeds ($0.1\text{-}12\text{ mm}\cdot\text{s}^{-1}$) have been examined to select the best conditions for sample preparation. After cutting, the lamellas were placed on Cu TEM grid with 200 meshes.

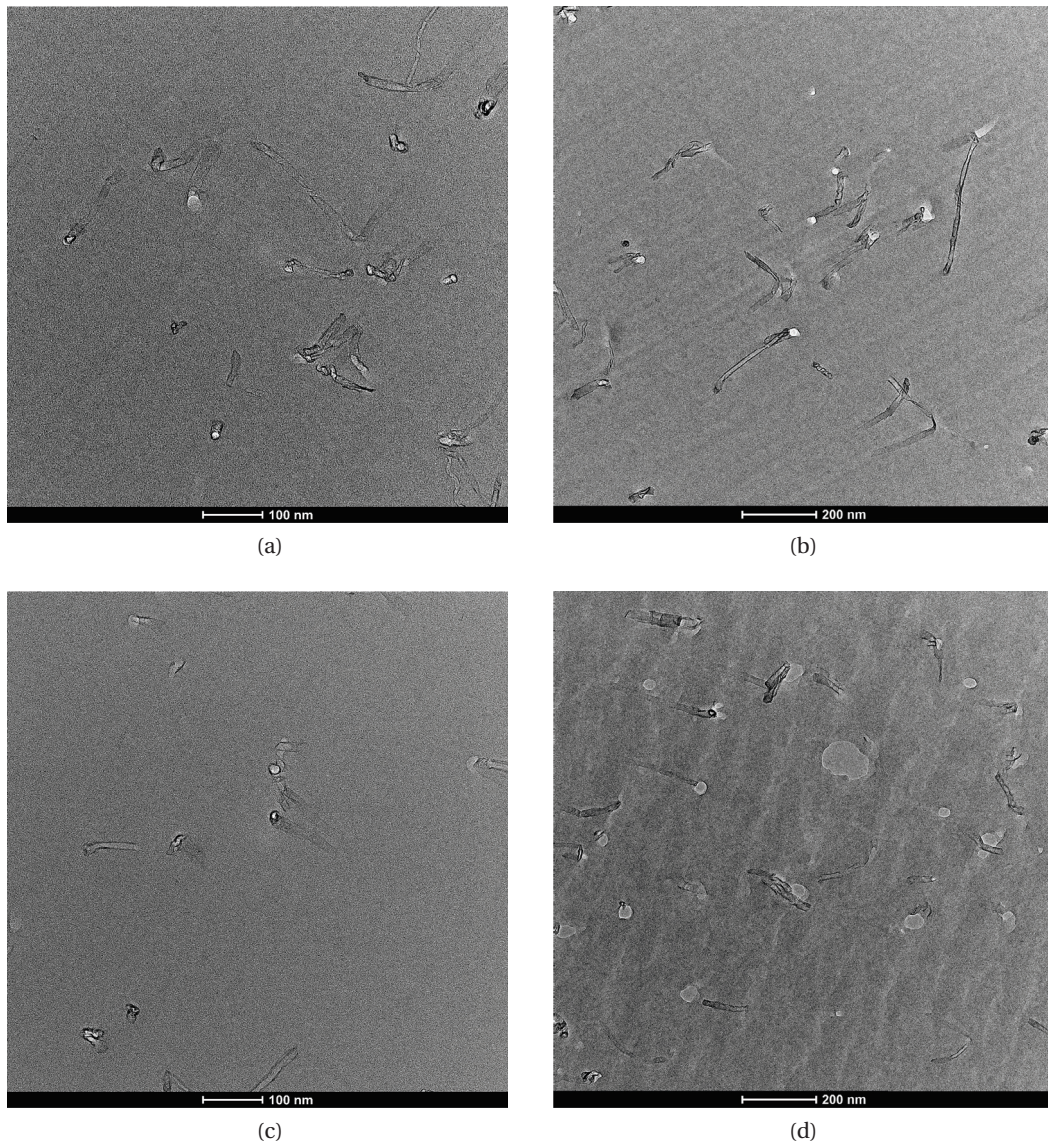


Figure 3.11: SU8-CNT lamellas prepared with (a) standard diamond knife, 100 nm thickness, (b) standard diamond knife, 50 nm thickness, (c) oscillatory diamond knife, 100 nm thickness, (d) oscillatory diamond knife, 100 nm thickness, for proton channeling measurements. The lamella displayed in image (d) was the one used for the channeling measurements.

Chapter 3. Composites with 1D fillers: SU8-carbon nanotube composites

Figure 3.11a and b present TEM images of CNT-SU8 lamellas with thickness of 100 *nm* and 50 *nm* cut with standard diamond knife. Due to the weak bonding between CNTs and epoxy and probably because of the difference between their stiffness, while the knife passes through the polymer, does not cut the nanotubes, but pull them out or bend them. In order to overcome this problem we have used oscillatory diamond knife which was effective to some extent, and provided clean cuts specially at lower thicknesses as presented in Figure 3.11d.

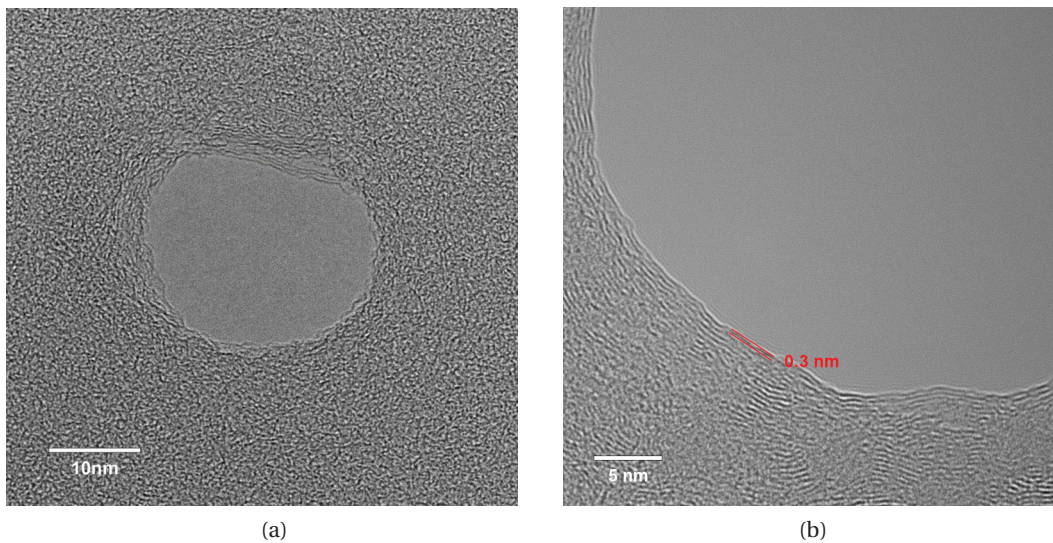


Figure 3.12: Transmission electron microscope images of SU8-CNT lamella around a carbon nanotube channel (a). The walls of the carbon nanotube with inter-layer distance of 0.3 *nm* is visible in image (b).

The density of carbon nanotubes is varying between 100 and 1000 per μm^2 . The diameter is not monodisperse, it is in the 20 ± 10 *nm* range. The larger holes are probably coming from breaking out of pieces of SU8 due to the mechanical stress exerted by the diamond knife. Figure 3.12 shows a zoom on a carbon nanotube embedded in the SU8. One can observe the walls of the MWNTs as the rims of the holes. The lamella shown on Figure 3.11d was the first sample which was tested for the channeling measurements. The length of the nanotubes were 50 *nm*. The idea was, that if one sees the rainbow effect, it would be more visible on short nanotubes.

Preliminary measurements

The measurement shown below is the first one ever done on oriented carbon nanotubes of tailored length, and embedded in an epoxy. Figure 3.13 shows the transmitted channeling pattern as recorded by photograph of a highly sensitive aluminium-coated YAG scintillator

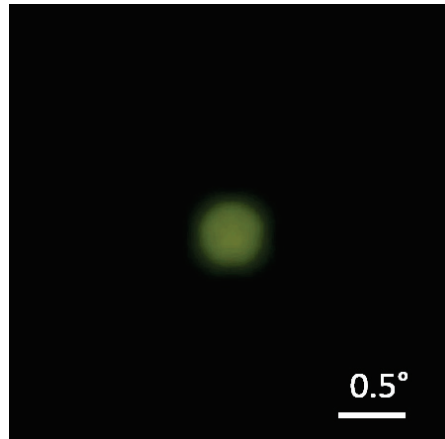


Figure 3.13: The transmitted channeling pattern were recorded by photographing a highly sensitive aluminium-coated YAG scintillator screen placed at ~ 70 cm away from the sample. Focused 2 MeV protons were used for this experiment, and the spot size of the beam is around 500 nm at the surface of the sample. The CNT sample thickness is around 50 nm. The measurement was done in the group of Prof. Mark Breese, NUS, Singapore by Mallikarjuna Rao Motapothula.

screen placed at ~ 70 cm away from the sample. Focused 2 MeV protons were used for this experiment, and the spot size of the beam is around 500 nm at the surface of the sample. The estimated angle between the nanotube axis (normal vector to the lamella) and the velocity vector of protons (the beam direction) is 0.5° . We observe some channeling effect, however even though the CNT sample length is around 50 nm, the observed angular distributions does not have any fine structure. One of the main reasons for the absence of fine structure in channeling angular pattern is that, the density of CNT's is low in SU8 matrix, so that the fine structure generated by CNTs is overlapped by the non-structured transmitted beam from SU8.

This pioneering experiment did not give the rainbow effect, nevertheless it is very encouraging. It has shown that we are able to prepare an array of carbon nanotubes embedded into SU8 and adjust the length of the nanotubes at will. In the future, one has to work on the increase of the density of nanotubes and their functionalization to improve their binding to the matrix. This last step would facilitate their cutting without pulling them from the matrix. One can imagine binding the CNTs to the matrix not just by chemical means, but by electron irradiation, as well.

We are confident that this topic will gain in importance in the near future.

3.2.2 Anisotropic thermal conductivity

Motivation

The theoretical thermal conductivity (κ) values predicted for carbon nanotubes makes them exceptional candidates for thermal management applications. In this regard, using well-aligned CNT as fillers in SU8 matrix can bring the potential functionality of anisotropic thermal conductivity to the composite. Even if the theory neglects the imperfection of real-world CNTs and overestimates their thermal conductivity, there is still plenty of room for improvement of thermally insulated epoxy.

The well-oriented SU8-CNT composites would evacuate the heat generated in, or applied to electronic devices in controlled manner due to the anisotropy in κ . Moreover, SU8 as a robust material can be advantageous in extreme environmental conditions. As an example SU8-CNT composite could be used for radiation detector cooling thanks to its resistance to irradiation. It was reported that the effect of neutron and proton irradiation on hardness and plastic deformation of SU8 coatings is negligible [196, 197].

This wide range of potential applications of SU8-CNT composites provokes a high interest in the characterization of their anisotropic thermal conductivity. In this section, we report the preparation and physical characterization of SU8-aligned CNT composites.

State of the art

An intriguing characteristics of CNTs is the theoretical prediction of unusually high room temperature longitudinal thermal conductivity for an isolated (10, 10) single walled CNTs (SWCNTs) to be close to $6600 \text{ W m}^{-1} \text{ K}^{-1}$, due to the large phonon mean free paths in these systems which are held together by strong sp^2 carbon bonds [198]. This would be valid in the case of absence of atomic defects, coupling to soft phonon modes of the embedding medium [198] and intertube coupling [199].

The highest experimentally measured value of thermal conductivity at room temperature is over $3000 \text{ W m}^{-1} \text{ K}^{-1}$ and it was measured for individual suspended Multi wall carbon nanotube (MWCNT) [67]. Discrepancy with the theory is probably due to the CNTs' imperfections and the fact that thermal conductivity decreases with an increase of tube's diameter [200]. But, even for low diameter tubes, like arc discharged SWCNTs with average radius of 1.4 nm , measured thermal conductivity is far from that predicted and shows a correlation with CNTs' spatial arrangement. Namely, room temperature thermal conductivity of a SWCNTs disor-

3.2. SU8 composites with aligned carbon nanotubes

dered structure in the form of loosely-packed, tangled mat was only $0.7 \text{ Wm}^{-1}\text{K}^{-1}$, which upon correction for low density of the mat gives $36 \text{ Wm}^{-1}\text{K}^{-1}$ for a dense-packed SWCNTs mat [201]. On the other hand, the same tubes, aligned and vacuum annealed at 1200°C , to improve the crystallinity, have a room temperature thermal conductivity of $200 \text{ Wm}^{-1}\text{K}^{-1}$ measured in the parallel direction [202].

We can notice that measuring thermal conductivity of bulk CNT's may not reflect intrinsic CNTs thermal conductivity due to the effect of volume filling fraction. Since thermal conductivity of CNTs significantly depends on the concentration of vacancies and defects in CNTs, the synthesis method have strong influence as well. The thermal conductivity of millimeter-long aligned MWCNTs prepared by chemical vapor deposition (CVD) was $25 \text{ Wm}^{-1}\text{K}^{-1}$ which is quite low due to the substantial amount of defects caused by the synthesis method [203]. In addition, according to Maruyama et al. [95, 96], it should be taken into account that thermal conductivity of CNTs may diverge from the theoretically predicted value when the tube length is much longer than the phonon mean free path, since it has been shown that thermal conductivity strongly depends on the CNTs length in the cases of realistic length scale for device applications [95, 96]. Based on both theory and experiments, it is reasonable to consider CNTs as a promising material for thermal management.

Such materials are in the focus of experimental research on used for heat dissipation which is an essential problem towards microelectronics future development [204, 205]. Besides that, it is also crucial in particle detector systems at large scale [206, 207] as well as in the future of ultrafast laser-switched magnetic storage [208].

Thermal interface materials are usually composites consisting of some polymer which enables material processing, and fillers which provide thermal conductivity [209]. Therefore, it would be reasonable to choose CNTs as highly thermally conductive fillers for composites used for thermal management applications, instead of conventional additives, such as metal particles or ceramic particles [68]. Recently, there were many attempts in this direction which yield an enhancement of thermal conductivity for 40% by adding 0.5 wt% of SWCNTs [210] or 60 % by adding 5 wt% of MWCNTs [211]. Even the recently reported significant increase of 684 % with the addition of 5 wt% of MWCNTs resulted in the moderate thermal conductivity value of $0.96 \text{ Wm}^{-1}\text{K}^{-1}$ [212]. All mentioned examples contain randomly oriented CNTs. However, homogeneous dispersion of CNTs in random manner obliges to use high energy mechanical methods (like sonication) which alter the CNTs quality. Furthermore, they are usually effective for very limited CNTs volume fractions but they could even degrade the properties of composites when the volume fraction of CNTs reaches $\sim 5 \text{ wt\%}$ [1]. Therefore, it

Chapter 3. Composites with 1D fillers: SU8-carbon nanotube composites

is not surprising that a room temperature thermal conductivity value can be as low as $0.34 \text{ Wm}^{-1}\text{K}^{-1}$ for composite with 20 wt% of few walls CNTs [213]. Further obstacles towards the enhancement of the thermal properties of composites by CNTs would be intertube contacts and heat transfer from CNTs to the surrounding material [214]. To overcome at least the problem of intertube contacts and to ensure that each tube can be used as direct thermal conductor from the heat source to the sink, it was proposed to create composites close to the ideal morphology by making high volume fraction of aligned CNTs [215, 13]. This would imply the creation of anisotropic thermal management composites with direction dependent properties that result from the alignment of CNTs [215, 13]. Thermal conductivity enhancement of 125% was achieved with 1 wt% of magnetically aligned SWCNTs [215] and 280% with 0.3 wt% of CVD growth carpet from aligned MWCNTs [205]. In the last case authors reported an achieved thermal conductivity value of $0.88 \text{ Wm}^{-1}\text{K}^{-1}$, ascribing this moderate value to the low CNT fraction and estimating that values as high as $6.5 \text{ Wm}^{-1}\text{K}^{-1}$ could be obtained if the weight fraction of the aligned CNTs array was as high as 3 wt% [205].

Measurement methods

Synthesis of MWCNTs and their impregnation with SU8 using the submersion method are described in Figure 3.2.1.

In the following results part the properties of another sample prepared by the so-called 'dropwise' method are also presented. These samples were provided by Marijana Mionic, the former PhD student working on this project [15]. We will compare the data coming from sample prepared with these two methods in order to have an insight of the influence of sample preparation conditions on the final properties of the composite.

In the dropwise method, SU8 GM1040 (containing 60 wt% of solvent) was dropped onto the MWCNT carpet at room temperature. Subsequently, impregnated carpets were prebaked in the oven at $95 \text{ }^\circ\text{C}$ over 10 hours in order to provide uniform solvent evaporation, which was followed by a $120 \text{ }^\circ\text{C}$ baking for 2 hours in order to cross-link the SU8.

Figure 3.14 illustrates the SEM image of MWCNT carpets before and after impregnation with SU8.

For the thermal conductivity measurements, a thin rectangular shaped piece of stainless steel reference and a chip resistor are attached on either side of the sample using Stycast FT 2850 electrical insulating glue. A thermal gradient was generated by dissipating current in the attached resistor and the other part of the stainless steel was thermally anchored to the

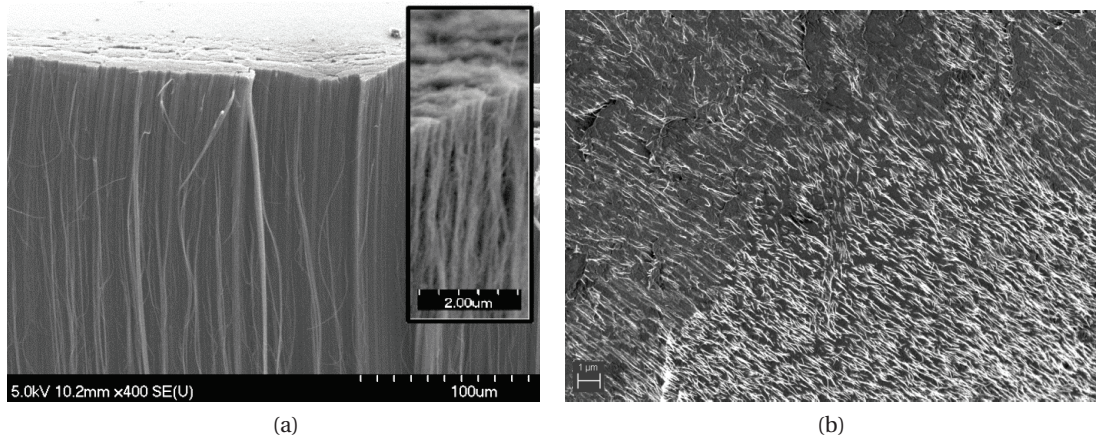


Figure 3.14: SEM images of the carbon nanotube carpet before (a) and after (b) impregnation with SU8 epoxy . The CNTs fill up 3% of the volume of the composite.

copper probe head block. Chromel-constantan (type E) thermocouples are attached with electrical insulator glue to the surfaces of both, the stainless steel piece and the sample in order to probe the thermal gradient. The heating power of the chip resistor is regulated to maintain a maximum temperature gradient of 1 K across the sample at all temperatures. In the probe head we employed dynamic vacuum better than $5 \times 10^{-6} \text{ mbar}$ to reduce thermal effects. Assuming that the same amount of heat flows through the stainless steel reference and the sample, the thermal conductivity of the sample is calculated with multiplying the achieved temperature gradient ratios by the geometrical factor of the sample.

In the Thermo electric power (TEP) measurement a temperature gradient has been employed using an attached resistor. The temperature gradient is measured by an E-type thermocouple, the generated TEP has been recorded by a Keithley 2182A nanovoltmeter. In the same setup electrical resistivity has also been measured using standard 4-in line method on rectangular samples of typical dimensions $1 \text{ mm} \times 0.5 \text{ mm} \times 1.5 \text{ mm}$. Four gold wires were attached on the sample surface using carbon paste. $1 \mu\text{A}$ current has been applied to the sample through the wires at the ends. The potential difference was measured by a Keithley 2182A nanovoltmeter on the two wires in the middle. The absence of Joule heating has been monitored by changing the applied current occasionally.

Thermal conductivity

Thermal conductivities have been measured both parallel and perpendicular to the nanotubes direction and the results are depicted in Figure 3.15a. Perpendicular to the MWCNTs, the

thermal conductivity (κ_{\perp}) is dominated by SU8. Along the tubes the thermal conductivity (κ_{\parallel}) is enhanced as MWCNTs take part. At low temperatures, ($\kappa_{\parallel}(T)$) is linear which indicates a 1D phonon mediated mechanism for thermal conductivity. The absolute value of (κ_{\parallel}) and thus the calculated anisotropy ($\kappa_{\parallel}/\kappa_{\perp}$) (see Figure 3.15b) is much higher for the sample prepared using the submersion method than the one prepared by the dropwise method.

This finding confirms that the former sample preparation method creates less defects therefore results higher thermal conductivity. In both materials, $\kappa(T)$ has been fitted by Callaway's model [216] in the following way.

Due to the high electrical conductivity of the nanotubes, the electronic contribution to the thermal conductivity is negligible in comparison to the phonons' part. Thermal conductivity can be calculated using Boltzmann's transport equation for phonons in the relaxation time approximation, and one yields the following expression:

$$\kappa(T) = \int_0^{\omega_D} d\omega g(\omega) C_{ph}(\omega, T) v_g^2 \tau_{tot}(\omega, T) \quad (3.3)$$

$$= \int_0^{\omega_D} d\omega g(\omega) v_g^2 \tau_{tot}(\omega, T) \frac{\exp \frac{\hbar\omega}{k_B T}}{(\exp \frac{\hbar\omega}{k_B T} - 1)^2} k_B \left(\frac{\hbar\omega}{k_B T} \right)^2 \quad (3.4)$$

$$= \frac{k_B^2 T}{h} \int_0^{x_D = \frac{\hbar\omega_D}{k_B T} = \frac{\Theta_D}{T}} dx \frac{x^2 \exp x}{(\exp x - 1)^2} g(x) v_g^2 \tau_{tot}(\omega, T) \quad (3.5)$$

where $g(\omega)$ is the number of modes of the macroscopic system normalized by unit volume and unit frequency, $C_{ph}(\omega, T)$ is the specific heat of phonons, v_g is the group velocity of phonon mode, $\tau_{tot}(\omega, T)$ is the relaxation time, ω_D is the Debye angular frequency and k_B is the Boltzmann constant. At low temperatures ($\Theta_D \gg T$), in the absence of Umklapp scattering the main contribution to thermal conductivity is the inelastic phonon scattering due to fixed sample boundaries or defects which usually give a constant relaxation time. Whereas at high temperatures, the Umklapp scattering becomes the dominant scattering mechanism limiting the τ relaxation time. As a consequence of Umklapp scattering, the thermal conductivity displays a peak and decreases with increasing temperature. In the case of nanotubes as they are a less crystalline form of carbon, the peak in $\kappa(T)$ occurs at higher temperatures because defect scattering remains the dominant mechanism over Umklapp scattering to higher temperature. Summarily, we consider two scattering mechanism:

$$\tau_{tot} = (\tau_1^{-1} + \tau_U^{-1})^{-1} = (a_1 + a_U T^3 x^2)^{-1} \quad (3.6)$$

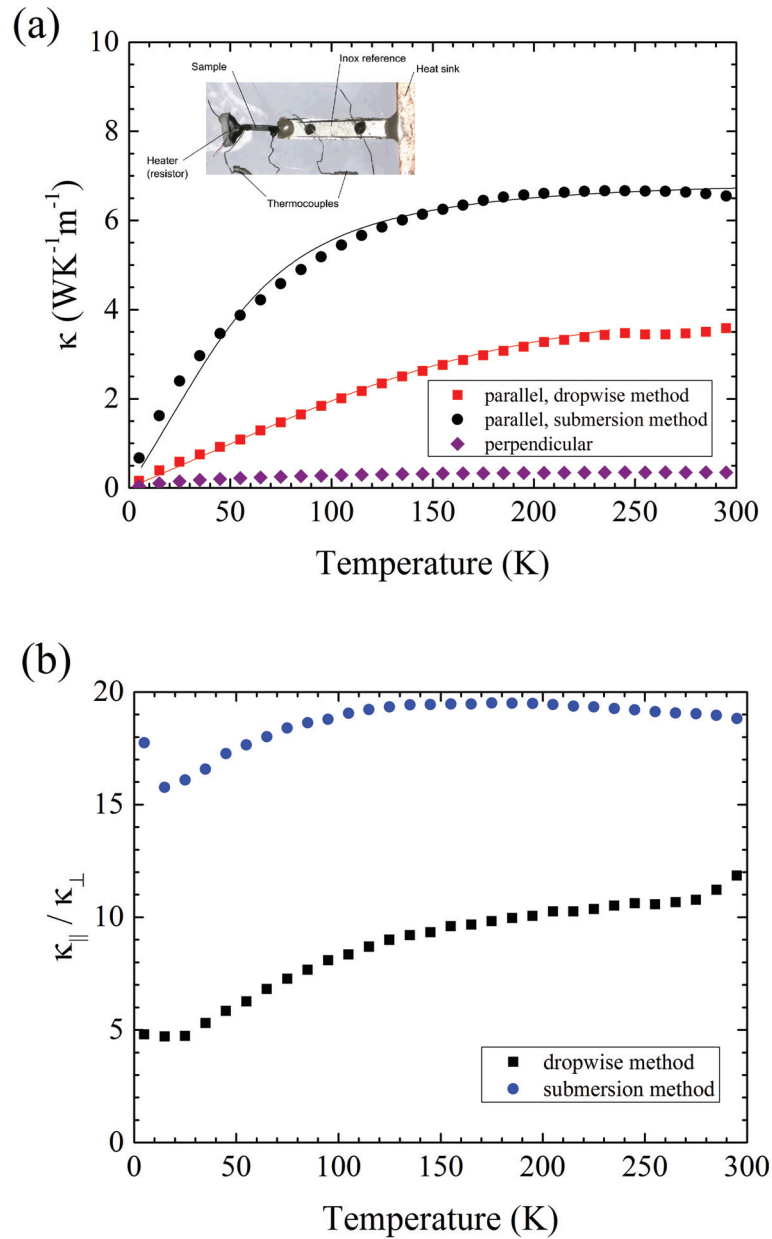


Figure 3.15: (a) Temperature dependence of thermal conductivity of the MWCNT-SU8 composite, perpendicular and parallel to the tubes axis. For the epoxy $\kappa = 0.2 \text{ Wm}^{-1}\text{K}^{-1}$ at room temperature. The solid lines are fits described in the text. The inset illustrates the measurement setup. (b) Temperature dependence of anisotropy of the thermal conductivity ($\kappa_{||}/\kappa_{\perp}$) for dropwise and submersion samples.

where a_1 and a_U are constants, characteristic of boundary and Umklapp scattering, respectively. Assuming a quasi-onedimensional density of states for acoustical phonons (g_0), and

Chapter 3. Composites with 1D fillers: SU8-carbon nanotube composites

constant group velocity and the expression will be the following:

$$\kappa(T) = \frac{k_B^2 T}{h} \frac{g_0 v_g^2}{a_1} \int_0^{\frac{\Theta_D}{T}} dx \frac{x^2 e^x}{(e^x - 1)^2} \frac{1}{1 + \frac{a_U}{a_1}} T^3 x^2 \quad (3.7)$$

In the low temperature limit the above expression reduces to a linearly temperature dependent formula:

$$\kappa(T) = \frac{k_B^2 T}{h} \frac{g_0 v_g^2}{a_1} \int_0^{\infty} dx \frac{x^2 e^x}{(e^x - 1)^2} = \frac{k_B^2 T}{h} \frac{g_0 v_g^2}{a_1} I_{\infty} = A.T \quad (3.8)$$

where A is constant and $I_{\infty} \approx 3.28$. Furthermore, we define $A_U = a_U/a_1$ and with the notation above the measured thermal conductivity data can be fitted as

$$\kappa(T) = A.T \int_0^{\frac{\Theta_D}{T}} dx \frac{x^2 e^x}{(e^x - 1)^2} \frac{1}{1 + A_U T^3 x^2} \quad (3.9)$$

using fit parameters: A, A_U and Θ_D . For the dropwise sample the fit parameters are $A = 0.006 WK^{-2} m^{-1}, \Theta_D = 750K$ and $A_U = 3.510^{-11} K^{-3}$, and for the submersion sample are $A = 0.023 WK^{-2} m^{-1}, \Theta_D = 300K$ and $A_U = 1.110^{-15} K^{-3}$. These fits are shown as solid lines in Figure 3.15.

The fit parameters are remarkably different for the different preparations. The fits give an indication that in the submersion sample both scattering mechanisms have fewer events than in dropwise one and the decrease of κ due to the Umklapp processes is better evolved due to the lower level of boundary scattering.

Additionally, we estimate the phonon mean free path $l_{ph} = v_g \tau$. For the sake of simplicity we use the low temperature, linear part of the thermal conductivity:

$$A = \frac{k_B^2}{h} g_0 v_g^2 \tau I_{\infty} = \frac{k_B^2}{h} g_0 v_g I_{\infty} l_{ph} \quad (3.10)$$

The next step is that g_0 is to be expressed in terms of the number of modes N_{mod} per unit-cell volume V_0 :

$$g_0 = \frac{N_{mod}}{V_0 \omega_D} = \frac{h N_{mod}}{V_0 k_B \Theta_D} \quad (3.11)$$

thus the mean free path of the phonons

$$l_{ph} = A \frac{\Theta_D V_0}{k_B v_g I_{\infty}} \cdot \frac{1}{N_{mod}} \quad (3.12)$$

3.2. SU8 composites with aligned carbon nanotubes

As N_{mod} is the effective number of phonon modes per unit cell that carry the heat, thus it may be quite small since the most of the volume is occupied by the SU8 epoxy, so the MWCNT volume fraction $\phi = 3\%$ should be taken into account. In addition, it should be noticed that the most of the phonon modes at low temperatures are inactive. The number of phonon modes in the direction along the carbon nanotubes for this thermally active part of the composite is n_{\parallel} together with the MWCNT volume fraction yield the effective number of phonon modes: $N_{mod} = n_{\parallel} \times \phi$.

We assume that the heat is carried by the low energy phonons propagating along the nanotubes only, whereas the modes perpendicular to the CNTs remain unexcited. Therefore n_{\parallel} depends of the MWCNT radius R in unit cell units as the phonon spectrum is discrete, R is small:

$$n_{\parallel} = \frac{1}{R^2 \pi} \quad (3.13)$$

In conclusion, the rough estimation for the maximum of the phonons' mean free path is:

$$l_{ph} = A \frac{\Theta_D V_0}{k_B v_g I_{\infty}} \cdot \frac{1}{n_{\parallel} \phi} = A \frac{\Theta_D V_0}{k_B v_g I_{\infty}} \cdot \frac{R^2 \pi}{\phi} \quad (3.14)$$

We use $v_g = 6000 \text{ m/s}$ and $V_0 = 40.45 \times 10^{-30} \text{ m}^3$ according to Ref. [217], and we estimate $R = 10$. Taking the filling ratio $\phi = 0.03$, as well as A and Θ_D from the fits, one can get $7 \mu\text{m}$ for the dropwise sample and $11 \mu\text{m}$ for the submersion sample.

Anisotropy

The low anisotropy of κ might come partially from the laterally touching nanotubes which can somewhat increase κ_{\parallel} and represent an additional scattering center for phonons. The less than ideal alignment might be the reason for the temperature independent anisotropy in the sample synthesized by submersion method, that is the temperature dependence of κ_{\perp} is dominated by κ_{\parallel} .

This conjecture could be tested by electrical resistivity and thermoelectric power (Seebeck coefficient) measurements in the two directions explored by κ . A rough estimate for the electrical resistivity anisotropy is the following. The catalog value of ρ for SU8 is $10^{16} \Omega\text{cm}$ (facts sheet). In laboratory conditions the highest measured value is $10^{10} \Omega\text{cm}$ [41]. For individual arc-discharge synthesized MWNTs the resistivity is in the $10^5 \Omega\text{cm}$ range [218], but for CVD prepared tubes this value could be two orders of magnitude higher. In any case $\rho_{\perp}/\rho_{\parallel}$ should be well above $10^{10} \Omega\text{cm}$ for an ideal sample. The low value of the measured

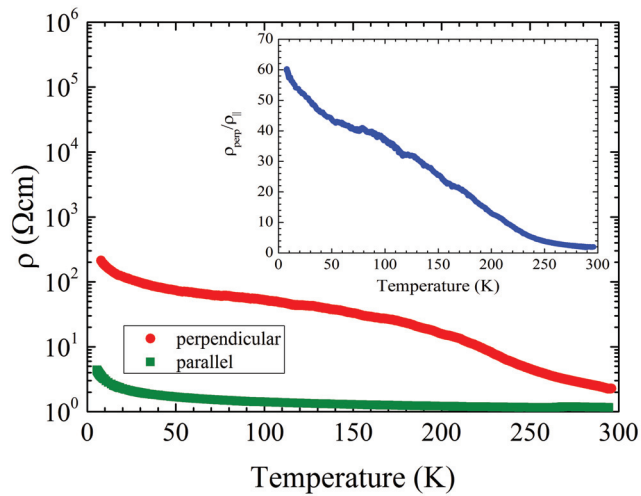


Figure 3.16: Temperature dependence of electrical resistivity in the tube direction (green squares) and perpendicular to the tube direction (red circles). Inset: Temperature dependence of electrical resistivity anisotropy.

anisotropy indicates that there are tubes which are touching each other, and they act as “short cuts” for perpendicular transport. The temperature dependence of the anisotropy shows that the tube-tube contacts are not necessarily direct contacts, but they communicate through a layer in which the electrical conduction happens through hopping. Indeed, the temperature dependence of the resistivities is consistent with a thermal fluctuation induced hopping (not shown) proposed by Sheng for metallic clusters embedded in an insulating matrix [219].

The Seebeck coefficient as a function of temperature for the two directions shown in Figure 3.17 is consistent with S measured for carbon nanotubes [220]. In this measurement the anisotropy between S_{\parallel} and S_{\perp} is even lower (~ 2) which is maintained over the whole temperature range. This measurement is another independent confirmation that misoriented carbon nanotubes are influencing the charge and thermal transport in the composite.

Summary

We have prepared a composite of oriented MWNTs and SU8 epoxy with the goal of having a material for a good and ideally anisotropic thermal management. The absolute value of κ along the tubes depends strongly on the preparation conditions of the composite. The highest value of κ (300 K) is in the $6\text{-}10 \text{ Wm}^{-1}\text{K}^{-1}$ range. Somewhat higher value has been reported for MWNTs/polymer composite where the filling was achieved by electrochemistry [221]. However, for certain applications (e.g. radiation detectors thermal management) the

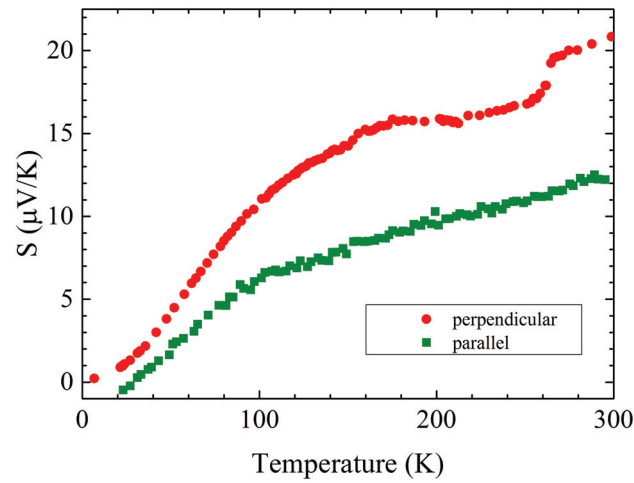


Figure 3.17: Temperature dependence of thermoelectric power. The anisotropy parameter is roughly constant throughout the investigated temperature range.

SU8-MWNTs is much more suitable due to the high resistance of the SU8 epoxy to radiation of energetic particles. The anisotropy of $\kappa_{\parallel}/\kappa_{\perp}$ of 10-20 could be improved by keeping a better alignment of the MWNTs in the epoxy, or increasing the density of CNTs.

3.3 Conclusion

In this chapter, the preparation and characterization of CNT-SU8 composites of different types have been presented. The goal was to investigate the influence of the aspect ratio and polydispersity, as well as the alignment of the nanotubes on the final properties of the composites.

In the first part, we argued that the length polydispersity is a major disadvantage for full optimization of electrical and mechanical properties of randomly distributed CNT-polymer nanocomposites. Therefore, it must be well realized in order to have a better control of the composite systems. For this purpose, we have designed a set of experiments to evaluate the theoretical models for the dependence of the electrical conductivity of the CNT polymer nanocomposites on the CNT length polydispersity. Our findings challenge the dominant theory which suggests that the conductivity is proportional to the weighted average length, L_w , as our experimental data showed the relevant dependence on the mean length, L_n . We attributed this behavior to the waviness and local clustering of the nanotubes, which should be common in CNT polymer composites, and must be considered in theoretical calculations.

Chapter 3. Composites with 1D fillers: SU8-carbon nanotube composites

In the second part, we showed that having oriented CNTs in SU8 matrix can significantly enhance the thermal conductivity, κ , of the composites in the direction of the alignment. The anisotropy of $\kappa_{\parallel}/\kappa_{\perp} \sim 19$ is obtained for the composites at room temperature. The importance of anisotropy is for thermal management applications. We observed that the absolute values of κ and $\kappa_{\parallel}/\kappa_{\perp}$ are influenced by the sample preparation method and can be improved by a better alignment of the tubes.

In addition, lamellas of SU8-aligned CNT composites were prepared for proton channeling applications. The successful sample preparation and pioneering channeling experiment give an encouraging outlook for future investigations in this field.

4 Composites with 0D fillers: PMMA-carbon nano-onion composites

4.1 Motivation

The electrical and mechanical properties of the composite materials are directly dependent on the filler properties, including their morphology. So far, we have studied the transport properties of the polymer based composites filled with 2D graphene sheets (RGO) and 1D-carbon nanotubes. To complete these studies and depict a comprehensive portrait of the transport behavior of polymer based composites, in the last part of this work we are using the Onion-Like Carbons (OLCs), as spherical filler particles. The OLC particles were produced in the laboratory of Prof. Vladimir Kuznetsov in Russia [16].

The importance of this study is from a fundamental science point of view, where we monitor the temperature and pressure-dependence of transport properties of Polymer-OLC composites. Indeed, applying the pressure will reduce the inter-particle distance and may influence the transport regime. This project was initiated using SU8 epoxy as the composite matrix, but since its tolerance for applied pressure especially with temperature drop is limited, It was replaced with PMMA, a thermoplastic which is also widely used as a resist in MEMS technology. In the following section, first PMMA will be introduced and then the preparation procedure of the composite as well as the measurement techniques will be briefly mentioned.

4.2 Materials and measurement techniques

PMMA is a thermoplastic with wide industrial applications such as in aircraft glazing, architecture, transportation, and food-handling equipments. As a nontoxic, odorless and tasteless polymer, PMMA has found important applications in medicine and dentures as well [222]. PMMA is a member of the family of polyacrylic and methacrylic esters. Having properties such as exceptional optical clarity, high strength, and excellent dimensional stability [223], PMMA has become a popular resist in microelectronics. In MEMS technology, PMMA is most frequently used as a positive resist for e-beam, x-ray and deep UV lithographic processes. However, it has been shown that PMMA can also be used as a high resolution negative resist as well [224].

In the literature, there have been several reports of PMMA being used as a polymer matrix in composites. PMMA nanocomposites have displayed improved physical performances without a sacrifice, and the potential for reduced gas permeability [223]. PMMA has been used as a host polymer for OLC particles for electromagnetic shielding applications [18] as well. In this project, we have also used PMMA for the preparation of composites containing OLCs, aiming to study of the transport mechanism of electrons through the network of the filler within the matrix, based on the composite structure.

As already mentioned in the previous chapters, the main challenge of the composite preparation is to achieve a high degree of fillers dispersion. In the case of the OLC particles despite using different techniques (pre-dispersion in solvents, use of surfactant, high shear mixing in polymer matrix), we could not obtain a composite containing well-dispersed spherical particles (see section 4.3), neither in SU8 nor in PMMA. We believe that the reason is the aggregation of the onions due to the covalent bonding, which has remained from the production process. In fact, when heat-treating the OLCs powder, we could remove the graphitic layers present in between the onions and improve their dispersity to some extent, but since the covalent bonds stayed intact, they prohibit an efficient dispersion.

The PMMA-OLC composites with different volume fraction of fillers were prepared as follow: In the first step, OLCs were heat treated in a furnace at 400°C for 2 hours, in order to eliminate the graphitic layers present between the onions and functionalize their surface. In the next step, isopropyl alcohol was used for the pre-dispersion of the OLCs. A few drops of IPA (enough to wet the OLC powder) were added to the OLC powder and the suspension was sonicated in a bath for 1 hour. The PMMA solution was added immediately afterwards. The polymer-OLC mixture was stirred for 1 hour followed by probe sonication for 15 minutes. The obtained ink

was deposited on a glass slide and baked on a hotplate at 100°C for 30 minutes. The samples were kept at 50°C over night to assure the complete polymerization of the composite. (This process is similar to the one reported in Ref. [225]. However, the time intervals that we have used are much shorter since the quantities that we have used for the sample preparation were very small.)

The resistivity, σ , of the composites were measured using the standard 4 probe method. The golden wires were attached to the samples by means of carbon paste. The typical dimensions of the samples were about $5\text{mm} \times 2\text{mm} \times 100\mu\text{m}$, however for each sample the geometrical factor was measured and applied for resistivity measurement. The pressure dependence of σ was measured under hydrostatic pressure up to 20 *Kbar*, in a piston cylinder cell, using Daphne oil 7373 as pressure transmitting medium.

4.3 Structural characterization

The microstructure of the composites were analyzed using electron microscopy. As illustrated in the TEM images of Figure 4.1, the dispersion of the OLC fillers is far from being homogeneous: the almost spherical OLCs form local clusters of nearly touching particles, as seen in Figure 4.1a, due to the strong covalent interactions between the OLC fillers. The resulting microstructure of the OLC-PMMA composite is therefore characterized by a strongly non-homogeneous distribution of the conducting particles inside the polymer, which gives rise to ramified regions that are rich in OLC particles interdispersed with regions of almost pure PMMA, as shown in Figure 4.1b.

Similar microstructures are encountered also in other conductor-insulator composites such as conducting polymer blends and ruthenate-glass thick-film resistors (see e.g. [178]). In these systems, the high conductivity at small filler loadings is qualitatively understood in terms of a reduced available volume occupied by the conducting particles: in the regions of enhanced particle occupation the mean interparticle distance is reduced with respect to the case of an homogeneous distribution at equal filler concentrations, which leads to the increase of the tunneling processes between the particles and so to a larger conductivity.

Other mechanisms which may lead to strong spatial variations of the filler concentrations like what is shown in Figure 4.1 may originate from strong effective particle attractions, as in colloidal systems with van der Waals interactions or in polymers with depletants. In the latter case, the interaction is mediated by the depletant polymer particles, which give rise to an effective attraction between the conducting fillers [226].

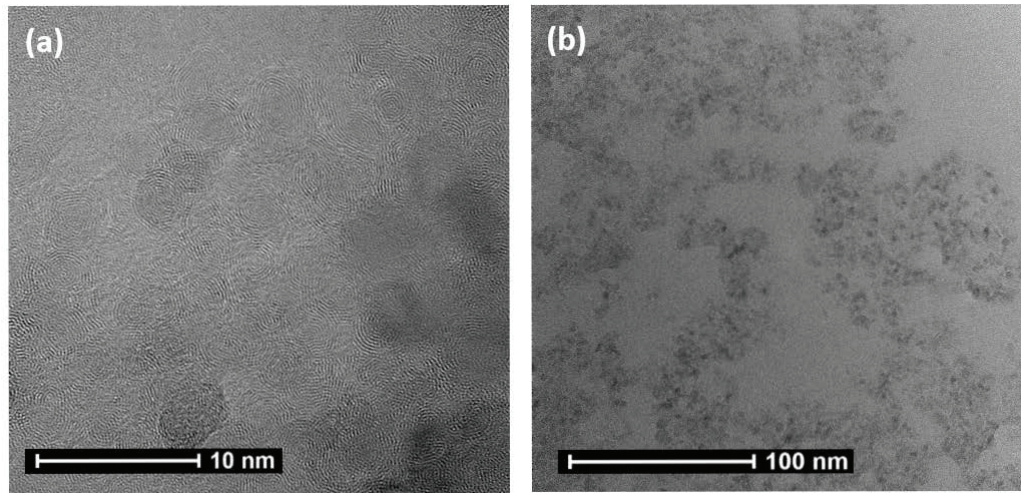


Figure 4.1: TEM images of a OLC-PMMA composite. The image in (a) and shows that the OLCs form clusters of touching or nearly touching particles. The clusters are dispersed in the PMMA matrix giving rise to a non-homogeneous microstructure, as shown in (b).

4.4 Room temperature electrical conductivity

The room temperature electrical conductivity (σ) of OLCs dispersed in PMMA is shown in Figure 4.2 (filled circles) as a function of the OLC volume fraction $\phi = x\rho_{\text{PMMA}}/(\rho_{\text{OLC}} + x\rho_{\text{PMMA}})$, where x is the weight fraction of OLC with respect to the PMMA, and $\rho_{\text{PMMA}} = 1.18 \text{ gm cm}^{-3}$ and $\rho_{\text{OLC}} = 2.25 \text{ gm cm}^{-3}$ are the mass density values of the PMMA and OLC, respectively. There are two interesting features in the conductivity data of Figure 4.2. First, σ decreases by just one order of magnitude as ϕ decreases from $\approx 2\%$ ($x = 4\%$ wt) to $\approx 0.25\%$ ($x = 0.5\%$ wt), which indicates a rather weak dependence of transport upon the filler loading. Second, and more important, the conductivity of OLC-PMMA is comparable or even larger than the conductivity of polymers filled with carbon nanotubes or graphene sheets at similar loadings. This is illustrated in Figure 4.2 where we report the conductivity data of CNT-SU8 (triangles) and RGO-SU8 (squares) nanocomposites [41, 42]. It is well known that the large excluded volume associated with fillers of high aspect-ratios as nanotubes or platelets entails high values of the conductivity even at very small particle loading (see e.g. Ref.[48]). It is therefore surprising that PMMA filled with OLC nanoparticles, which have a unit aspect-ratio due to their quasi-spherical shape, display large values of σ at such small volume fractions. (One should point out that here we are discussing the nominal volume fraction which can be different from the actual one in case of heterogeneous structures. For this reason, comparing the conductivity of homogeneous composites with inhomogeneous ones is difficult.)

The conductivity of OLC-PMMA composites becomes even larger under an applied hydro-

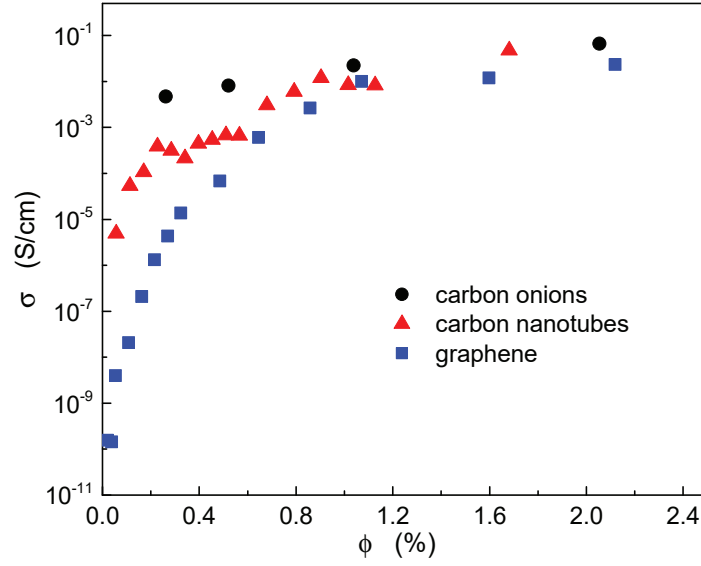


Figure 4.2: Room temperature electrical conductivity of OLC-PMMA composites as a function of the volume fraction ϕ of OLC fillers. The data for the carbon nanotube and graphene dispersed in SU8 composites are taken from Refs. [41] and [42], respectively.

static pressure, as seen in Figure 4.3 where σ is shown as a function of pressure (P) which ranges from ambient pressure up to $P=20$ Kbar. For conductive particles dispersed within an insulating matrix, the increase of σ with P is intuitive. This is so because, in general, the electrical connections between the conducting particles in polymer nanocomposites are established by tunneling of electrons across the thin polymer layer separating the conductive fillers. Since under high pressure the inter-particle distances get reduced, the probability of tunneling of electrons between the conductive fillers increases, which leads to an enhanced bulk conductivity.

To better illustrate the reason of why the conductivity values of OLC-PMMA in Figure 4.2 are remarkably large, let us consider what would be the expected conductivity behavior of conducting spherical particles, like the OLC fillers, dispersed homogeneously within a polymer matrix. The conductivity of the system follows approximately the critical distance approximation [120, 121]:

$$\sigma \approx \sigma_0 \exp\left(-\frac{2\delta_c}{\xi}\right) \quad (4.1)$$

where σ_0 is a conductivity prefactor, ξ is the tunneling decay length, which ranges between a fraction to a few nanometers depending on the nature of the composite constituents, and δ_c is a typical distance between the surfaces of the conducting particles. Within the framework

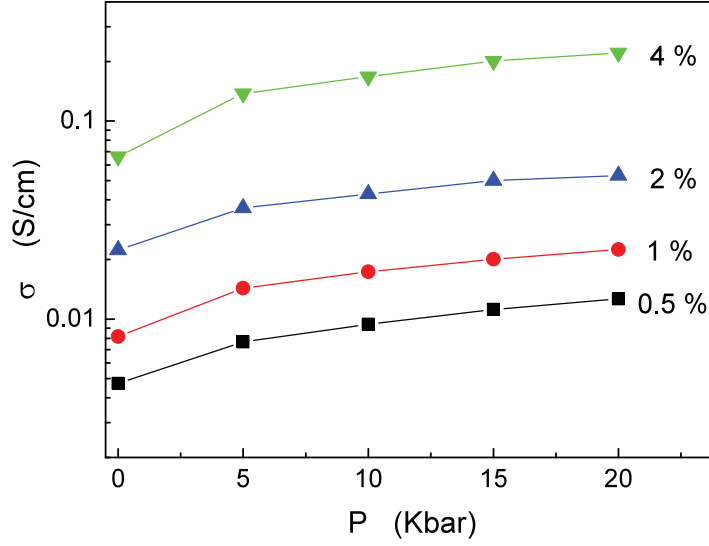


Figure 4.3: Electrical conductivity at room temperature of OLC-PMMA composites as a function of an applied hydrostatic pressure P for different amounts (in %wt) of the OLC particles.

of the continuum percolation, δ_c is identified with the critical distance, that is the minimum inter-particle distance that the electrons have to tunnel in order to establish a system-spanning conductivity [120]. For homogeneous dispersions of spherical particles, δ_c can be approximated by the mean distance between nearest neighboring particles [121]. For the small loadings of Figure 4.2 we can therefore assume that there is in average one particle contained within the volume δ_c^3 centered about a given particle: $\rho\delta_c^3 \approx 1$, where ρ is the number density of the OLCs. Using $\phi = \rho\pi D^3/6$, where D is the diameter of a single OLC particle, we find thus $\delta_c \approx 0.8D/\phi^{1/3}$, which when inserted in Equation 4.1 gives

$$\sigma_{\text{OLC}} \approx \sigma_0 \exp\left(-\frac{1.6D}{\xi\phi^{1/3}}\right) \quad (4.2)$$

For OLC particles with $D \approx 5$ nm and assuming $\xi \approx 1$ nm and $\sigma_0 \approx 0.1$ S cm⁻¹, from the above expression we find $\sigma_{\text{OLC}} \approx 10^{-17}$ S cm⁻¹ for $\phi = 1\%$ at room temperature, which is about 15 orders of magnitude smaller than the measured conductivity at the same volume fraction.

In order to understand the origin of the dramatic difference between the conductivity predicted by Equation 4.2 and the conductivity actually measured in OLC-PMMA nanocomposites, we note that Equation 4.2 rests on the hypothesis that the conducting particles are homogeneously dispersed within the polymer matrix. However, this is not the case for our composites as one can see a notable non-homogeneous dispersion of OLCs in Figure 4.1.

Regardless of the particular mechanism leading to the structures observed in Figure 4.1, the net

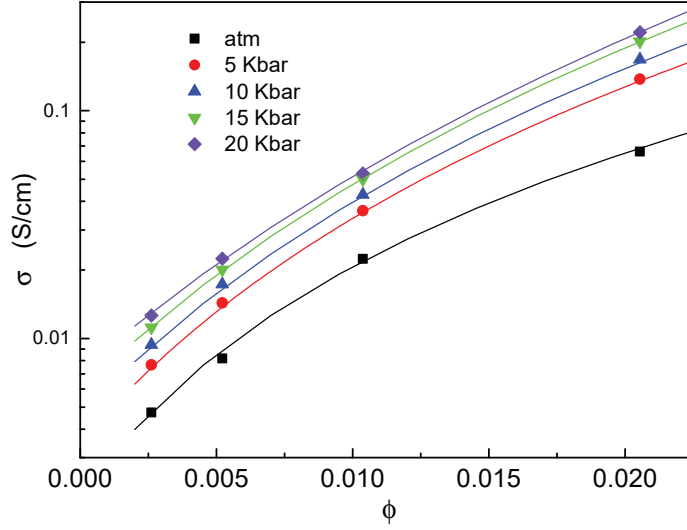


Figure 4.4: Room temperature electrical conductivity of OLC-PMMA composites as a function of OLC volume fraction for different applied pressures. The solid lines are the best fits to Equation 4.3. The fitting parameters are reported in Table 4.1.

effect of the particle clustering is that of forming ramified structures in which the conducting particles nearly touch each other. Let us assume that the set of particles in a close contact governs the overall conductivity and that $\sigma \neq 0$ only if there exists a macroscopic cluster of such particles spanning the entire system. The minimum filler concentration which leads to a percolating cluster of touching particles is known as the critical volume fraction ϕ_c . It is interesting to estimate ϕ_c from the conductivity measurements of OLC-PMMA composites. To this end, we use the percolation formula for the conductivity

$$\sigma \simeq \sigma_0(\phi - \phi_c)^t \quad (4.3)$$

where σ_0 is a prefactor and t is the conductivity transport exponent. In Figure 4.4 we report the fits of Equation 4.3 to the measured conductivity for different values of the hydrostatic pressure P . Although Equation 4.3 formally fits the measured σ for all values of P , the resulting best fitting values for σ_0 , ϕ_c , and t are unphysical, as shown in Table 4.1. We find indeed exceedingly large values of the prefactor σ_0 and of the transport exponent t . More importantly, the percolation threshold ϕ_c is always negative, which is manifestly unphysical.

The results in Table 4.1 indicate clearly that the assumption of percolating clusters of nearly touching particles is inadequate in describing the conductivity of OLC-PMMA composites. As discussed above, also a model based on tunneling between homogeneously dispersed conducting spherical particles is unable to reproduce the experimental results with realistic

Chapter 4. Composites with 0D fillers: PMMA-carbon nano-onion composites

Table 4.1: Values of σ_0 , ϕ_c , and t that best fit the measured conductivity of OLC-PMMA composites.

P (Kbar)	σ_0 (S/cm)	ϕ_c	t
0	3.7×10^2	-0.006	2.4
5	1.3×10^4	-0.01	3.3
10	4.5×10^4	-0.013	3.7
15	1.6×10^5	-0.015	4.1
20	1.2×10^6	-0.02	4.8

values of the microscopic parameters. We have tried to fit the measured σ with a generalized version of Equation 4.1 of the form $\sigma \simeq \sigma_0 \exp(-a/\phi^\alpha)$. This ansatz stems from assuming that the critical distance scales as $\delta_c \propto \phi^{-\alpha}$, where α can take any positive value (a negative value of α is unphysical, as it would imply that δ_c increases when the particle concentration gets bigger). As shown in Figure 4.5, the conductivity data at ambient pressure is increasingly better fitted when α decreases towards values much smaller than the unity. At the moment, however, we lack a solid physical justification for such small α values.

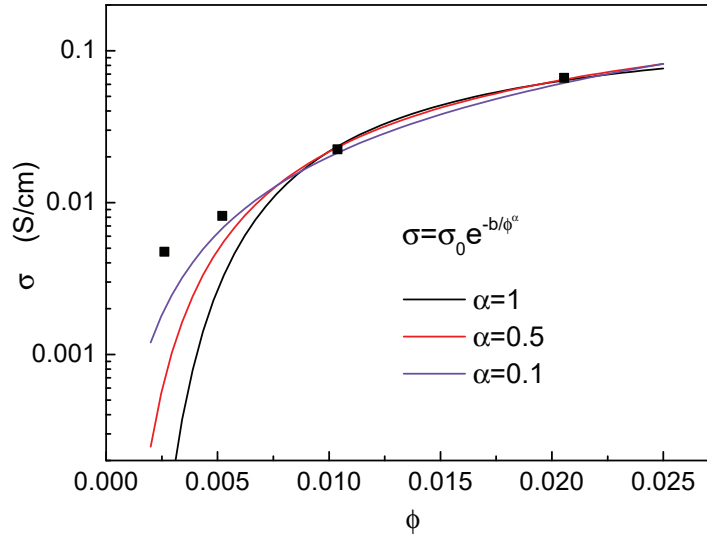


Figure 4.5: Room temperature electrical conductivity of OLC-PMMA composites at ambient pressure (filled squares). The solid lines are fits to $\sigma = \sigma_0 \exp(-b/\phi^\alpha)$. Note that the quality of the fits increases as the value of α diminishes.

4.5 Temperature dependence of the electrical conductivity

The conductivity σ measured as the temperature T ranges between ≈ 6 K and room temperature is plotted in Figure 4.6 for different concentration of the OLC particles. At ambient

4.5. Temperature dependence of the electrical conductivity

pressure, Figure 4.6(a), the low-temperature conductivity for all concentrations follows to a stretched exponential behavior of the form

$$\sigma \propto \exp\left(-\frac{T_0}{T}\right)^\alpha \quad (4.4)$$

where $\alpha = 1/2$ to a very good approximation, while at $P = 20$ Kbar the conductivity displays an activated behavior with $\alpha = 1$. The change of the exponent from $\alpha = 1/2$ to $\alpha = 1$ as P increases to 20 Kbar is gradual, as shown in Figure 4.7 for a sample with 2 %wt of OLC particles. Furthermore, as seen in Table 4.2, the temperature parameter T_0 decreases as P increases. In particular, T_0 is of several hundreds Kelvin at ambient pressure (with some dependence on the OLC concentration), while at $P = 20$ Kbar $T_0 \approx 20$ K with almost no effect of the filler loading.

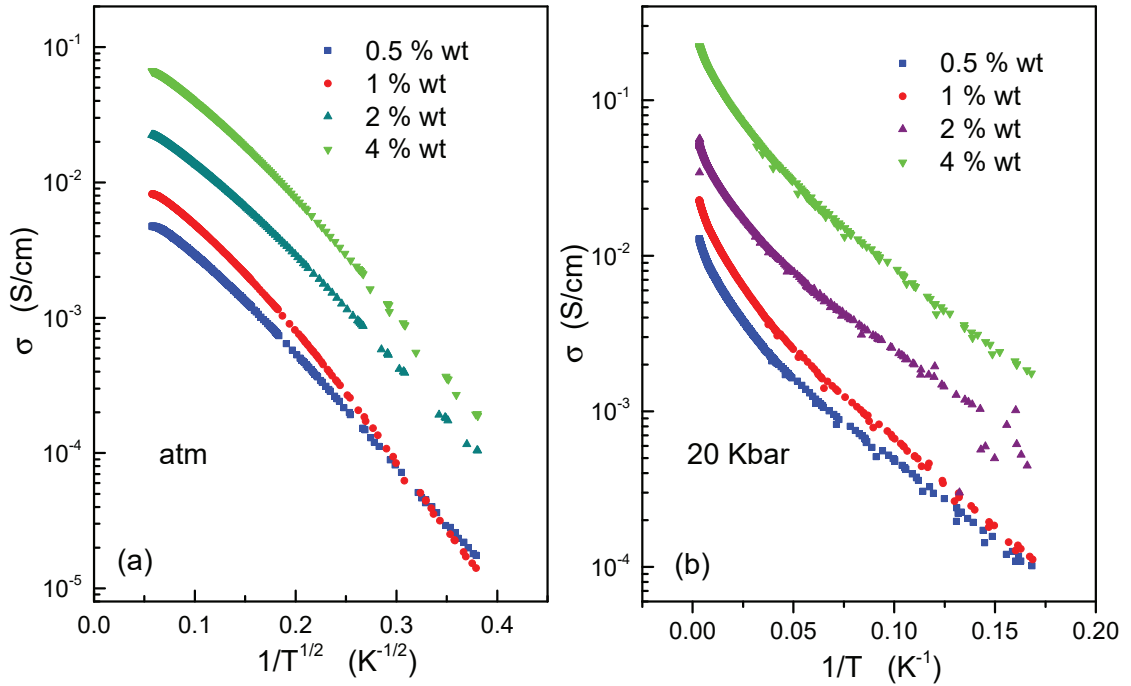


Figure 4.6: Effect of the temperature on the electrical conductivity of OLC-PMMA composites at (a) ambient pressure and at (b) $P = 20$ Kbar. Note that in (a) the conductivity follows the stretched exponential behavior of Equation 4.4 with $\alpha \approx 1/2$, while the data at 20 Kbar (b) have activated behavior.

The behavior of α and T_0 as P changes is best illustrated in the T_0 vs. α plot of Figure 4.8. Interestingly, the data for all concentrations considered seem to collapse into a single curve (dashed line), which indicates that the OLC concentration has only a marginal effect on the evolution of Equation 4.4 with the pressure.

Let us give now a tentative explanation of the effect of pressure on the temperature dependent

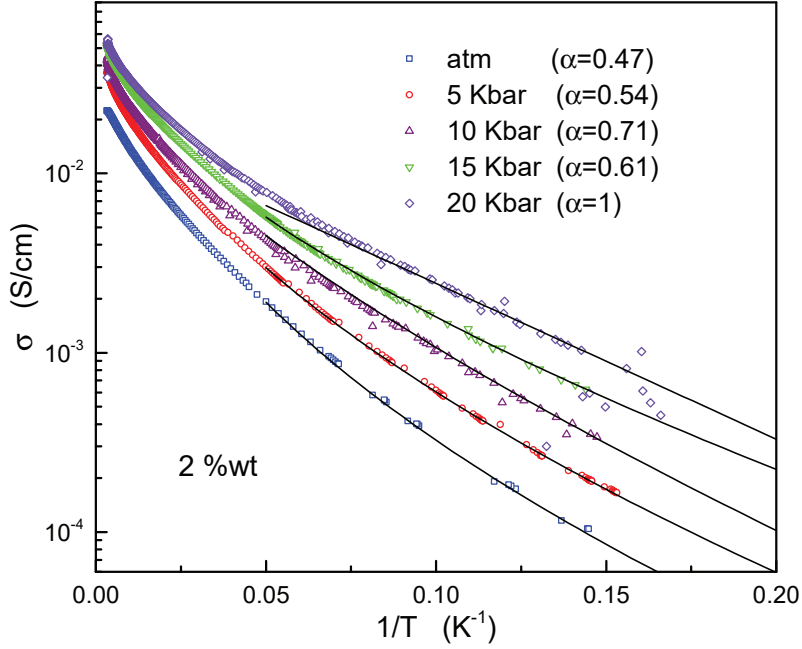


Figure 4.7: Temperature dependence of the electrical conductivity at different values of the applied pressure for a sample with 2 % wt of OLC particles. The solid lines are fits of Equation 4.4 with parameters T_0 and α reported in Table 4.2

behavior of the conductivity. It is well known that Equation 4.4 with $\alpha = 1/2$ describes the conductivity behavior in the Coulomb blockade regime [227, 228, 229]. Tunneling between nearest neighboring particles is suppressed by the Coulomb interaction, so that the electron is forced to hop to farther particles to overcome the Coulomb energy barrier. As we have seen above, the microstructure of our OLC-PMMA composites is characterized by clusters of OLC particles that are in near contact between each other. In this case, a proper discussion of the Coulomb interaction must take into account the effect of the capacitance of the single (quasi-spherical) OLC particles, so that the Coulomb interaction between a pair i and j of particles assumes the form [228]

$$E_C = \frac{e^2}{2\epsilon} \hat{C}_{ij}^{-1}, \quad (4.5)$$

where e is the electron charge, ϵ is the dielectric constant, and \hat{C}^{-1} is the inverse of the capacitance matrix [230]

$$\hat{C} = \begin{pmatrix} C_{ii} & C_{ij} \\ C_{ji} & C_{jj} \end{pmatrix}, \quad (4.6)$$

4.5. Temperature dependence of the electrical conductivity

Table 4.2: Values of α that best fit the measured conductivity of OLC-PMMA composites. The corresponding best fits for T_0 are reported in brackets.

P (Kbar)	0.5 %wt	1 %wt	2 %wt	4 %wt
0	0.45 (711 K)	0.5 (529 K)	0.47 (514 K)	0.52 (321 K)
5			0.54 (205 K)	0.64 (121 K)
10	0.47 (374 K)	0.54 (252 K)	0.71 (63 K)	0.71 (73 K)
15			0.61 (86 K)	0.67 (77 K)
20	1 (23 K)	1 (26 K)	1.1 (20 K)	1 (26 K)

In the following, we shall regard the OLC particles as perfect conductors of identical spherical form (so that $C_{ii} = C_{jj}$ and $C_{ij} = C_{ji}$). In the limiting situation in which the inter-particle center-to-center distance r_{ij} is much larger than the particle diameter D , the diagonal elements of \hat{C} are $C_{ii} = D/2$ while the off-diagonal elements reduce to $C_{ij} \simeq -(D/2)^2/r_{ij}$. At close approach of the two particles i and j , the diagonal and off-diagonal elements of \hat{C} take the following form [230]:

$$C_{ii} \simeq \frac{D}{4} (\ln \sqrt{D/2\delta_{ij}} + \gamma + 2 \ln 2), \quad C_{ij} \simeq -\frac{D}{4} (\ln \sqrt{D/2\delta_{ij}} + \gamma), \quad (4.7)$$

where $\gamma \simeq 0.5772$ and $\delta_{ij} = r_{ij} - D$ is the distance between the surfaces of the two particles. From the inversion of Equation 4.6 and making use of the limiting values of C_{ii} and C_{ij} at $r_{ij} \gg D$ and $r_{ij} = D$ we find

$$\hat{C}_{ij}^{-1} = -\frac{C_{ij}}{C_{ii}^2 - C_{ij}^2} \simeq \begin{cases} 1/r_{ij}, & r_{ij} \gg D \\ 1/(D \ln 2), & r_{ij} = D \end{cases}. \quad (4.8)$$

The above expression can be approximated by the following ansatz $\hat{C}_{ij}^{-1} \simeq (\delta_{ij} + D \ln 2)^{-1}$, so that the Coulomb interaction Equation 4.5 reduces to

$$E_C \simeq \frac{e^2}{2\epsilon(\delta_{ij} + D \ln 2)} \quad (4.9)$$

Let us now consider the rate of hopping of one electron from particle i to particle j . For a given temperature T this is given by

$$\Gamma \simeq e^{-2\delta_{ij}/\xi - E_C/K_B T} \quad (4.10)$$

where K_B is the Boltzmann constant which we take equal to unity in the following. We suppose that at high pressures the set of OLC particles that are relevant for transport are such that

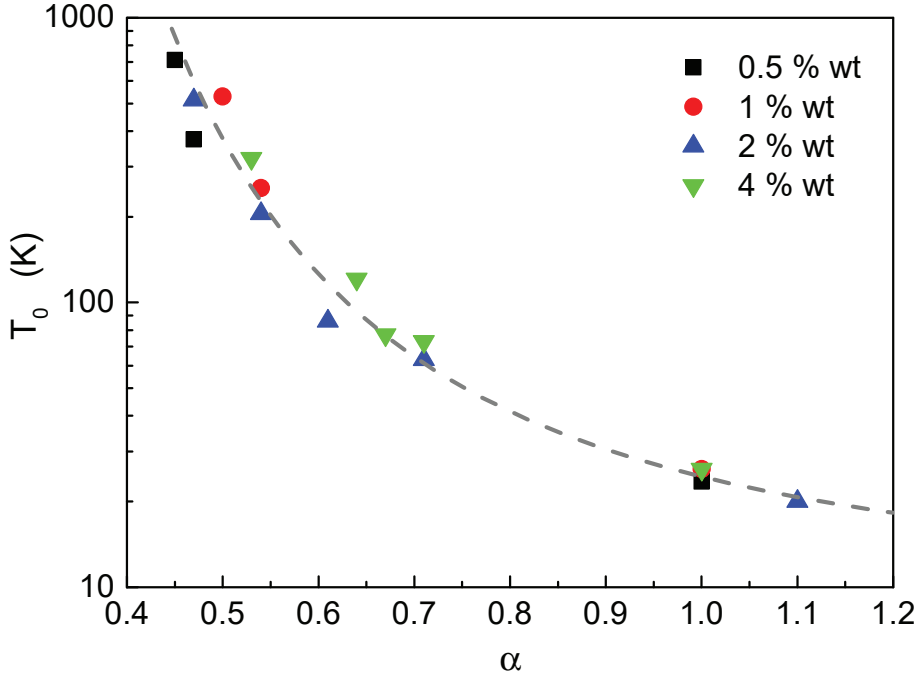


Figure 4.8: T_0 versus α plot. The pressure increases in going from the top-left to the bottom-right. The dashed line is a guide to the eye.

$\delta_{ij} = 0$. From Equation 4.9 and Equation 4.10 we obtain therefore an activated behavior of Γ (and so of σ) of the form $\sigma \approx \gamma \approx \exp(-\Delta/T)$ where

$$\Delta \simeq \frac{e^2}{2\epsilon D \ln 2} \quad (4.11)$$

At ambient pressure, we make the assumption that the interparticle distances are sufficiently dispersed in such a way that the main contribution of γ comes from the value of δ_{ij} such that Equation 4.10 is maximum. We therefore obtain the Coulomb blockade regime $\sigma \approx \gamma \approx \exp(-T_C/T)^{1/2}$ where

$$T_C \simeq \frac{4e^2}{\xi\epsilon} = 8 \ln 2 \frac{D\Delta}{\xi} \quad (4.12)$$

If we identify Δ with T_0 at $P = 20$ Kbar and T_C with T_0 at ambient pressure, from Table 4.2 we find $\Delta \approx 20$ K and, from Equation 4.12 and using $D \approx 5$ nm, $T_C \approx 554$ K. Although this value for T_C is in fair good agreement with the T_0 values at ambient pressure reported in Table 4.2 and in Figure 4.8, the analysis presented here is only qualitative. A more refined theory should take into account the (moderate) effect of the OLC concentration at ambient pressure and, more importantly, should be able to describe in a unified manner the dependence upon

concentration, pressure and temperature. At present, due to the difficulty of modeling the non-homogeneous dispersion of our OLC-PMMA composites and its effect on the transport properties, we do not have such unified picture.

4.6 Conclusion

In this section, we reported the preparation and transport property measurements of PMMA-OLC composites. Strong non-homogeneity of the filler dispersion was observed in the microstructure of the composites. This is most probably due to the unbreakable aggregations of the onions with covalent bondings, which have remained from their production process.

The first unexpected feature visible in the measurements of these composites is their surprisingly high electrical conductivity, which is even larger than the conductivity of polymers containing RGOs and CNTs. The conductivity becomes even larger under applied hydrostatic pressure, owing to the decrease in inter-particle distances. In addition, the dependence of transport upon the filler loading is rather weak. We attribute these behaviors to heterogeneity of the composites structure. These experimental results cannot be explained neither by percolation nor by tunneling between homogeneously dispersed particles.

We also have studied the temperature dependent transport properties at ambient and under high pressure. We suppose that at high pressure an activated behavior of conductivity is the dominant mechanism, while at ambient pressure the coulomb blockade regime governs.

At the moment, due to the complexity of modeling the heterogeneous structure of PMMA-OLC composites, we do not have a unified picture for the conductivity dependence upon OLCs concentration, pressure and temperature.

5 Conclusions and outlook

This dissertation displays four years of my research on polymer-carbon nanostructure composites. It represents a multidisciplinary endeavor where not only material science but chemistry and a broad arsenal of physical measurements, theoretical modellings were involved. The goal was to better understand the art of making good, not to say exceptional, but at least original composites based on carbon nanostructures and SU8 epoxy. I am confident that this dissertation, and the accompanying publications, testify a decent contribution to this field. I have to mention that although it is my doctoral dissertation, by no means it is a one-man-show, as it is the case for research in general. I was fully integrated in a research team, and fully supported by my supervisors and associated collaborators. The highlights (with all my modesty) of my work are listed below.

The matrix of interest is the SU8 epoxy. This material is in use in many fields starting with microfluidics, biology to military applications. It can polymerize with UV illumination or with thermal treatment. The problem with this epoxy is that it is brittle, electrically and thermally it is an insulator. Carbon nanostructures as additive can improve its properties nevertheless they have to keep its ability to polymerize, the ease towards processibility. As the first highlight of my work, it was figured out that the surface functional groups on graphene or on carbon nanotubes can assist the opening of the epoxy rings by forming covalent bonds between the fillers and the epoxy. It was confirmed by the means of FTIR and Raman spectroscopy. This finding has not been reported before.

The property of the composites that is studied the most in the literature, probably because it seems to be the easiest, is the electrical conductivity. It is considered that by improving the charge transport in the matrix, usually half of the job is done, because it prevents the building up of static charges, it can screen electromagnetic radiation, it could be used for electrodes

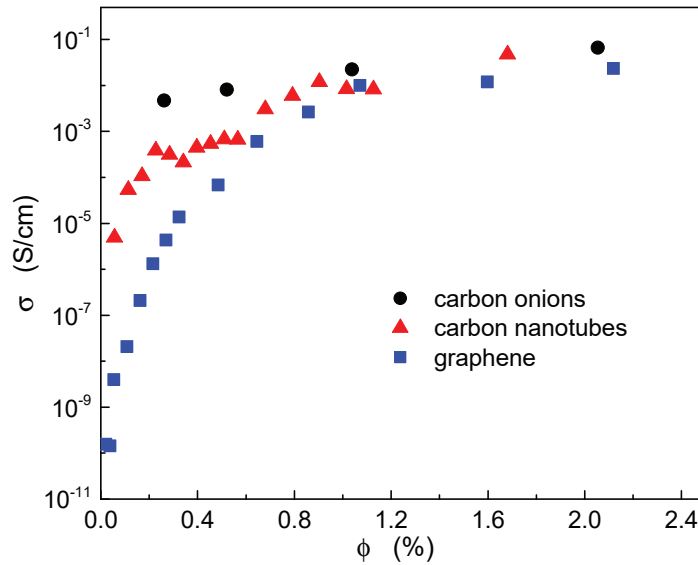


Figure 5.1: Room temperature electrical conductivity of polymer composites containing various types carbon nanofillers as a function of the volume fraction ϕ of OLC fillers.

etc. However, it looks easy to do it in a controlled way just at the first sight. If one wants to do it right, it is more difficult because one has to understand the detailed mechanism of the percolated conduction of various forms of carbon nanofillers, their threshold etc. We did a very detailed study of graphene (2D), carbon nanotubes (1D) and carbon onions (0D) nanofillers in the insulating matrix. The key requirement of these nano-objects is the dispersivity and their rigidity to keep their form in the matrix because the conduction threshold strongly depends on the shape of the filler. Strange enough, but resistivity measurements as a function of filler concentration served us to have some prediction about the morphology of the fillers. In fact, inside the composites the graphene flakes are flexible and crumpled, the long nanotubes curl and may form rings, and the onions are covalently interconnected, so they show the characteristics of 1D fillers. These will affect the transport properties of the composites which could be nicely read from Figure 5.1, where all 3 nano-objects conductivity is plotted as a function of their concentration in an insulating matrix. From now on we can, we could, and we should design better fillers and their concentration in the desired conductivity range of the composites.

Beyond the traditional randomly dispersed composites, we have reported the preparation of the aligned CNT-SU8 composites with enhanced anisotrope thermal conductivity in the direction of tubes alignment. Synthesis of such composites at wafer scales can offer a perspective for various possible applications. One is in the field of large density data storage using magnetic particles. A substrate consisting of oriented CNTs-SU8 composite would evacuate

the unwanted heat to the thermal bath and not laterally due to its high anisotropy in thermal conductivity.

An important direction in the preparation of such composites is the use of oriented carpets of carbon nanotubes and impregnate them with SU8. One possibility for using them is in thermal management, for the efficient cooling of radiation detectors, e.g. at CERN. The oriented carbon nanotubes could evacuate heat in a very efficient way (much better than randomly dispersed nanotubes) and SU8 is highly resistant to radiation, which is an important parameter in environment with energetic particles.

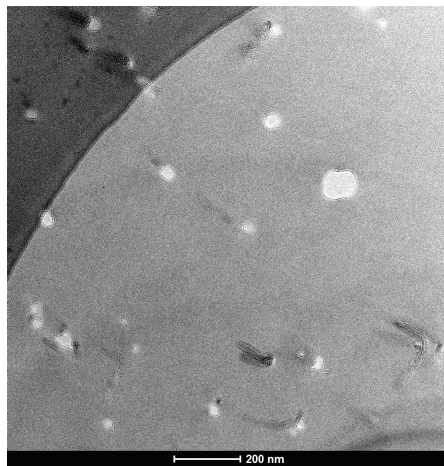


Figure 5.2: SU8-CNT membrane prepared with ultramicrotomy for proton channeling application. the CNT channels have the length of 50 *nm* and diameter of 10-30 *nm*.

A more ambitious possible application of these composites could be the channeling of the charged particles through the array of the nanotubes embedded in SU8 for e.g. production of ultra-stable low emittance beams for medical and biological applications. For example, short carbon nanotubes channel, if it were available, could focus protons as good as magnetic field of 1000 Tesla. Nowadays, with the advance of the synthesis of well-ordered carbon nanotubes this is becoming a real possibility.

We have successfully prepared the membranes of oriented CNTs-SU8 composites with the hole diameter of 10-30 *nm* (diameter of the tubes) with ultramicrotomy technique (shown in Figure 5.2). The channeling distance could be tuned according to the thickness of the lamella. Our preliminary experiments of proton channeling could be a head start for future studies in this direction. This brings us to the outlook, to future directions for composites. We feel that the community should go for advanced structures like the membranes shown in Figure 5.2. Another goal could be to develop the water desalination filters. Functionalizing of the inner

Chapter 5. Conclusions and outlook

walls of the CNT channels could selectively impeach the transport of chlorine or sodium ions. For example, oxidation of the inner surface could exclude the passage of Cl^- , while amine functionalization in a subsequent filter could stop the Na^+ . Since the sp^2 bonded carbon chemistry is quite difficult the bonds could be opened by electron irradiation (this could help the crosslinking of the polymer and carbon nanotubes, as well) and react with the appropriate functional groups. This process could be advantageous over complex and less controllable chemical procedures.

We believe that this and similar ideas, where one goes beyond the traditional composite preparation could represent an exciting field of research in the future and could have high impact in our society.

A Statistical analysis of the nanotube lengths

A.1 Distribution of the length for as-milled CNTs

We have performed graphic probability analyses of the nanotube lengths L measured from SEM images of the five CNT batches denoted Long, M_1 , M_2 , M_3 , and Short. Each set is obtained by a specific combination of the milling time and of the rotational speed, as indicated in Figure A.1 of the main paper. In Figure A.1 we plot the empirical data (empty circles) against a lognormal (left column) and a Weibull distribution (right column). The solid lines denote the corresponding theoretical probabilities. For all five batches, the data are best fitted by a lognormal distribution of the lengths.

A.2 CNTs with bimodal distribution of lengths

We produced CNTs with bimodal distributions of the nanotube lengths by mixing the Long and Short batches of the as-milled CNTs with chosen values of the number fraction $p = N_{\text{Long}}/(N_{\text{Long}} + N_{\text{Short}})$, where N_{Long} and N_{Short} are the number of the Long and Short nanotubes, respectively. In practice, for a given value of p we took the weight ratio of the Long nanotubes over the Short nanotubes such that

$$\frac{M_{\text{Long}}}{M_{\text{Short}}} = \frac{N_{\text{Long}}\langle L \rangle_{\text{Long}}}{N_{\text{Short}}\langle L \rangle_{\text{Short}}} = \frac{p}{1-p} \frac{\langle L \rangle_{\text{Long}}}{\langle L \rangle_{\text{Short}}},$$

where $\langle L \rangle_{\text{Long}} \simeq 2277$ nm and $\langle L \rangle_{\text{Short}} \simeq 590$ nm are the mean nanotube lengths measured from the Long and Short CNT batches, respectively. Figure A.2 shows the cumulative distribution function (CDF) of the nanotube lengths for $p = 0.2$ ($M_{\text{Long}}/M_{\text{Short}} \simeq 0.965$) obtained from 510 values of L measured from SEM images (red line). The measured CDF agrees well with the

Appendix A. Statistical analysis of the nanotube lengths

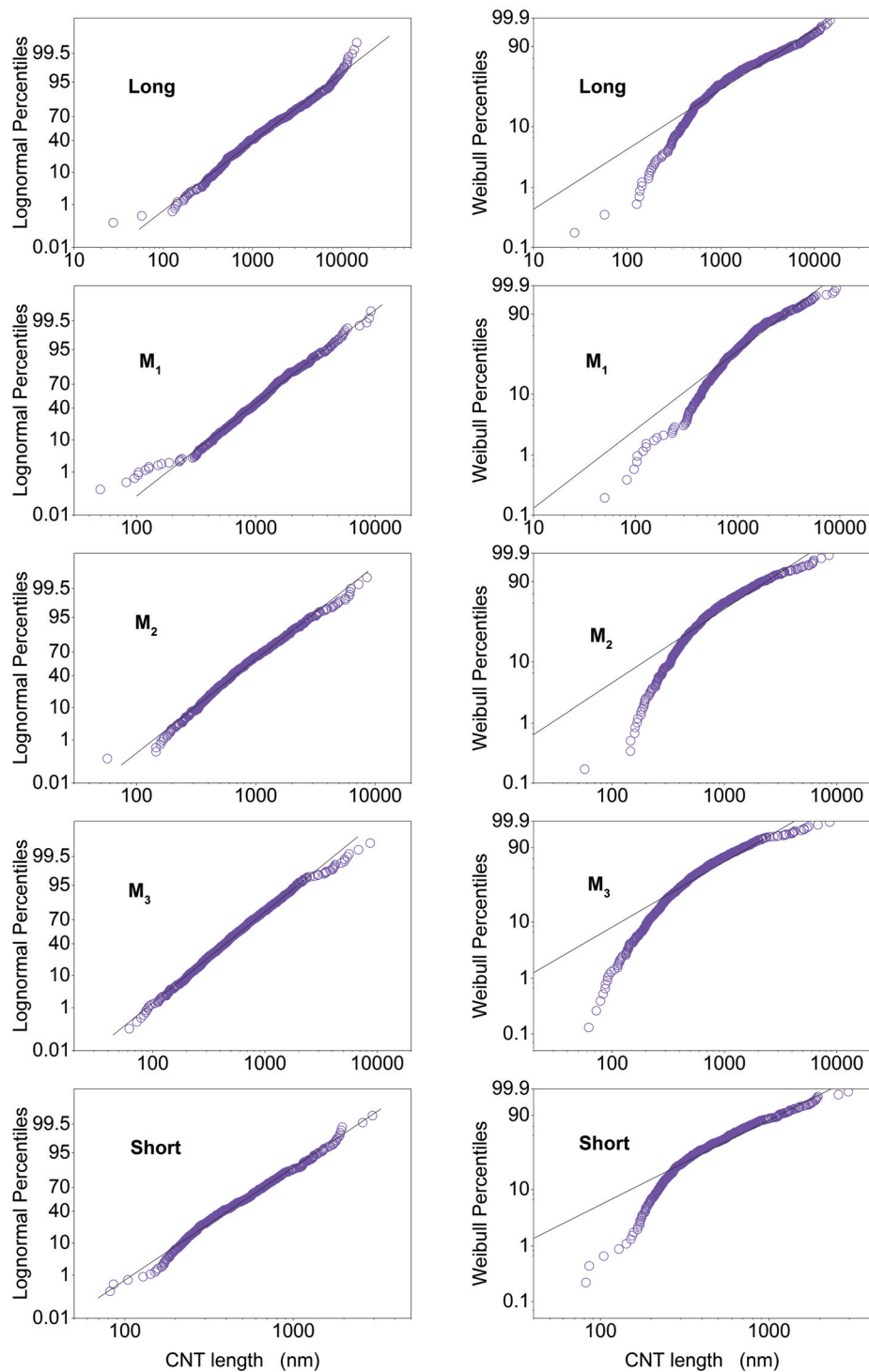


Figure A.1: Probability plots of the measured CNT lengths for five different batches obtained from chosen combinations of the milling time and the rotational speed. The probabilities are plotted assuming a lognormal distribution (left column) and a Weibull distribution (right column). The solid lines indicate the corresponding theoretical probabilities.

A.2. CNTs with bimodal distribution of lengths

expected CDF of a bimodal distribution for the same value of p (blue line).

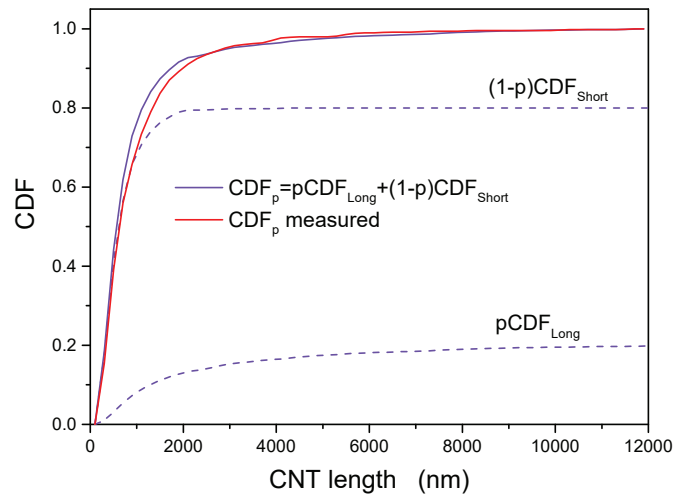


Figure A.2: Comparison between the calculated and the measured cumulative distribution functions (CDFs) of the bimodal distribution of CNT lengths for $p = 0.2$. The dashed curves are the partial contributions of the measured CDFs of the Long and Short batches.

Bibliography

- [1] E. T. Thostenson, C. Li, and T. W. Chou, "Nanocomposites in context," *Composites Science and Technology*, vol. 65, no. 3-4, pp. 491–516, 2005.
- [2] J. R. Potts, D. R. Dreyer, C. W. Bielawski, and R. S. Ruoff, "Graphene-based polymer nanocomposites," *Polymer*, vol. 52, pp. 5–25, jan 2011.
- [3] T. Ramanathan, A. A. Abdala, S. Stankovich, D. A. Dikin, M. Herrera-Alonso, R. D. Piner, D. H. Adamson, H. C. Schniepp, X. Chen, R. S. Ruoff, S. T. Nguyen, I. A. Aksay, R. K. Prud'homme, and L. C. Brinson, "Functionalized graphene sheets for polymer nanocomposites.," *Nature Nanotechnology*, vol. 3, no. 6, pp. 327–331, 2008.
- [4] G. Pandey and E. T. Thostenson, "Carbon Nanotube-Based Multifunctional Polymer Nanocomposites," *Polymer Reviews*, vol. 52, no. 3-4, pp. 355–416, 2012.
- [5] A. Geim and K. Novoselov, "The rise of graphene.," *Nat. Mater.*, pp. 183–191, 2007.
- [6] K.-H. Kim, J. L. Ong, and O. Okuno, "The effect of filler loading and morphology on the mechanical properties of contemporary composites," *The Journal of Prosthetic Dentistry*, vol. 87, pp. 642–649, jun 2002.
- [7] K. S. Novoselov, A. K. Geim, S. V. Morozov, D. Jiang, Y. Zhang, S. V. Dubonos, I. V. Grigorieva, and A. A. Firsov, "Electric field effect in atomically thin carbon films.," *Science (New York, N.Y.)*, vol. 306, pp. 666–9, oct 2004.
- [8] S. Stankovich, D. A. Dikin, G. H. B. Dommett, K. M. Kohlhaas, E. J. Zimney, E. A. Stach, R. D. Piner, S. T. Nguyen, and R. S. Ruoff, "Graphene-based composite materials," *Nature*, vol. 442, pp. 282–286, jul 2006.
- [9] H. Kim, A. A. Abdala, and C. W. Macosko, "Graphene/Polymer Nanocomposites," *Macromolecules*, vol. 43, pp. 6515–6530, aug 2010.

Bibliography

- [10] W. S. Hummers and R. E. Offeman, "Preparation of Graphitic Oxide," *Journal of the American Chemical Society*, vol. 80, no. 6, pp. 1339–1339, 1958.
- [11] S. Park, R. S. Ruoff, and M. Engineering, "Chemical methods for the production of graphenes.," *Nat. Nanotechnol.*, vol. 4, no. 4, pp. 217–224, 2009.
- [12] I. K. Moon, J. Lee, R. S. Ruoff, and H. Lee, "Reduced graphene oxide by chemical graphitization," *Nature Communications*, vol. 1, no. 6, p. 73, 2010.
- [13] E. Thostenson, "Advances in the science and technology of carbon nanotubes and their composites: a review," *Composites Science and Technology*, vol. 61, pp. 1899–1912, oct 2001.
- [14] E. T. Thostenson and T.-W. Chou, "On the elastic properties of carbon nanotube-based composites: modelling and characterization," *Journal of Physics D: Applied Physics*, vol. 36, pp. 573–582, mar 2003.
- [15] M. MIONIC, A. MAGREZ, L. FORRO, M. JIGUET, Sébastien, M. P. JUDELEWICZ, and T. STORA, "CARBON NANOTUBES NANOCOMPOSITES FOR MICROFABRICATION APPLICATIONS," 2011.
- [16] V. L. Kuznetsov, A. L. Chuvilin, Y. V. Butenko, I. Yu Mal, and V. M. Titov, "Onion-like carbon from ultra-disperse diamond," *Chemical Physics Letters*, vol. 222, pp. 343–348, 1994.
- [17] J. Macutkevic, I. Kranauskaite, J. Banyas, S. Moseenkov, V. Kuznetsov, and O. Shenderova, "Metal-insulator transition and size dependent electrical percolation in onion-like carbon/polydimethylsiloxane composites," *Journal of Applied Physics*, vol. 115, no. 21, 2014.
- [18] P. P. Kuzhir, A. G. Paddubskaya, S. A. Maksimenko, V. L. Kuznetsov, S. Moseenkov, A. I. Romanenko, O. A. Shenderova, J. MacUtkevic, G. Valu??is, and P. Lambin, "Carbon onion composites for EMC applications," *IEEE Transactions on Electromagnetic Compatibility*, vol. 54, no. 1, pp. 6–16, 2012.
- [19] P. Ganesh, P. R. C. Kent, and V. Mochalin, "Formation, characterization, and dynamics of onion-like carbon structures for electrical energy storage from nanodiamonds using reactive force fields," *Journal of Applied Physics*, vol. 110, no. 7, 2011.
- [20] V. L. Kuznetsov, Y. V. Butenko, A. L. Chuvilin, A. I. Romanenko, and A. V. Okotrub, "Electrical resistivity of graphitized ultra-disperse diamond and onion-like carbon," *Chemical Physics Letters*, vol. 336, no. 5-6, pp. 397–404, 2001.

- [21] A. del Campo and C. Greiner, "SU-8: a photoresist for high-aspect-ratio and 3D sub-micron lithography," *Journal of Micromechanics and Microengineering*, vol. 17, no. 6, pp. R81–R95, 2007.
- [22] M. Heuschkel, L. Guérin, B. Buisson, D. Bertrand, and P. Renaud, "Buried microchannels in photopolymer for delivering of solutions to neurons in a network," *Sensors and Actuators B: Chemical*, vol. 48, pp. 356–361, may 1998.
- [23] H. Lorenz, M. Despont, N. Fahrni, N. LaBianca, P. Renaud, and P. Vettiger, "SU-8: a low-cost negative resist for MEMS," *Journal of Micromechanics and Microengineering*, vol. 7, pp. 121–124, sep 1997.
- [24] K. Y. Lee, "Micromachining applications of a high resolution ultrathick photoresist," *Journal of Vacuum Science & Technology B: Microelectronics and Nanometer Structures*, vol. 13, p. 3012, nov 1995.
- [25] A. Olziersky, P. Barquinha, A. Vila, L. Pereira, G. Goncalves, E. Fortunato, R. Martins, and J. R. Morante, "Insight on the SU-8 resist as passivation layer for transparent Ga[sub 2]O[sub 3]–In[sub 2]O[sub 3]–ZnO thin-film transistors," *Journal of Applied Physics*, vol. 108, no. 6, p. 064505, 2010.
- [26] P. Abgrall, V. Conedera, H. Camon, A. M. Gue, and N. T. Nguyen, "SU-8 as a structural material for labs-on-chips and microelectromechanical systems (review)," *Electrophoresis*, vol. 28, no. 24, pp. 4539–4551, 2007.
- [27] M. Thiel, M. S. Rill, G. Von Freymann, and M. Wegener, "Three-dimensional bi-chiral photonic crystals," *Advanced Materials*, vol. 21, no. 46, pp. 4680–4682, 2009.
- [28] S. Jiguet, M. Judelewicz, S. Mischler, A. Bertch, and P. Renaud, "Effect of filler behavior on nanocomposite SU8 photoresist for moving micro-parts," *Microelectronic Engineering*, vol. 83, pp. 1273–1276, apr 2006.
- [29] H. Moser and C. Rockstuhl, "3D THz metamaterials from micro/nanomanufacturing," *Laser & Photonics Reviews*, vol. 6, pp. 219–244, apr 2012.
- [30] P. HAMMOND, "Encapsulation of a liquid-sensing microchip using SU-8 photoresist," *Microelectronic Engineering*, vol. 73-74, pp. 893–897, jun 2004.
- [31] M. Joshi, N. Kale, R. Lal, V. Ramgopal Rao, and S. Mukherji, "A novel dry method for surface modification of SU-8 for immobilization of biomolecules in Bio-MEMS," *Biosensors and Bioelectronics*, vol. 22, pp. 2429–2435, may 2007.

Bibliography

- [32] J. Ransley, M. Watari, D. Sukumaran, R. McKendry, and A. Seshia, "SU8 bio-chemical sensor microarrays," *Microelectronic Engineering*, vol. 83, pp. 1621–1625, apr 2006.
- [33] E. Koukharenko, M. Kraft, G. J. Ensell, and N. Hollinshead, "A comparative study of different thick photoresists for MEMS applications," *Journal of Materials Science: Materials in Electronics*, vol. 16, no. 11-12, pp. 741–747, 2005.
- [34] S. Jiguet, A. Bertsch, H. Hofmann, and P. Renaud, "Conductive SU8 photoresist for microfabrication," *Advanced Functional Materials*, vol. 15, no. 9, pp. 1511–1516, 2005.
- [35] H. C. Chiamori, J. W. Brown, E. V. Adhiprakasha, E. T. Hantsoo, J. B. Straalsund, N. A. Melosh, and B. L. Pruitt, "Suspension of nanoparticles in SU-8: Processing and characterization of nanocomposite polymers," *Microelectronics Journal*, vol. 39, no. 2, pp. 228–236, 2008.
- [36] N. Damean, B. A. Parviz, J. N. Lee, T. Odom, and G. M. Whitesides, "Composite ferromagnetic photoresist for the fabrication of microelectromechanical systems," *Journal of Micromechanics and Microengineering*, vol. 15, pp. 29–34, jan 2005.
- [37] M. Mionić, S. Jiguet, M. Judelewicz, L. Forró, and A. Magrez, "Preparation and characterization of SU8-carbon nanotube composites," *physica status solidi (b)*, vol. 246, pp. 2461–2464, dec 2009.
- [38] A. Magrez, J. W. Seo, C. Mikó, K. Hernádi, and L. Forró, "Growth of Carbon Nanotubes with Alkaline Earth Carbonate as Support," *The Journal of Physical Chemistry B*, vol. 109, pp. 10087–10091, may 2005.
- [39] A. Magrez, J. W. Seo, V. L. Kuznetsov, and L. Forró, "Evidence of an Equimolar C₂H₂–CO₂ Reaction in the Synthesis of Carbon Nanotubes," *Angewandte Chemie International Edition*, vol. 46, pp. 441–444, jan 2007.
- [40] N. Zhang, J. Xie, M. Guers, and V. K. Varadan, "Chemical bonding of multiwalled carbon nanotubes to polydimethylsiloxanes and modification of the photoinitiator system for microstereolithography processing," *Smart Materials and Structures*, vol. 13, pp. N1–N4, feb 2004.
- [41] C. Grimaldi, M. Mionić, R. Gaal, L. Forró, and A. Magrez, "Electrical conductivity of multiwalled carbon nanotubes-SU8 epoxy composites," *Applied Physics Letters*, vol. 102, jun 2013.

-
- [42] M. Majidian, C. Grimaldi, A. Pisoni, L. Forró, and A. Magrez, “Electrical conduction of photo-patternable SU8–graphene composites,” *Carbon*, vol. 80, pp. 364–372, dec 2014.
- [43] L. J. Huijbregts, *Charge transport and morphology in nanofillers and polymer nanocomposites proefschrift door*. 2008.
- [44] D. Stauffer and A. Aharony, *Introduction to percolation theory*. CRC press, 1992.
- [45] M. Sahimi, *Heterogeneous materials. I, Linear transport and optical properties*. Springer, 2003.
- [46] M. D, B. M, and N. R, “Electrical Resistivity of Composites,” *Journal of the American Ceramic Society*, vol. 73, no. 8, pp. 2187–2203, 1990.
- [47] I. Balberg, “The importance of bendability in the percolation behavior of carbon nanotube and graphene-polymer composites,” *Journal of Applied Physics*, vol. 112, no. 6, pp. 10–13, 2012.
- [48] I. Balberg, C. H. Anderson, S. Alexander, and N. Wagner, “Excluded volume and its reation to the onset of percolation,” *Physical Review B*, vol. 30, no. 7, pp. 3933–3943, 1984.
- [49] A. Celzard, E. McRae, C. Deleuze, M. Dufort, G. Furdin, and J. Marêché, “Critical concentration in percolating systems containing a high-aspect-ratio filler,” *Physical Review B*, vol. 53, no. 10, pp. 6209–6214, 1996.
- [50] N. F. N. F. Mott and E. A. E. A. Davis, *Electronic processes in non-crystalline materials*. Oxford University Press, 2012.
- [51] A. Miller and E. Abrahams, “Impurity Conduction at Low Concentrations,” *Physical Review*, vol. 120, pp. 745–755, nov 1960.
- [52] J. N. Coleman, U. Khan, W. J. Blau, and Y. K. Gunko, “Small but strong: A review of the mechanical properties of carbon nanotube–polymer composites,” *Carbon*, vol. 44, pp. 1624–1652, aug 2006.
- [53] Z. Spitalsky, D. Tasis, K. Papagelis, and C. Galiotis, “Carbon nanotube-polymer composites: Chemistry, processing, mechanical and electrical properties,” *Progress in Polymer Science (Oxford)*, vol. 35, no. 3, pp. 357–401, 2010.
- [54] C. Lee, X. Wei, J. W. Kysar, and J. Hone, “Measurement of the Elastic Properties and Intrinsic Strength of Monolayer Graphene,” *Science*, vol. 321, pp. 385–388, jul 2008.

Bibliography

- [55] C. Gómez-Navarro, J. C. Meyer, R. S. Sundaram, A. Chuvilin, S. Kurasch, M. Burghard, K. Kern, and U. Kaiser, "Atomic structure of reduced graphene oxide," *Nano Letters*, vol. 10, no. 4, pp. 1144–1148, 2010.
- [56] M. L. Manchado, L. Valentini, J. Biagiotti, and J. Kenny, "Thermal and mechanical properties of single-walled carbon nanotubes–polypropylene composites prepared by melt processing," *Carbon*, vol. 43, pp. 1499–1505, jun 2005.
- [57] M. A. Rafiee, J. Rafiee, Z. Wang, H. Song, Z. Z. Yu, and N. Koratkar, "Enhanced mechanical properties of nanocomposites at low graphene content," *ACS Nano*, vol. 3, no. 12, pp. 3884–3890, 2009.
- [58] H. L. Cox, "The elasticity and strength of paper and other fibrous materials," *British Journal of Applied Physics*, vol. 3, pp. 72–79, mar 1952.
- [59] G. Carman and K. Reifsnider, "Micromechanics of short-fiber composites," *Composites Science and Technology*, vol. 43, pp. 137–146, jan 1992.
- [60] J. N. Coleman, M. Cadek, R. Blake, V. Nicolosi, K. P. Ryan, C. Belton, A. Fonseca, J. B. Nagy, Y. K. Gun'ko, and W. J. Blau, "High Performance Nanotube-Reinforced Plastics: Understanding the Mechanism of Strength Increase," *Advanced Functional Materials*, vol. 14, pp. 791–798, aug 2004.
- [61] J. C. Halpin, S. Louis, and J. L. Kardos, "The Halpin-Tsai Equations: A Review," *Polym Eng Sci*, vol. 16, no. 5, pp. 344–352, 1976.
- [62] R. Hill, "Theory of mechanical properties of fibre-strengthened materials: I. Elastic behaviour," *Journal of the Mechanics and Physics of Solids*, vol. 12, pp. 199–212, sep 1964.
- [63] P. May, U. Khan, A. O'Neill, and J. N. Coleman, "Approaching the theoretical limit for reinforcing polymers with graphene," *J. Mater. Chem.*, vol. 22, no. 4, pp. 1278–1282, 2012.
- [64] A. Majumdar, "Microscale transport phenomena," in *Handbook of heat transfer* (W. M. Rohsenow, J. R. Hartnett, and Y. I. Cho, eds.), vol. 1, New York: McGraw-Hill, 1998.
- [65] Y. Agari, A. Ueda, Y. Omura, and S. Nagai, "Thermal diffusivity and conductivity of PMMA/PC blends," *Polymer*, vol. 38, pp. 801–807, feb 1997.
- [66] C. Yu, L. Shi, Z. Yao, D. Li, and A. Majumdar, "Thermal Conductance and Thermopower of an Individual Single-Wall Carbon Nanotube," *Nano Letters*, vol. 5, pp. 1842–1846, sep 2005.

-
- [67] P. Kim, L. Shi, A. Majumdar, and P. L. McEuen, "Thermal Transport Measurements of Individual Multiwalled Nanotubes," *Physical Review Letters*, vol. 87, p. 215502, oct 2001.
- [68] Z. Han and A. Fina, "Thermal conductivity of carbon nanotubes and their polymer nanocomposites: A review," *Progress in Polymer Science*, vol. 36, pp. 914–944, jul 2011.
- [69] D. M. Bigg, "Thermal conductivity of heterophase polymer compositions," in *Thermal and Electrical Conductivity of Polymer Materials*, pp. 1–30, Berlin/Heidelberg: Springer-Verlag, 1995.
- [70] H. ZHOU, S. ZHANG, and M. YANG, "The effect of heat-transfer passages on the effective thermal conductivity of high filler loading composite materials," *Composites Science and Technology*, vol. 67, pp. 1035–1040, may 2007.
- [71] J. Zeng, R. Fu, S. Agathopoulos, S. Zhang, X. Song, and H. He, "Numerical Simulation of Thermal Conductivity of Particle Filled Epoxy Composites," *Journal of Electronic Packaging*, vol. 131, no. 4, p. 041006, 2009.
- [72] J. Wang, J. K. Carson, M. F. North, and D. J. Cleland, "A new structural model of effective thermal conductivity for heterogeneous materials with co-continuous phases," *International Journal of Heat and Mass Transfer*, vol. 51, pp. 2389–2397, may 2008.
- [73] Y.-T. Chen and D. Lee, "A bonding technique using hydrophilic SU-8," *Journal of Micromechanics and Microengineering*, vol. 17, no. 10, pp. 1978–1984, 2007.
- [74] V. Kumar and N. N. Sharma, "Synthesis of hydrophilic to superhydrophobic SU8 surfaces," *Journal of Applied Polymer Science*, vol. 132, no. 18, 2015.
- [75] S. Keller, G. Blagoi, M. Lillemose, D. Haefliger, and A. Boisen, "Processing of thin SU-8 films," *Journal of Micromechanics and Microengineering*, vol. 18, p. 125020, 2008.
- [76] S. K. Rath, F. Y. C. Boey, and M. J. M. Abadie, "Cationic electron-beam curing of a high-functionality epoxy: Effect of post-curing on glass transition and conversion," *Polymer International*, vol. 53, no. 7, pp. 857–862, 2004.
- [77] J. D. Cho, H. T. Ju, Y. S. Park, and J. W. Hong, "Kinetics of cationic photopolymerizations of UV-curable epoxy-based SU8-negative photoresists with and without silica nanoparticles," *Macromolecular Materials and Engineering*, vol. 291, no. 9, pp. 1155–1163, 2006.
- [78] E. Mitri, G. Birarda, L. Vaccari, S. Kenig, M. Tormen, and G. Grenzi, "SU-8 bonding protocol for the fabrication of microfluidic devices dedicated to FTIR microspectroscopy of live cells," *Lab on a chip*, vol. 14, no. 1, pp. 210–8, 2014.

Bibliography

- [79] R. S. Lima, P. A. G. C. Leão, M. H. O. Piazzetta, A. M. Monteiro, L. Y. Shiroma, A. L. Gobbi, and E. Carrilho, "Sacrificial adhesive bonding: a powerful method for fabrication of glass microchips.," *Scientific reports*, vol. 5, p. 13276, 2015.
- [80] A. C. Ferrari, "Raman spectroscopy of graphene and graphite: Disorder, electron-phonon coupling, doping and nonadiabatic effects," *Solid State Communications*, vol. 143, pp. 47–57, jul 2007.
- [81] W. Herres and J. Gronholz, "Series Understanding FT-IR Data Processing Part 1: Data Acquisition and Fourier Transformation,"
- [82] J. BICERANO, J. F. DOUGLAS, and D. A. BRUNE, "Model for the Viscosity of Particle Dispersions," *Journal of Macromolecular Science, Part C: Polymer Reviews*, vol. 39, pp. 561–642, sep 1999.
- [83] V. Geiser, Y. Leterrier, and J.-A. E. Månson, "Rheological Behavior of Concentrated Hyperbranched Polymer/Silica Nanocomposite Suspensions," *Macromolecules*, vol. 43, pp. 7705–7712, sep 2010.
- [84] J. Vermant, S. Ceccia, M. K. Dolgovskij, P. L. Maffettone, and C. W. Macosko, "Quantifying dispersion of layered nanocomposites via melt rheology," *Journal of Rheology*, vol. 51, no. 3, p. 429, 2007.
- [85] K. L. White, H. Yao, X. Zhang, and H.-J. Sue, "Rheology of electrostatically tethered nanoplatelets and multi-walled carbon nanotubes in epoxy," *Polymer*, vol. 84, pp. 223–233, feb 2016.
- [86] I. Mahbubul, R. Saidur, and M. Amalina, "Latest developments on the viscosity of nanofluids," *International Journal of Heat and Mass Transfer*, vol. 55, pp. 874–885, jan 2012.
- [87] A. Einstein, "Eine neue Bestimmung der Moleküldimensionen," *Annalen der Physik*, vol. 324, pp. 289–306, feb 1906.
- [88] J. F. Douglas and E. J. Garboczi, "Intrinsic Viscosity and the Polarizability of Particles Having a Wide Range of Shapes," in *Advances in chemical physics*, pp. 85–153, John Wiley & Sons, Inc., 1995.
- [89] H. Kim and C. W. Macosko, "Processing-property relationships of polycarbonate/graphene composites," *Polymer*, vol. 50, pp. 3797–3809, jul 2009.

-
- [90] S. Savithiri, A. Pattamatta, and S. K. Das, "Scaling analysis for the investigation of slip mechanisms in nanofluids," *Nanoscale Research Letters*, vol. 6, no. 1, p. 471, 2011.
- [91] M. Mionić, K. Pataky, R. Gaal, A. Magrez, J. Brugger, and L. Forró, "Carbon nanotubes–SU8 composite for flexible conductive inkjet printable applications," *Journal of Materials Chemistry*, vol. 22, no. 28, p. 14030, 2012.
- [92] M. Zhang, "Strong, Transparent, Multifunctional, Carbon Nanotube Sheets," *Science*, vol. 309, pp. 1215–1219, aug 2005.
- [93] J. A. Rud, L. S. Lovell, J. W. Senn, Q. Qiao, and J. T. Mcleskey, "Water soluble polymer/-carbon nanotube bulk heterojunction solar cells," *Journal of Materials Science*, vol. 40, pp. 1455–1458, mar 2005.
- [94] Y. Kanai and J. C. Grossman, "Role of Semiconducting and Metallic Tubes in P3HT/Carbon-Nanotube Photovoltaic Heterojunctions: Density Functional Theory Calculations," *Nano Letters*, vol. 8, pp. 908–912, mar 2008.
- [95] S. Maruyama, "A molecular dynamics simulation of heat conduction in finite length SWNTs," *Physica B: Condensed Matter*, vol. 323, pp. 193–195, oct 2002.
- [96] S. Maruyama, "A MOLECULAR DYNAMICS SIMULATION OF HEAT CONDUCTION OF A FINITE LENGTH SINGLE-WALLED CARBON NANOTUBE," *Microscale Thermophysical Engineering*, vol. 7, pp. 41–50, jan 2003.
- [97] T. K. Das and S. Prusty, "Graphene-Based Polymer Composites and Their Applications," *Polymer-Plastics Technology and Engineering*, vol. 52, pp. 319–331, mar 2013.
- [98] A. C. Ferrari, J. C. Meyer, V. Scardaci, C. Casiraghi, M. Lazzeri, F. Mauri, S. Piscanec, D. Jiang, K. S. Novoselov, S. Roth, and A. K. Geim, "Raman Spectrum of Graphene and Graphene Layers," *Physical Review Letters*, vol. 97, p. 187401, oct 2006.
- [99] G. Eda, G. Fanchini, and M. Chhowalla, "Large-area ultrathin films of reduced graphene oxide as a transparent and flexible electronic material," *Nature Nanotechnology*, vol. 3, pp. 270–274, may 2008.
- [100] J.-J. Luo, "Characterization and modeling of mechanical behavior of polymer/clay nanocomposites," *Composites Science and Technology*, vol. 63, pp. 1607–1616, aug 2003.
- [101] J. N. Coleman, W. J. Blau, A. B. Dalton, E. Munoz, S. Collins, B. G. Kim, J. Razal, M. Selvidge, G. Vieiro, and R. H. Baughman, "Improving the mechanical properties

Bibliography

- of single-walled carbon nanotube sheets by intercalation of polymeric adhesives," *Applied Physics Letters*, vol. 82, no. 11, p. 1682, 2003.
- [102] M. Alexandre and P. Dubois, "Polymer-layered silicate nanocomposites: Preparation, properties and uses of a new class of materials," *Materials Science and Engineering R: Reports*, vol. 28, no. 1, pp. 1–63, 2000.
- [103] F. d. C. Fim, J. M. Guterres, N. R. S. Basso, and G. B. Galland, "Polyethylene/graphite nanocomposites obtained by in situ polymerization," *Journal of Polymer Science Part A: Polymer Chemistry*, vol. 48, pp. 692–698, feb 2010.
- [104] Z. Gu, C. Li, G. Wang, L. Zhang, X. Li, W. Wang, and S. Jin, "Synthesis and characterization of polypyrrole/graphite oxide composite by in situ emulsion polymerization," *Journal of Polymer Science Part B: Polymer Physics*, vol. 48, pp. 1329–1335, jun 2010.
- [105] H. Yang, C. Shan, F. Li, Q. Zhang, D. Han, and L. Niu, "Convenient preparation of tunably loaded chemically converted graphene oxide/epoxy resin nanocomposites from graphene oxide sheets through two-phase extraction," *Journal of Materials Chemistry*, vol. 19, no. 46, p. 8856, 2009.
- [106] H. Kim, Y. Miura, and C. W. Macosko, "Graphene/Polyurethane Nanocomposites for Improved Gas Barrier and Electrical Conductivity," *Chem. Mater*, vol. 22, pp. 3441–3450, 2010.
- [107] M. Sangermano, S. Pegel, P. Pötschke, and B. Voit, "Antistatic epoxy coatings with carbon nanotubes obtained by cationic photopolymerization," *Macromolecular Rapid Communications*, vol. 29, no. 5, pp. 396–400, 2008.
- [108] H. Cong, L. Hong, R. S. Harake, and T. Pan, "CNT-based photopatternable nanocomposites with high electrical conductivity and optical transparency," *Journal of Micromechanics and Microengineering*, vol. 20, p. 025002, feb 2010.
- [109] J. Du and H.-M. Cheng, "The Fabrication, Properties, and Uses of Graphene/Polymer Composites," *Macromolecular Chemistry and Physics*, vol. 213, pp. 1060–1077, jun 2012.
- [110] S. Vadukumpully, J. Paul, N. Mahanta, and S. Valiyaveetil, "Flexible conductive graphene/poly(vinyl chloride) composite thin films with high mechanical strength and thermal stability," *Carbon*, vol. 49, pp. 198–205, jan 2011.
- [111] T. Wei, G. Luo, Z. Fan, C. Zheng, J. Yan, C. Yao, W. Li, and C. Zhang, "Preparation of graphene nanosheet/polymer composites using in situ reduction–extractive dispersion," *Carbon*, vol. 47, pp. 2296–2299, aug 2009.

- [112] J. Liang, Y. Wang, Y. Huang, Y. Ma, Z. Liu, J. Cai, C. Zhang, H. Gao, and Y. Chen, "Electromagnetic interference shielding of graphene/epoxy composites," *Carbon*, vol. 47, pp. 922–925, mar 2009.
- [113] H.-B. Zhang, W.-G. Zheng, Q. Yan, Y. Yang, J.-W. Wang, Z.-H. Lu, G.-Y. Ji, and Z.-Z. Yu, "Electrically conductive polyethylene terephthalate/graphene nanocomposites prepared by melt compounding," *Polymer*, vol. 51, pp. 1191–1196, mar 2010.
- [114] V. H. Pham, T. V. Cuong, T. T. Dang, S. H. Hur, B.-S. Kong, E. J. Kim, E. W. Shin, and J. S. Chung, "Superior conductive polystyrene – chemically converted graphene nanocomposite," *Journal of Materials Chemistry*, vol. 21, no. 30, p. 11312, 2011.
- [115] I. Zaman, H. C. Kuan, Q. Meng, A. Michelmore, N. Kawashima, T. Pitt, L. Zhang, S. Gouda, L. Luong, and J. Ma, "A facile approach to chemically modified graphene and its polymer nanocomposites," *Advanced Functional Materials*, vol. 22, no. 13, pp. 2735–2743, 2012.
- [116] W. Bauhofer and J. Z. Kovacs, "A review and analysis of electrical percolation in carbon nanotube polymer composites," *Composites Science and Technology*, vol. 69, pp. 1486–1498, aug 2009.
- [117] S. Vionnet-Menot, C. Grimaldi, T. Maeder, S. Strässler, and P. Ryser, "Tunneling-percolation origin of nonuniversality: Theory and experiments," *Physical Review B*, vol. 71, p. 064201, feb 2005.
- [118] I. Balberg, D. Azulay, O. Millo, G. Ambrosetti, and C. Grimaldi, "Comment on "Direct Measurement of the Percolation Probability in Carbon Nanofiber-Polyimide Nanocomposites","" *Physical Review Letters*, vol. 106, p. 079701, feb 2011.
- [119] G. Ambrosetti, I. Balberg, and C. Grimaldi, "Percolation-to-hopping crossover in conductor-insulator composites," *Physical Review B*, vol. 82, p. 134201, oct 2010.
- [120] V. Ambegaokar, B. I. Halperin, and J. S. Langer, "Hopping Conductivity in Disordered Systems," *Physical Review B*, vol. 4, no. 8, 1971.
- [121] G. Ambrosetti, C. Grimaldi, I. Balberg, T. Maeder, A. Danani, and P. Ryser, "Solution of the tunneling-percolation problem in the nanocomposite regime," *Physical Review B*, vol. 81, p. 155434, apr 2010.
- [122] M. Pollak, "A percolation treatment of dc hopping conduction," *Journal of Non-Crystalline Solids*, vol. 11, no. 1, pp. 1–24, 1972.

Bibliography

- [123] B. I. Shklovskii and A. L. Éfros, "Transition from Metallic to Activation Conductivity in Compensated Semiconductors," *Soviet Journal of Experimental and Theoretical Physics*, Vol. 34, p.435, vol. 34, p. 435, 1972.
- [124] B. I. Shklovskii and A. L. Éfros, "Impurity Band and Conductivity of Compensated Semiconductors," *Soviet Journal of Experimental and Theoretical Physics*, Vol. 33, p.468, vol. 33, p. 468, 1971.
- [125] M. Castellino, A. Chiolerio, M. I. Shahzad, P. V. Jagdale, and A. Tagliaferro, "Electrical conductivity phenomena in an epoxy resin-carbon-based materials composite," *Composites Part A: Applied Science and Manufacturing*, vol. 61, pp. 108–114, jun 2014.
- [126] R. H. J. Otten and P. van der Schoot, "Connectivity percolation of polydisperse anisotropic nanofillers," *The Journal of Chemical Physics*, vol. 134, no. 9, p. 094902, 2011.
- [127] M. Mathew, T. Schilling, and M. Oettel, "Connectivity percolation in suspensions of hard platelets," *Physical Review E*, vol. 85, p. 061407, jun 2012.
- [128] T. A. Ezquerra, M. Kulescza, C. S. Cruz, and F. J. Baltá-Calleja, "Charge transport in polyethylene-graphite composite materials," *Advanced Materials*, vol. 2, pp. 597–600, dec 1990.
- [129] A. Allaoui, S. Hoa, and M. Pugh, "The electronic transport properties and microstructure of carbon nanofiber/epoxy composites," *Composites Science and Technology*, vol. 68, pp. 410–416, feb 2008.
- [130] C. H. Seager and G. E. Pike, "Percolation and conductivity: A computer study. II," *Physical Review B*, vol. 10, pp. 1435–1446, aug 1974.
- [131] A. M. Díez-Pascual, M. A. Gómez-Fatou, F. Ania, and A. Flores, "Nanoindentation in polymer nanocomposites," *Progress in Materials Science*, vol. 67, pp. 1–94, jan 2015.
- [132] T. Liu, I. Y. Phang, L. Shen, S. Y. Chow, and W. D. Zhang, "Morphology and mechanical properties of multiwalled carbon nanotubes reinforced nylon-6 composites," *Macromolecules*, vol. 37, no. 19, pp. 7214–7222, 2004.
- [133] B. Das, K. Eswar Prasad, U. Ramamurty, and C. N. R. Rao, "Nano-indentation studies on polymer matrix composites reinforced by few-layer graphene.," *Nanotechnology*, vol. 20, no. 12, pp. 125705(1)–125705(5), 2009.

- [134] A. Dutta, D. Penumadu, and B. Files, "Nanoindentation testing for evaluating modulus and hardness of single-walled carbon nanotube–reinforced epoxy composites," *Journal of Materials Research*, vol. 19, pp. 158–164, 2004.
- [135] L. Shen, I. Y. Phang, L. Chen, T. Liu, and K. Zeng, "Nanoindentation and morphological studies on nylon 66 nanocomposites. I. Effect of clay loading," *Polymer*, vol. 45, pp. 3341–3349, may 2004.
- [136] Z. Chen, X. J. Dai, K. Magniez, P. R. Lamb, D. Rubin de Celis Leal, B. L. Fox, and X. Wang, "Improving the mechanical properties of epoxy using multiwalled carbon nanotubes functionalized by a novel plasma treatment," *Composites Part A: Applied Science and Manufacturing*, vol. 45, pp. 145–152, feb 2013.
- [137] H. Wang, J. Feng, X. Hu, and K. M. Ng, "Tribological behaviors of aligned carbon nanotube/fullerene epoxy nanocomposites," *Polymer Engineering & Science*, vol. 48, pp. 1467–1475, aug 2008.
- [138] X. LI, K. LAU, and Y. YIN, "Mechanical properties of epoxy-based composites using coiled carbon nanotubes," *Composites Science and Technology*, vol. 68, pp. 2876–2881, nov 2008.
- [139] D. Penumadu, A. Dutta, G. M. Pharr, and B. Files, "Mechanical properties of blended single-wall carbon nanotube composites," *Journal of Materials Research*, vol. 18, pp. 1849–1853, aug 2003.
- [140] H. Cebeci, R. G. de Villoria, A. J. Hart, and B. L. Wardle, "Multifunctional properties of high volume fraction aligned carbon nanotube polymer composites with controlled morphology," *Composites Science and Technology*, vol. 69, pp. 2649–2656, dec 2009.
- [141] W. Oliver and G. Pharr, "An improved technique for determining hardness and elastic modulus using load and displacement sensing indentation experiments," *Journal of Materials Research*, vol. 7, pp. 1564–1583, jun 1992.
- [142] E. G. Herbert, W. C. Oliver, and G. M. Pharr, "Nanoindentation and the dynamic characterization of viscoelastic solids," *Journal of Physics D: Applied Physics*, vol. 41, p. 074021, apr 2008.
- [143] G. M. Odegard, T. S. Gates, and H. M. Herring, "Characterization of viscoelastic properties of polymeric materials through nanoindentation," *Experimental Mechanics*, vol. 45, pp. 130–136, apr 2005.

Bibliography

- [144] S. Hayes, A. Goruppa, and F Jones, "Dynamic nanoindentation as a tool for the examination of polymeric materials," *Journal of Materials Research*, vol. 19, pp. 3298–3306, nov 2004.
- [145] H. Kim and C. W. Macosko, "Morphology and properties of polyester/exfoliated graphite nanocomposites," *Macromolecules*, vol. 41, no. 9, pp. 3317–3327, 2008.
- [146] X.-B. Wang, J. Sun, C.-M. Chen, X.-Q. Sun, F. Wang, and D.-M. Zhang, "Thermal UV treatment on SU-8 polymer for integrated optics," *Optical Materials Express*, vol. 4, no. 3, p. 509, 2014.
- [147] B. L. Aekbote, J. Jacak, G. J. Schutz, E. Csanyi, Z. Szegletes, P. Ormos, and L. Kelemen, "Aminosilane-based functionalization of two-photon polymerized 3D SU-8 microstructures," *European Polymer Journal*, vol. 48, no. 10, pp. 1745–1754, 2012.
- [148] J. Zhang, M. B. Chan-Park, and C. M. Li, "Network properties and acid degradability of epoxy-based SU-8 resists containing reactive gamma-butyrolactone," *Sensors and Actuators B: Chemical*, vol. 131, pp. 609–620, may 2008.
- [149] J. B. Lambert, *Introduction to organic spectroscopy*. New York: Macmillan, 1st ed., 1987.
- [150] X. Ramis, J. M. Salla, C. Mas, A. Manteco, and A. Serra, "Kinetic Study by FTIR, TMA, and DSC of the Curing of a Mixture of DGEBA Resin and γ -Butyrolactone Catalyzed by Ytterbium Triflate," *Journal of Applied Polymer Science*, vol. 92, no. 1, pp. 381–393, 2004.
- [151] B. Chen, H. Liu, X. Li, C. Lu, Y. Ding, and B. Lu, "Fabrication of a graphene field effect transistor array on microchannels for ethanol sensing," *Applied Surface Science*, vol. 258, pp. 1971–1975, jan 2012.
- [152] Y. Peng and D. Huang, "Fabrication of patterned reduced graphene oxide nanosheet field-emission cathodic film at room-temperature," *Applied Surface Science*, vol. 283, pp. 81–86, oct 2013.
- [153] V. Dukhi, A. Bissessur, and B. S. Martincigh, "Formation of Corrosive Sulfur with Dibenzyl Disulfide in Fluid-Filled Transformers," *Industrial & Engineering Chemistry Research*, vol. 55, no. 11, pp. 2911–2920, 2016.
- [154] G. Varsanyi and S. Szoke, *Vibrational spectra of benzene derivatives*. New York ;London: Academic Press, 1969.
- [155] K. Shimizu, F. Helen Blaikie, M. Kongsfelt, K. Damgaard Schøller Sørensen, S. Uttrup Pedersen, and K. Daasbjerg, "Electrochemical procedure for constructing poly(phenylene

- sulfide) brushes on glassy carbon and stainless steel,” *Journal of Polymer Science, Part A: Polymer Chemistry*, vol. 54, no. 1, pp. 91–98, 2016.
- [156] D. Weitz, H. Wyss, and R. Larsen, “Oscillatory Rheology Measuring the Viscoelastic Behaviour of Soft Materials,” in *G.I.T. Laboratory Journal 3-4*, pp. pp 68–70, 2007.
- [157] J. F. Ryder and J. M. Yeomans, “Shear thinning in dilute polymer solutions,” *Journal of Chemical Physics*, vol. 125, no. 19, 2006.
- [158] R. Wagener and T. J. Reisinger, “A rheological method to compare the degree of exfoliation of nanocomposites,” *Polymer*, vol. 44, pp. 7513–7518, nov 2003.
- [159] F. Du, R. C. Scogna, W. Zhou, S. Brand, J. E. Fischer, and K. I. Winey, “Nanotube networks in polymer nanocomposites: Rheology and electrical conductivity,” *Macromolecules*, vol. 37, no. 24, pp. 9048–9055, 2004.
- [160] S. Iijima, “Helical microtubules of graphitic carbon,” *Nature*, vol. 354, pp. 56–58, nov 1991.
- [161] A. V. Kyrylyuk and P. van der Schoot, “Continuum percolation of carbon nanotubes in polymeric and colloidal media,” *Proceedings of the National Academy of Sciences*, vol. 105, pp. 8221–8226, jun 2008.
- [162] A. P. Chatterjee, “Percolation thresholds for rod-like particles: polydispersity effects,” *Journal of Physics: Condensed Matter*, vol. 20, no. 25, p. 255250, 2008.
- [163] A. P. Chatterjee, “Connectedness percolation in polydisperse rod systems: A modified Bethe lattice approach,” *The Journal of Chemical Physics*, vol. 132, no. 22, p. 224905, 2010.
- [164] A. P. Chatterjee, “Geometric percolation in polydisperse systems of finite-diameter rods: Effects due to particle clustering and inter-particle correlations,” *Journal of Chemical Physics*, vol. 137, no. 13, 2012.
- [165] R. H. J. Otten and P. van der Schoot, “Continuum Percolation of Polydisperse Nanofillers,” *Physical Review Letters*, vol. 103, p. 225704, nov 2009.
- [166] I. A.L.R. Bug, S.A. Safran, “Physical review letters,” *Physical Review Letters*, vol. 54, no. 13, pp. 2–5, 1985.
- [167] M. Safdari and M. Al-Haik, “Electrical conductivity of synergistically hybridized nanocomposites based on graphite nanoplatelets and carbon nanotubes,” *Nanotechnology*, vol. 23, no. 40, p. 405202, 2012.

Bibliography

- [168] C. E. Alvarez and S. H. L. Klapp, "Percolation and orientational ordering in systems of magnetic nanorods," *Soft Matter*, vol. 8, no. 28, p. 7480, 2012.
- [169] B. Nigro, C. Grimaldi, P. Ryser, A. P. Chatterjee, and P. Van Der Schoot, "Quasiuniversal connectedness percolation of polydisperse rod systems," *Physical Review Letters*, vol. 110, no. 1, pp. 1–5, 2013.
- [170] B. Nigro, C. Grimaldi, M. A. Miller, P. Ryser, and T. Schilling, "Depletion-interaction effects on the tunneling conductivity of nanorod suspensions," *Physical Review E*, vol. 88, p. 042140, oct 2013.
- [171] S. Kale, F. A. Sabet, I. Jasiuk, and M. Ostojca-Starzewski, "Tunneling-percolation behavior of polydisperse prolate and oblate ellipsoids," *Journal of Applied Physics*, vol. 118, no. 15, 2015.
- [172] F. Inam, M. J. Reece, and T. Peijs, "Shortened carbon nanotubes and their influence on the electrical properties of polymer nanocomposites," *Journal of Composite Materials*, vol. 46, no. 11, pp. 1313–1322, 2012.
- [173] F. Y. Castillo, R. Socher, B. Krause, R. Headrick, B. P. Grady, R. Prada-Silvy, and P. Pötschke, "Electrical, mechanical, and glass transition behavior of polycarbonate-based nanocomposites with different multi-walled carbon nanotubes," *Polymer*, vol. 52, pp. 3835–3845, aug 2011.
- [174] H. Deng, R. Zhang, E. Bilotti, J. Loos, and T. Peijs, "Conductive polymer tape containing highly oriented carbon nanofillers," *Journal of Applied Polymer Science*, vol. 113, pp. 742–751, jul 2009.
- [175] R. M. Mutiso, M. C. Sherrott, J. Li, and K. I. Winey, "Simulations and generalized model of the effect of filler size dispersity on electrical percolation in rod networks," *Physical Review B - Condensed Matter and Materials Physics*, vol. 86, no. 21, pp. 1–6, 2012.
- [176] H. Meyer, P. van der Schoot, and T. Schilling, "Percolation in suspensions of polydisperse hard rods: Quasi universality and finite-size effects," *The Journal of Chemical Physics*, vol. 143, no. 4, p. 044901, 2015.
- [177] A. P. Chatterjee, "A percolation-based model for the conductivity of nanofiber composites," *Journal of Chemical Physics*, vol. 139, no. 22, 2013.
- [178] B. Nigro, G. Ambrosetti, C. Grimaldi, T. Maeder, and P. Ryser, "Transport properties of nonhomogeneous segregated composites," *Physical Review B - Condensed Matter and Materials Physics*, vol. 83, no. 6, pp. 1–9, 2011.

- [179] B. Nigro, C. Grimaldi, M. A. Miller, P. Ryser, and T. Schilling, "Tunneling conductivity in composites of attractive colloids," *The Journal of Chemical Physics*, vol. 136, no. 16, p. 164903, 2012.
- [180] R. Smajda, M. Mionic, M. Duchamp, J. C. Andresen, L. Forró, and A. Magrez, "Production of high quality carbon nanotubes for less than \$1 per gram," *physica status solidi (c)*, vol. 7, pp. NA–NA, feb 2010.
- [181] L. Forro, R. Gaal, C. Grimaldi, M. Mionic, P. R. Ribic, R. Smajda, and A. Magrez, "Tuning the length dispersion of multi-walled carbon nanotubes by ball milling," *AIP Advances*, vol. 3, no. 9, 2013.
- [182] L. Berhan and A. M. Sastry, "Modeling percolation in high-aspect-ratio fiber systems. II. The effect of waviness on the percolation onset," *Physical Review E*, vol. 75, p. 041121, apr 2007.
- [183] N. Hu, Z. Masuda, C. Yan, G. Yamamoto, H. Fukunaga, and T. Hashida, "The electrical properties of polymer nanocomposites with carbon nanotube fillers," *Nanotechnology*, vol. 19, no. 21, p. 215701, 2008.
- [184] W. S. Bao, S. A. Meguid, Z. H. Zhu, Y. Pan, and G. J. Weng, "Effect of carbon nanotube geometry upon tunneling assisted electrical network in nanocomposites," *Journal of Applied Physics*, vol. 113, no. 23, 2013.
- [185] L. P. Simoneau, J. Villeneuve, and A. Rochefort, "Electron percolation in realistic models of carbon nanotube networks," *Journal of Applied Physics*, vol. 118, no. 12, 2015.
- [186] Y. Jinbo, T. Sato, and A. Teramoto, "Light Scattering Study of Semiflexible Polymer Solutions. 1. Dilute through Semidilute Solutions of Poly(n-hexyl isocyanate) Dissolved in Dichloromethane," *Macromolecules*, vol. 27, pp. 6080–6087, oct 1994.
- [187] S. Petrovic, D. Borka, I. Telecki, and N. Neskovic, "Angular distributions of high energy protons channeled in long (10,10) single-wall carbon nanotubes," *Nuclear Instruments and Methods in Physics Research Section B: Beam Interactions with Materials and Atoms*, vol. 267, pp. 2365–2368, jul 2009.
- [188] V. Klimov and V. Letokhov, "Hard X-radiation emitted by a charged particle moving in a carbon nanotube," *Physics Letters A*, vol. 222, pp. 424–428, nov 1996.
- [189] Z. Zhu, D. Zhu, R. Lu, Z. Xu, W. Zhang, and H. Xia, "The experimental progress in studying of channeling of charged particles along nanostructure," pp. 597413–597413–8, International Society for Optics and Photonics, aug 2005.

Bibliography

- [190] S. Petrovic, D. Borka, and N. Neskovic, "Rainbows in transmission of high energy protons through carbon nanotubes," *The European Physical Journal B*, vol. 44, pp. 41–45, mar 2005.
- [191] Z. Miskovic, F. O. Goodman, D. J. Mowbray, J. Zuloaga, S. Chung, Y.-N. Wang, D.-P. Zhou, N. Neskovic, S. Petrovic, and D. Borka, "Prospects of ion channelling through carbon nanotubes."
- [192] D. Borka, S. Petrović, N. Nešković, D. J. Mowbray, and Z. L. Mišković, "Influence of the dynamical image potential on the rainbows in ion channeling through short carbon nanotubes," *Physical Review A*, vol. 73, p. 062902, jun 2006.
- [193] D. Borka, D. J. Mowbray, Z. L. Mišković, S. Petrović, and N. Nešković, "Dynamic polarization effects on the angular distributions of protons channeled through carbon nanotubes in dielectric media," *Physical Review A*, vol. 77, p. 032903, mar 2008.
- [194] B. J. Hinds, N. Chopra, T. Rantell, R. Andrews, V. Gavalas, and L. G. Bachas, "Aligned multiwalled carbon nanotube membranes," *Science*, vol. 303, no. 5654, pp. 62–65, 2004.
- [195] E. J. García, a. J. Hart, B. L. Wardle, and a. H. Slocum, "Fabrication of composite microstructures by capillarity-driven wetting of aligned carbon nanotubes with polymers," *Nanotechnology*, vol. 18, p. 165602, apr 2007.
- [196] T. Bandi, J. Polido-Gomes, A. Neels, A. Dommann, L. Marchand, and H. R. Shea, "Proton-Radiation Tolerance of Silicon and SU-8 as Structural Materials for High-Reliability MEMS," *Journal of Microelectromechanical Systems*, vol. 22, pp. 1395–1402, dec 2013.
- [197] M. Key, V. Cindro, and M. Lozano, "On the radiation tolerance of SU-8, a new material for gaseous microstructure radiation detector fabrication," *Radiation Physics and Chemistry*, vol. 71, pp. 1003–1007, dec 2004.
- [198] S. Berber, Y.-K. Kwon, and D. Tománek, "Unusually High Thermal Conductivity of Carbon Nanotubes," *Physical Review Letters*, vol. 84, pp. 4613–4616, may 2000.
- [199] J. Hone, "Quantized Phonon Spectrum of Single-Wall Carbon Nanotubes," *Science*, vol. 289, pp. 1730–1733, sep 2000.
- [200] J. Shiomi and S. Maruyama, "Molecular Dynamics of Diffusive-Ballistic Heat Conduction in Single-Walled Carbon Nanotubes," *Japanese Journal of Applied Physics*, vol. 47, pp. 2005–2009, apr 2008.

- [201] J. Hone, M. Whitney, C. Piskoti, and A. Zettl, "Thermal conductivity of single-walled carbon nanotubes," *Physical Review B*, vol. 59, pp. R2514–R2516, jan 1999.
- [202] J. Hone, M. C. Llaguno, N. M. Nemes, A. T. Johnson, J. E. Fischer, D. A. Walters, M. J. Casavant, J. Schmidt, and R. E. Smalley, "Electrical and thermal transport properties of magnetically aligned single wall carbon nanotube films," *Applied Physics Letters*, vol. 77, no. 5, p. 666, 2000.
- [203] W. Yi, L. Lu, Z. Dian-lin, Z. W. Pan, and S. S. Xie, "Linear specific heat of carbon nanotubes," *Physical Review B*, vol. 59, pp. R9015–R9018, apr 1999.
- [204] R. Mahajan, R. Nair, V. Wakharkar, J. Swan, J. Tang, and G. Vandentop, "Emerging Directions for Packaging Technologies," *Intel Technology Journal*, vol. 06, no. 02, 2002.
- [205] H. Huang, C. H. Liu, Y. Wu, and S. Fan, "Aligned Carbon Nanotube Composite Films for Thermal Management," *Advanced Materials*, vol. 17, pp. 1652–1656, jul 2005.
- [206] M. Olcese, "Mechanics and cooling of pixel detectors," *Nuclear Instruments and Methods in Physics Research Section A: Accelerators, Spectrometers, Detectors and Associated Equipment*, vol. 465, pp. 51–59, jun 2001.
- [207] G. Viehhauser, "Thermal management and mechanical structures for silicon detector systems," *Journal of Instrumentation*, vol. 10, pp. P09001–P09001, sep 2015.
- [208] T. Li, A. Patz, L. Mouchliadis, J. Yan, T. A. Lograsso, I. E. Perakis, and J. Wang, "Femtosecond switching of magnetism via strongly correlated spin–charge quantum excitations," *Nature*, vol. 496, pp. 69–73, apr 2013.
- [209] D. Chung, "Materials for thermal conduction," *Applied Thermal Engineering*, vol. 21, pp. 1593–1605, nov 2001.
- [210] S. Wang, R. Liang, B. Wang, and C. Zhang, "Dispersion and thermal conductivity of carbon nanotube composites," *Carbon*, vol. 47, pp. 53–57, jan 2009.
- [211] X. Gong, J. Liu, S. Baskaran, R. D. Voise, and J. S. Young, "Surfactant-Assisted Processing of Carbon Nanotube/Polymer Composites," *Chemistry of Materials*, vol. 12, pp. 1049–1052, apr 2000.
- [212] S.-Y. Yang, C.-C. M. Ma, C.-C. Teng, Y.-W. Huang, S.-H. Liao, Y.-L. Huang, H.-W. Tien, T.-M. Lee, and K.-C. Chiou, "Effect of functionalized carbon nanotubes on the thermal conductivity of epoxy composites," *Carbon*, vol. 48, pp. 592–603, mar 2010.

Bibliography

- [213] C. Yu, Y. S. Kim, D. Kim, and J. C. Grunlan, "Thermoelectric Behavior of Segregated-Network Polymer Nanocomposites," *Nano Letters*, vol. 8, pp. 4428–4432, dec 2008.
- [214] Y. Igarashi, Y. Shibuta, and S. Maruyama, "HEAT TRANSFER PROBLEMS RELATED WITH CARBON NANOTUBES BY MOLECULAR DYNAMICS-BASED SIMULATIONS," *Proceeding of the 1st International Forum on Heat Transfer*, 2004.
- [215] M. J. Biercuk, M. C. Llaguno, M. Radosavljevic, J. K. Hyun, A. T. Johnson, and J. E. Fischer, "Carbon nanotube composites for thermal management," *Applied Physics Letters*, vol. 80, no. 15, p. 2767, 2002.
- [216] J. Callaway, "Model for Lattice Thermal Conductivity at Low Temperatures," *Physical Review*, vol. 113, pp. 1046–1051, feb 1959.
- [217] J. Hone, "Phonons and Thermal Properties of Carbon Nanotubes," in *Carbon nanotubes : synthesis, structure, properties, and applications* (M. S. Dresselhaus, G. Dresselhaus, and P. Avouris, eds.), Springer-Verlag, 2001.
- [218] C. Schönenberger, A. Bachtold, C. Strunk, J.-P. Salvetat, and L. Forró, "Interference and Interaction in multi-wall carbon nanotubes," *Applied Physics A: Materials Science & Processing*, vol. 69, pp. 283–295, sep 1999.
- [219] P. Sheng, B. Abeles, and Y. Arie, "Hopping conductivity in granular metals," *Physical Review Letters*, vol. 31, no. 1, pp. 44–47, 1973.
- [220] N. Barisic, R. Gaal, I. Kezsmarki, G. Mihaly, and L. Forro, "Pressure dependence of the thermoelectric power of single-walled carbon nanotubes," *Physical Review B*, vol. 65, p. 241403, may 2002.
- [221] B. Endrődi, G. F. Samu, D. Fejes, Z. Németh, E. Horváth, A. Pisoni, P. K. Matus, K. Hernádi, C. Visy, L. Forró, and C. Janáky, "Challenges and rewards of the electrosynthesis of macroscopic aligned carbon nanotube array/conducting polymer hybrid assemblies," *Journal of Polymer Science Part B: Polymer Physics*, vol. 53, pp. 1507–1518, nov 2015.
- [222] C. Duval-Terrié and L. Lebrun, "Polymerization and Characterization of PMMA. Polymer Chemistry Laboratory Experiments for Undergraduate Students," *Journal of Chemical Education*, vol. 83, no. 3, p. 443, 2006.
- [223] X. Huang and W. J. Brittain, "Synthesis and characterization of PMMA nanocomposites by suspension and emulsion polymerization," *Macromolecules*, vol. 34, no. 10, pp. 3255–3260, 2001.

- [224] a. C. F. Hoole, M. E. Welland, and a. N. Broers, “Negative PMMA as a high-resolution resist - the limits and possibilities,” *Semiconductor Science and Technology*, vol. 12, no. 9, pp. 1166–1170, 1997.
- [225] M. Avella, M. E. Errico, and E. Martuscelli, “Novel PMMA/CaCO₃ Nanocomposites Abrasion Resistant Prepared by an in Situ Polymerization Process,” *Nano Letters*, vol. 1, no. 4, pp. 213–217, 2001.
- [226] R. Lekkerkerker, H. N. W. and Tuinier, *Colloids and the Depletion Interaction*, vol. 1-222, Ind. 2011.
- [227] B. I. Shklovskii and A. L. Efros, “Electronic Properties of Doped Semiconductors,” *Springer Series in Solid-State Sciences*, vol. 45, pp. 72–93, 1984.
- [228] I. S. Beloborodov, A. V. Lopatin, V. M. Vinokur, and K. B. Efetov, “Granular electronic systems,” *Reviews of Modern Physics*, vol. 79, pp. 469–518, apr 2007.
- [229] A. F. M. Pollak, M. Ortuño, *The Electron Glass*. New York: Cambridge University Press, 2012.
- [230] J. Lekner, “Capacitance coefficients of two spheres,” *Journal of Electrostatics*, vol. 69, pp. 11–14, feb 2011.

List of acronyms

0D zero-dimensional

1D one-dimensional

2D two-dimensional

CNT carbon nanotube

FTIR Fourier transform infrared

GBL gamma-butyrolactone

HRSEM high resolution scanning electron microscope

MEMS microelectromechanical systems

MWCNT Multi wall carbon nanotube

OLC Onion-like carbon

PGMEA Propylene glycol methyl ether acetate

PL Photoluminescence

PMMA Poly (methyl methacrylate)

RGO Reduced Graphene Oxide

SEM scanning electron microscope

SWCNT single wall carbon nanotube

TEM transmission electron microscope

TEP Thermo electric power

TSHAS triarylsulfonium hexafluoroantimonate salt

UV Ultra violet

List of Figures

1	A limited number of illustrations showing the omnipresence of composite materials in everyday life (from upper left to lower right). Solarimpulse, revolutionizing aviation, is made of carbon and glass composites; Orion space capsule's heat shield made of a titanium and carbon fibers withstanding temperatures beyond 2000°C; antibacterial tissue using silver nanowires; bioprosthetics made of carbon composites; metallic composite of superconducting wires made up of Nb_3Sn filaments, surrounded by a low resistivity copper matrix; transparent concrete composite with thousands of parallel optical fibers. (Source: Google's image gallery).	2
2	The main matrix of the composites in this dissertation is the SU8 epoxy. The sketch of the chemical formula is shown, and few representative structures made of this epoxy by UV lithography: pillars, channels, gears, cantilever. (Source: google image gallery).	3
3	HRTEM images of graphene, multi-walled carbon nanotubes and carbon onions and their graphical sketches for easier visualization. (Source: google image gallery).	3
4	Illustration of the steps in research, from synthesis to lithographic processing, for graphene-SU8 composites.	4
1.1	Various morphologies and dimensionalities of carbon nanostructures [5]. Copyright 2007, Nature Publishing Group.	8
1.2	Chemical structure of graphene oxide (GO) [11]. Copyright 2009, Nature Publishing Group.	10

List of Figures

1.3	Chemical process of reduced graphene oxide synthesis.(1) Oxidation of graphite to graphite oxide. (2) Exfoliation of graphene oxide in water by sonication of graphite oxide. (3) Controlled reduction of graphene oxide sheets [11]. Copyright 2009, Nature Publishing Group	10
1.4	Atomic structures of (a) armchair and (b) zig-zag carbon nanotubes [13]. Copyright 2001 Elsevier Science Ltd.	11
1.5	(a) Diameter distribution of CVD-grown multi-walled carbon nanotubes (b) TEM micrographs of a multiwall carbon nanotube taken from Ref.[14]. Copyright 2003 IOP Publishing.	11
1.6	TEM images of OLC aggregates with average primary particle size of 4-7 nm [17].	12
1.7	The scheme of OLC formation model [20]. Copyright 2001 Elsevier B.V.	13
1.8	(a) Chemical structure of the Bisphenol A Novolak epoxy oligomer contained in SU-8 formulations. Eight reactive epoxy functionalities allow a high degree of cross-linking after photo-activation [21]. (b) Table of properties for the SU8. . .	14
1.9	The mechanism of cationic polymerization of the SU8 [25]. Rights managed by AIP Publishing LLC.	14
1.10	(a) High aspect ratio pillars made out of SU8 [26] (b) 3D bi-chiral structures made from SU-8 negative photoresist by two-photon polymerization [27] (Copyright 2009 WILEY-VCH Verlag GmbH & Co. KGaA, Weinheim), (c) Optical image of a 5 mm diameter wheel made out of SU8 nanocomposite [28] (Copyright 2006 Elsevier B.V.).	15
1.11	Evolution of the electrical resistivity of the SU8 silver composites versus silver volume fraction, before and after thermal treatment. The percolation threshold is at 6 vol% [34]. Copyright © 2005 WILEY-VCH Verlag GmbH & Co. KGaA, Weinheim.	16
1.12	(a) Variation of electrical resistivity of the SU8-CNTs composites as function of CNT volume fraction [41] (Rights managed by AIP Publishing LLC.), (b) evolution of young modulus as function of CNT contents [15].	18
1.13	Conductivity as a function of the filler fraction. A steep increase in conductivity is observed at a critical filler fraction ϕ_c [43].	19

1.14 exponential decay of the wave functions. The overlap of the wave functions allows the tunneling from one site to the other [43].	21
1.15 Illustration of a disordered material with localized wave functions and energies which vary from site to site. [43]	22
1.16 Hopping of charge carriers from site i to j , separated by the distance r_{ij} and by the energy E_{ij} at (a) low temperatures and (b) high temperatures. At low temperatures the hopping is of variable range hopping type, while at high temperatures it is a fixed range hopping.	22
1.17 Sketch of a granular metallic system imbedded in an insulating matrix. In such a case the charging energy of the fillers determines the hopping transport.	24
1.18 Basic process happening in Raman spectroscopy	32
1.19 Raman spectra graphene sheet [80]. Copyright 2007 Elsevier Ltd.	32
1.20 Basic principle of FTIR	33
1.21 Schematic diagram of a Michelson interferometer	33
1.22 examples of spectrums (on the left) and theirs corresponding interferograms, A) one monochromatic beam, B) Two monochromatic beams, C) lorentzian beam [81]	34
1.23 a) Reference spectrum, b) Spectrum of the absorbing sample, c) Transmittance spectrum equal to spectrum b divided by spectrum a. [81]	35
1.24 Isotropically averaged $[\eta]$ of dilute dispersions of ellipsoids as a function of their aspect ratio [82]. Copyright 1999 Taylor & Francis.	36
1.25 (a)Effect of shear on intrinsic viscosity $[\eta]$ of ellipsoids with different aspect ratio as a function of the rotary Peclet number (Pe). (b)Effect of the coefficient k_H in Equation 1.29 for the viscosity of the spherical particles [82]. Copyright 1999 Taylor & Francis.	37
1.26 Range of applications of Graphene/polymer in different fields [97].	39
2.1 Raman spectrum of RGO fillers.	42

List of Figures

2.2	(a) Scanning electron micrograph of RGO fillers (b) and (c) Transmission electron micrograph of RGO fillers.	43
2.3	Intercalation and exfoliation of layered fillers in polymer matrix (image taken from Ref.[102]. Copyright © 2000 Elsevier Science S.A.)	44
2.4	(a) The preparation steps of SU8-RGO samples for characterization [41] (Rights managed by AIP Publishing LLC.). (b) SU8-RGO film deposited on a glass slide.	45
2.5	Scanning electron microscopy image of SU8 nanocomposites with (a) 0.2 wt% and (b) 0.9 wt% RGO, and (c) 0.2 wt% and (d) 0.9 wt% SRGO. The inset of (a) shows SEM image of pure SU8. Good dispersion of RGO flakes within the SU8 matrix is observed [42]. Copyright 2014 Elsevier Ltd.	46
2.6	Transmission electron microscopy image of microtome slice of SU8 nanocomposites with (a) 0.2 wt% and (b) 0.9 wt% RGO, and (c) 0.2 wt% and (d) 0.9 wt% SRGO [42]. Copyright 2014 Elsevier Ltd.	47
2.7	different steps of photolithography process for SU8.	48
2.8	Photo-patterned SU8-RGO composite on a four inch Pyrex wafer.	49
2.9	Well defined SU8–RGO nanocomposite, patterned by UV-lithography process containing: (a) 1.2 wt%, (b) 0.9 wt%, (c) 0.6 wt% and (d) 0.3 wt% reduced graphene oxide as filler. The transparency of the composite can be tuned with RGO content. Higher magnification of patterned structure is illustrated for (e) SU8–1.2wt% RGO and (f and g) SU8–0.3wt% RGO. The last two images demonstrate very good lateral resolution of the patterned structures. Minimal feature resolution of 10 μm was obtained for SU8–0.3 wt% RGO composite. Copyright 2014 Elsevier Ltd.	50
2.10	Optical transmission versus RGO loading at $\lambda = 700nm$	51
2.11	Measured conductivity σ as a function of RGO volume fraction ϕ for both RGO (filled squares) and SRGO (filled circles) SU8 composites. Inset: ln-ln plot of σ as a function of $\phi - \phi_c$. Solid lines are the best fits of Equation 2.1 to the data. As a comparison, we plot Equation 2.1 with $t = 2$ (dashed line) [42]. Copyright 2014 Elsevier Ltd.	52

2.12 Conductivity of SU8–RGO and SU8–SRGO composites (filled symbols) as a function of the volume fraction (ϕ) of reduced graphene oxide. Open symbols are the measured conductivity values of different polymer-graphene composites derived from Refs. [8, 110, 111, 112, 113, 114, 115] (Plot taken from Ref. [42]. Copyright 2014 Elsevier Ltd.)	54
2.13 Natural logarithm of the measured conductivity of SU8–RGO and SU8–SRGO composites as a function of (a) $1/\phi$ and (b) $1/\phi^{1/3}$. Copyright 2014 Elsevier Ltd.	56
2.14 (a) Schematic representation of a Nanoindentation test. (b) A typical load-displacement curve.	58
2.15 Load-displacement curves for composite SU8-0.6 wt% RGO. The obtained curves for all 9 indents overlap implying the homogeneity of the sample.	60
2.16 The average (a) Young's modulus and (b) hardness of SU8-graphene composites versus RGO loading at the displacement of 750 nm. The line is guide for the eye.	61
2.17 General trend for the dependence of (a) E and (b) H to penetration depth of the indenter. Representative Load-displacement curves for composite SU8-0.3 wt% RGO (blue) and SU8-5 wt% RGO (red) are demonstrated.	62
2.18 (a) The evolution of the PL spectra of A_1 sample UV-irradiated for 3 hours. (b) The dependence of the intensities of PL bands peaked at 2.39 eV (518 nm) and 2.96 eV (418 nm) ($I_{2.39}/I_{2.96}$) as a function of UV-irradiation time.	64
2.19 FTIR spectra of the (a) A_1 and (b) S_1 samples.	65
2.20 The evolution of the PL spectra of the A_2 (a), A_3 (b), A_4 (c) and A_5 (d) samples exposed to the UV-irradiation for 3 hours.	67
2.21 (a) Evolution of PL intensity, as a function of RGO content for samples $A_1 - A_5$ at the time $t = 0$ (filled square), and after 3 hours of UV illumination (open square). (b) The ratio between the intensity of PL bands at 3.06 and 2.39 eV as a function of RGO content after 3h UV-illumination of the samples $A_1 - A_5$	68
2.22 FTIR spectra of the samples (a) A_2, A_3, A_5 and (b) S_2, S_3, S_5 , with a concentration of RGO of 0.001 %wt. (green curves), 0.005 %wt. (red curves) and 0.01%wt. (blue curves), respectively.	69
2.23 The FTIR spectra of the samples A_1, A_5, S_1, S_5 and RGO.	70

List of Figures

2.24 Raman spectra of the samples (a) A_1, A_2, A_3 and A_5 and (b) S_1, S_2, S_3 and S_5 , with a RGO concentration of 0 wt% (black curves), 0.001 wt% (red curves), 0.005 wt% (green curves) and 0.01 wt% (blue curves), respectively. The inset of (b) shows Raman spectrum of RGO.	71
2.25 (a) Activation role of TSHAS photoinitiator in the cure process of the SU8 photoresist; (b) the propagation reactions and (c) the termination reactions of polymerization process of the SU8 photoresist in the presence of RGO (in all SU8 formulas, $R = C_{87}H_{95}O_{15}$).	73
2.26 Raman spectra of the samples of TSHAS in initial state and after the photochemical activation reaction in the presence of RGO.	74
2.27 (a) Schematic representation of a typical rheometry setup. (b) Schematic stress response to oscillatory strain deformation for an elastic solid, a viscous fluid and a viscoelastic material [156].	76
2.28 Viscosity of SU8-RGO composites as a function of frequency and filler weight fraction for 0 to 2 wt%.	77
2.29 (a) Storage shear modulus, G' , and (b) loss shear modulus, G'' , of SU8-RGO composites as a function of angular frequency and RGO weight fraction.	78
2.30 Storage modulus, G' , of the SU8-RGO nanocomposites as a function of the RGO volume fraction at a fixed frequency of 0.1 rad/s.	79
3.1 Histogram of the CNT diameters obtained from 140 values measured from TEM images of CNT-SU8 composites.	84
3.2 Normalized distribution of the as-milled CNT lengths as measured from SEM images. From the top panel to the bottom panel, the distributions become increasingly narrow.	85
3.3 The weighted average L_w and the number average L_n of the CNT lengths for the as-milled nanotubes (filled squares) and for the bimodal length distributions (filled circles).	86
3.4 SEM (a) and TEM (b) images of the CNTs dispersed in the SU8 epoxy matrix. . .	87

3.5	Natural logarithm of the conductivity measured in CNT-SU8 nanocomposites as a function of $1/L_w$ (a) and $1/L_n$ (b). Each symbol represents an average over five independent conductivity measurements. Data for the composites with as-milled CNTs are shown by filled squares, while those with bi-modal CNT length distributions are shown by filled circles.	89
3.6	Illustration of the focusing capability of carbon nanotube of a beam of charged particles. Angular distributions of 1 GeV protons channeled in (10, 10) SWCNTs of length: (a) $10 \mu m$ (b) $30 \mu m$. The intensity of the particle flux is plotted as the angle (θ) between the velocity vector and the tube axis [187]. Copyright 2009 Elsevier B.V.	92
3.7	Bundles of multi walled (MWNTs) and single walled (SWNTs) carbon nanotubes which should be imbedded into a matrix (preferentially SU8 epoxy) and cut to a length $L \sim 0.1-1 \mu m$. They could serve as excellent structures for channeling (illustrated on right). The typical diameter d are $20 nm$ and $1.4 nm$ for MWNTs and SWNTs, respectively.	93
3.8	Simulation of rainbow channeling pattern of a $1 \mu m$ long rope of (10,10) single walled (SWNTs) carbon nanotubes[190, 191]. Copyright 2005, EDP Sciences/Società Italiana di Fisica/Springer-Verlag.	94
3.9	SEM micrograph of aligned CNT carpets.	95
3.10	Schematic of the submersion method used to prepare SU8-oriented CNT composites [195]. Copyright 2007 IOP Publishing.	96
3.11	SU8-CNT lamellas prepared with (a) standard diamond knife, $100 nm$ thickness, (b) standard diamond knife, $50 nm$ thickness,(c) oscillatory diamond knife, $100 nm$ thickness,(d) oscillatory diamond knife, $100 nm$ thickness, for proton channeling measurements. The lamella displayed in image (d) was the one used for the channeling measurements.	97
3.12	Transmission electron microscope images of SU8-CNT lamella around a carbon nanotube channel (a). The walls of the carbon nanotube with inter-layer distance of $0.3 nm$ is visible in image (b).	98

List of Figures

- 3.13 The transmitted channeling pattern were recorded by photographing a highly sensitive aluminium-coated YAG scintillator screen placed at ~ 70 cm away from the sample. Focused 2 MeV protons were used for this experiment, and the spot size of the beam is around 500 nm at the surface of the sample. The CNT sample thickness is around 50 nm. The measurement was done in the group of Prof. Mark Breese, NUS, Singapore by Mallikarjuna Rao Motapothula. 99
- 3.14 SEM images of the carbon nanotube carpet before (a) and after (b) impregnation with SU8 epoxy . The CNTs fill up 3% of the volume of the composite. 103
- 3.15 (a) Temperature dependence of thermal conductivity of the MWCNT-SU8 composite, perpendicular and parallel to the tubes axis. For the epoxy $\kappa = 0.2$ $Wm^{-1}K^{-1}$ at room temperature. The solid lines are fits described in the text. The inset illustrates the measurement setup. (b) Temperature dependence of anisotropy of the thermal conductivity ($\kappa_{\parallel}/\kappa_{\perp}$) for dropwise and submersion samples. 105
- 3.16 Temperature dependence of electrical resistivity in the tube direction (green squares) and perpendicular to the tube direction (red circles). Inset: Temperature dependence of electrical resistivity anisotropy. 108
- 3.17 Temperature dependence of thermoelectric power. The anisotropy parameter is roughly constant throughout the investigated temperature range. 109
- 4.1 TEM images of a OLC-PMMA composite. The image in (a) and shows that the OLCs form clusters of touching or nearly touching particles. The clusters are dispersed in the PMMA matrix giving rise to a non-homogeneous microstructure, as shown in (b). 114
- 4.2 Room temperature electrical conductivity of OLC-PMMA composites as a function of the volume fraction ϕ of OLC fillers. The data for the carbon nanotube and graphene dispersed in SU8 composites are taken from Refs. [41] and [42], respectively. 115
- 4.3 Electrical conductivity at room temperature of OLC-PMMA compsites as a function of an applied hydrostatic pressure P for different amounts (in %wt) of the OLC particles. 116

4.4	Room temperature electrical conductivity of OLC-PMMA composites as a function of OLC volume fraction for different applied pressures. The solid lines are the best fits to Equation 4.3. The fitting parameters are reported in Table 4.1. . .	117
4.5	Room temperature electrical conductivity of OLC-PMMA composites at ambient pressure (filled squares). The solid lines are fits to $\sigma = \sigma_0 \exp(-b/\phi^\alpha)$. Note that the quality of the fits increases as the value of α diminishes.	118
4.6	Effect of the temperature on the electrical conductivity of OLC-PMMA composites at (a) ambient pressure and at (b) $P = 20 \text{ Kbar}$. Note that in (a) the conductivity follows the stretched exponential behavior of Equation 4.4 with $\alpha \approx 1/2$, while the data at 20 Kbar (b) have activated behavior.	119
4.7	Temperature dependence of the electrical conductivity at different values of the applied pressure for a sample with 2 % wt of OLC particles. The solid lines are fits of Equation 4.4 with parameters T_0 and α reported in Table 4.2	120
4.8	T_0 versus α plot. The pressure increases in going from the top-left to the bottom-right. The dashed line is a guide to the eye.	122
5.1	Room temperature electrical conductivity of polymer composites containing various types carbon nanofillers as a function of the volume fraction ϕ of OLC fillers.	126
5.2	SU8-CNT membrane prepared with ultramicrotomy for proton channeling application. the CNT channels have the length of 50 nm and diameter of 10-30 nm.	127
A.1	Probability plots of the measured CNT lengths for five different batches obtained from chosen combinations of the milling time and the rotational speed. The probabilities are plotted assuming a lognormal distribution (left column) and a Weibull distribution (right column). The solid lines indicate the corresponding theoretical probabilities.	130
A.2	Comparison between the calculated and the measured cumulative distribution functions (CDFs) of the bimodal distribution of CNT lengths for $p = 0.2$. The dashed curves are the partial contributions of the measured CDFs of the Long and Short batches.	131

List of Tables

1.1	Approximation of the percolation threshold for composites containing permeable fillers with different morphologies.	20
2.1	Characteristics of the RGO flakes (http://www.acsmaterial.com).	42
2.2	Vibration modes observed by IR spectroscopy in the SU8 sample.	66
2.3	Vibration modes observed by Raman spectroscopy of the SU8 sample [74, 149].	72
2.4	Vibration modes observed by Raman spectroscopy of the TSHAS photoinitiator.	75
4.1	Values of σ_0 , ϕ_c , and t that best fit the measured conductivity of OLC-PMMA composites.	118
4.2	Values of α that best fit the measured conductivity of OLC-PMMA composites. The corresponding best fits for T_0 are reported in brackets.	121

Acknowledgements

This dissertation would not have been possible without support of numerous people, colleagues and friends who have helped me during my Ph.D journey at EPFL. I would like to sincerely thank each and every one of them.

First and foremost, I am profoundly grateful to my thesis director Prof. László Forró for giving me the opportunity to join his group, for the freedom and trusting me to work in my own way, and for fully supporting me throughout this Ph.D. His broad knowledge in physics and deep insight in different scientific subjects was the best guide all through my thesis.

I am especially thankful to my thesis co-director, Dr. Arnaud Magrez, for scientifically guiding me during my Ph.D. He taught me a lot about research and how to clearly present my ideas and work. Most of all I am very grateful to his positive attitude, his encouragements and his kind supports during past four years.

I owe my deepest gratitude to Dr. Claudio Grimaldi, who has kindly and patiently taught me everything I know on the theory side. Without his help this thesis would not exist. I am very grateful for all the time he spent for disusing, correcting and helping with preparation of my papers.

I would like to acknowledge Prof. Paul Muralt, Prof. Jurgen Brugger, Prof. Jonathan Coleman and Prof. Jin Won Seo for accepting to be members of the jury of my doctoral exam. I would also like to acknowledge Prof. Heinrich Hofmann and Dr. Yves Leterrier for attending my candidacy exam and annual presentations and for their constructive comments which helped to improve the quality of my work. I particularly thank Yves for our collaboration, fruitful discussions and letting me use the facilities of LTC laboratory.

I am very thankful to our collaborators in the National Institute of Materials Physics in Romania for welcoming me warmly in their country and their group, and for their scientific contribution to my thesis. I send my regards to the memory of Prof. Ioan Baltog and greatly thank Dr.

Acknowledgements

Mihaela Baibarac and her group members.

My gratitude also goes to Dr. Ayat Karimi, Dr. Andrzej Sienkiewicz and Dr. Richard Gaal for their time and fruitful discussions.

Huge thank for all administrative support that I got from Evelyn and Nicole (LPMC), Laurence (GCMP), Erika, Chrystelle and Anne (EDMX). Thanks to CMi, CIME and GCMP staff for their outstanding service and help they provided. Special thanks to Daniele and Gérald for their kind helps in sample preparation.

I am delighted for working in a lab with a friendly atmosphere, among great colleagues who are always ready to share their knowledge and experience. I am grateful to Andrea, Peter and Xavier for their valuable help in the transport lab. Thanks to Endre for numerous discussions which gave me a better insight into the chemistry. Thanks to Dori for the preparation of carbon nanotube carpets. Thanks to Luka and Gaétan for pleasant coffee times. A special thank goes to Gaétan for carefully proof reading my thesis. Thanks to Ines and Lidia for their warm friendship. Many thanks to Peter, Edoardo, Márton, Daniela, Alex, Adolfo, Bibe, Pavao, Konstantis and Sergiy for being super-nice colleagues and friends. I would like to thank Massimo and Laurent, our former group members, for their kindness and help at the earlier stage of my Ph.D. I am thankful to Egon and Juan, the smart and hardworking students that I have supervised, for their contribution.

I would also like to acknowledge the Iranian community at EPFL who made the life far away from home less difficult. Special thanks to Elmira, Mahmoud, Sareh, Payam, Mohammad, and Sina, also my old friend Negar, for their friendship, for scientific, philosophical and funny lunch discussions, and all great memories at EPFL and Lausanne.

Finally, I express my deepest gratitude to my most beloved ones. My parents Zohreh and Hossein, and my sisters Mojdeh and Saba. No matter how hard it gets or how far I am, my heart is always warm for having their unconditional love and support. I cannot thank them enough.

Last but not least, I would like to thank Ramin for being my best friend and for sharing his life with me. For all his helps and supports, his patience and his sense of humor which make us laugh through the ups and downs of our life.

Thank you, Thank you all!

Lausanne, November 2016

Maryam



Maryam Majidian

Date of Birth: August 26, 1985

Address: Avenue de Lavaux 4, Pully

E-mail: maryam.majidian@epfl.ch

Phone Number: +41 (0)78 941 5696

Education:

- 2012 – 2016** Doctoral Assistant, in Materials science and materials engineering (EDMX), École polytechnique fédérale de Lausanne EPFL, Lausanne, Switzerland.
PhD Thesis: *Polymer-Carbon Nanostructure Composites: from Physics, to Chemistry, to Materials Science.*
- 2007 – 2010** Master of Science in Materials Engineering, Sharif University of Technology, Tehran, Iran.
- 2003 – 2007** Bachelor of Science in Materials Engineering, Tehran Polytechnic, Tehran, Iran,

Professional Experiences / Internships:

- Jan–Aug 2012** Trainee, Simulation of the quantum dot ion implantation in III-V nanowires, Laboratory of Semiconductor Materials, EPFL.
- 2008 – 2009** Researcher of the team for preparing Atlas of Corrosion of Iran, Niroo Research Institute, Tehran, Iran (www.nri.ac.ir)
- Jul– Sep 2006** Trainee in Razi Metallurgical Research Center (<http://www.razi-center.net>) Laboratories of metallography, mechanical tests (Tensile, Impact, Bend, Compression and Hardness) and Chemistry.

Technical Skills

- Design of experiment (DOE)
- Synthesis, graphene (CVD growth, Chemical exfoliation), carbon nanotubes (CVD growth), nano-composites
- Electron Microscopy, SEM, TEM
- Characterization, Electrical transport, Mechanical properties (nano-indentation), Optical spectroscopy (Raman, FTIR, Photoluminescence UV-Vis), Rheology and Photo-Rheology, Thermal analysis (DSC, TG).
- Clean room skills, Process Design, Photolithography, Wet etching, Dry etching.
- Soft wares: Microsoft office (Word, Excel, Power point), Photoshop, illustrator, Latex, Origin.

Honors and Awards:

- 2015 Best assistant for practical work of Physics, School of basic sciences (SB), EPFL
2015 Best Poster of EDMX research day 2015, School of engineering (STI), EPFL

Languages:

English: C2- Professional, French: B2- Intermediate, Arabic: A2- Elementary, German: A1-Basic
Persian: Native speaker

References:

- Prof. L. Forró Laboratory of Nanostructures and Novel Electronic Materials, LPMC, EPFL
Email: laszlo.forro@epfl.ch, Phone: +41 21 69 34306
- Dr. A. Magrez Crystal Growth Facility, GCMP, EPFL
Email: arnaud.magrez@epfl.ch, Phone: +41 21 69 37656

Main Publications:

- **M. Majidian**, C. Grimaldi, A. Pisoni, L. Forró, and A. Magrez, “Electrical conduction of photo-patternable SU8-graphene composite”, *Carbon* 80 (2014): 364-372.
- **M. Majidian**, C. Grimaldi, M. Baibarac, I. Baltog, A. Karimi, L. Forro, A. Magrez, “SU8-graphene: a new photo-patternable conductive polymer composite”, *Nanotech 2016 conference and expo, Washington*.
- **M. Majidian**, C. Grimaldi, L. Forró, and A. Magrez, “Quasi-universal dependence upon the nanotube mean length of the electrical conduction of carbon nanotube-epoxy composite”, *Submitted to Physical Review letters*.
- **M. Majidian**, M. Baibarac, I. Smaranda, I. Baltog, L. Forró, A. Magrez, “Influence of reduced graphene oxide on cationic photo-polymerization reactions of the SU8 photoresist”, *In preparation*.
- **M. Majidian**, A. Karsa, M. Mionić, R. Smajda, D. Fejes, A. Magrez, L. Ćirić, S. O. S. Barišić, R. Gaál, L. Forró, P. Matus, “Anisotropic thermal conductivity of carbon nanotube/SU8 composites with aligned carbon nanotubes”, *In preparation*.
- **M. Majidian**, C. Grimaldi, L. Forró, and A. Magrez, “Electrical transport in carbon onion-PMMA nanocomposites”, *In preparation*.
- A. Azizi, M. Mohammadi, S.K. Sadrnezhad, **M. Majidian**, “Morphological Study of CoNiFe-B Thin Film Fabricated on Si Substrate by Electroless Method”, *The 3rd Conference of Nanostructures (NS 2010)*, March 10-12, 2010, Kish Island, Iran
- **M. Majidian**, M. Ghorbani, A. Afshar, “Effect of Surfactant PVP on Co-deposition of MoS₂ Nano-particles with Electroless Ni-P Coating”, *The 3rd Conference of Nanostructures (NS 2010)*, March 10-12, 2010, Kish Island, Iran

